Influence of Particle Geometry on Hydrodynamic and Electrostatic Interactions

A Thesis

Submitted to the
Tata Institute of Fundamental Research, Mumbai
Subject Board of Physics
for the degree of Doctor of Philosophy

by

Harshit Joshi

International Centre for Theoretical Sciences
Tata Institute of Fundamental Research
Bengaluru, India
December, 2025

DECLARATION

This thesis is a presentation of my original research work. Wherever contributions of others are involved, every effort is made to indicate this clearly, with due reference to the literature, and acknowledgement of collaborative research and discussions.

The work was done under the guidance of Professor Rama Govindarajan at the International Centre for Theoretical Sciences, Tata Institute of Fundamental Research, Bengaluru. Prof. Samriddhi Sankar Ray served as co-supervisor.

Harshit Joshi

Harshit Joshi

In my capacity as supervisor of the candidate's thesis, I certify that the above statements are true to the best of my knowledge.

Rama Govindarajan

Date: 23 December 2025

In loving memory of my father.

ACKNOWLEDGEMENTS

I once came across a perspective that I find both amusing and deeply humbling: the sheer improbability of existing as an individual. Every past event leading to our existence is fragile, hinging on countless possibilities. What if just one of our ancestors had taken a different path? When you reflect on this, it feels even more extraordinary to have met the people who shape our lives. With this thought in mind, I pause to express my gratitude to all the wonderful people who are part of my life, and to those whose memories I continue to carry with me.

To the academic family...

I consider myself incredibly fortunate to have had Professor Rama Govindarajan and Professor Samriddhi Sankar Ray as my advisors. Their academic brilliance, coupled with their humility, understanding, and empathy, has profoundly shaped my outlook on both research and life. I owe this thesis to their invaluable guidance, encouragement, and belief in me.

I will always miss the Monday morning discussions with Professor Rama, where she would grasp my thoughts even before I finished scribbling on the board. This kind of intuitive compatibility with an advisor is something every student wishes for. I admire how she formulates research problems with a strong sense of practical relevance, a reflection of her genuine societal responsibility.

Professor Samriddhi is an artist when it comes to numerical simulations and data interpretation. His ability to build a narrative, connect seemingly unrelated ideas, and match it with boundless energy and unpredictability reminds me of artists who begin with random marks only to eventually reveal a stunning image. He is also one of the kindest people I have met, though he always shies away from hearing that.

Both Professor Rama and Professor Samriddhi have stood by me through difficult times with unwavering kindness, for which I am forever indebted.

It was a privilege to collaborate with Rahul Chajwa, Professor Sriram Ramaswamy, Professor Narayanan Menon, and Professor Anubhab Roy during my PhD. Rahul was always accessible and helpful in our discussions, and I am especially grateful for the brilliant experiments he performed during his PhD. While I had heard of Professor Sriram's genius, I had the fortune of witnessing it firsthand when he pointed out a subtle detail I had overlooked in an approximation.

Meeting Professor Narayanan during one of his visits to ICTS was an absolute delight. His patience to work together for an entire day and the enthusiasm he brought to our discussions played a vital role in completing our project.

I learned a great deal from Professor Anubhab's methodical and effective approach, from framing a research problem to identifying a compact parametric space to explore, and seeing it through to completion. I am also thankful to him for organizing a wonderful conference at IIT Madras and for kindly inviting me to participate even after the official deadline.

I am grateful to have met Dr. Brato during the final years of my PhD. His wisdom and humility have been truly inspiring. I am thankful for all the discussions we shared; they enriched my knowledge and rekindled my curiosity.

It has been a great pleasure to be part of the fluid dynamics group at ICTS. The weekly group meetings helped us connect better, support one another, and gain fresh perspectives on our work. Divya has been a constant source of inspiration through her perseverance, and I am especially thankful for her help with postdoc opportunities. I regard Saumav as someone with the most brilliant intuition I have encountered. I am particularly grateful to him for spending an evening with me, drawing flutterer shapes on my laptop using just a mouse! Anup's resilience and cheerful spirit, even in the face of challenges, have always been admirable. I appreciate Rajarshi's style of explanations, which can turn a summary into a feature film. I have truly enjoyed every interaction with Aditya Pujari, Saumyakanta, Ritwick, and Mrinal, each one filled with joy and good cheer. Despite her brief stay at ICTS, I am grateful to count Sumithra as a good friend. Siddhartha's ability to bring out visual art from data is nothing short of awe-inspiring. Sharath's calm and humble presence will always remain in my memory. Debating finite-Re effects with Arun was both fun and intellectually enriching. Prateek's friendship and support have meant a lot, especially in introducing me to souls-like games, which allowed me to feel miserable not just in research but also in video games. I am glad to know that Dylan, Anjali, and Durbar will carry forward the group's legacy. I thank Ritwick, Mrinal, Sandip, Anikat, Swapan, Answesha, Rukmani, Arun, and Prateek for making the Hyderabad trip so memorable.

To my friends...

One of the many beauties of ICTS is the absence of boundaries between different groups, which naturally fosters collaborations and, more importantly, meaningful friendships. Ankush's humor and endless chatter have been a constant source of entertainment throughout my PhD journey. Sparsh's impulsive actions, coupled with the occasional deep life talks, made him an incredibly fun and engaging presence. Aditya Rajput, the all-knowing, has been a dependable source of both academic and non-academic advice. I consider myself very fortunate that my batchmates, Ankush and Aditya, were also my office mates. I will always cherish our 4 PM breaks, Prateek entering office G109 with an apple in hand, ready for some *gupshup* with Aditya, Ankush, and me, with Sparsh occasionally joining in for laughs. Shivam's quick wit and sharp, funny remarks will be sorely missed. With his calmness and few yet wise words, Bhanu has always been delightful company. The late-night Grand Theft Auto sessions, where Akash led heists as the boss and Prateek and I acted as bodyguards, remain some of my fondest memories. Mahaveer's humor, paired with his ever-equivocal opinions, was always entertaining. Udeepta, with his polite nature and exceptional badminton skills, has become a truly memorable friend. I've also been lucky to have such wonderful batchmates in Priyadarshi, Souvik, Mukesh, Tuneer, and Omkar. The intense PES matches with Ashik were not just competitive but immensely fun. Dinner conversations with Aditya Thorat were often engaging and thought-provoking. As a member of the TIFR family, I'm grateful for access to the sports and canteen facilities at NCBS. The memories of playing badminton with friends from both ICTS and NCBS will stay with me forever. Special thanks to Soumyadeep, Udeepta, Anup, Ankush, Sparsh, Aishwariya, Kaustubh, Seema, and Swapan from the ICTS side for showing up and making the matches so much fun. From the NCBS side, it was an absolute joy to play with and against Reuben, Jitesh, Rashmi, Debosmita, Shruti, Shivani, Meghana, Sudhanand, Anantu, Rakesh, Arnab, Sweety, Ajay, and Bhushan. I will surely miss all the action on the badminton court!

I also thank all my school and undergraduate friends who stayed in touch over the years, especially Lokesh, Pranav, Rohan, Himanshu, Devender, Tanuj, and Naaz. Meeting and talking with them always felt like reconnecting with my younger self.

To my family...

If it were not for my family, I would not be here writing any of this. The sacrifices my parents have made so that I can live a comfortable life, the sacrifices my sisters have made so that their brother gets the best, these have kept me going through the hardest times.

My father was calm, decisive, and deeply responsible. He taught me the value of discipline and of owning one's actions and decisions. I remember our evening walks just after I finished school, when I would share fascinating stories of scientific discoveries I had learned from the show *Cosmos*. Perhaps, through those stories, he sensed my passion, for he was happy when I chose the path of scientific research. He supported me throughout this long PhD marathon; I only wish he could see me cross the finish line. His qualities will always inspire me to become a better person, and I will forever cherish his memory.

My mother has always been the most loving and overprotective person in my life. Being the youngest and only son, she was always hesitant to send me away from home. Even today, she worries if she doesn't hear from me in the morning or by late evening. Yet she understands the paradox of sacrificing comfort in order to earn comfort. Her unconditional love and support, and my sisters' willingness to shoulder responsibilities, are the reasons I was able to continue and finish my PhD after the loss of my father.

My eldest sister, Kunnu Di, has always been as overprotective of me as our mother, making sure I didn't get even a scratch as a kid. Neetu Di, on the other hand, is the tough one, never hesitating to scold or even smack me if needed, just to make sure I didn't get spoiled! I commend Bhawana Di for her hard work, earning a great job, and helping our family move to Dehradun. I have the happiest memories from that time and place. I am grateful to Suman and my cute, talkative niece Shivansh for staying with our mother and taking care of her when she needed it the most. I also cherish the little fights Suman and I had as kids. Our beloved dog Tuffy joined our family when I began school and stayed until I finished it. His memory inspires me to create a life where I can care for both my family and the dogs yet to come. My brother-in laws: Anil Jijaji, Prafull Jijaji, Ravindra Jijaji, and Ujjawal Jijaji have been very helpful and supportive at all times. I am grateful for each one of my family members.

I extend my heartfelt thanks to my family and extended family for their encouragement throughout this journey. Though I may not be able to list every name, I carry deep gratitude for each of you. I'm especially happy to see our youngest cousin, Rahul, becoming so responsible and mature; it fills me with pride.

It is only through my family's unwavering support and countless sacrifices that I have made it this far. I will forever be indebted to them.

To the stars shining in the background...

I extend my heartfelt gratitude to the working force of ICTS, the administrative and academic staff, housekeeping staff, security personnel, and all others, whose efforts have created a warm and supportive environment, much like a family. I am also thankful to the Department of Atomic Energy, Government of India, for the stipend and contingency grants, which not only facilitate research but also affirm the value of research scholars. My thanks also go to the Infosys International Exchange Program at ICTS for funding my visit to a conference in France, where I had the opportunity to present my work and learn from others.

I would also like to thank the developers of the NovaThesis template for their effort in making it so well-designed and accessible [1].

This thesis is not mine alone; it is woven from the guidance, encouragement, and generosity of many. They have lifted me onto their shoulders, allowing me to see a little farther into the vast expanse of the unknown and the undiscovered.

"And medicine, law, business, engineering, these are noble pursuits and necessary to sustain life. But poetry, beauty, romance, love, these are what we stay alive for. To quote from Whitman, "O me! O life!... of the questions of these recurring; of the endless trains of the faithless... of cities filled with the foolish; what good amid these, O me, O life?" Answer. That you are here - that life exists, and identity; that the powerful play goes on and you may contribute a verse.
What will your verse be?"

— **Dead Poets Society (1989)**, dir. Peter Weir
(written by Tom Schulman)

LIST OF FIGURES

CONTENTS

Appendices

ABSTRACT

This thesis investigates the role of geometry in shaping the interactions and dynamics of particles in fluid and electrostatic environments. Motivated by asymmetric geometries and the resulting adaptive motion in nature, particularly in sedimentation in the viscosity-dominated regime, we use a theoretical and simulation-based framework to study the dynamical behaviour of both single and multiple particles.

At the single-particle level, we show that geometric asymmetries give rise to couplings between translation and rotation, leading to settling behaviours as complex as quasi-periodic motion with chiral trajectories. At the collective level, we explore how interparticle interactions mediated by hydrodynamic fields can lead to instabilities and clustering. The mathematical analogy between electrostatics and microhydrodynamics is used to derive a set of generalized Faxén's laws, enabling a unified treatment of interactions across physical domains through the method of reflections. A unifying simulation framework based on the boundary-integral method is used to study problems in both microhydrodynamics and electrostatics. We also investigate how particle–fluid momentum coupling shapes two-dimensional turbulence.

The results shed light on fundamental mechanisms underlying aperiodic dynamics that can lead to enhanced mixing at low Reynolds number, instabilities that result in pattern and cluster formation due to hydrodynamic and electrostatic interactions in soft matter systems, and provide theoretical foundations for future experimental and computational studies in microfluidics and colloidal science.

Keywords: Quasi-periodic sedimentation, Chiral trajectories, Non-modal instability, Pseudospectrum, Generalized Faxén's laws, Electrostatic torque, Dusty turbulence, Intermittency, Energy & Enstrophy cascade

1

INTRODUCTION

"I went to the woods because I wished to live deliberately,
to front only the essential facts of life,
and see if I could not learn what it had to teach,
and not, when I came to die, discover that I had not lived."
— Henry David Thoreau, Walden (1854)

The challenge of modeling nature's complexity is vividly captured in the opening lines of Mandelbrot's The Fractal Geometry of Nature [2]: *"Clouds are not spheres, mountains are not cones, coastlines are not circles, and bark is not smooth, nor does lightning travel in a straight line."* Despite the intricate and irregular shapes found in nature, simple and symmetrical geometries have long been the go-to choice for mathematical models, primarily due to their analytical tractability. Spheres, for instance, have served as idealized representations in problems ranging from the theory of gravitation and electromagnetism to fluid dynamics, offering mathematical clarity and solvable forms. While such simplifications often provide valuable first-order insights, they also risk conveying the impression that shape is merely a passive detail when, in many systems, from the self-assembly of nanocrystals [3, 4] and the phase behaviour of bent-core liquid crystals [5, 6], to the mechanical response of granular media [7] and the deformation dynamics of atomic nuclei [8], shape actively determines the underlying physics.

A common setting where geometry plays a central role is in how objects interact with their surrounding environment, such as a fluid, or with one another. Striking examples of this arise in the realm of *microhydrodynamics*. Before exploring these examples, let us first build some intuition about this regime, which forms the central focus of this thesis.

1.1 The essence of microhydrodynamics

Microhydrodynamics refers to fluid dynamics at microscales. The Reynolds number governs the physics of fluid flow and the motion of objects within it. For bodies moving in a fluid, it is defined as the ratio of inertial forces to the viscous forces (see Figure 1.1):

$$Re = \frac{f_{inertial}}{f_{viscous}} = \frac{\rho_f V^2 a^2}{\mu a V} = \frac{\rho_f V a}{\mu}. \tag{1.1}$$

Here, ρ_f is the density of the fluid, V is the speed of the moving body, a is the size of the body, and μ is the dynamic viscosity of the fluid.

For a human swimming in water, the Reynolds number can be on the order of 10^5. This high-Re regime is the one we are most familiar with in everyday life. To experience a low Reynolds number, one would have to swim very slowly in a fluid like honey (where very slowly is relative to the typical human swimming speed of about 1m/s). Another way to reduce Re is by decreasing the characteristic length scale a. Fishes, for instance, swim at relatively lower Reynolds numbers, around $Re \approx 10^2$. Microorganisms, on the other hand, operate at extremely low Reynolds numbers, on the order of $Re \approx 10^{-4}$. This is the essence of microhydrodynamics: it concerns length scales so small that inertial effects become negligible, and viscous forces dominate. To put this into perspective, if you were to shrink down to about 100μm, moving through water would feel like swimming through a pool of honey! In this thesis, we explore the realm of microhydrodynamics, a viscosity-dominated regime characterized by negligible Reynolds numbers.

A lot of flow features can be understood by looking at the governing equations of the fluid. We delay the detailed mathematical derivations to the next chapter and discuss only the qualitative features of the subject. The fluid flow in the negligible Re regime is governed by the *steady Stokes equation*, given by

$$\mu \nabla^2 \boldsymbol{u} - \boldsymbol{\nabla} p + \boldsymbol{f} = \boldsymbol{0}, \quad \boldsymbol{\nabla} \cdot \boldsymbol{u} = 0. \tag{1.2}$$

Here μ is the dynamic viscosity, $\boldsymbol{u}$ is the velocity field, p is the pressure field, and $\boldsymbol{f}$ is an external force per unit volume acting *on* the fluid. Contrasting this with the Navier-Stokes equation, which has finite Re effects in the form of convection terms $\partial_t \boldsymbol{u}$ and $\boldsymbol{u} \cdot \boldsymbol{\nabla} \boldsymbol{u}$, it is clear that the Stokes equation is a linear partial differential equation. The absence of the convective terms has the following important implications:

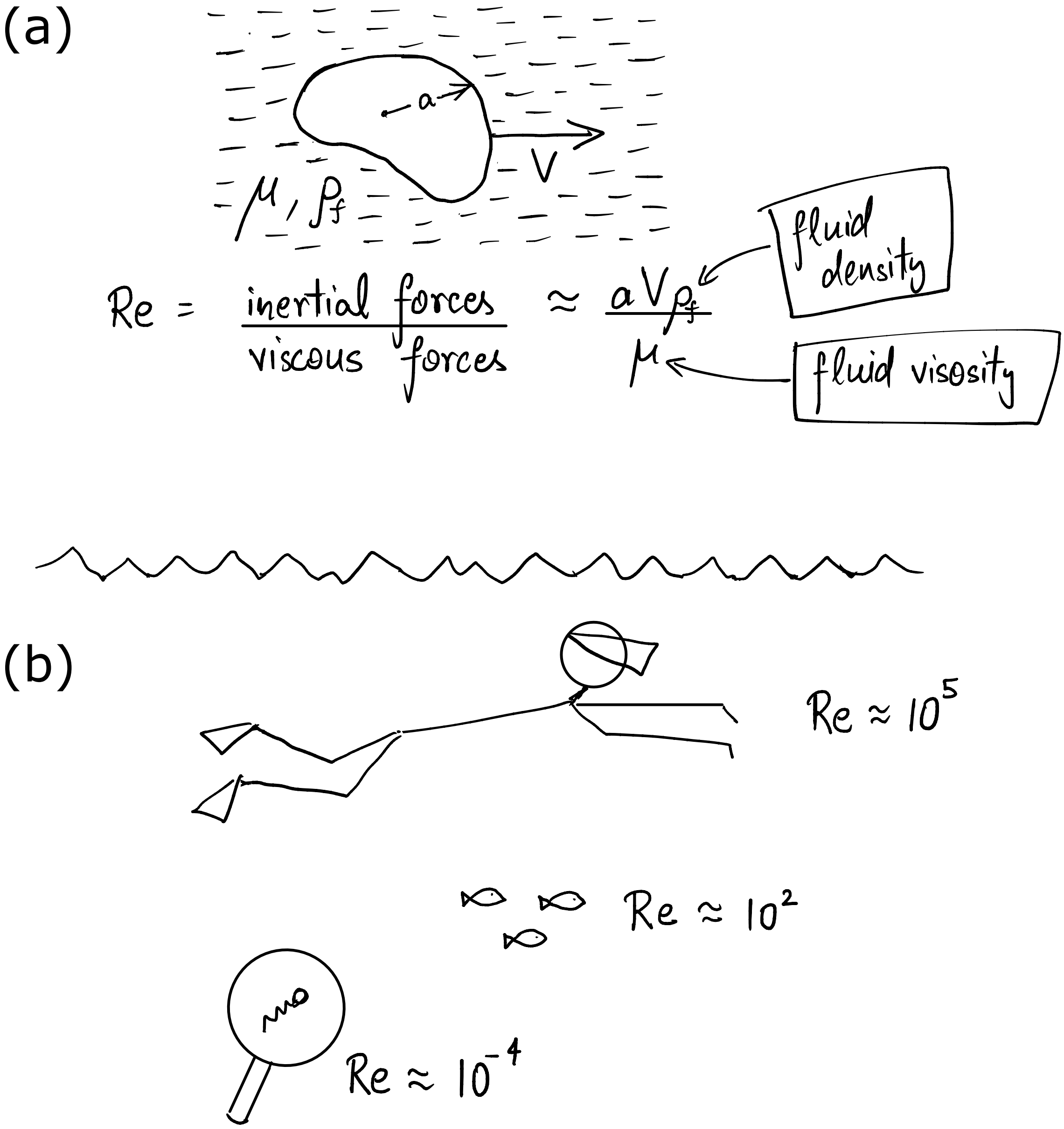

Figure 1.1: Redrawn from Purcell's "Life at low Reynolds number" [9]. (a) shows the definition of the Reynolds number for a body moving in a fluid. (b) shows how the Reynolds number decreases as one goes towards the microscopic scale.

1.1.1 Linearity

This is the most important feature of the flow in microhydrodynamics. It says that the fluid velocity field depends linearly on the external forcings. It further implies that the linear velocity $\boldsymbol{V}$ and the angular velocity $\boldsymbol{\Omega}$ of a body are linearly related to the hydrodynamic force $\boldsymbol{F}^h$ and torque $\boldsymbol{T}^h$ acting on the body [10–14],

$$\begin{bmatrix} \boldsymbol{V} \\ \boldsymbol{\Omega} \end{bmatrix} = -\mu^{-1} \boldsymbol{\mathcal{M}} \cdot \begin{bmatrix} \boldsymbol{F}^h \\ \boldsymbol{T}^h \end{bmatrix}. \tag{1.3}$$

The proportionality constant $\boldsymbol{\mathcal{M}}$ is called the mobility matrix, which only depends on the size and geometry of the body. Note that we have assumed zero background flow while writing equation (1.3). Thus, the idea that geometry influences dynamics arises naturally in the realm of microhydrodynamics. As we shall see, the geometric symmetries of a body can be used to determine the structure of its mobility matrix [14, 15].

This linearity of the Stokes equation enables powerful analytical techniques, including the use of Green's functions, singularity solutions, the principle of superposition, and boundary integral formulations [10, 16]. These four tools form the foundation on which this thesis is built.

In contrast, the nonlinear term $\boldsymbol{u} \cdot \nabla \boldsymbol{u}$ in the Navier-Stokes equation is responsible for transferring energy and momentum across different length scales, as can be examined using the Fourier transform of the equation. The absence of this nonlinear term in the Stokes equation implies that the flow structures at different length scales remain decoupled. This is in contrast to our intuition from high Reynolds-number flows, where structures at one length scale can give rise to structures at other scales, for example, the wake behind a moving object [17, 18].

1.1.2 Instantaneity

The absence of a time-derivative term in the Stokes equation implies that the fluid's response is instantaneous: the state of the fluid at any moment depends only on the instantaneous configuration of the immersed bodies, not on their history. As a result, any motion of a body is immediately reflected in the entire velocity field. Physically, however, the propagation of flow disturbances in a viscous fluid occurs via diffusion of momentum. For a disturbance to reach a distance l, the characteristic time scale is the *diffusive time* $\tau_d \sim (l^2/\nu)$, where ν is the kinematic viscosity. Instantaneity is a valid assumption only when this time scale is smaller than other relevant dynamical time scales, most notably, the *convective time* scale $\tau_c \sim (l/V)$, where V is a typical velocity of the body.

Since τ_d grows quadratically with l while τ_c grows linearly, there exists a critical length scale l_c beyond which this assumption breaks down. Setting $\tau_d = \tau_c$ gives

$$l_c = \frac{\nu}{V} = \frac{a}{Re}, \tag{1.4}$$

where a is the size of the body and Re is the Reynolds number based on that scale. This shows that even in flows with very small Re, the assumption of instantaneity eventually fails at distances much larger than the body size. Thus, in unbounded domains, one must be cautious: finite-Re effects become important at distances of order a/Re. In this thesis, we will work in the theoretical limit of $Re = 0$, where such effects are formally absent.

While the absence of the nonlinear convective term precludes the formation of wakes with multiple interacting length scales, the instantaneity of Stokes flow further rules out phenomena like vortex shedding, commonly seen in high-Re flows. Nevertheless, recirculation zones can still occur behind asymmetric or bluff bodies [19, 20], though they remain steady and fixed relative to the body rather than evolving or shedding downstream.

1.1.3 Reversibility

The Stokes equation possesses a key symmetry: under the transformation $p \to -p$, $\boldsymbol{f} \to -\boldsymbol{f}$, and $\boldsymbol{u} \to -\boldsymbol{u}$, the equations remain unchanged. This implies that the reversed flow field $-\boldsymbol{u}$ is also a valid solution, provided the pressure and force fields are simultaneously reversed. This property is known as reversibility and has powerful consequences when combined with the geometric symmetries of a system [11, 12].

For instance, it can be shown that a pair of identical spheres sedimenting under gravity will maintain their relative positions during descent [11]. Similarly, a sphere sedimenting near a rigid wall cannot drift toward or away from the wall [12]. A spheroid cannot change its orientation as it settles, as illustrated in Figure 1.2. More broadly, a body undergoing a reciprocal (time-reversible) cyclic deformation cannot achieve net locomotion, an insight formalized in Purcell's *scallop theorem* [9, 21, 22]. These results illustrate how far one can go by exploiting the symmetries of the governing equations, even without solving them explicitly.

Importantly, such reversibility and the constraints it imposes break down at a finite Reynolds number. In high-Re regimes and unsteady Stokes regimes, history matters, and such symmetry-based arguments no longer suffice.

While we have highlighted some key properties of Stokes flow and contrasted them with the finite Re effects, the discussion here has focused selectively on

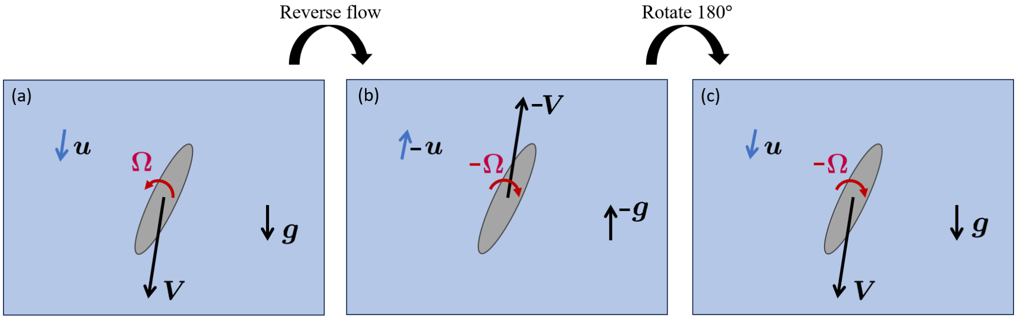

Figure 1.2: **Demonstration of reversibility ruling out rotation in a settling spheroid**. (a) A spheroid settles under gravity with linear velocity $\boldsymbol{V}$ and angular velocity Ω, dragging nearby fluid with it. The surrounding fluid velocity field is denoted by $\boldsymbol{u}$ and gravity points in the direction of $\boldsymbol{g}$. (b) Upon reversing the forces (i.e., $\boldsymbol{g} \to -\boldsymbol{g}$), the flow and the dynamics reverse. (c) Rotating the system by 180° restores the original geometric configuration, except for the sign of the angular velocity. By the uniqueness of Stokes flow, it follows that $\boldsymbol{\Omega} = \boldsymbol{0}$.

aspects most relevant to the thesis. For a broader and pedagogically rich treatment of fluid mechanics, the National Committee for Fluid Mechanics Films (NCFMF) released an excellent series of educational videos and accompanying texts in the 1960s, available online at MIT's website. Despite their age, the concepts are conveyed through remarkably clear demonstrations and remain invaluable. In particular, the film by G.I. Taylor on *Low Reynolds Number Flow* beautifully illustrates many features of microhydrodynamics discussed here, and more. Another excellent source is EM Purcell's classic lecture, *Life at Low Reynolds number* [9], which captures the essence of how strikingly different our experience would be if we lived in a low *Re* world, especially in the context of swimming.

1.2 Asymmetric Geometries and Adaptive Motion in Nature

As seen in the last section, the physics of fluid flow changes fundamentally with the Reynolds number. In the high-*Re* regime, the motion of objects through a fluid depends crucially on the wake structures they generate. For example, by simply flapping their tails, fish can transfer momentum backward into the wake, thereby propelling themselves forward [23, 24]. However, this strategy fails in the low-Reynolds-number regime: as stated by the scallop theorem [9, 21, 22], a fish cannot achieve net propulsion by simply flapping its tail in such highly viscous environments. This constraint was elegantly demonstrated by G.

I. Taylor through his classic experiments on low Reynolds number flows. At low Re, inertial effects are negligible, and viscous forces dominate. To overcome this, microorganisms have evolved remarkably clever strategies to achieve directed motion by exploiting shape asymmetry. Bacteria, for instance, possess filament-like appendages called *flagella*, each of which adopts a helical shape and rotates like a rigid corkscrew to generate propulsion through viscous drag [13, 21]. In contrast, eukaryotic cells such as spermatozoa use flexible flagella, which they deform in the form of travelling waves to achieve propulsion [13, 21]. This type of drag-based propulsion can be understood through the concept of *drag anisotropy*, which refers to the directional dependence of viscous drag on an elongated body (such as a slender rod). Unlike a sphere, which experiences a drag force directly opposite to its direction of motion, an anisotropic body encounters drag forces that vary with orientation, resulting in a net force that is not necessarily aligned opposite to its motion. This principle of drag anisotropy is beautifully illustrated in [13] for microorganisms that use flagella for propulsion. Each segment of a flagellum can be treated as a slender rod that experiences a local drag force with a nonzero component in the axial direction. These axial components add up constructively along the length of the flagellum, resulting in a net propulsive force.

Another interesting example where shape asymmetry plays a crucial role in dynamics is that of plankton. Plankton are a diverse group of organisms that inhabit the ocean and, being unable to swim against the current, typically drift along with the surrounding flow. Among them, Phytoplankton, which rely on photosynthesis, perform diel vertical migration, descending to nutrient-rich deeper layers at night and ascending to well-lit surface waters during the day for light [25, 26]. However, turbulence in the upper layers of the surface can be harmful to these organisms [27–29]. A recent study [30] showed that certain phytoplankton, upon sensing turbulent conditions, can alter their migration strategies by changing their shape. Specifically, phytoplankton with fore-aft asymmetry, shapes that allow them to swim upward against gravity, can transition to fore-aft symmetric shapes and begin migrating downward, along gravity. The stable orientation of the body in flow is determined by a balance between the gravitational torque and the hydrodynamic torque about the geometric center. The latter is influenced by the position of the hydrodynamic center of resistance, which in turn depends sensitively on the shape of the organism. By modulating their shape, these organisms effectively tune the hydrodynamic torque, demonstrating the critical role that particle geometry plays in governing dynamics in fluid environments.

Plankton play a foundational role in the oceanic carbon cycle by converting atmospheric CO_2 into organic matter via photosynthesis [31, 32]. As these organisms die or are consumed, their remains, along with fecal pellets and other detritus, form marine snow that sinks into the deep ocean. This sedimentation is central to the *biological carbon pump*, by which carbon is effectively sequestered for periods ranging from months to millennia [33, 34]. Understanding the physical mechanisms that govern the sedimentation of such anisotropic and often irregularly shaped particles is crucial, not just for marine ecology, but also for global climate models.

1.3 Role of geometry in single body sedimentation

Although the ecological significance of sedimentation in marine environments has only been realized relatively recently, sedimentation itself has long been exploited in practical applications, particularly for separating particles based on their size or density. It is also a ubiquitous natural process, evident in phenomena such as the descent of raindrops and dust in the atmosphere, or the deposition of sediments in rivers. Consequently, the sedimentation behaviour of bodies ranging from spheres to ellipsoids has been the subject of extensive study for many decades [12, 14, 35, 36].

As previously discussed, the Reynolds number (Re) plays a crucial role in their settling behaviours. However, another key parameter is the density ratio ρ_r between the particle and the surrounding fluid. As we shall see in Chapter 2, if $\rho_r Re \ll \mathcal{O}(1)$, the particle inertia becomes negligible. This, along with $Re \ll \mathcal{O}(1)$, defines the so-called *overdamped limit*, in which the external forces and torques acting on the body are instantaneously balanced by the corresponding hydrodynamic resistances. The steady sedimentation of a single sphere in the overdamped limit has been understood since Stokes' seminal solution in 1851, over 170 years ago. The simplicity of the overdamped limit as well as the geometry of the sphere allows one to determine its linear velocity $\boldsymbol{V}$ and angular velocity $\boldsymbol{\Omega}$ analytically, given by the well-known Stokes law:

$$\mu \begin{bmatrix} \boldsymbol{V} \\ \boldsymbol{\Omega} \end{bmatrix} = - \begin{bmatrix} (6\pi a)^{-1}\mathbb{1} & \boldsymbol{0} \\ \boldsymbol{0} & (8\pi a^3)^{-1}\mathbb{1} \end{bmatrix} \cdot \begin{bmatrix} \boldsymbol{F}^h \\ \boldsymbol{T}^h \end{bmatrix} = \begin{bmatrix} (6\pi a)^{-1}\mathbb{1} & \boldsymbol{0} \\ \boldsymbol{0} & (8\pi a^3)^{-1}\mathbb{1} \end{bmatrix} \cdot \begin{bmatrix} \boldsymbol{F}^g \\ \boldsymbol{0} \end{bmatrix}, \quad (1.5)$$

where $\boldsymbol{F}^g$ is the buoyancy corrected weight of the sphere, a is the radius of the sphere, μ is the dynamic viscosity of the fluid. In writing the second equality in equation (1.5), we have used the fact that in the overdamped limit, hydrodynamic force and torque are always balanced by external force and torque. Here external force is due to gravity, i.e., $\boldsymbol{F}^h + \boldsymbol{F}^g = \boldsymbol{0}$, and the gravitational torque about the centre of a sphere of uniform density is zero, i.e., $\boldsymbol{T}^h = \mathbf{0}$. Comparing this with equation (1.3), we see that the structure of $\boldsymbol{\mathcal{M}}$ consists of only diagonal submatrices, which are proportional to the 3×3 identity matrix $\mathbb{1}$. This simplicity in the structure of $\boldsymbol{\mathcal{M}}$ of a sphere is a result of its geometric symmetries.

We emphasize an important feature of the overdamped limit: the linear relationship between external forces and the velocity of a body, unlike the Newtonian regime, where external forces are proportional to the rate of change of velocity. Thus, one can think of the overdamped limit as the Aristotelian world where force is needed to maintain motion.

This overdamped limit may seem uneventful since a sphere settling in this limit falls with its terminal velocity. However, a sphere possesses numerous geometric symmetries. If one instead considers an ellipsoid, it can drift horizontally as it settles vertically [10, 13, 14], a consequence of the drag anisotropy, as mentioned before. The mobility matrix $\boldsymbol{\mathcal{M}}$ of an ellipsoid is a diagonal matrix in the coordinate axes aligned with its principal axes frame. Drag anisotropy manifests itself as the diagonal elements being unequal [10, 14]. It can be shown (see Chapter 3) that any shape with an inversion symmetry ($\boldsymbol{x} \to -\boldsymbol{x}$) simply settles without rotating, in the absence of any external torque. In other words, the off-diagonal terms in the mobility matrix of a body with inversion symmetry are zero. This includes a wide range of shapes from spheres to ellipsoids. To achieve rotation upon sedimentation without an external torque, and hence non-trivial settling patterns, one needs to break the inversion symmetry. The *translation-rotation coupling* arises when the mobility matrix $\boldsymbol{\mathcal{M}}$ of a body has non-zero off-diagonal elements, which couples hydrodynamic force and torque. Note that lack of inversion symmetry is a necessary but not sufficient condition for translation-rotation coupling; additional symmetries like rotational symmetry about an axis can further restrict the translation-rotation coupling [14].

An intriguing example of translation–rotation coupling in a geometrically symmetric object was proposed by Lord Kelvin in 1871 [14, 37], in the form of the *isotropic helicoid*, a chiral body resembling a sphere with fins that remains isotropic in its resistance properties. With the widespread occurrence of chirality in microorganisms, the dynamics of chiral bodies and the resulting coupling between translation and rotation have attracted considerable interest [38–41]. More recently, it has been observed that even achiral bodies can exhibit chiral settling trajectories, revealing unexpected richness in sedimentation dynamics [42, 43]. While there have been studies addressing the settling behaviour of arbitrarily shaped bodies [38, 44–46], their abstract formulations often obscure specific dynamical features that emerge in more structured cases, particularly those that admit translation–rotation coupling while preserving certain geometric symmetries. One such feature is the presence of a conserved quantity that governs the dynamics of bodies with two planes of symmetry, a feature absent in the fully general case of asymmetric bodies. Chapter 3 is dedicated to the study of such bodies with two planes of symmetry, which we refer to as *di-bilaterals*. These can be viewed as a natural generalization of ellipsoids, which possess three planes of symmetry. Thus, di-bilaterals help bridge the gap between the well-understood case of ellipsoids and the general category of arbitrarily shaped bodies. The study presented in Chapter 3 offers a systematic and predictive framework for classifying and understanding their settling dynamics.

1.4 Role of geometry in collective sedimentation

In most of the practical scenarios, multiple bodies are involved in the sedimentation process. While each body may exhibit intricate settling patterns due to its complex geometry, the presence of nearby bodies can significantly alter its dynamics. Even highly symmetric bodies such as spheres or spheroids can experience translation-rotation coupling as a result of hydrodynamic interactions [10–12, 14].

A helpful way to conceptualize these interactions is by adapting a quote from John Archibald Wheeler to the context of fluid dynamics: *fluid tells particles how to move; particles tell fluid how to flow*. In this way, the fluid acts as a mediator of the coupling between bodies. This mediation is conceptually similar to other physical systems: spacetime mediates interactions between massive bodies in general relativity, while electromagnetic fields mediate forces between charged particles. There exists a close mathematical analogy between microhydodynamics and electrostatics, an analogy that is explored in detail in Chapter 5 of this thesis.

Hydrodynamic interactions between multiple bodies in a viscous fluid play a central role in shaping their collective behaviour. These interactions arise because each body disturbs the surrounding fluid, and this disturbance, in turn, influences the motion of neighbouring bodies. Hydrodynamic interactions between two force-driven bodies are long-range interactions that decay as $1/R$ in an unbounded domain, where R is the dimensionless separation between the two bodies [10–12, 14]. Therefore, in the context of sedimentation, where the external flow field is typically absent, these long-range interactions play a dominant role in determining the dynamics.

There is a natural way to generalize the concept of the mobility matrix for multiple bodies. In the overdamped limit, for two hydrodynamically interacting bodies in an otherwise quiescent fluid, the mobility formulation looks like

$$\begin{bmatrix} \boldsymbol{V}_1 \\ \boldsymbol{V}_2 \\ \boldsymbol{\Omega}_1 \\ \boldsymbol{\Omega}_2 \end{bmatrix} = \mu^{-1} \begin{bmatrix} \begin{bmatrix} \boldsymbol{a}_{11} & \boldsymbol{a}_{12} \\ \boldsymbol{a}_{12} & \boldsymbol{a}_{22} \end{bmatrix} & \begin{bmatrix} \boldsymbol{b}_{11} & \boldsymbol{b}_{21} \\ \boldsymbol{b}_{12} & \boldsymbol{b}_{22} \end{bmatrix} \\ \begin{bmatrix} \boldsymbol{b}_{11} & \boldsymbol{b}_{12} \\ \boldsymbol{b}_{21} & \boldsymbol{b}_{22} \end{bmatrix} & \begin{bmatrix} \boldsymbol{c}_{11} & \boldsymbol{c}_{12} \\ \boldsymbol{c}_{12} & \boldsymbol{c}_{22} \end{bmatrix} \end{bmatrix} \cdot \begin{bmatrix} \boldsymbol{F}_1^e \\ \boldsymbol{F}_2^e \\ \boldsymbol{T}_1^e \\ \boldsymbol{T}_2^e \end{bmatrix}. \tag{1.6}$$

Note that we have used the fact that the mobility matrix is symmetric [10–12] while writing equation (1.6). Hydrodynamic interactions manifest both as couplings in the off-diagonal elements and as corrections to the diagonal elements of the mobility matrix. These couplings and corrections not only depend on the relative positions of the bodies but also on the orientations of their principal axes, an aspect not explicitly highlighted in equation (1.6) for notational clarity. In the far field regime, the mobility matrix can be computed using the method of reflections, as demonstrated in Chapter 2. It is straightforward to generalize the mobility formulation to more than two interacting bodies.

An interesting example of viscosity-driven instability was demonstrated by Crowley [47] in 1971. Through both theoretical analysis and experiments, he showed that a one-dimensional lattice of spheres sedimenting in a viscous fluid is unstable to perturbations in particle positions. Hydrodynamic interactions between the spheres reinforce clustering in regions where the spheres are initially closer together, leading to the formation of valley-like regions of concentrated particles, as shown in Figure 1.3. We refer to this clustering mechanism as *Crowley mechanism*.

A more recent study by Chajwa et al. [48] investigated a similar setup, replacing spheres with discs arranged in a one-dimensional lattice. This problem, explored both theoretically and experimentally, highlights yet another important role of particle geometry in sedimentation dynamics. Due to drag anisotropy, each disc experiences lateral drift during settling, depending on its orientation. As with the spheres, hydrodynamic interactions drive clustering; however, the orientation-dependent drift allows discs to escape the clustering process (see Figure 1.3). We refer to this counter-mechanism as the *drift mechanism*.

A linear stability analysis revealed that beyond a critical lattice spacing, the fixed point becomes neutrally stable rather than unstable. Interestingly, despite this neutral stability, experiments showed a different form of lattice disruption: the discs formed pairs and separated, rather than aggregating in valleys (see Figure 1.4). This behaviour was explained by non-modal growth of perturbations, a feature often missed by classical eigenvalue-based stability analyses.

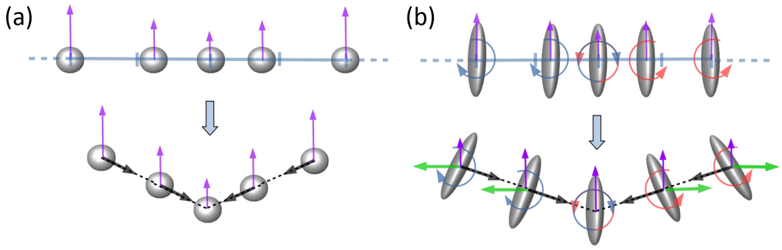

Figure 1.3: **Schematic illustrating the disruption of a one-dimensional lattice of sedimenting (a) spheres and (b) discs upon perturbation**. Adapted from Chajwa et al. [48]. (a) The sphere near the center sediments faster due to the downward flow induced by neighboring spheres. As a valley forms, spheres on either side are drawn inward (black arrows) by hydrodynamic interactions, leading to clustering. (b) Similar hydrodynamic interactions promote clustering at valleys (black arrows). However, for discs, orientation-dependent lateral drift (green arrows) counteracts this clustering, allowing escape from the valley.

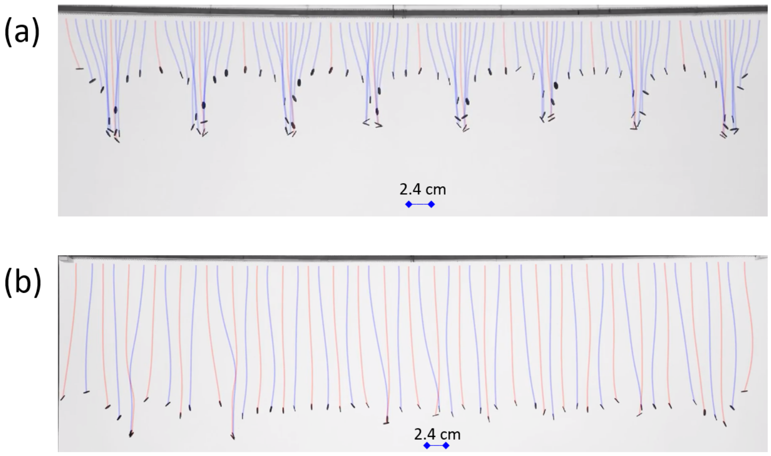

Figure 1.4: **Experiments showing different types of clustering following lattice disruption of sedimenting discs**. Experiments by Rahul Chajwa. (a) For lattice spacings smaller than the critical value, discs cluster at the valleys due to dominant Crowley-type instability. (b) For spacings larger than the critical value, discs separate into pairs away from the valleys, as the orientation-induced drift mechanism dominates over the Crowley mechanism.

The far-field model used to describe hydrodynamic interactions loses accuracy as the discs approach one another to form clusters. To capture the close-range dynamics more accurately and to quantify the nature of these clusters, it was necessary to improve the interaction model. Beyond quantification, an improved model also has implications for the system's stability. In the neutrally stable regime, all eigenvalues lie precisely on the imaginary axis, making the system structurally unstable. Small changes in the interaction model can shift the eigenvalues off the axis, thereby altering the qualitative nature of the stability. Moreover, since the original system was shown to be non-normal, and a hallmark of non-normal operators is that their eigenvalues are highly sensitive to small perturbations [49], stability analysis using the improved interaction model becomes essential. These issues are addressed in detail in Chapter 4 of this thesis.

1.5 Connections to Electrostatics

Ice crystals in atmospheric clouds often grow into complex hexagonal shapes, but for many modeling purposes, particularly in fluid and electrostatic interactions, they are effectively approximated as spheroids due to their elongated or flattened forms [50–52]. This simplification captures their essential anisotropy while allowing analytical or semi-analytical approaches to their dynamics and interactions.

In turbulent storm clouds, ice crystals undergo frequent collisions and interactions with supercooled water droplets. These collisions, especially in the presence of differential terminal velocities and turbulent flow, result in the separation and transfer of electrical charges [53–57]. The process, known as non-inductive charging, is one of the primary mechanisms believed to be responsible for charge separation in thunderstorms, eventually leading to lightning. This naturally leads to the question of how anisotropic charged bodies like spheroids interact electrostatically. Unlike spheres, the interaction between charged spheroids depends not only on their separation but also on their relative orientations, adding a layer of geometric complexity. These considerations motivate the study of electrostatic interactions between anisotropic bodies, such as spheroids, to better understand the role of shape in the collective dynamics of charged particles in both atmospheric and synthetic systems.

The equations governing electrostatics are one tensorial level lower than those of Stokes flow. To draw a direct analogy: the electric potential, which satisfies the Poisson equation, corresponds to the fluid velocity field in Stokes flow, which also satisfies a Poisson-like equation, with the pressure field acting as a Lagrange multiplier enforcing incompressibility [11]. The electric field, being the gradient of the potential, corresponds to the stress tensor in Stokes flow. Similarly, charge density in electrostatics is analogous to force density in Stokes flow. Thus, at the level of governing equations and their associated physical quantities, a direct correspondence can be made between the two systems. From the perspective of boundary conditions, the no-slip condition on the surface of a rigid body in Stokes flow requires specifying the rigid body velocity on the surface. This is analogous to specifying the total charge (or, equivalently, constant potential) on the surface of a perfect conductor in electrostatics.

With this analogy in place, one can see that the mobility formulation in Stokes flow has an electrostatic counterpart, known as the potential matrix formulation [58]. In the electrostatic setting, two perfect conductors carrying charges Q_1 and Q_2 interact such that constant potentials V_1 and V_2 are maintained on their surfaces. The charges and potentials are linearly related through the potential matrix $\mathbf{\Phi}_M$, in direct analogy with how forces and velocities are related via the mobility matrix in Stokes flow. This linear relation is given by,

$$\begin{bmatrix} V_1 \\ V_2 \end{bmatrix} = \mathbf{\Phi}_M \cdot \begin{bmatrix} Q_1 \\ Q_2 \end{bmatrix}, \quad \mathbf{\Phi}_M = \frac{1}{4\pi\epsilon_0 a} \begin{bmatrix} \Phi_{11} & \Phi_{12} \\ \Phi_{12} & \Phi_{22} \end{bmatrix}, \tag{1.7}$$

where we have used the fact that the potential matrix is symmetric. Here ϵ_0 is the permittivity of the free space and a is the typical size of the conductor. One can compare equation (1.7) with the equation (1.6) to see the similarities between the two formulations. Since the length scale is factored out, the elements of $\mathbf{\Phi}_M$ only depend on the geometry of the conductors. In the far field regime, the potential matrix can be computed by extending the idea of the method of reflections from microhydrodynamics to electrostatics, as demonstrated in Chapter 2.

Since electrostatic systems are conservative, the energy of a given configuration of two conductors can be expressed as [59, 60]

$$W = \boldsymbol{Q}^T \cdot \mathbf{\Phi}_M \cdot \boldsymbol{Q}, \tag{1.8}$$

where $\boldsymbol{Q} = (Q_1, Q_2)$ is the vector of charges. By differentiating this energy with respect to the positions and orientations of the conductors, one can compute the electrostatic forces and torques acting on them. This formulation naturally extends to systems with more than two conductors using the potential matrix approach.

While spheroids serve as effective models for ice crystals, detailed analyses of electrostatic interactions between anisotropic bodies remain limited [61–65]. In contrast, electrostatic interactions between charged spheres have been studied extensively using methods of images and bi-spherical coordinates since the time of Maxwell [66–72]. Notably, it has been shown that even like-charged spheres can attract each other due to induced polarization effects [67, 73–75]. Such induction-driven forces have important implications for the collision efficiency of charged sedimenting particles [74–76]. However, these studies are largely confined to pairs of spheres.

For anisotropic bodies such as spheroids, the lack of symmetry and absence of convenient coordinate systems limit the applicability of analytical or semi-analytical methods. Chapter 5 of this thesis addresses this challenge by applying ideas from microhydrodynamics to the electrostatic context, providing both analytical insights and numerical solutions to capture the anisotropic effects in electrostatic interactions.

1.6 Dusty 2D Turbulence: A Leap into the Inertial World

Up to this point, we have focused on the *overdamped limit*, where both particle and fluid inertia are negligible. The central theme has been how particle geometry can give rise to novel dynamical features through hydrodynamic coupling between the body and the surrounding fluid. These discussions have primarily addressed the dynamical features of either a single body or small collectives. When a large number of particles are involved, geometry continues to affect individual dynamics, but collective interactions can also modify the macroscopic behaviour of the fluid itself, as seen, for instance, in how the rheology of a suspension differs from that of the pure solvent [77–80]. Considerable effort has gone into understanding such complex fluids through their underlying microstructure [10–12, 81].

In many practical scenarios, such as protoplanetary disks [82], clouds [53], and aeolian processes [83], we encounter *dusty flows*, a term used to describe fluids laden with suspended particles. In most of these contexts, the fluid is air, and the particle-to-fluid density ratio is large. In this limit, particle inertia can no longer be neglected. One key consequence of including particle inertia is *preferential concentration*, where inertial particles tend to avoid vortical regions and accumulate in strain-dominated zones [84–86]. This mechanism has been proposed as a potential explanation for the droplet-growth bottleneck in clouds [87].

Despite significant attention, most studies of particles in turbulence have considered *one-way coupling* [88], where the particles respond to the fluid but do not influence it. However, this assumption breaks down at high particle number densities. For instance, the streaming instability in protoplanetary disks [89, 90], believed to play a crucial role in planet formation, relies on two-way momentum coupling. A natural question that arises is: how does the presence of dust affect the universal properties of turbulence, such as energy spectra or structure functions?

Simulating fully coupled dusty turbulence in three dimensions is computationally prohibitive, especially with a large number of particles. As an alternative, two-dimensional turbulence provides a more tractable setting to explore the effects of particle-fluid momentum exchange. A notable study by Pandey et al. [91] used the point-particle approximation to investigate this problem. They reported a suppression of clustering and the emergence of a dusty scaling regime in the energy spectra, though these effects were found to be non-universal, depending on parameters like the Stokes number and dust concentration.

The point-particle approximation assumes that particle size is much smaller than the smallest eddy scale (the Kolmogorov scale η), thereby ignoring geometric effects of the particles. Investigating such effects would require going beyond the point-particle model, but computational techniques like the immersed boundary method [92, 93] become increasingly expensive with large particle counts. Before tackling geometric effects, several unexplored questions remain even under the point-particle framework. For instance, how does intermittency in the vorticity and velocity fields vary with dust concentration? How is the flow topology, as characterized by the Okubo-Weiss parameter, influenced by dust? These are among the questions addressed in Chapter 6 of this thesis, which presents results from an ongoing investigation into dusty two-dimensional turbulence.

1.7 Thesis Outline & Main results

With the context, motivation, and problem statements discussed in the previous sections, we now outline the structure of the thesis and summarize its main contributions.

Chapter 2 presents the mathematical background essential for analyzing arbitrarily shaped bodies in both microhydrodynamics and electrostatics. It introduces the foundational tools and techniques that underpin the rest of the thesis. These include analytical methods based on singularity solutions, perturbative approaches for many-body interactions, and numerical schemes that enable high-accuracy simulations. A key aspect of this chapter is the development and extension of these tools, originally designed for hydrodynamics, into the context of electrostatics, thereby establishing a unified framework. The major components discussed in this chapter are:

- **Singularity solutions** of the Stokes and Laplace equations, which serve as the building blocks for constructing solutions around spheres and spheroids, are reviewed.
- **Faxén's laws**, which relate the structure of singularity solutions to hydrodynamic resistance tensors, are discussed and systematically extended to electrostatics, offering a new perspective on how conductors respond to arbitrary background electric fields.
- **The method of reflections**, a perturbative technique for computing the mobility matrix of multiple interacting bodies in viscous flow, is revisited and generalized to electrostatic interactions between conductors, demonstrating the strength of the hydrodynamic-electrostatic analogy.
- **Boundary integral formulations** using the double-layer potential are developed for both Stokes and Laplace equations. Particular attention is given to the spectral properties of the electrostatic double-layer operator, drawing insights from its hydrodynamic counterpart.

The method of reflections provides a tractable analytical framework in the far-field regime, whereas the boundary integral method allows for uniformly accurate treatment of near-field and far-field interactions in both hydrodynamic and electrostatic settings.

Chapter 3 bridges the gap between the well-understood sedimentation dynamics of single ellipsoids and the more complex behaviour of arbitrarily shaped bodies. It focuses on a specific class of geometries, bodies with two planes of symmetry, referred to as *di-bilaterals*. These bodies exhibit a rich spectrum of sedimentation dynamics, ranging from simple vertical settling to persistent drifting, periodic spiraling, and quasi-periodic fluttering. The main findings of this chapter are summarized below:

- **Conserved quantity**: Di-bilaterals possess a conserved quantity that plays a central role in governing their sedimentation dynamics.
- **Shape-based classification**: Di-bilaterals can be grouped into three distinct classes based solely on a shape factor:
    1. **Settlers** - bodies that settle vertically without rotation.

2. **Drifters** - bodies that drift and settle obliquely without rotating.
3. **Flutterers** – bodies that rotate indefinitely, exhibiting periodic or quasi-periodic motion.

- **Origin of quasi-periodicity**: For flutterers, the dynamics decouple into a periodic driving component and a response (Floquet) component, leading to either periodic or quasi-periodic behaviour.

- **Geometric realization**: Using boundary integral methods, we show that all three dynamical classes can be realized from a continuous family of shapes constructed by bending a prolate spheroid and modifying its cross-section from convex to concave.

Chapter 4 explores the collective sedimentation behaviour of a one-dimensional lattice of discs. This work develops an improved hydrodynamic interaction model that accurately accounts for close-range dynamics, enabling quantitative insights into cluster formation and lattice disruption. The main findings are summarized below:

- **Limitations of the Stokeslet model**: The Stokeslet or point-particle approximation fails to capture certain close-range behaviours of sedimenting discs, such as the experimentally observed rocking orbits [94]. Including first reflection corrections qualitatively captures these dynamics and aligns well with experimental observations.

- **Impact on stability**: Incorporating first reflections alters the qualitative nature of fixed points. Neutral modes seen under the Stokeslet approximation become unstable. Despite the exponential instability across all lattice spacings $\tilde{d}$, at large $\tilde{d}$ the perturbation amplitude is dominated by more rapid algebraic growth, which ultimately leads to lattice disruption.

- **Growth rate scaling**: The instability growth rate follows a power-law scaling of $\tilde{d}^{-4.5}$ at large spacings, significantly steeper than the $\tilde{d}^{-2}$ scaling observed for spheres [47].

- **Cluster morphology**: At large lattice spacings, sedimenting disc pairs predominantly form an inverted ‘T’ or $\perp$ configuration. This geometry is explained through an analysis that builds on Koch and Shaqfeh (1989) [95].

Chapter 5 applies ideas from microhydrodynamics to electrostatics, focusing on the interaction between a sphere and a spheroid. This minimal configuration is sufficient to reveal anisotropic effects such as electrostatic torque between conductors. The main findings are summarized below:

- **Accuracy of method of reflections**: Electrostatic forces and torques computed using the second reflection approximation remain accurate down to separations comparable to the size of the conductors, as validated against results from the boundary integral method.

- **Near-contact asymptotics**: In axisymmetric configurations, boundary integral results can be extrapolated to near-contact regimes using lubrication approximations, enabling accurate predictions at vanishingly small separations.

- **Like-charge attraction via induction**: The boundary integral method captures attractive interactions between like-charged bodies arising from induced charges, which become significant at separations below one-tenth of the conductor size. Although the method of reflections predicts like-charge attraction, it becomes unreliable at very small separations.

- **Competing alignment mechanisms**: Electrostatic torques can either reinforce or counteract hydrodynamic alignment of spheroids, depending on the configuration. This suggests that electrostatic effects could influence the onset of instabilities in dilute suspensions of sedimenting spheroids [95].

Chapter 6 explores inertial effects in the context of two-dimensional dusty turbulence. Building on a recent study by Pandey et al. [91], this work investigates the implications of *mass loading*, a dimensionless parameter quantifying the influence of dust on the flow, on intermittency and flow topology. The key findings are summarized below:

- The skewness of the Okubo–Weiss parameter retains its negative sign across varying mass loading values, suggesting that the underlying flow regions remain vorticity-dominated. The increase in the extreme values of the Okubo-Weiss parameter with the mass loading shows more intense vorticity and strain-dominated regions.

- The one-point Eulerian vorticity statistics show intense values of vorticity become more frequent as the mass loading is increased.

- The probability distribution function of two-point Eulerian vorticity differences lacks scale invariance, signaling intermittency regardless of mass loading. Increased mass loading leads to a loss of spatial correlation in the vorticity field, and the corresponding second-order structure function exponents tend toward zero.
- No negative energy flux is observed at large wavenumbers, indicating that dust feedback cannot be captured by a simple small-scale forcing model.

Chapter 7 brings together the insights from the preceding chapters, offering an outlook on future directions and open problems emerging from this thesis.

2

MATHEMATICAL BACKGROUND

> *"Mathematics is the art of giving the same name to different things."*
> *— Henri Poincaré*

In this chapter, we develop the mathematical framework used to study hydrodynamic and electrostatic interactions between bodies in three dimensions. Two principal approaches are employed: a perturbative technique known as the *method of reflections*, and a numerical approach based on the *boundary integral method*.

The method of reflections yields semi-analytical expressions for multi-body interactions, provided the solution for each body in isolation is known. While applicable to a range of shapes, it is most commonly used for canonical geometries such as spheres and spheroids. In contrast, the boundary integral method enables accurate computation of interactions between arbitrarily shaped bodies, and its key advantage lies in dimensionality reduction: only the surfaces of bodies must be discretized, not the surrounding fluid domain. This makes it especially well-suited for problems in unbounded domains.

We begin in Section 2.1 with a review of basic concepts in microhydrodynamics. This is followed by a focused overview of electrostatics in Section 2.2, emphasizing concepts relevant to the implementation of the two methods. We then present singularity solutions in electrostatics in Section 2.3 and extend Faxén's laws, originally derived in the context of hydrodynamics, to electrostatics for arbitrarily shaped bodies in Section 2.4.

Subsequently, we revisit the singularity solutions and Faxén's laws specifically for spheroidal bodies in microhydrodynamics in Sections 2.5 and 2.6. With these tools in hand, including multipole expansions, singularity solutions, and generalised Faxén's laws, we introduce the method of reflections in Section 2.7.

Finally, we describe the boundary integral method, with particular attention to its formulation in electrostatics in Section 2.9. The presentation draws heavily from analogous formulations in microhydrodynamics, particularly those found in the work of Pozrikidis [16], which we briefly review in the last Section 2.10.

2.1 A Quick Review of Microhydrodynamics

The equation of motion for a fluid can be obtained using mass, momentum, and energy conservation. For an incompressible fluid, momentum conservation leads to the Navier-Stokes equation, given by,

$$\rho_f \partial_t \boldsymbol{u} + \rho_f \boldsymbol{u} \cdot \boldsymbol{\nabla} \boldsymbol{u} = -\boldsymbol{\nabla} p + \mu \nabla^2 \boldsymbol{u} + \boldsymbol{f}, \quad \boldsymbol{\nabla} \cdot \boldsymbol{u} = 0. \tag{2.1}$$

Here $\boldsymbol{u}$ is the fluid velocity field, p is the fluid pressure field, μ is the dynamic viscosity, ρ_f is the fluid density, and $\boldsymbol{f}$ is the force per unit volume acting *on* the fluid. To solve for a flow field, one needs to supplement the Navier-Stokes equation with an initial condition and boundary conditions.

The fluid stress tensor σ_{ij} describes internal stresses within the fluid, where $(\boldsymbol{\sigma} \cdot \hat{\boldsymbol{n}})_i = \sigma_{ij} n_j$ gives the i-th component of the force per unit area acting on a surface with normal $\hat{\boldsymbol{n}}$, exerted by the fluid on the side facing the $\hat{\boldsymbol{n}}$ direction. The Navier-Stokes equation (2.1) describes a *Newtonian* fluid, for which the stress tensor is given by

$$\sigma_{ij} = -p\delta_{ij} + \mu[\partial_j u_i + \partial_i u_j]. \tag{2.2}$$

This is a constitutive relation derived using the assumptions of isotropy and a gradient expansion of the velocity field [81, 96]. Certain fluids, such as blood, colloidal suspensions, and polymer solutions, violate this relation and are known as complex fluids. In this thesis, we will restrict our attention to Newtonian fluids satisfying the equation (2.2).

The Navier-Stokes equation (2.1) is capable of describing a wide variety of fluid flows around us, from the laminar regime to the turbulent regime. Most of the cases require numerical solutions, owing to the non-linearity of the Navier-Stokes equation. Since we are interested in the realm of microhydrodynamics, a significant simplification is possible, which can allow us to 'ignore' the nonlinear effects. To estimate the relative importance of each term in the equation (2.1), let us non-dimensionalize the equation. Let V be the fluid velocity scale, a be the fluid length scale, τ_f be the fluid time scale. We denote the dimensionless quantities with a dash. Thus, we have $\boldsymbol{u}' = \boldsymbol{u}/V$, $\boldsymbol{x}' = \boldsymbol{x}/a$, $t' = t/\tau_f$, $p' = p/(\mu a^{-1} V)$ and $\boldsymbol{f}' = \boldsymbol{f}/(\mu a^{-2} V)$. Note that we have defined pressure and force scales based on the dynamic viscosity μ, consistent with the viscosity-dominated regime, where the internal pressure scales with the dominant viscous forces. Using the dimensionless quantities in equation (2.1) gives

$$\frac{\rho_f V}{\tau_f}\partial_{t'}\boldsymbol{u}' + \frac{\rho_f V^2}{a}\boldsymbol{u}'\cdot\boldsymbol{\nabla}_{\boldsymbol{x}'}\boldsymbol{u}' = -\frac{\mu V}{a^2}\boldsymbol{\nabla}_{\boldsymbol{x}'}p' + \frac{\mu V}{a^2}\nabla^2_{\boldsymbol{x}'}\boldsymbol{u}' + \frac{\mu V}{a^2}\boldsymbol{f}' \tag{2.3a}$$

$$\implies Re(Sl\,\partial_{t'}\boldsymbol{u}' + \boldsymbol{u}'\cdot\boldsymbol{\nabla}_{\boldsymbol{x}'}\boldsymbol{u}') = -\boldsymbol{\nabla}_{\boldsymbol{x}'}p' + \nabla^2_{\boldsymbol{x}'}\boldsymbol{u}' + \boldsymbol{f}', \tag{2.3b}$$

where

$$Re \equiv \frac{\rho_f V a}{\mu}, \quad Sl \equiv \frac{a}{V\tau_f}. \tag{2.4}$$

The two non-dimensional numbers are the Reynolds number Re and the Strouhal number Sl, which compares the inertia to the viscous effects. In the viscosity-dominated regime of microhydrodynamics, we have $Re \ll 1$ and $Sl \ll 1$. Therefore, to the leading order, we have

$$\boldsymbol{\nabla}_{\boldsymbol{x}'}p' + \nabla^2_{\boldsymbol{x}'}\boldsymbol{u}' + \boldsymbol{f}' = 0.$$

In the dimensional form, we get the *steady Stokes equation*,

$$\boldsymbol{\nabla}p + \nabla^2\boldsymbol{u} + \boldsymbol{f} = \boldsymbol{0}, \quad \boldsymbol{\nabla}\cdot\boldsymbol{u} = 0. \tag{2.5}$$

Note that the lack of a time derivative and non-linear term considerably simplifies the problems in microhydrodynamics. Solving the steady Stokes equation requires appropriate boundary conditions. Throughout this thesis, we will be looking at the dynamics of rigid bodies in an unbounded fluid domain. The surface of the rigid bodies and the surface at infinity act as boundaries, with the boundary conditions given by,

$$\boldsymbol{u}(\boldsymbol{x}) = \boldsymbol{V} + \boldsymbol{\Omega}\times(\boldsymbol{x}-\boldsymbol{x}_c), \quad \boldsymbol{x}\in S \tag{2.6a}$$

$$\boldsymbol{u}(\boldsymbol{x}) \longrightarrow \boldsymbol{0} \quad \text{as} \quad |\boldsymbol{x}| \longrightarrow \infty. \tag{2.6b}$$

Here $\boldsymbol{V}$ and $\boldsymbol{\Omega}$ denote linear and angular velocities of the rigid body with its surface denoted by S, and $\boldsymbol{x}_c$ is the centre of mass of the rigid body. For multiple bodies in the flow, the no-slip boundary condition is imposed on the surface of each of the rigid bodies.

The force and torque acting on a body immersed in the fluid can be computed using the stress tensor as:

$$\boldsymbol{F}^h = \oint_S \boldsymbol{\sigma}\cdot\hat{\boldsymbol{n}}\,dS, \quad \boldsymbol{T}^h = \oint_S (\boldsymbol{x}-\boldsymbol{x}_c)\times(\boldsymbol{\sigma}\cdot\hat{\boldsymbol{n}})\,dS, \tag{2.7}$$

where $\hat{\boldsymbol{n}}$ is the normal vector pointing *out* of the surface, towards the fluid.

Some of the interesting properties of the steady Stokes equation are discussed in Chapter 1. The linearity of the steady Stokes equation allows powerful analytical techniques that are discussed in the subsequent sections.

2.1.1 Lorentz Reciprocal Theorem

This is one of the most useful theorems for obtaining integral representations of Stokes flow, as well as for computing the force and torque on a body without solving the complete flow field. Consider two flow fields $\boldsymbol{u}^{(1)}$ and $\boldsymbol{u}^{(2)}$ with their respective stress tensors $\boldsymbol{\sigma}^{(1)}$ and $\boldsymbol{\sigma}^{(2)}$ in the same fluid domain $\mathcal{D}$. Then, using the divergence theorem and the incompressibility condition, we have

$$\oint_{\partial\mathcal{D}} \boldsymbol{u}^{(1)}\cdot(\boldsymbol{\sigma}^{(2)}\cdot\boldsymbol{n})\,dS - \oint_{\partial\mathcal{D}} \boldsymbol{u}^{(2)}\cdot(\boldsymbol{\sigma}^{(1)}\cdot\boldsymbol{n})\,dS = \int_{\mathcal{D}} \boldsymbol{u}^{(1)}\cdot(\boldsymbol{\nabla}\cdot\boldsymbol{\sigma}^{(2)})\,dV - \int_{\mathcal{D}} \boldsymbol{u}^{(2)}\cdot(\boldsymbol{\nabla}\cdot\boldsymbol{\sigma}^{(1)})\,dV. \tag{2.8}$$

Here $\boldsymbol{n}$ is the normal vector to the boundary of the fluid domain, denoted by $\partial\mathcal{D}$, pointing *away* from the fluid domain $\mathcal{D}$. The equation (2.8) is called the generalised reciprocal theorem. If we further require that the two velocity fields satisfy the steady Stokes equation, we have

$$\oint_{\partial\mathcal{D}} \boldsymbol{u}^{(1)}\cdot(\boldsymbol{\sigma}^{(2)}\cdot\boldsymbol{n})\,dS = \oint_{\partial\mathcal{D}} \boldsymbol{u}^{(2)}\cdot(\boldsymbol{\sigma}^{(1)}\cdot\boldsymbol{n})\,dS. \tag{2.9}$$

One of the corollaries of the reciprocal theorem is the linear relationship between force and velocity acting on a rigid body in Stokes flow. Following Kim & Karilla [10], consider two separate configurations, each involving a homogeneous, steady Stokes flow generated by a rigid body moving through an otherwise quiescent fluid. The bodies move with velocities $\boldsymbol{V}'$ and $\boldsymbol{V}''$, and experience total forces $\boldsymbol{F}'$ and $\boldsymbol{F}''$, respectively. Let $\boldsymbol{F} = \boldsymbol{f}(\boldsymbol{V})$ be the relation between force and velocity. Using the reciprocal theorem (2.9), we have

$$\boldsymbol{V}'\cdot\boldsymbol{F}'' = \boldsymbol{V}''\cdot\boldsymbol{F}' \implies \boldsymbol{V}'\cdot\boldsymbol{f}(\boldsymbol{V}'') = \boldsymbol{V}''\cdot\boldsymbol{f}(\boldsymbol{V}').$$

We have used the fact that the velocity fields decay at infinity, so the only contribution from the boundary is due to the surface of the particle, where the fluid velocity is constant. The above relation implies that

$$\boldsymbol{f}(\boldsymbol{V}) = (\boldsymbol{f}(\boldsymbol{V})\cdot\boldsymbol{e}_i)\boldsymbol{e}_i = (\boldsymbol{f}(\boldsymbol{e}_i)\cdot\boldsymbol{V})\boldsymbol{e}_i = (\boldsymbol{e}_i\boldsymbol{f}(\boldsymbol{e}_i))\cdot\boldsymbol{V}, \tag{2.10}$$

where $\boldsymbol{e}_i$ is the i-th basis vector and the summation convention is used in the equation (2.10). This shows that the function $\boldsymbol{f}(\boldsymbol{V})$ is linear in the velocity. This idea can be generalised for a rigid body moving with linear velocity $\boldsymbol{V}$ and angular velocity $\boldsymbol{\Omega}$, in which case the motion is linearly related to the hydrodynamic force $\boldsymbol{F}^h$ and hydrodynamic torque $\boldsymbol{T}^h$ as

$$\begin{bmatrix}\boldsymbol{V}\\ \boldsymbol{\Omega}\end{bmatrix} = -\mu^{-1}\begin{bmatrix}\boldsymbol{a} & \tilde{\boldsymbol{b}}\\ \boldsymbol{b} & \boldsymbol{c}\end{bmatrix}\cdot\begin{bmatrix}\boldsymbol{F}^h\\ \boldsymbol{T}^h\end{bmatrix} = -\mu^{-1}\boldsymbol{\mathcal{M}}\cdot\begin{bmatrix}\boldsymbol{F}^h\\ \boldsymbol{T}^h\end{bmatrix}. \tag{2.11}$$

The matrix $\boldsymbol{\mathcal{M}}$ in the equation (2.11) is called the *mobility matrix*, which depends only on the size and geometry of the rigid body. It can be further shown using the reciprocal theorem that the mobility matrix is symmetric [10–13, 16], i.e., $\boldsymbol{a}^T = \boldsymbol{a}$, $\tilde{\boldsymbol{b}} = \boldsymbol{b}^T$, $\boldsymbol{c}^T = \boldsymbol{c}$. It should be noted that equation (2.11) is written for a zero background flow field. In the presence of an external flow, equation (2.11) has to include the background velocity, background vorticity, and background strain-rate. We will restrict ourselves to zero background flow in this thesis; for extensions of mobility formulation to incorporate background flow, see [10–13].

2.1.2 Equation of Motion of Rigid Bodies in Overdamped Limit

The equation of motion of a rigid body in the presence of gravity $\boldsymbol{g}$, fluid, and some other external force $\boldsymbol{F}^{\text{other}}$ is given by:

$$\rho_p V_p \frac{d\boldsymbol{V}}{dt} = \boldsymbol{F}^h + (\rho_p - \rho_f) V_p \boldsymbol{g} + \boldsymbol{F}^{\text{other}}, \tag{2.12}$$

where ρ_p is the density of the body and V_p is the volume enclosed by the body. The buoyancy force is separated from the hydrodynamic force $\boldsymbol{F}^h$ since it comes from the hydrostatic part of the pressure, $\rho_f \boldsymbol{g} \cdot \boldsymbol{x}$. Similarly, the angular momentum $\boldsymbol{L}$ of the body about its centre of mass $\boldsymbol{x}_c$ satisfies

$$\frac{d\boldsymbol{L}}{dt} = \boldsymbol{T}^h - \rho_f V_p [\boldsymbol{x}_b - \boldsymbol{x}_c] \times \boldsymbol{g} + \boldsymbol{T}^{\text{other}}, \tag{2.13}$$

where $\boldsymbol{x}_b \equiv V_p^{-1} \int_V \boldsymbol{x} dV$ is the geometric centre of the body, and $\boldsymbol{T}^{\text{other}}$ is some other external torque acting on the body. In the viscosity-dominated regime, the equations (2.12) and (2.13) can be simplified as follows. In the viscosity-dominated regime, the hydrodynamic force $\boldsymbol{F}^h$ scales with viscosity as $\mu a V$, where $a = V_p^{1/3}$ is the length scale based on the size of the body, and V is the velocity scale of the body. Moreover, the relevant flow time scale in case of a body moving with speed V in the fluid is $\tau_f = a/V$, and $g = |\boldsymbol{g}|$ provides an acceleration scale. Thus, we define the dimensionless quantities as $\boldsymbol{V}' = \boldsymbol{V}/V$, $\boldsymbol{x}' = \boldsymbol{x}/a$, $t' = tV/a$, and $\boldsymbol{g}' = \boldsymbol{g}/|\boldsymbol{g}|$. Using these to non-dimensionalize equation (2.12), we get

$$\frac{\rho_p}{\rho_f} \frac{\rho_f a V}{\mu} \frac{d\boldsymbol{V}'}{dt'} = \frac{1}{\mu a V}(\boldsymbol{F}^h + \boldsymbol{F}^{\text{other}}) + \frac{\rho_f a V}{\mu} \frac{g a}{V^2} (\rho_p/\rho_f - 1) \boldsymbol{g}'.$$

This defines three non-dimensional numbers, namely the Reynolds number Re, the Stokes number St and the Froude number Fr, given by

$$Re \equiv \frac{\rho_f V a}{\mu}, \quad St \equiv (\rho_p/\rho_f) Re, \quad Fr^2 \equiv \frac{V^2}{g a}. \tag{2.14}$$

The non-dimensional force balance is

$$St\frac{d\boldsymbol{V}'}{dt'} = \frac{1}{\mu a V}(\boldsymbol{F}^h + \boldsymbol{F}^{\text{other}}) + \frac{Re}{Fr^2}(\rho_p/\rho_f - 1)\boldsymbol{g}'. \tag{2.15}$$

Equation (2.15) suggests that the Stokes number St can be interpreted as the dimensionless measure of inertia of the particle, while equation (2.14) shows that the Froude number Fr compares inertia with gravity. We shall work in the *overdamped limit* where particle inertia and fluid inertia are negligible, i.e., $Re \ll 1$ and $St \ll 1$. Moreover, we are interested in the regime where the dominant viscous forces balance gravity, i.e., $Fr^2 \sim \mathcal{O}(Re)$. Then, the leading order physics in the overdamped limit is governed by the right-hand side of equation (2.15) equated to zero. Returning to dimensional form, this implies

$$\boldsymbol{F}^h + (\rho_p - \rho_f)V_p\boldsymbol{g} + \boldsymbol{F}^{\text{other}} = \boldsymbol{0}.$$

A similar argument for the angular momentum equation (2.13) leads to

$$\boldsymbol{T}^h - \rho_f V_p[\boldsymbol{x}_b - \boldsymbol{x}_c] \times \boldsymbol{g} + \boldsymbol{T}^{\text{other}} = \boldsymbol{0}.$$

Using the mobility formulation, one can then obtain the equation of motion of a rigid body falling under gravity in otherwise quiescent fluid as:

$$\begin{bmatrix} \boldsymbol{V} \\ \boldsymbol{\Omega} \end{bmatrix} = \mu^{-1}\boldsymbol{\mathcal{M}} \cdot \begin{bmatrix} (\rho_p - \rho_f)V_p\boldsymbol{g} + \boldsymbol{F}^{\text{other}} \\ -\rho_f V_p[\boldsymbol{x}_b - \boldsymbol{x}_c] \times \boldsymbol{g} + \boldsymbol{T}^{\text{other}} \end{bmatrix}, \tag{2.16}$$

where we have used equation (2.11) to rewrite hydrodynamic forces and torques. Therefore, given the mobility matrix $\boldsymbol{\mathcal{M}}$ for a given geometry of a rigid body, one can obtain the dynamics of the rigid body. The extension of this to multiple bodies is straightforward, with the mobility matrix of a multi-body system depending not only on the individual geometry of the bodies but also on their relative positions and orientations [10, 11].

2.1.3 Free Space Green's Functions for Steady Stokes Flow

Consider the fundamental solution of the steady Stokes equation

$$-\boldsymbol{\nabla} p + \mu\nabla^2\mathbf{u} + \mathbf{F}\delta(\boldsymbol{x} - \boldsymbol{x_0}) = \boldsymbol{0}, \quad \boldsymbol{\nabla}\cdot\mathbf{u} = 0, \tag{2.17}$$

where p is the pressure field, $\mathbf{u}$ is the velocity field, and $\mathbf{F}\delta(\boldsymbol{x} - \boldsymbol{x_0})$ is the force per unit volume acting on the fluid at $\boldsymbol{x_0}$. The linearity of the Stokes equation allows us to write the velocity field as

$$u_i(\boldsymbol{x}) = \frac{1}{8\pi\mu}\mathcal{G}_{ij}(\boldsymbol{x}, \boldsymbol{x_0})F_j. \tag{2.18}$$

Here $\boldsymbol{x}$ is the target point, $\boldsymbol{x_0}$ is the source point, and $\boldsymbol{\mathcal{G}}$ is the velocity Green's function of the Stokes equation. Similarly, the pressure field and the stress tensor can be written in terms of their Green's function as:

$$p(\boldsymbol{x}) = \frac{1}{8\pi}\mathcal{P}_j(\boldsymbol{x}, \boldsymbol{x_0})F_j, \quad \sigma_{ij}(\boldsymbol{x}) = \frac{1}{8\pi}\mathcal{T}_{ijk}(\boldsymbol{x}, \boldsymbol{x_0})F_k. \tag{2.19}$$

There are different types of Green's functions based on the domain of the flow. We are interested in the unbounded domain, which requires the velocity field of equation (2.17) to decay at infinity. Taking the divergence of equation (2.17) gives

$$\nabla^2 p = \boldsymbol{F}\cdot\boldsymbol{\nabla}\delta(\boldsymbol{x}-\boldsymbol{x_0}) = -\boldsymbol{F}\cdot\boldsymbol{\nabla}\nabla^2\left[\frac{1}{4\pi r}\right], \quad \boldsymbol{r}\equiv\boldsymbol{x}-\boldsymbol{x_0},\ r\equiv|\boldsymbol{r}|,$$

where we have used the free space Green's function of the Laplace equation to rewrite the $\delta(\boldsymbol{r})$ function in three dimensions. Requiring that the pressure goes to zero at infinity, we get

$$p(\boldsymbol{x}) = \frac{1}{8\pi}\boldsymbol{F}\cdot\frac{2\boldsymbol{r}}{r^3} \implies \boldsymbol{\mathcal{P}}(\boldsymbol{x}, \boldsymbol{x_0}) = \frac{2\boldsymbol{r}}{r^3}. \tag{2.20}$$

Using this solution for pressure in equation (2.17), we have

$$\mu\nabla^2\boldsymbol{u} = \frac{1}{4\pi}\boldsymbol{F}\cdot\left[\boldsymbol{\delta}\nabla^2 - \boldsymbol{\nabla\nabla}\right]\frac{1}{r}.$$

Note that $\boldsymbol{\delta}$ denotes the identity tensor. Since $r^{-1} = \nabla^2(r/2)$, we have

$$\mu\nabla^2\boldsymbol{u} = \frac{1}{4\pi}\boldsymbol{F}\cdot\left[\boldsymbol{\delta}\nabla^2 - \boldsymbol{\nabla\nabla}\right]\frac{1}{2}\nabla^2 r$$

The Laplacian can be factored out from the above equation, given that the velocity field decays at infinity. Therefore, the Stokeslet, or the velocity Green's function, is given by

$$\boldsymbol{u}(\boldsymbol{x}) = \frac{1}{8\pi\mu}\boldsymbol{F}\cdot\boldsymbol{\mathcal{G}}(\boldsymbol{x}, \boldsymbol{x_0}), \quad \boldsymbol{\mathcal{G}}(\boldsymbol{x}, \boldsymbol{x_0}) = \frac{\boldsymbol{\delta}}{r} + \frac{\boldsymbol{rr}}{r^3}. \tag{2.21}$$

The velocity field due to a point force is commonly referred to as *Stokeslet*, and is shown in Figure 2.2. By construction, we have

$$\partial_j\mathcal{G}_{ij}(\boldsymbol{x}, \boldsymbol{x_0}) = 0. \tag{2.22}$$

Note that $\sigma_{ij} = -p\delta_{ij} + \mu(\partial_j u_i + \partial_i u_j)$, which gives the Green's function of the stress tensor as

$$\mathcal{T}_{ijk}(\boldsymbol{x}, \boldsymbol{x_0}) = -\mathcal{P}_k\delta_{ij} + \partial_j\mathcal{G}_{ik} + \partial_i\mathcal{G}_{jk} = -\frac{6r_ir_jr_k}{r^5}. \tag{2.23}$$

Using (2.20) and (2.21) in (2.17) we have

$$-\partial_i\mathcal{P}_j + \nabla^2\mathcal{G}_{ij} = -8\pi\delta_{ij}\delta(\boldsymbol{x}-\boldsymbol{x_0}). \tag{2.24}$$

Using (2.23) and (2.24) gives

$$\partial_j \mathcal{T}_{ijk}(\boldsymbol{x}, \boldsymbol{x_0}) = -8\pi \delta_{ik} \delta(\boldsymbol{x} - \boldsymbol{x_0}). \tag{2.25}$$

Equations (2.25) will be used in proving integral properties of the Green's function of the stress tensor.

2.1.4 Integral Representation of the Steady Stokes Equation

We want to represent the velocity field, satisfying the steady Stokes equation, outside a rigid body in an unbounded domain in terms of integrals over the surface of the body. Recall the generalised reciprocal theorem given by equation (2.8). Let us use $(\boldsymbol{u}^{(1)}, \boldsymbol{\sigma}^{(1)}) = (\boldsymbol{u}, \boldsymbol{\sigma})$ as the desired fields satisfying the homogeneous steady Stokes equation in the fluid domain $\mathcal{D}$, and $(\boldsymbol{u}^{(2)}, \boldsymbol{\sigma}^{(2)})$ as the auxiliary fields due to a point force $\boldsymbol{F}$ located at $\boldsymbol{x_0}$, either inside the open fluid domain $\mathcal{D}$ or outside the domain $\mathbb{R}^3 \backslash \overline{\mathcal{D}}$, but not at the boundary $\partial\mathcal{D}$. Note that $\overline{\mathcal{D}}$ denotes closure of the open domain $\mathcal{D}$, i.e. $\overline{\mathcal{D}} = \mathcal{D} \cup \partial\mathcal{D}$. Therefore, the auxiliary fields satisfy

$$\nabla \cdot \boldsymbol{\sigma}^{(2)}(\boldsymbol{x}) = -\boldsymbol{F}\delta(\boldsymbol{x} - \boldsymbol{x_0}), \tag{2.26a}$$

$$\boldsymbol{u}^{(2)}(\boldsymbol{x}) = \frac{1}{8\pi\mu}\boldsymbol{F} \cdot \boldsymbol{\mathcal{G}}(\boldsymbol{x}, \boldsymbol{x_0}), \quad \boldsymbol{\sigma}^{(2)}(\boldsymbol{x}) = \frac{1}{8\pi}\boldsymbol{F} \cdot \boldsymbol{\mathcal{T}}(\boldsymbol{x}, \boldsymbol{x_0}). \tag{2.26b}$$

Using equation (2.26) in the generalised reciprocal theorem (equation (2.8)), and factoring out the arbitrary force $\boldsymbol{F}$, we have

$$\begin{aligned} &-\frac{1}{8\pi} \oint_{\partial\mathcal{D}} u_j(\boldsymbol{x}) \mathcal{T}_{ijk}(\boldsymbol{x_0}, \boldsymbol{x}) \hat{n}_k(\boldsymbol{x}) \, dS(\boldsymbol{x}) \\ &\qquad -\frac{1}{8\pi\mu} \oint_{\partial\mathcal{D}} \mathcal{G}_{ij}(\boldsymbol{x_0}, \boldsymbol{x}) \sigma_{jk}(\boldsymbol{x}) \hat{n}_k(\boldsymbol{x}) \, dS(\boldsymbol{x}) = \begin{cases} u_i(\boldsymbol{x_0}), & \boldsymbol{x_0} \in \mathcal{D}, \\ 0, & \boldsymbol{x_0} \notin \overline{\mathcal{D}}. \end{cases} \end{aligned} \tag{2.27}$$

Here we have used the fact that $\boldsymbol{\mathcal{G}}(\boldsymbol{x}, \boldsymbol{x_0}) = \boldsymbol{\mathcal{G}}(\boldsymbol{x_0}, \boldsymbol{x})$, $\boldsymbol{\mathcal{T}}(\boldsymbol{x}, \boldsymbol{x_0}) = -\boldsymbol{\mathcal{T}}(\boldsymbol{x_0}, \boldsymbol{x})$, and $\hat{\boldsymbol{n}} = -\boldsymbol{n}$ is the normal vector pointing *towards* the fluid domain $\mathcal{D}$, as shown in Figure 2.1. The integral representation of the Stokes equation, given by (2.27), states that the velocity field inside any point in the fluid domain $\mathcal{D}$ can be obtained using the information on the boundary of the domain $\partial\mathcal{D}$.

The above integral equation (2.27) can be simplified for the case of a rigid body in Stokes flow. We note that for the Stokes flow outside a rigid body, the boundary $\partial\mathcal{D}$ consists of the particle surface S_p and the surface 'at infinity' S_∞. Moreover, the boundary condition for the fluid velocity is

$$\boldsymbol{u}(\boldsymbol{x}) = \boldsymbol{V} + \boldsymbol{\Omega} \times (\boldsymbol{x} - \boldsymbol{x}_c) = \boldsymbol{v}^{\mathrm{RBM}}(\boldsymbol{x}), \quad \boldsymbol{x} \in S_p$$

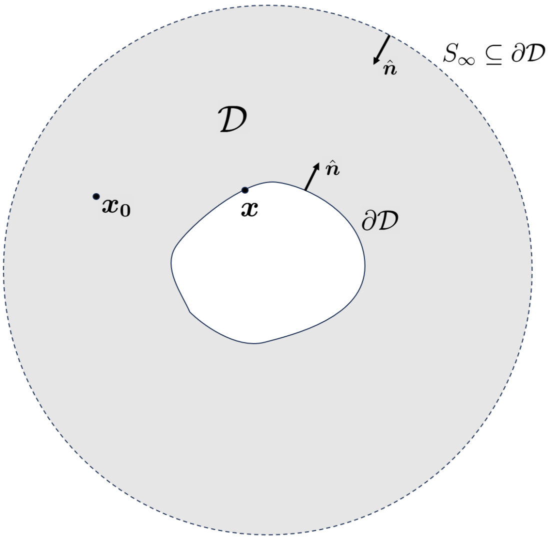

Figure 2.1: The domain of interest, $\mathcal{D}$, with normal vectors $\hat{\boldsymbol{n}}$ pointing towards $\mathcal{D}$. Fluid velocity at any point in the domain $\mathcal{D}$ can be obtained by integrating over the boundary of the domain, $\partial\mathcal{D}$, which, in the case of an unbounded domain, includes the 'surface at infinity' S_∞.

and $\boldsymbol{u}(\boldsymbol{x}) \to \boldsymbol{0}$ as $|\boldsymbol{x}| \to \infty$. Here $\boldsymbol{V}$ and $\boldsymbol{\Omega}$ are respectively the linear and angular velocity of the rigid body with centre of mass at $\boldsymbol{x}_c$. Therefore, we have

$$u_i(\boldsymbol{x}_0) = -\frac{1}{8\pi}\oint_{S_p} v_j^{\mathrm{RBM}}(\boldsymbol{x})\mathcal{T}_{ijk}(\boldsymbol{x_0},\boldsymbol{x})\hat{n}_k(\boldsymbol{x})\,dS(\boldsymbol{x}) \\ -\frac{1}{8\pi\mu}\oint_{S_p} \sigma_{jk}(\boldsymbol{x})\hat{n}_k(\boldsymbol{x})\mathcal{G}_{ij}(\boldsymbol{x_0},\boldsymbol{x})\,dS(\boldsymbol{x}), \quad \boldsymbol{x_0} \in \mathcal{D}. \tag{2.28}$$

The contribution from S_∞ is zero because the velocity field decays to zero at infinity. Note that the rigid body velocity also satisfies the steady Stokes equation with stress tensor given by a constant isotropic pressure p_0. Using the integral representation for $\boldsymbol{v}^{\mathrm{RBM}}$ *inside* the rigid body, we have

$$0 = -\frac{1}{8\pi}\oint_{S_p} v_j^{\mathrm{RBM}}(\boldsymbol{x})\mathcal{T}_{ijk}(\boldsymbol{x_0},\boldsymbol{x})\hat{n}_k(\boldsymbol{x})\,dS + \frac{p_0}{8\pi\mu}\oint_{S_p} \hat{n}_j(\boldsymbol{x})\mathcal{G}_{ij}(\boldsymbol{x_0},\boldsymbol{x})\,dS, \quad x_0 \in \mathcal{D} \tag{2.29}$$

Owing to the incompressibility of the Stokeslet (equation (2.22)), the second term on the right-hand side of equation (2.29) is zero. Therefore, equation (2.28) reduces to

$$u_i(\boldsymbol{x}_0) = -\frac{1}{8\pi\mu}\oint_{S_p} \sigma_{jk}(\boldsymbol{x})\hat{n}_k(\boldsymbol{x})\mathcal{G}_{ij}(\boldsymbol{x_0},\boldsymbol{x})\,dS(\boldsymbol{x}), \quad \boldsymbol{x_0} \in \mathcal{D}. \tag{2.30}$$

The generalization of equation (2.30) to multiple bodies in the presence of external steady Stokes flow is straightforward. The complete solution in this case is given by the sum of the Stokeslet integrals over the surfaces of each rigid body, supplemented by the external flow velocity [10].

It is easy to interpret equation (2.30). The term on the right-hand side of equation (2.30) is called the *single-layer* potential, and it denotes the velocity field due to a 'single layer' of forces of strength $\boldsymbol{\sigma} \cdot \hat{\boldsymbol{n}}$ distributed on the surface of the rigid body.

Returning to the general form of integral representation given by equation (2.27), the second term on the left-hand side of equation (2.27) is called the *double-layer* potential. The interpretation of the double-layer potential is more subtle, as discussed below.

2.1.5 Interpretation of The Double-Layer Potential

Recall from equation (2.23) we have,

$$\mathcal{T}_{ijk} = -\mathcal{P}_k \delta_{ij} + (\partial_j \mathcal{G}_{ik} + \partial_i \mathcal{G}_{jk}).$$

Let us understand each of the terms on the right-hand side in more detail.

2.1.5.1 The Potential Source

Consider a potential flow due to a point source, described by $\boldsymbol{u} = \boldsymbol{\nabla}\phi$, with $\boldsymbol{\nabla} \cdot \boldsymbol{u} = \nabla^2 \phi = Q\delta(\boldsymbol{x})$, where $Q > 0$ denotes the strength of the point source. The solution is simply given by

$$\phi(\boldsymbol{x}) = -\frac{Q}{4\pi|\boldsymbol{x}|}, \quad \boldsymbol{u}(\boldsymbol{x}) = \frac{Q\boldsymbol{x}}{4\pi|\boldsymbol{x}|^3}. \tag{2.31}$$

Comparing the flow due to a source to the Green's function of the pressure $\boldsymbol{\mathcal{P}}$, it is clear that $\boldsymbol{\mathcal{P}}(\boldsymbol{x}, \boldsymbol{x_0})$ represents fluid flow at point $\boldsymbol{x}$, due to a point source of unit strength located at $\boldsymbol{x_0}$.

2.1.5.2 The Rotlet and the Stresslet

Consider steady Stokes fluid flow due to two point forces of equal and opposite strength $|\boldsymbol{F}|$, acting at $\boldsymbol{x_0} + \boldsymbol{d}/2$ and $\boldsymbol{x_0} - \boldsymbol{d}/2$, *on* the fluid. The velocity field for such a flow is given by

$$\boldsymbol{u}(\boldsymbol{x}) = \frac{1}{8\pi\mu}\boldsymbol{F} \cdot [\boldsymbol{\mathcal{G}}(\boldsymbol{x}, \boldsymbol{x_0} + \boldsymbol{d}/2) - \boldsymbol{\mathcal{G}}(\boldsymbol{x}, \boldsymbol{x_0} - \boldsymbol{d}/2)].$$

Taking the limit $|\boldsymbol{F}| \to \infty$, $|\boldsymbol{d}| \to 0$, such that $F_j d_k \equiv -D_{jk}$ remains constant, we get flow due to a *force dipole* as

$$u_i(\boldsymbol{x}) = -\frac{1}{8\pi\mu} D_{jk} \frac{\partial}{\partial x_{0k}} \mathcal{G}_{ij}(\boldsymbol{x}, \boldsymbol{x_0}) = \frac{1}{8\pi\mu} D_{jk} \partial_k \mathcal{G}_{ij}(\boldsymbol{x}, \boldsymbol{x_0}). \tag{2.32}$$

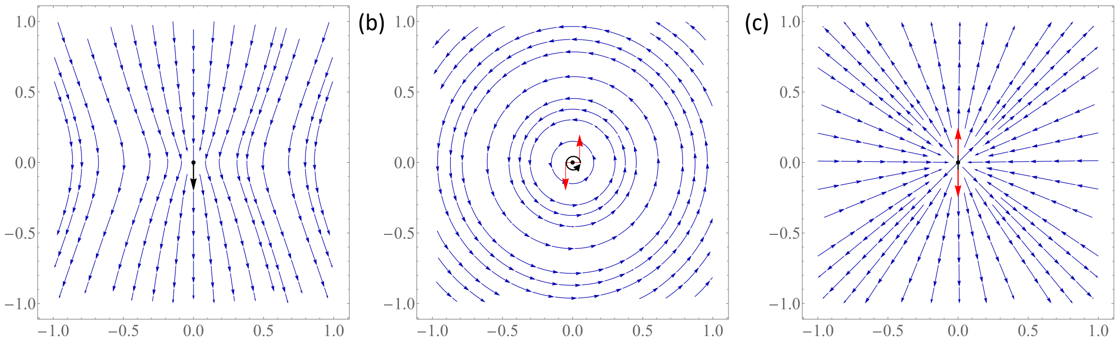

Figure 2.2: Streamlines of the velocity fields produced by various singularities at the origin. (a) Stokeslet centered at the origin with the force on the fluid indicated by the black arrow. (b) Rotlet centered at the origin, with the torque on the fluid indicated by the black arrow. The red arrows represent two equal and opposite forces, which, in the limit of vanishing separation and increasing magnitude, produce a point torque. (c) Stresslet centered at the origin. The red arrows show two equal and opposite forces that, in the same limit, give rise to the stresslet field.

Since $\partial_j \mathcal{G}_{ij} = 0$, the isotropic part of the dipole D_{jk} does not contribute to the velocity field. Therefore, we will only deal with the traceless part of D_{jk} given by $D_{jk} - (1/3)D_{nn}\delta_{jk}$. We can further decompose the traceless dipole into symmetric part $S_{jk} = S_{kj}$ and antisymmetric part $T_{jk} = -T_{kj}$ as

$$D_{jk} - \frac{1}{3}D_{nn}\delta_{jk} = T_{jk} + S_{jk}. \tag{2.33}$$

Note that by construction, $T_{jj} = 0$, $S_{jj} = 0$. Using equation (2.33) in equation (2.32), we have

$$u_i = \underbrace{\frac{1}{8\pi\mu}\frac{T_{jk}}{2}(\partial_k \mathcal{G}_{ij} - \partial_j \mathcal{G}_{ik})}_{\text{Rotlet}} + \underbrace{\frac{1}{8\pi\mu}\frac{S_{jk}}{2}(\partial_k \mathcal{G}_{ij} + \partial_j \mathcal{G}_{ik})}_{\text{Stresslet}}. \tag{2.34}$$

The antisymmetric dipole contribution to the velocity field is called the *rotlet*, and the symmetric dipole contribution is called the *stresslet* [10, 11], as shown in Figure 2.2.

To understand the stresslet and the rotlet in more detail, it is informative to look at the force density due to the dipole D_{jk}. The velocity field in equation (2.32) corresponds to the stress tensor σ_{ij} which satisfies

$$\partial_j \sigma_{ij}(\boldsymbol{x}) = -\lim_{\substack{|\boldsymbol{F}|\to\infty \\ |\boldsymbol{d}|\to 0}} F_i[\delta(\boldsymbol{x} - \boldsymbol{x_0} - \boldsymbol{d}/2) - \delta(\boldsymbol{x} - \boldsymbol{x_0} + \boldsymbol{d}/2)] = -\partial_j(D_{ij}\delta(\boldsymbol{x} - \boldsymbol{x_0})).$$

Therefore, the dipole D_{ij} can be thought of as the point stress acting *on* the fluid due to the dipole. Rewriting the antisymmetric part of the dipole T_{ij} in terms of a

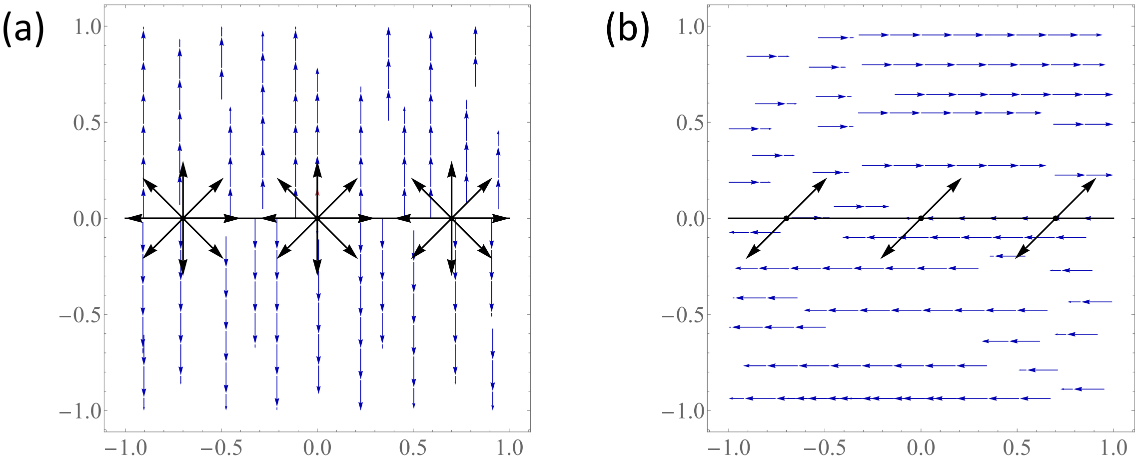

Figure 2.3: Redrawn from Kim & Karilla [10]. Schematic of the velocity streamlines due to double-layer potential. The double-layer potential consists of two contributions: (a) from point sources (black arrows), and (b) from stresslets (force bilayer, shown as black arrows), both distributed along the boundaries of the domain (taken here to be the x-axis). (a) Point sources contribute to a discontinuity in the normal component of the velocity field across the boundary. (b) Stresslets contribute to a discontinuity in the tangential component of the velocity field across the boundary.

pseudo-vector T_k, we have

$$T_{ij} = \frac{1}{2}\epsilon_{ijk}T_k \implies T_k = \epsilon_{kij}T_{ij} = \lim_{\substack{|\boldsymbol{F}|\to\infty \\ |\boldsymbol{d}|\to 0}} (\boldsymbol{d}\times\boldsymbol{F})_k, \tag{2.35}$$

where ϵ_{ijk} is the Levi-Civita symbol. Therefore, the antisymmetric part $T_{ij}\delta(\boldsymbol{x}-\boldsymbol{x_0})$ can be understood in terms of a point torque $T_k\delta(\boldsymbol{x}-\boldsymbol{x_0})$ acting *on* the fluid. Using the decomposition (2.33), the steady Stokes equation in the presence of a force dipole reads,

$$\nabla\cdot\boldsymbol{\sigma}(\boldsymbol{x}) + \nabla\cdot[\boldsymbol{S}\delta(\boldsymbol{x}-\boldsymbol{x_0})] + \frac{1}{2}\nabla\times[\boldsymbol{T}\delta(\boldsymbol{x}-\boldsymbol{x_0})] + \nabla\left[\frac{1}{3}D_{nn}\delta(\boldsymbol{x}-\boldsymbol{x_0})\right] = \boldsymbol{0}. \tag{2.36}$$

Since $\boldsymbol{S}$ represents a symmetric stress acting *on* the fluid, the flow associated with $\boldsymbol{S}$ is called a stresslet. Similarly, $\boldsymbol{T}$ represents the torque due to a dipole *on* the fluid, and the associated flow is called a rotlet. The last term on the right-hand side of equation (2.36) appears as an isotropic stress acting radially outwards *on* the fluid. This isotropic stress is balanced by the pressure to enforce incompressibility and does not lead to any flow field, as seen by its absence from equation (2.34).

Now that we understand each part that makes up $\mathcal{T}_{ijk} = -\mathcal{P}_i\delta_{kj} + (\partial_j\mathcal{G}_{ik} + \partial_k\mathcal{G}_{ij})$ (see equation (2.23)), we can see why the first term on the right-hand side of equation (2.27) is called the double layer potential. The term $u_j\mathcal{T}_{ijk}\hat{n}_k$ represents the flow due to a point source of strength $u_j\hat{n}_j$ and the stresslet of strength $u_j\hat{n}_k$. The integral of these quantities over the boundaries represents point sources and force dipoles (two layers of forces) distributed on the surface of the body, as shown in Figure 2.3. This interpretation highlights an important point about the double-layer potential. The flow due to the double-layer potential is discontinuous across a boundary, as shown in Figure 2.3. This fact plays a central role in the boundary integral formulation in terms of the double-layer potential, yielding a second-kind integral equation.

2.1.6 Multipole Expansion

Returning to the case of a rigid body in steady Stokes flow, we have the integral form for the fluid velocity outside the rigid body given by equation (2.30). Since the integral is evaluated over the surface of the body, the resulting velocity field inherently depends on the geometry of the rigid body. However, at distances much larger than the characteristic size of the body, the influence of these geometric details diminishes, and the velocity field exhibits universal features. This asymptotic behaviour is systematically captured through a multipole expansion. Multipole expansion relies on the idea that the evaluation point $\boldsymbol{x_0}$ of the velocity field is far away from the source point $\boldsymbol{x}$, i.e., $|\boldsymbol{x}| \ll |\boldsymbol{x_0}|$, with the origin located somewhere inside the rigid body. One can then use the Taylor expansion to write

$$\mathcal{G}_{ij}(\boldsymbol{x_0}, \boldsymbol{x}) = \sum_{n=0}^{\infty} \frac{1}{n!}(\boldsymbol{x} \cdot \boldsymbol{\nabla}_{\boldsymbol{x}})^n \, \mathcal{G}_{ij}(\boldsymbol{x_0}, \boldsymbol{x})\bigg|_{\boldsymbol{x}=\boldsymbol{0}} = \sum_{n=0}^{\infty} \frac{(-1)^n}{n!}(\boldsymbol{x} \cdot \boldsymbol{\nabla}_{\boldsymbol{x_0}})^n \, \mathcal{G}_{ij}(\boldsymbol{x_0}, \boldsymbol{0}).$$

Using this in equation (2.30), we get the far-field fluid velocity outside the rigid body as

$$\begin{aligned} u_i(\boldsymbol{x_0}) &= -\frac{1}{8\pi\mu} \oint_{S_p} \sigma_{jk}(\boldsymbol{x})\hat{n}_k(\boldsymbol{x}) \sum_{n=0}^{\infty} \frac{(-1)^n}{n!}(\boldsymbol{x} \cdot \boldsymbol{\nabla}_{\boldsymbol{x_0}})^n \, \mathcal{G}_{ij}(\boldsymbol{x_0}, \boldsymbol{0}) \, dS(\boldsymbol{x}) \\ &= -\frac{1}{8\pi\mu} F^h_j \mathcal{G}_{ij}(\boldsymbol{x_0}, \boldsymbol{0}) + \frac{1}{8\pi\mu} D_{jk} \frac{\partial}{\partial x_{0k}} \mathcal{G}_{ij}(\boldsymbol{x_0}, \boldsymbol{0}) + \ldots, \end{aligned} \tag{2.37}$$

where

$$F^h_j = \oint_{S_p} \sigma_{jk}(\boldsymbol{x})\hat{n}_k(\boldsymbol{x}) \, dS(\boldsymbol{x}), \tag{2.38a}$$

$$D_{jk} = \oint_{S_p} x_k \sigma_{jm}(\boldsymbol{x})\hat{n}_m(\boldsymbol{x}) \, dS(\boldsymbol{x}). \tag{2.38b}$$

Therefore, the far field velocity from a body can be written in terms of a Stokeslet with strength equal to the hydrodynamic force on the body $\boldsymbol{F}^h$ which decays as

$|\boldsymbol{x_0}|^{-1}$, a force dipole with strength $\boldsymbol{D}$ which decays as $|\boldsymbol{x_0}|^{-2}$ and higher order multipole moments which decays faster than $|\boldsymbol{x_0}|^{-2}$. From our previous discussion, we can decompose the force dipole $\boldsymbol{D}$ into a symmetric traceless part $\boldsymbol{S}$ with the associated flow called a stresslet and an antisymmetric part $\boldsymbol{T}$ with the associated flow called a rotlet. Using equations (2.33) and (2.35), we have

$$T_{jk} = \frac{1}{2}(D_{jk} - D_{kj}) = \frac{1}{2}\oint_{S_p} [(\boldsymbol{\sigma}\cdot\hat{\boldsymbol{n}})_j x_k - (\boldsymbol{\sigma}\cdot\hat{\boldsymbol{n}})_k x_j]\, dS(\boldsymbol{x}) \tag{2.39a}$$

$$T_i = \epsilon_{ijk}T_{jk} = \epsilon_{ijk}\oint_{S_p} (\boldsymbol{\sigma}\cdot\hat{\boldsymbol{n}})_j x_k\, dS(\boldsymbol{x}) = -T_i^h, \tag{2.39b}$$

$$S_{jk} = \frac{1}{2}(D_{jk} + D_{kj}) - \frac{1}{3}D_{mm}\delta_{jk} = \frac{1}{2}\oint_{S_p} [(\boldsymbol{\sigma}\cdot\hat{\boldsymbol{n}})_j x_k + (\boldsymbol{\sigma}\cdot\hat{\boldsymbol{n}})_k x_j]\, dS(\boldsymbol{x}) - \frac{1}{3}\delta_{jk}\oint_{S_p} (\boldsymbol{\sigma}\cdot\hat{\boldsymbol{n}})_m x_m\, dS(\boldsymbol{x}). \tag{2.39c}$$

Note that equation (2.39b) shows that the antisymmetric part of the force dipole $\boldsymbol{D}$ corresponds to the negative of the hydrodynamic torque $\boldsymbol{T}^h$ on the body. Therefore, the far-field velocity due to a body can be written in terms of Stokeslet, rotlet, and stresslet as

$$u_i(\boldsymbol{x_0}) = \frac{1}{8\pi\mu}\left[\underbrace{-F_j^h \mathcal{G}_{ij}(\boldsymbol{x_0},\boldsymbol{0})}_{\text{Stokeslet}} + \underbrace{\frac{1}{2}\epsilon_{jmk}T_m^h \frac{\partial}{\partial x_{0k}}\mathcal{G}_{ij}(\boldsymbol{x_0},\boldsymbol{0})}_{\text{Rotlet}} + \underbrace{S_{jk}\frac{\partial}{\partial x_{0k}}\mathcal{G}_{ij}(\boldsymbol{x_0},\boldsymbol{0})}_{\text{Stresslet}}\right] + \ldots \tag{2.40}$$

In the overdamped limit, the hydrodynamic force $\boldsymbol{F}^h$ and hydrodynamic torque $\boldsymbol{T}^h$ are negative of the external force and torque acting on the body. Therefore, for a body under an external force, like gravity, the leading order flow field is produced due to the Stokeslet. For neutrally buoyant bodies experiencing no external torque, the leading-order contribution to the flow field arises from the stresslet. This is typically the case for many microorganisms [11, 13]. As discussed previously, the stresslet contributes to the symmetric stress tensor in the fluid (see equation (2.36)). Thus, a suspension of neutrally buoyant particles leads to a change in the viscosity of the fluid.

2.2 A Quicker Review of Electrostatics

The governing equation for the electric field $\boldsymbol{E}$ in the realm of electrostatics is given by [59, 60, 97]

$$\nabla\cdot\boldsymbol{E}(\boldsymbol{x}) = \rho(\boldsymbol{x})/\epsilon_0, \quad \nabla\times\boldsymbol{E}(\boldsymbol{x}) = \boldsymbol{0} \tag{2.41a}$$

$$\implies \boldsymbol{E}(\boldsymbol{x}) = -\boldsymbol{\nabla}\phi(\boldsymbol{x}), \quad \nabla^2\phi(\boldsymbol{x}) = -\rho(\boldsymbol{x})/\epsilon_0. \tag{2.41b}$$

Here ρ is the charge density, ϵ_0 is the permittivity of the free space, and $\phi(\boldsymbol{x})$ is the scalar potential. The charge density on the surface S_p of a perfect conductor can be obtained in terms of the potential *outside* its surface as [59, 60, 97]

$$\sigma(\boldsymbol{x}) = -\epsilon_0\hat{\boldsymbol{n}}(\boldsymbol{x})\cdot\boldsymbol{\nabla}\phi(\boldsymbol{x}), \quad \boldsymbol{x}\in S_p.$$

The normal vector $\hat{\boldsymbol{n}}$ points *outside* the surface of the conductor. Therefore, the total charge on the surface is given by

$$Q = \oint_{S_p}\sigma(\boldsymbol{x})dS(\boldsymbol{x}) = -\epsilon_0\oint_{S_p}\hat{\boldsymbol{n}}(\boldsymbol{x})\cdot\boldsymbol{\nabla}\phi(\boldsymbol{x})\,dS(\boldsymbol{x}), \quad \boldsymbol{x}\in S_p. \tag{2.42}$$

We shall exclusively work with the scalar potential, which is sufficient to describe various phenomena in electrostatics.

2.2.0.1 Free Space Green's Function in Electrostatics

Consider the fundamental solution of the electrostatic potential in an unbounded domain

$$\nabla^2\phi(\boldsymbol{x}) = -\frac{Q}{\epsilon_0}\delta(\boldsymbol{x}-\boldsymbol{x_0}); \quad \phi(\boldsymbol{x})\to 0 \text{ as } |\boldsymbol{x}|\to\infty, \tag{2.43}$$

where $Q\delta(\boldsymbol{x}-\boldsymbol{x_0})$ is the point charge density located at $\boldsymbol{x_0}$. This can be easily solved either using Fourier transforms or by noting that $\nabla^2|\boldsymbol{x}|^{-1} = -4\pi\delta(\boldsymbol{x})$. The fundamental solution is given by [59, 60, 98]

$$\phi(\boldsymbol{x}) = \frac{Q}{4\pi\epsilon_0}\mathcal{G}(\boldsymbol{x},\boldsymbol{x_0}), \quad \mathcal{G}(\boldsymbol{x},\boldsymbol{x_0}) \equiv \frac{1}{|\boldsymbol{x}-\boldsymbol{x_0}|}. \tag{2.44}$$

Here $\boldsymbol{x}$ is the target point, $\boldsymbol{x_0}$ is the source point, and $\mathcal{G}$ is the Green's function for the electrostatic potential. Note that the Green's function satisfies

$$\nabla^2\mathcal{G}(\boldsymbol{x},\boldsymbol{x_0}) = -4\pi\delta(\boldsymbol{x}). \tag{2.45}$$

2.2.1 Green's Reciprocal Theorem in Electrostatics

The Lorentz reciprocal theorem in microhydrodynamics has an analog in electrostatics, known as Green's reciprocal theorem. Both theorems are based on the same principle of relating the integrals of two fields over a common domain. Consider two electrostatic potentials $\phi^{(1)}$ and $\phi^{(2)}$ in the same domain $\mathcal{D}$. Using the divergence theorem, we have

$$\oint_{\partial\mathcal{D}}\phi^{(1)}[\boldsymbol{n}\cdot\boldsymbol{\nabla}\phi^{(2)}]\,dS - \oint_{\partial\mathcal{D}}\phi^{(2)}[\boldsymbol{n}\cdot\boldsymbol{\nabla}\phi^{(1)}]\,dS = \int_{\mathcal{D}}\phi^{(1)}\nabla^2\phi^{(2)}\,dV - \int_{\mathcal{D}}\phi^{(2)}\nabla^2\phi^{(1)}\,dV. \tag{2.46}$$

Here $\boldsymbol{n}$ is the normal vector to the boundary of the domain, denoted by $\partial\mathcal{D}$, pointing *away* from the domain $\mathcal{D}$. Equation (2.46) is called the generalised reciprocal theorem in electrostatics.

A corollary of the reciprocal theorem is the linear relationship between total charge and the potential on the surface of a perfect conductor. Consider two separate configurations, each involving a single perfect conductor. The electrostatic potentials $\phi_1(\boldsymbol{x})$ and $\phi_2(\boldsymbol{x})$ correspond to conductors carrying charges Q_1 and Q_2, and held at surface potentials V_1 and V_2, respectively. Since the potential field satisfies the homogeneous Laplace equation outside the conductor in both cases, the reciprocal theorem yields

$$V_1 \oint_{S_p} [\boldsymbol{n} \cdot \nabla\phi_2]\, dS = V_2 \oint_{S_p} [\boldsymbol{n} \cdot \nabla\phi_1]\, dS \implies V_1 Q_2 = V_2 Q_1.$$

The fact that Q/V is identical in both cases implies that it depends solely on the surface geometry, which remains unchanged between the two configurations. This proportionality constant $C = Q/V$, which relates charge to potential on a conductor, is called *capacitance* of a conductor, which only depends on the geometry of the conductor. The concept of capacitance, or its inverse called the *potential matrix*, straightforwardly generalises to multiple conductors. The potential matrix is thoroughly used in Chapter 5 of this thesis.

2.2.2 Integral Representation of Electrostatic Potential

Let $\phi^{(1)} = \phi(\boldsymbol{x})$ be the desired electrostatic potential satisfying the homogeneous Laplace equation in the domain $\mathcal{D}$. Let $\phi^{(2)}$ be the auxiliary electrostatic potential due to a point charge Q located at $\boldsymbol{x_0}$, either in the domain $\mathcal{D}$, or outside the domain $\mathbb{R}^3\backslash\overline{\mathcal{D}}$, but not at the boundary $\partial\mathcal{D}$. The auxiliary potential satisfies

$$\nabla^2\phi^{(2)}(\boldsymbol{x}) = -\frac{Q}{\epsilon_0}\delta(\boldsymbol{x} - \boldsymbol{x_0}), \quad \phi^{(2)}(\boldsymbol{x}) = \frac{Q}{4\pi\epsilon_0}\mathcal{G}(\boldsymbol{x}, \boldsymbol{x_0}).$$

Using the reciprocal theorem for electrostatics (2.46) and factoring out the arbitrary charge Q, we have

$$\frac{1}{4\pi}\oint_{\partial\mathcal{D}} \phi(\boldsymbol{x})\hat{\boldsymbol{n}}(\boldsymbol{x}) \cdot \nabla\mathcal{G}(\boldsymbol{x}, \boldsymbol{x}_0)\, dS(\boldsymbol{x}) \\ - \frac{1}{4\pi}\oint_{\partial\mathcal{D}} \mathcal{G}(\boldsymbol{x}, \boldsymbol{x_0})\hat{\boldsymbol{n}}(\boldsymbol{x}) \cdot \nabla\phi(\boldsymbol{x})\, dS(\boldsymbol{x}) = \begin{cases} \phi(\boldsymbol{x_0}), & \boldsymbol{x_0} \in \mathcal{D}, \\ 0, & \boldsymbol{x_0} \notin \overline{\mathcal{D}}. \end{cases} \tag{2.47}$$

Here $\hat{\boldsymbol{n}}$ again points towards the domain of interest $\mathcal{D}$ (see figure 2.1). The first term on the left-hand side of equation (2.47) is called the double-layer potential, and the second term is called the single-layer potential. The nomenclature is clear as they represent potential due to a dipole layer and a single layer of charges distributed over the boundaries of the domain.

The integral representation for the potential outside a perfect conductor can be simplified using the fact that the potential inside a perfect conductor is constant and equal to its surface value, V_0. This is similar to the single-layer representation of rigid bodies in Stokes flow. Applying the reciprocal theorem inside the surface of the conductor with the target point $\boldsymbol{x_0}$ lying in the domain $\mathcal{D}$, which is outside the conductor, we have

$$0 = \frac{1}{4\pi} \oint_{S_p} \hat{\boldsymbol{n}}(\boldsymbol{x}) \cdot \boldsymbol{\nabla} \mathcal{G}(\boldsymbol{x}, \boldsymbol{x_0})\, dS(\boldsymbol{x}), \quad \boldsymbol{x_0} \in \mathcal{D} \tag{2.48}$$

Equation (2.48) can also be interpreted as stating that the flux of fluid through a closed surface, due to a source located outside the enclosed volume, is zero. Using equation (2.48) in the equation (2.47) and noting that, as the potential fields decay to zero at infinity, the boundary contribution comes only from the surface of the conductor, we have

$$\phi(\boldsymbol{x}_0) = -\frac{1}{4\pi} \oint_{S_p} \mathcal{G}(\boldsymbol{x_0}, \boldsymbol{x}) \hat{\boldsymbol{n}}(\boldsymbol{x}) \cdot \boldsymbol{\nabla} \phi(\boldsymbol{x})\, dS(\boldsymbol{x}), \quad \boldsymbol{x_0} \in \mathcal{D}. \tag{2.49}$$

2.2.3 Multipole Expansion in Electrostatics

Similar to the case in Stokes flow, one can obtain the universal structure of the potential field outside a conductor at distances much larger than the typical size of the conductor using the multipole expansion. For simplicity, we assume that the origin is located somewhere inside the conductor and $|\boldsymbol{x}| \ll |\boldsymbol{x_0}|$. Using the Taylor expansion

$$\mathcal{G}(\boldsymbol{x_0}, \boldsymbol{x}) = \sum_{n=0}^{\infty} \frac{1}{n!} (\boldsymbol{x} \cdot \boldsymbol{\nabla}_{\boldsymbol{x}})^n \mathcal{G}(\boldsymbol{x_0}, \boldsymbol{x}) \bigg|_{\boldsymbol{x}=\boldsymbol{0}} = \sum_{n=0}^{\infty} \frac{(-1)^n}{n!} (\boldsymbol{x} \cdot \boldsymbol{\nabla}_{\boldsymbol{x_0}})^n \mathcal{G}(\boldsymbol{x_0}, \boldsymbol{0}),$$

in equation (2.49), we have

$$\begin{aligned} \phi(\boldsymbol{x_0}) = -\frac{1}{4\pi} \oint_{S_p} \hat{\boldsymbol{n}}(\boldsymbol{x}) \cdot \boldsymbol{\nabla} \phi(\boldsymbol{x}) \sum_{n=0}^{\infty} \frac{(-1)^n}{n!} (\boldsymbol{x} \cdot \boldsymbol{\nabla}_{\boldsymbol{x_0}})^n \mathcal{G}(\boldsymbol{x_0}, \boldsymbol{0})\, dS(\boldsymbol{x}) \\ = \frac{Q}{4\pi\epsilon_0} \mathcal{G}(\boldsymbol{x_0}, \boldsymbol{0}) - \frac{\boldsymbol{d}}{4\pi\epsilon_0} \cdot \boldsymbol{\nabla}_{\boldsymbol{x}_0} \mathcal{G}(\boldsymbol{x}_0, \boldsymbol{0}) + \ldots, \end{aligned} \tag{2.50}$$

where Q is the total charge on the conductor and $\boldsymbol{d}$ is the dipole moment of the conductor, given by

$$Q = -\epsilon_0 \oint_{S_p} \hat{\boldsymbol{n}}(\boldsymbol{x}) \cdot \boldsymbol{\nabla} \phi(\boldsymbol{x})\, dS(\boldsymbol{x}), \tag{2.51a}$$

$$\boldsymbol{d} = -\epsilon_0 \oint_{S_p} \boldsymbol{x}[\hat{\boldsymbol{n}}(\boldsymbol{x}) \cdot \nabla\phi(\boldsymbol{x})]\, dS(\boldsymbol{x}). \tag{2.51b}$$

The higher-order multipole moments can be computed by taking higher-order moments of the surface charge density $-\epsilon_0 \hat{\boldsymbol{n}} \cdot \nabla\phi$. Note that for a charged conductor, the leading order contribution to the potential decays as $|\boldsymbol{x}_0|^{-1}$. For an uncharged conductor, the dipole moment contributes to the leading-order potential field, which decays as $|\boldsymbol{x}_0|^{-2}$.

The main ideas covered up to now for both microhydrodynamics and electrostatics will help in studying the hydrodynamic and electrostatic interactions between multiple rigid bodies and conductors, respectively. Comprehensive details on these topics can be found in [10, 59, 60].

2.3 Singularity Solutions in Electrostatics

We are interested in obtaining the electrostatic potential outside a perfect conductor in an unbounded domain. Let S_p denote the surface of the conductor. This requires solving the boundary value problem given by

$$\nabla^2\phi(\boldsymbol{x}) = 0, \tag{2.52a}$$

$$\phi(\boldsymbol{x}) = \phi_0, \quad \boldsymbol{x} \in S_p, \tag{2.52b}$$

$$\phi(\boldsymbol{x}) \to 0 \quad \text{as} \quad |\boldsymbol{x}| \to \infty. \tag{2.52c}$$

Here ϕ_0 is the constant potential over the surface of the conductor. Note that any linear functional of the electrostatic Green's function, whether an integral or a differential operator, satisfies the homogeneous Laplace equation outside the region S_p, provided the source of the Green's function lies outside the domain, i.e., within the conductor. This forms the basis of singularity solutions. A singularity solution to a given boundary value problem consists of a superposition of such linear functionals of the Green's function, constructed to satisfy the prescribed boundary conditions. We now review singularity solutions for spherical and spheroidal conductors [99].

2.3.1 Charged Sphere

Consider a sphere with radius a, centered at the origin. The singularity solution is simply given by the point charge placed at the centre of the sphere as

$$\phi(\boldsymbol{x}) = a\phi_0 \mathcal{G}(\boldsymbol{x}, \boldsymbol{0}) = \phi_0 \frac{a}{|\boldsymbol{x}|}. \tag{2.53}$$

It is easy to see that the solution satisfies the Laplace equation outside the sphere and the boundary conditions given by equation (2.52). The total charge Q on the surface of the sphere is given by

$$Q = -\varepsilon_0 \oint_{S_p} \hat{\boldsymbol{n}} \cdot \nabla\phi \, dS = -\,\varepsilon_0 \int_{V_p} \nabla^2\phi \, dV = (4\pi a\epsilon_0)\phi_0. \tag{2.54}$$

Consequently, the capacitance of the sphere is given by $C = Q/\phi_0 = 4\pi a\epsilon_0$ [60, 64, 97, 100].

2.3.2 Charged Prolate Spheroid

Any point $\boldsymbol{x}$ on a prolate spheroid S_p with semi-major axis a and aspect ratio $\kappa(>1)$, oriented along the unit vector $\boldsymbol{p}$ and centered at origin is given by

$$\boldsymbol{x} \cdot \left[\frac{1}{a^2}\boldsymbol{pp} + \frac{1}{a^2\kappa^{-2}}(\boldsymbol{\delta} - \boldsymbol{pp})\right] \cdot \boldsymbol{x} = 1, \quad \boldsymbol{x} \in S_p. \tag{2.55}$$

The singularity solution to equation (2.52) can be represented in terms of a uniform charge distribution located along the symmetry axis of S_p as [99]

$$\phi(\boldsymbol{x}) = \phi_0 \left\{ \frac{1}{2\,\mathrm{arctanh}\, e} \int_{-ae}^{ae} \mathcal{G}(\boldsymbol{x}, \xi\boldsymbol{p})\, d\xi \right\}, \tag{2.56}$$

where $e = \sqrt{1-\kappa^{-2}}$ is the eccentricity. The total charge Q on the surface of S_p is given by

$$Q = -\varepsilon_0 \oint_{S_p} \hat{\boldsymbol{n}} \cdot \nabla\phi \, dS = -\,\varepsilon_0 \int_{V_p} \nabla^2\phi \, dV = \left[\frac{4\pi a\,\varepsilon_0 e}{\mathrm{arctanh}\, e}\right]\phi_0, \tag{2.57}$$

Consequently, the capacitance $C \equiv Q/\phi_0$ of the perfectly conducting prolate spheroid S_p is given by [60, 64, 97, 100]

$$C = \frac{4\pi a\,\varepsilon_0 e}{\mathrm{arctanh}\, e}. \tag{2.58}$$

Note that as $\lim_{e\to 0} \mathrm{C} = 4\pi a\,\varepsilon_0$, which is the capacitance of a sphere of radius a.

2.3.3 Charged Oblate Spheroid

The singularity solution of an oblate spheroid can be derived from that of a prolate spheroid using the eccentricity transformation [101]

$$e \to \frac{ie}{\sqrt{1-e^2}}. \tag{2.59}$$

Therefore, the potential field due to an isolated oblate spheroid described by equation (2.55) with $\kappa < 1$[1] is given by:

$$\phi(\boldsymbol{x}) = \phi_0 \left\{ \frac{1}{2 \arcsin e} \int_{-ae/\kappa}^{ae/\kappa} \mathcal{G}(\boldsymbol{x}, i\xi \boldsymbol{p})\, d\xi \right\}. \tag{2.60}$$

Note that for cartesian coordinates aligned such that the unit vector $\boldsymbol{p}$ is along the z-axis, $\mathcal{G}(\boldsymbol{x}, i\xi\boldsymbol{p})$ gives rise to a term $\dfrac{1}{\sqrt{x^2 + y^2 + (z - i\xi)^2}}$ which is singular on the disk of radius ξ in the $x - y$ plane ($z = 0$), which corresponds to the singularity distribution for an oblate spheroid [10].

Correspondingly, the capacitance of an isolated oblate spheroid is given by [60, 64, 97, 100]

$$C = \frac{4\pi a \varepsilon_0 e}{\kappa \arcsin e}. \tag{2.61}$$

2.3.4 Grounded Prolate Spheroid in Presence of a Uniform Electric Field

The potential field in this case can be divided into two parts as $\phi = \phi^d + \phi^\infty$. Here ϕ^d is the disturbance potential produced by the grounded prolate spheroid to maintain zero potential on its surface, and $\phi^\infty = -\boldsymbol{E}^\infty \cdot \boldsymbol{x}$, with $\boldsymbol{E}^\infty$ being the ambient uniform electric field. The boundary value problem to be solved for $\phi^d(\boldsymbol{x})$ outside S_p in this case is

$$\nabla^2 \phi^d(\boldsymbol{x}) = 0, \tag{2.62a}$$

$$\phi^d(\boldsymbol{x}) = \boldsymbol{E}^\infty \cdot \boldsymbol{x}, \quad \boldsymbol{x} \in S_p, \tag{2.62b}$$

$$\phi^d(\boldsymbol{x}) \to 0 \quad \text{as} \quad |\boldsymbol{x}| \to \infty. \tag{2.62c}$$

The singularity solution can be represented as [99]

$$\phi^d(\boldsymbol{x}) = \boldsymbol{E}^\infty \cdot \left\{ \frac{3X_p^C}{2e^3} \boldsymbol{p} \int_{-ae}^{ae} \xi\, \mathcal{G}(\boldsymbol{x}, \xi\boldsymbol{p})\, d\xi \right. \\ \left. - \frac{3Y_p^C}{4e^3} (\boldsymbol{\delta} - \boldsymbol{pp}) \cdot \nabla \int_{-ae}^{ae} (a^2e^2 - \xi^2) \mathcal{G}(\boldsymbol{x}, \xi\boldsymbol{p})\, d\xi \right\}, \tag{2.63}$$

where

$$X_p^C \equiv \frac{e^3}{3} (\operatorname{arctanh} e - e)^{-1}, \quad Y_p^C \equiv \frac{2e^3}{3} \left(\frac{e}{1 - e^2} - \operatorname{arctanh} e \right)^{-1}. \tag{2.64}$$

---

[1] the eccentricity is now given by $\sqrt{1 - \kappa^2}$

The first integral term in equation (2.63) represents a linear charge distribution along the symmetry axis, whereas the second integral term represents the parabolic distribution of dipole moments pointing perpendicular to the symmetry axis. Note that the charge distribution in the first integral term has a non-zero dipole moment but zero net charge. The induced dipole moment $\boldsymbol{d}$ is given by (see equation (2.51b))

$$\boldsymbol{d} = -\varepsilon_0 \oint_{S_p} \boldsymbol{x}\, \hat{\boldsymbol{n}} \cdot \nabla\phi \, dS = -\varepsilon_0 \int_{V_p} [\nabla\phi + \boldsymbol{x}\, \nabla^2\phi]\, dV \tag{2.65}$$

The volume integral of the gradient term doesn't contribute since $\phi = 0$ on S_p and

$$\int_{V_p} \nabla\phi \, dV = \oint_{S_p} \phi\, \hat{\boldsymbol{n}}\, dS = 0. \tag{2.66}$$

Therefore, the dipole moment is given by

$$\boldsymbol{d} = -\varepsilon_0 \int_{V_p} \boldsymbol{x}\, \nabla^2\phi^d \, dV = \quad 4\pi a^3 \varepsilon_0 [X_p^C \boldsymbol{pp} + Y_p^C (\boldsymbol{\delta} - \boldsymbol{pp})] \cdot \boldsymbol{E}^\infty. \tag{2.67}$$

Note that $\lim_{e\to 0} X_p^C = \lim_{e\to 0} Y_p^C = 1$, resulting in $\lim_{e\to 0} \boldsymbol{d} = 4\pi a^3 \varepsilon_0 \boldsymbol{E}^\infty$ and we get the dipole moment of a sphere of radius a. We can rewrite equation (2.63) in terms of the dipole moment $\boldsymbol{d}$ as

$$\begin{aligned}\phi^d(\boldsymbol{x}) = {} & \frac{3}{8\pi a^3 e^3 \varepsilon_0} \boldsymbol{d} \cdot \boldsymbol{p} \int_{-ae}^{ae} \xi\, \mathcal{G}(\boldsymbol{x}, \xi\boldsymbol{p})\, d\xi \\ & - \frac{3}{16\pi a^3 e^3 \varepsilon_0} \boldsymbol{d} \cdot (\boldsymbol{\delta} - \boldsymbol{pp}) \cdot \nabla_x \int_{-ae}^{ae} (a^2e^2 - \xi^2)\, \mathcal{G}(\boldsymbol{x}, \xi\boldsymbol{p})\, d\xi. \end{aligned} \tag{2.68}$$

2.3.5 Grounded Oblate Spheroid in Presence of a Uniform Electric Field

We again use the eccentricity transformation (2.59) to obtain the dipole moment $\boldsymbol{d}$ and disturbance potential field $\phi^d(\boldsymbol{x})$ due to a grounded oblate spheroid in the presence of a uniform background electric field $\boldsymbol{E}^\infty$. The dipole moment is given by

$$\boldsymbol{d} = 4\pi a^3 \varepsilon_0 [X_o^C \boldsymbol{pp} + Y_o^C (\boldsymbol{\delta} - \boldsymbol{pp})] \cdot \boldsymbol{E}^\infty, \tag{2.69}$$

where

$$X_o^C \equiv \frac{e^3}{3} [e(1-e^2) - (1-e^2)^{3/2} \arcsin e]^{-1}, \tag{2.70a}$$

$$Y_o^C \equiv \frac{2e^3}{3} \left[e(1-e^2)^2 - (1-e^2)^{3/2} \arcsin e\right]^{-1}. \tag{2.70b}$$

The disturbance potential field is given by:

$$\phi^d(\boldsymbol{x}) = \frac{3\kappa^3}{8\pi a^3 e^3 \varepsilon_0}\left\{\boldsymbol{d}\cdot\boldsymbol{p}\int_{-ae/\kappa}^{ae/\kappa} -i\xi\,\mathcal{G}(\boldsymbol{x}, i\xi\boldsymbol{p})\,d\xi \right.$$
$$\left. -\frac{1}{2}\boldsymbol{d}\cdot(\boldsymbol{\delta}-\boldsymbol{pp})\cdot\nabla_x\int_{-ae/\kappa}^{ae/\kappa}\left(\frac{a^2e^2}{\kappa^2}-\xi^2\right)\mathcal{G}(\boldsymbol{x}, i\xi\boldsymbol{p})\,d\xi\right\}. \quad (2.71)$$

2.4 Faxén's Laws for Arbitrarily Shaped Conductors in Electrostatics

Once the singularity solutions are known for a given conductor geometry, Faxén's laws can be used to determine the induced multipole moments on the conductor due to an *arbitrary* background potential field. This approach enables analytical expressions for the electrostatic potential outside a collection of conductors, as each conductor induces multipole moments in response to the others. The power of the reciprocal theorem lies in its ability to relate these induced multipole moments to the singularity solutions. Faxén's laws for electrostatics can be derived analogously to those in microhydrodynamics [10], using the reciprocal theorem. The electrostatic counterpart for spheres is detailed in [58], and we extend this framework to arbitrarily shaped conductors.

2.4.1 Faxén's Law for Total Charge and Potential on a Conductor

We follow the approach of [10] to relate the total charge Q on the surface of a conductor to its surface potential V in presence of an arbitrary background potential field $\boldsymbol{\phi}^\infty(\boldsymbol{x})$, such that $\phi^\infty(\boldsymbol{x}) \sim \mathcal{O}(1/|\boldsymbol{x}|)$ as $\boldsymbol{x}$ goes to infinity. Let us denote the surface of an arbitrary-shaped conductor by S_p. Note that total charge on S_p due to a potential $\phi(\boldsymbol{x})$ outside it, is given by

$$Q = -\varepsilon_0 \oint_{S_p} \nabla\phi\cdot\hat{\boldsymbol{n}}\,dS, \quad (2.72)$$

where $\hat{\boldsymbol{n}}$ is the outward pointing normal vector to S_p and ε_0 is the permittivity of free space.

We use the reciprocal theorem with the details of the two fields as follows:

1. Take ϕ_1 to be the potential field satisfying the Laplace equation outside the isolated conductor with $\phi_1 = \phi_{10}$ on S_p, where ϕ_{10} is some constant and ϕ_1 goes to zero at infinity. This is a case of an isolated conductor with some charge Q_1 on its surface given by $Q_1 = C\phi_{10}$, where C is the capacitance of the conductor.

2. Take ϕ_2 to be the potential field given by the solution of $\nabla^2\phi_2(\boldsymbol{x}) = -Q'\varepsilon_0^{-1}\,\delta(\boldsymbol{x}-\boldsymbol{y})$, where $\boldsymbol{y} \in D$, with $\phi_2 = V$ on S_p. Here, the ambient potential field $\phi_2^\infty(\boldsymbol{x})$ is given by a point charge located at $\boldsymbol{y}$, and the conductor produces a disturbance field in order to satisfy the boundary condition on its surface. Let Q_2 be the charge on the conductor, which is to be determined using the reciprocal theorem.

Using equations (2.46) and (2.72), we have[2],

$$\begin{aligned} Q'\phi_1(\boldsymbol{y}) &= Q_1 V - Q_2\phi_{10} \\ \implies Q_2\phi_{10} &= C\phi_{10}V - Q'\phi_1(\boldsymbol{y}). \end{aligned} \tag{2.73}$$

Now, $\phi_1(\boldsymbol{y})$ can be represented in terms of singularity solution as

$$\phi_1(\boldsymbol{y}) = \phi_{10}\mathcal{F}_V\{\mathcal{G}(\boldsymbol{y},\boldsymbol{\xi})\} = \phi_{10}\mathcal{F}_V\{\mathcal{G}(\boldsymbol{\xi},\boldsymbol{y})\}. \tag{2.74}$$

Here $\mathcal{F}_V$ is the corresponding linear functional and $\boldsymbol{\xi}$ represents the region inside the conductor over which the singularities are distributed. Using equations (2.4.1) and (2.74), we have

$$Q_2 = CV - Q'\mathcal{F}_V\{\mathcal{G}(\boldsymbol{\xi},\boldsymbol{y})\} = CV - 4\pi\epsilon_0\mathcal{F}_V\{\phi_2^\infty(\boldsymbol{\xi})\}. \tag{2.75}$$

Here we have used the fact that $Q'\mathcal{G}(\boldsymbol{\xi},\boldsymbol{y}) = 4\pi\epsilon_0\phi_2^\infty(\boldsymbol{\xi})$. However, all ambient fields $\phi^\infty(\boldsymbol{x})$ that decay at infinity and satisfy the Laplace equation can be constructed using an appropriate set of point charges. Therefore, equation (2.75) applies to a general ambient field $\phi^\infty(\boldsymbol{x})$. Thus, the relation between charge Q on a conductor and the potential V on its surface in presence of a background potential field $\phi^\infty(\boldsymbol{x})$ is given by

$$Q = CV - 4\pi\epsilon_0\mathcal{F}_V\{\phi^\infty(\boldsymbol{\xi})\}. \tag{2.76}$$

This result can be directly applied to the bodies with a known singularity solution of the form given in equation (2.74). In particular, for a prolate spheroid with semi-major axis a, eccentricity e, and orientation vector $\boldsymbol{p}$, we have the singularity representation given by equation (2.56) and capacitance by equation (2.58). Therefore, the charge Q on the prolate spheroid in the presence of a background potential field ϕ^∞ is given by

$$Q = \frac{4\pi a\,\varepsilon_0 e}{\operatorname{arctanh} e}\left\{V - \frac{1}{2ae}\int_{-ae}^{ae}\phi^\infty(\boldsymbol{x}_c + \xi\boldsymbol{p})\,d\xi\right\}, \tag{2.77}$$

---

[2] We have used the fact that the fields involved in the problems decay fast enough far from the conductor to have zero contribution from the surface "at infinity".

where $c = ae$ and $\boldsymbol{x}_c$ denotes the centre of the prolate spheroid.

Similarly, the charge relation for an oblate spheroid with semi-major axis a and orientation vector $\boldsymbol{p}$ in the presence of a background potential field ϕ^∞ is given by

$$Q = \frac{4\pi a\varepsilon_0 e}{\kappa \arcsin e}\left\{V - \frac{\kappa}{2ae}\int_{-ae/\kappa}^{ae/\kappa} \phi^\infty(\boldsymbol{x}_c + i\xi\boldsymbol{p})\, d\xi\right\}, \tag{2.78}$$

2.4.2 Faxén's Law for Induced Dipole Moment on a Conductor

To relate the induced dipole moment $\boldsymbol{d}$ on a conductor in the presence of an ambient potential field $\phi^\infty(\boldsymbol{x})$, we again use the reciprocal theorem with the details of the two fields as follows:

1. Take ϕ_1 to be the potential field satisfying the Laplace equation outside the isolated conductor with $\phi_1 = \boldsymbol{E}_{10}^\infty \cdot \boldsymbol{x}$ on S_p, where $\boldsymbol{E}_{10}^\infty$ is a constant electric field and ϕ_1 goes to zero at infinity. This is a case of the disturbance potential produced by a grounded isolated conductor placed in a uniform ambient field $\boldsymbol{E}_{10}^\infty$.
2. Take ϕ_2 to be the potential field given by the solution of $\nabla^2\phi_2(\boldsymbol{x}) = -Q'\varepsilon_0^{-1}\,\delta(\boldsymbol{x}-\boldsymbol{y})$, where $\boldsymbol{y} \in D$, with $\phi_2 = 0$ on S_p. The goal is to determine the induced dipole moment $\boldsymbol{d}_2$ in this case.

Applying the reciprocal theorem in these two fields gives

$$Q'\phi_1(\boldsymbol{y}) = \varepsilon_0 \boldsymbol{E}_{10}^\infty \cdot \oint_{S_p} \boldsymbol{x}\nabla\phi_2 \cdot \hat{\boldsymbol{n}}\, dS = -\boldsymbol{E}_{10}^\infty \cdot \boldsymbol{d}_2, \tag{2.79}$$

where we have used the fact that the surface charge density on the conductor is given by $\sigma_2 = -\varepsilon_0\nabla\phi_2.\hat{\boldsymbol{n}}$ and dipole moment $\boldsymbol{d}_2$ is simply the first moment of this charge density on the conductor. Now, $\phi_1(\boldsymbol{y})$ can be represented in terms of singularity solution as

$$\phi_1(\boldsymbol{y}) = \boldsymbol{E}_{10}^\infty \cdot \boldsymbol{\mathcal{F}}_E\{\mathcal{G}(\boldsymbol{y}, \boldsymbol{\xi})\} = \boldsymbol{E}_{10}^\infty \cdot \boldsymbol{\mathcal{F}}_E\{\mathcal{G}(\boldsymbol{\xi}, \boldsymbol{y})\}. \tag{2.80}$$

Here $\boldsymbol{\mathcal{F}}_E$ is the corresponding linear functional and $\boldsymbol{\xi}$ represents the region inside the conductor over which the singularities are distributed. Using this in equation (2.79) and factoring out $\boldsymbol{E}_{10}^\infty$, we have

$$\boldsymbol{d}_2 = -\boldsymbol{\mathcal{F}}_E\{Q'\mathcal{G}(\boldsymbol{\xi}, \boldsymbol{y})\} = -4\pi\epsilon_0\boldsymbol{\mathcal{F}}_E\{\phi_2^\infty(\boldsymbol{\xi})\}, \tag{2.81}$$

where ϕ_2^∞ is the ambient potential field in the second case. Again, for the general ambient field $\phi^\infty(\boldsymbol{x})$ constructed using an appropriate set of point charges, the dipole moment $\boldsymbol{d}$ on the conductor is simply given by

$$\boldsymbol{d} = -4\pi\epsilon_0\boldsymbol{\mathcal{F}}_E\{\phi^\infty(\boldsymbol{\xi})\}. \tag{2.82}$$

This result can be directly applied to the bodies with a known singularity solution of the form given in equation (2.80). In particular, for a prolate spheroid with semi-major axis a, eccentricity e, and orientation vector $\boldsymbol{p}$ we have the singularity representation given by equation (2.63). Therefore, the induced dipole moment on the prolate spheroid in the presence of a background potential field ϕ^∞ is given by

$$\boldsymbol{d} = -4\pi a^3 \varepsilon_0 \left[\frac{3}{2a^3e^3} X_p^C \boldsymbol{p} \int_{-ae}^{ae} \xi \, \phi^\infty(\boldsymbol{x}_c + \xi \boldsymbol{p}) \, d\xi \right. \\ \left. + \frac{3}{4a^3e^3} Y_p^C (\boldsymbol{\delta} - \boldsymbol{pp}) \cdot \boldsymbol{\nabla}_{\boldsymbol{x}_c} \int_{-ae}^{ae} (a^2e^2 - \xi^2) \, \phi^\infty(\boldsymbol{x}_c + \xi \boldsymbol{p}) \, d\xi \right]. \quad (2.83)$$

Similarly, the dipole moment of an oblate spheroid with semi-major axis a and orientation vector $\boldsymbol{p}$ in the presence of a background potential field ϕ^∞ is given by

$$\boldsymbol{d} = -4\pi a^3 \varepsilon_0 \frac{3\kappa^3}{2a^3e^3} \left[X_o^C \boldsymbol{p} \int_{-ae/\kappa}^{ae/\kappa} i\xi \, \phi^\infty(\boldsymbol{x}_c + i\xi \boldsymbol{p}) \, d\xi \right. \\ \left. + \frac{Y_o^C}{2} (\boldsymbol{\delta} - \boldsymbol{pp}) \cdot \boldsymbol{\nabla}_{\boldsymbol{x}_c} \int_{-ae/\kappa}^{ae/\kappa} \left(\frac{a^2e^2}{\kappa^2} - \xi^2 \right) \phi^\infty(\boldsymbol{x}_c + i\xi \boldsymbol{p}) \, d\xi \right]. \quad (2.84)$$

2.5 Singularity Solutions in Microhydrodynamics

We are interested in solving for the fluid velocity field outside a rigid body moving in otherwise quiescent fluid. Let S_p denote the surface of the rigid body. This requires solving the boundary value problem given by

$$\mu \nabla^2 \boldsymbol{u}(\boldsymbol{x}) - \boldsymbol{\nabla} p(\boldsymbol{x}) = \boldsymbol{0}, \quad (2.85a)$$

$$\boldsymbol{u}(\boldsymbol{x}) = \boldsymbol{V} + \boldsymbol{\Omega} \times (\boldsymbol{x} - \boldsymbol{x}_c), \quad \boldsymbol{x} \in S_p, \quad (2.85b)$$

$$\boldsymbol{u}(\boldsymbol{x}) \to \boldsymbol{0}, \quad |\boldsymbol{x}| \to \infty. \quad (2.85c)$$

Here $\boldsymbol{V}$ and $\boldsymbol{\Omega}$ are the linear and angular velocity of the rigid body, and $\boldsymbol{x}_c$ is the centre of mass of the rigid body. The singularity solutions for spherical and spheroidal rigid bodies are well established. In this thesis, we require only the singularity solutions in the absence of an imposed background flow. Accordingly, we present the solutions in a quiescent fluid and refer the reader to Kim & Karrila [10] for the treatment of singularity solutions in the presence of a background flow.

2.5.1 Rigid Body Motion of a Sphere

Consider a sphere with radius a, centred at $\boldsymbol{x}_c$, moving with velocity $\boldsymbol{V}+\boldsymbol{\Omega}\times(\boldsymbol{x}-\boldsymbol{x}_c)$. The singularity solution corresponding to (2.85) involves a Stokeslet and a potential doublet (Laplacian of the Stokeslet), given by [10]

$$\boldsymbol{u}(\boldsymbol{x}) = 6\pi\mu a\boldsymbol{V}\cdot\left(1+\frac{a^2}{6}\nabla^2\right)\frac{\boldsymbol{\mathcal{G}}(\boldsymbol{x},\boldsymbol{x}_c)}{8\pi\mu}+\frac{1}{2}8\pi\mu a^3(\boldsymbol{\Omega}\times\boldsymbol{\nabla})\cdot\frac{\boldsymbol{\mathcal{G}}(\boldsymbol{x},\boldsymbol{x}_c)}{8\pi\mu}. \tag{2.86}$$

The structure of this singularity solution is richer than in the case of electrostatics (see equation (2.86)). One can understand the potential doublet term as follows. We saw that $\boldsymbol{\mathcal{P}}(\boldsymbol{x},\boldsymbol{x}_0)$ represents flow due to a point source of unit strength (see equation (2.31)). Therefore, $\boldsymbol{q}\cdot\boldsymbol{\nabla}\boldsymbol{\mathcal{P}}(\boldsymbol{x},\boldsymbol{x}_0)$ represents flow due to a source-sink dipole, i.e., source and sink placed at $\boldsymbol{x}_0$ and displaced along $\boldsymbol{q}/|\boldsymbol{q}|$ infinitesimally. This flow is called the *potential doublet* and occurs in many singular solutions in Stokes flow. One can use the steady Stokes equation to see that $\boldsymbol{q}\cdot\boldsymbol{\nabla}\boldsymbol{\mathcal{P}}(\boldsymbol{x},\boldsymbol{x}_{\boldsymbol{0}}) = \mu\boldsymbol{q}\cdot\nabla^2\boldsymbol{\mathcal{G}}(\boldsymbol{x},\boldsymbol{x}_{\boldsymbol{0}})$ for $\boldsymbol{x}\neq\boldsymbol{x}_{\boldsymbol{0}}$. Therefore, the structure of the singularity solution of a sphere consists of a Stokeslet, a potential doublet, and a rotlet (last term in equation (2.86)).

2.5.2 Rigid Body Motion of a Prolate Spheroid

Consider a prolate spheroid with semi-major axis a and aspect ratio $\kappa(>1)$, oriented along the unit vector $\boldsymbol{p}$ and centred at $\boldsymbol{x}_c$. The singularity solution corresponding to equation (2.85) involves a uniform distribution of Stokeslets along the symmetry axis of the spheroid, and a parabolic distribution of potential doublets and rotlets, along with a more complex distribution of stresslets and a quadrupole moment. The solution is given by [10]

$$\begin{aligned}\boldsymbol{u}(\boldsymbol{x}) = -\frac{\boldsymbol{F}^h}{8\pi\mu}\cdot\frac{1}{2ae}\int_{-ae}^{ae}\left\{1+(a^2e^2-\xi^2)\frac{1-e^2}{4e^2}\nabla^2\right\}\boldsymbol{\mathcal{G}}(\boldsymbol{x},\boldsymbol{x}_c+\xi\boldsymbol{p})\,d\xi \\ +\frac{1}{2}\frac{(\boldsymbol{T}^h\times\boldsymbol{\nabla})}{8\pi\mu}\cdot\frac{3}{4a^3e^3}\int_{-ae}^{ae}(a^2e^2-\xi^2)\boldsymbol{\mathcal{G}}(\boldsymbol{x},\boldsymbol{x}_c+\xi\boldsymbol{p})\,d\xi \\ +\frac{(\boldsymbol{S}^h\cdot\boldsymbol{\nabla})}{8\pi\mu}\cdot\frac{3}{4a^3e^3}\int_{-ae}^{ae}(a^2e^2-\xi^2)\left\{1+(a^2e^2-\xi^2)\frac{1-e^2}{8e^2}\nabla^2\right\}\boldsymbol{\mathcal{G}}(\boldsymbol{x},\boldsymbol{x}_c+\xi\boldsymbol{p})\,d\xi,\end{aligned} \tag{2.87}$$

where

$$\boldsymbol{F}^h = -6\pi\mu a[X_p^A\boldsymbol{pp}+Y_p^A(\boldsymbol{\delta}-\boldsymbol{pp})]\cdot\boldsymbol{V} \tag{2.88a}$$

$$\boldsymbol{T}^h = -8\pi\mu a^3[X_p^C\boldsymbol{pp}+Y_p^C(\boldsymbol{\delta}-\boldsymbol{pp})]\cdot\boldsymbol{\Omega} \tag{2.88b}$$

$$\boldsymbol{S}^h \equiv \frac{1}{2}\left(\frac{e^2}{2-e^2}\right)[(\boldsymbol{T}^h \times \boldsymbol{p})\boldsymbol{p} + \boldsymbol{p}(\boldsymbol{T}^h \times \boldsymbol{p})]. \tag{2.88c}$$

Here, the resistance functions are given by [10]

$$X_p^A \equiv \frac{8}{3}e^3[-2e + (1+e^2)L_e]^{-1}, \quad Y_p^A \equiv \frac{16}{3}e^3[2e + (3e^2-1)L_e]^{-1} \tag{2.89a}$$

$$X_p^C \equiv \frac{4}{3}e^3(1-e^2)[2e-(1-e^2)L_e]^{-1}, \quad Y_p^C \equiv \frac{4}{3}e^3(2-e^2)[-2e+(1+e^2)L_e]^{-1}, \tag{2.89b}$$

with $Le \equiv \log_e\left(\frac{1+e}{1-e}\right)$.

2.5.3 Rigid Body Motion of an Oblate Spheroid

The singularity solution of an oblate spheroid can again be obtained using the eccentricity transformation given by equation (2.59). Therefore, for an oblate spheroid described by

$$(\boldsymbol{x}-\boldsymbol{x}_c)\cdot\left[\frac{1}{a^2}\boldsymbol{pp} + \frac{\kappa^2}{a^2}(\boldsymbol{\delta}-\boldsymbol{pp})\right]\cdot(\boldsymbol{x}-\boldsymbol{x}_c) = 1, \quad \boldsymbol{x} \in S_p,$$

with $\kappa < 1$ and the eccentricity given by $e = \sqrt{1-\kappa^2}$, the singularity solution is given by [10]

$$\begin{aligned}\boldsymbol{u}(\boldsymbol{x}) = -\frac{\boldsymbol{F}^h}{8\pi\mu}\cdot\frac{\kappa}{2ae}\int_{-ae/\kappa}^{ae/\kappa}\left\{1+\left(\frac{a^2e^2}{\kappa^2}-\xi^2\right)\frac{1}{4e^2}\nabla^2\right\}\boldsymbol{\mathcal{G}}(\boldsymbol{x},\boldsymbol{x}_c+i\xi\boldsymbol{p})\,d\xi \\ +\frac{1}{2}\frac{(\boldsymbol{T}^h\times\boldsymbol{\nabla})}{8\pi\mu}\cdot\frac{3\kappa^3}{4a^3e^3}\int_{-ae/\kappa}^{ae/\kappa}\left(\frac{a^2e^2}{\kappa^2}-\xi^2\right)\boldsymbol{\mathcal{G}}(\boldsymbol{x},\boldsymbol{x}_c+i\xi\boldsymbol{p})\,d\xi \\ +\frac{(\boldsymbol{S}^h\cdot\boldsymbol{\nabla})}{8\pi\mu}\cdot\frac{3\kappa^3}{4a^3e^3}\int_{-ae/\kappa}^{ae/\kappa}\left(\frac{a^2e^2}{\kappa^2}-\xi^2\right)\left\{1+\left(\frac{a^2e^2}{\kappa^2}-\xi^2\right)\frac{1}{8e^2}\nabla^2\right\}\boldsymbol{\mathcal{G}}(\boldsymbol{x},\boldsymbol{x}_c+i\xi\boldsymbol{p})\,d\xi,\end{aligned} \tag{2.90}$$

where

$$\boldsymbol{F}^h = -6\pi\mu a[X_o^A\boldsymbol{pp} + Y_o^A(\boldsymbol{\delta}-\boldsymbol{pp})]\cdot\boldsymbol{V} \tag{2.91a}$$

$$\boldsymbol{T}^h = -8\pi\mu a^3[X_o^A\boldsymbol{pp} + Y_o^A(\boldsymbol{\delta}-\boldsymbol{pp})]\cdot\boldsymbol{\Omega} \tag{2.91b}$$

$$\boldsymbol{S}^h \equiv -\frac{1}{2}\left(\frac{e^2}{2-e^2}\right)[(\boldsymbol{T}^h \times \boldsymbol{p})\boldsymbol{p} + \boldsymbol{p}(\boldsymbol{T}^h \times \boldsymbol{p})]. \tag{2.91c}$$

Here, the resistance functions are given by [10]

$$X_o^A \equiv \frac{4}{3}e^3[(2e^2-1)K + e\sqrt{1-e^2}]^{-1}, \quad Y_o^A \equiv \frac{8}{3}e^3[(2e^2+1)K - e\sqrt{1-e^2}]^{-1} \tag{2.92a}$$

$$X_o^C \equiv \frac{2}{3}[K - e\sqrt{1-e^2}]^{-1}, \quad Y_o^C \equiv \frac{2}{3}e^3(2-e^2)[e\sqrt{1-e^2} - (1-2e^2)K]^{-1}, \tag{2.92b}$$

with $K \equiv \operatorname{arccot}\left(e^{-1}\sqrt{1-e^2}\right)$.

This singularity solution for an oblate spheroid will be used in Chapter 4 to study hydrodynamic interactions between multiple discs.

2.6 Faxén's Laws in Microhydrodynamics

The Faxén's laws relate the multipole moments, such as hydrodynamic force, torque, and stresslet, on the rigid body to the structure of their singularity solutions. The derivation of the Faxén's laws in microhydrodynamics follows the same ideas as discussed in Section 2.4, starting from the reciprocal theorem (2.8). With their derivation outlined in [10], we shall simply state them here for the case of spheres and spheroids. For a sphere with radius a centred at $\boldsymbol{x}_c$ and moving with velocity $\boldsymbol{V} + \boldsymbol{\Omega} \times (\boldsymbol{x} - \boldsymbol{x}_c)$ with a background Stokes flow $\boldsymbol{u}^\infty(\boldsymbol{x})$, the Faxén's laws give the hydrodynamic force and torque on the sphere as [10]

$$F_i^h = 6\pi\mu a \left(1 + \frac{a^2}{6}\nabla^2\right) \left[u_i^\infty(\boldsymbol{x}) - V_i\right]_{\boldsymbol{x}=\boldsymbol{x}_c} \tag{2.93a}$$

$$T_i^h = 8\pi\mu a^3 \left[\frac{1}{2}\omega_i^\infty(\boldsymbol{x}_c) - \Omega_i\right], \tag{2.93b}$$

where $\boldsymbol{\omega}(\boldsymbol{x})^\infty = \boldsymbol{\nabla} \times \boldsymbol{u}^\infty(\boldsymbol{x})$ is the background vorticity.

Similarly, for a prolate spheroid with semi-major axis a, aspect ratio $\kappa(> 1)$, eccentricity $e = \sqrt{1 - \kappa^{-2}}$, and symmetry axis along the unit vector $\boldsymbol{p}$, the Faxén's laws give the hydrodynamic force and torque on the spheroid as [10]

$$\begin{aligned} F_i^h = {} & 6\pi\mu a[X_p^A p_i p_j + Y_p^A(\delta_{ij} - p_i p_j)]\frac{1}{2ae} \\ & \times \int_{-ae}^{ae} \left\{1 + (a^2e^2 - \xi^2)\frac{1-e^2}{4e^2}\nabla^2\right\} [u_j^\infty(\boldsymbol{x}_c + \xi\boldsymbol{p}) - V_j]\, d\xi \end{aligned} \tag{2.94a}$$

$$\begin{aligned} T_i^h = {} & 8\pi\mu a^3[X_p^C p_i p_j + Y_p^C(\delta_{ij} - p_i p_j)]\frac{3}{8a^3e^3} \\ & \times \int_{-ae}^{ae} (a^2e^2 - \xi^2)[\omega_j^\infty(\boldsymbol{x}_c + \xi\boldsymbol{p}) - 2\Omega_j]\, d\xi \\ & - 8\pi\mu a^3 \epsilon_{ijl} p_l p_k Y_p^C \left(\frac{e^2}{2-e^2}\right) \\ & \times \frac{3}{4a^3e^3}\int_{-ae}^{ae} (a^2e^2 - \xi^2)\left\{1 + (a^2e^2 - \xi^2)\frac{1-e^2}{8e^2}\nabla^2\right\} E_{jk}^\infty(\boldsymbol{x}_c + \xi\boldsymbol{p})\, d\xi. \end{aligned} \tag{2.94b}$$

Here $\boldsymbol{E}^\infty(\boldsymbol{x})$ is the strain-rate associated with the background flow $\boldsymbol{u}^\infty(\boldsymbol{x})$. The resistance functions $X_p^A, Y_p^A, X_p^C, Y_p^C$ are given by equation (2.89).

One can use the eccentricity transformation (equation (2.59)) to obtain the Faxén's laws for an oblate spheroid with longer side a, aspect ratio $\kappa(< 1)$, eccentricity $e = \sqrt{1 - \kappa^2}$ and symmetry axis along the unit vector $\boldsymbol{p}$. These are given by

$$\begin{aligned} F_i^h &= 6\pi\mu a[X_o^A p_i p_j + Y_o^A(\delta_{ij} - p_i p_j)]\frac{\kappa}{2ae} \\ &\quad \times \int_{-ae/\kappa}^{ae/\kappa} \left\{1 + \left(\frac{a^2e^2}{\kappa^2} - \xi^2\right)\frac{1}{4e^2}\nabla^2\right\}[u_j^\infty(\boldsymbol{x}_c + i\xi\boldsymbol{p}) - V_j]\, d\xi \end{aligned} \tag{2.95a}$$

$$\begin{aligned} T_i^h &= 8\pi\mu a^3[X_o^C p_i p_j + Y_o^C(\delta_{ij} - p_i p_j)]\frac{3\kappa^3}{8a^3e^3} \\ &\quad \times \int_{-ae/\kappa}^{ae/\kappa} \left(\frac{a^2e^2}{\kappa^2} - \xi^2\right)[\omega_j^\infty(\boldsymbol{x}_c + i\xi\boldsymbol{p}) - 2\Omega_j]\, d\xi \\ &\qquad + 8\pi\mu a^3 \epsilon_{ijl} p_l p_k Y_o^C \left(\frac{e^2}{2 - e^2}\right) \\ &\times \frac{3\kappa^3}{4a^3e^3}\int_{-ae/\kappa}^{ae/\kappa} \left(\frac{a^2e^2}{\kappa^2} - \xi^2\right)\left\{1 + \left(\frac{a^2e^2}{\kappa^2} - \xi^2\right)\frac{1}{8e^2}\nabla^2\right\} E_{jk}^\infty(\boldsymbol{x}_c + i\xi\boldsymbol{p})\, d\xi. \end{aligned} \tag{2.95b}$$

The resistance functions $X_o^A, Y_o^A, X_o^C, Y_o^C$ are given by equation (2.92). The Faxén's laws and singularity solutions for an oblate spheroid will be used in Chapter 4 to study hydrodynamic interactions between multiple discs.

2.7 The Method of Reflections

The method of reflections is an iterative scheme widely used in micro-hydrodynamics to calculate hydrodynamic interactions between widely separated bodies [10]. This method produces a perturbation series in terms of the order a/R where a is the typical size of the objects and R is their typical separation. The method is described in [10] and is outlined for electrostatic interaction between two conductors as follows.

The exact way to incorporate electrostatic interaction between conductors would require obtaining a harmonic potential field that satisfies the constant potential boundary conditions on the surface of each conductor. This problem is barely tractable for two spheres, and hence we need to resort to some approximate methods, such as the method of reflections, for more complex shapes like spheroids.

In the zeroth-order approximation, the solution for two conductors (denoted S_1 and S_2) that are far apart is obtained by simply adding the potential fields of each isolated conductor, meaning the electrostatic interactions between them are

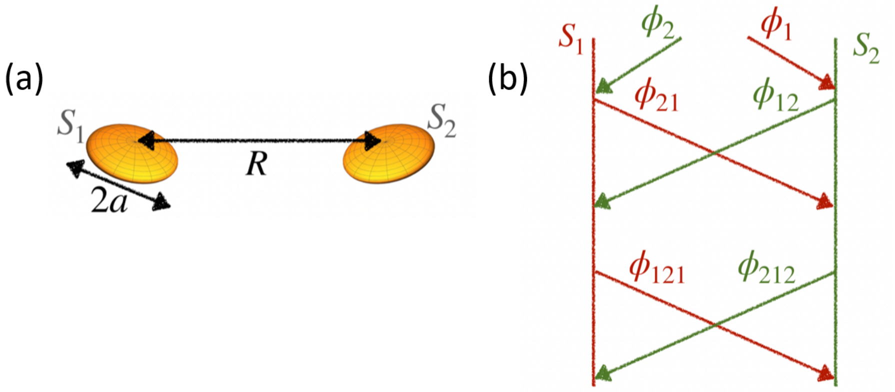

Figure 2.4: Depiction of the method of reflections, adapted from Kim & Karilla [10] (a) Two sample surfaces S_1 and S_2 with their typical size a, and their separation R. (b) The two surfaces create fields ϕ_1 and ϕ_2, respectively, each of which satisfies the boundary condition on its surface. The field ϕ_2 acts as an incident field on S_1, which in response creates a reflected field ϕ_{21}, and vice versa. These reflected fields then act as new incident fields on the opposite surfaces, continuing the process iteratively. This results in a perturbative series of the form $\phi_1 + \phi_2 + \phi_{21} + \phi_{12} + \ldots$, which, in the $a \ll R$ regime, converges to a solution that simultaneously satisfies the boundary conditions on both surfaces.

ignored. Let ϕ_1 and ϕ_2 be two potential fields such that

$$\phi_1(\boldsymbol{x}) = V_1 \quad \boldsymbol{x} \in S_1, \tag{2.96a}$$

$$\phi_2(\boldsymbol{x}) = V_2 \quad \boldsymbol{x} \in S_2. \tag{2.96b}$$

Note that these solutions can be obtained using the singularity solutions discussed in Section 2.3. However, $\phi = \phi_1 + \phi_2$ doesn't satisfy the boundary conditions on either of the surfaces. The error in the boundary condition on S_α is $\phi_{3-\alpha}(\boldsymbol{x})$, which is of the order of a/R. The fields $\phi_1(\boldsymbol{x})$ and $\phi_2(\boldsymbol{x})$ are called the first *incident fields* on the conductors S_2 and S_1, respectively. Now, S_1 produces a disturbance field ϕ_{21} and S_2 produces a disturbance field ϕ_{12} such that

$$\phi_{21}(\boldsymbol{x}) = -\phi_2(\boldsymbol{x}) \quad \boldsymbol{x} \in S_1, \tag{2.97a}$$

$$\phi_{12}(\boldsymbol{x}) = -\phi_1(\boldsymbol{x}) \quad \boldsymbol{x} \in S_2. \tag{2.97b}$$

These disturbance fields are called the *reflected fields*, which account for the correction in the boundary conditions. Note that the fields are uniquely labeled by augmenting the subscripts of the incident fields by the subscript corresponding to the particle on which the reflection is taking place.

These fields can be determined using the multipole expansion discussed in Section 2.2.3. The induced multipole moments are determined using the Faxén's laws discussed in Section 2.4 Now, $\phi = \phi_1 + \phi_2 + \phi_{21} + \phi_{12}$ is a better approximation to the complete solution because the error in the boundary conditions is now $O(\phi_{12}) \sim O(\phi_{21})$ which takes contributions from higher multipole moments and decays as $O(a^4/R^4)$. This procedure can be iterated with the reflected fields from one conductor being incident on the other conductor and producing subsequent reflected fields, as shown in Figure 2.4.

For microhydrodynamics, the velocity fields take the place of the potential fields in the method of reflections. A detailed outline of the method of reflections in microhydrodynamics can be found in Kim & Karilla [10]. We shall apply the method of reflections up to the first reflection in Chapter 4 of this thesis for the case of multiple discs sedimenting in Stokes flow.

The method of reflections is applied up to the second reflection for the case of a spheroidal and a spherical charged conductors in Chapter 5 of this thesis. We demonstrate the method of reflection for the case of two spheroidal charged conductors below.

2.7.1 Far Field Interaction of Two Charged Prolate Spheroids

Consider two prolate spheroids S_1 and S_2 with semi-major axes a_1 and a_2, eccentricities e_1 and e_2, position vectors $\boldsymbol{x}_1$ and $\boldsymbol{x}_2$ and orientations $\boldsymbol{p}_1$ and $\boldsymbol{p}_2$, respectively. Faxén's laws (see equation (2.77)) can be used to relate the potentials V_1 and V_2 on the surfaces of the spheroids to their total charges Q_1 and Q_2, respectively. The ambient field around the first spheroid is generated by the second spheroid and can be expressed perturbatively using the method of reflections. The same approach applies to the second spheroid, where its ambient field is influenced by the first spheroid. Using equation (2.77), we have for the first spheroid

$$V_1 = Q_1 \frac{\operatorname{arctanh} e_1}{4\pi a_1 \varepsilon_0 e_1} + \frac{1}{2a_1 e_1} \int_{-a_1 e_1}^{a_1 e_1} \phi_2^{\infty}(\boldsymbol{x}_1 + \xi_1 \boldsymbol{p}_1)\, d\xi_1, \tag{2.98a}$$

$$V_2 = Q_2 \frac{\operatorname{arctanh} e_2}{4\pi a_2 \varepsilon_0 e_2} + \frac{1}{2a_2 e_2} \int_{-a_2 e_2}^{a_2 e_2} \phi_1^{\infty}(\boldsymbol{x}_2 + \xi_1 \boldsymbol{p}_2)\, d\xi_1, \tag{2.98b}$$

Using the method of reflections, we have

$$\phi_1^{\infty}(\boldsymbol{y}) = \phi_1(\boldsymbol{y}) + \phi_{21}(\boldsymbol{y}) + \phi_{121}(\boldsymbol{y})... \tag{2.99a}$$

$$\phi_2^{\infty}(\boldsymbol{y}) = \phi_2(\boldsymbol{y}) + \phi_{12}(\boldsymbol{y}) + \phi_{212}(\boldsymbol{y})... \tag{2.99b}$$

Here $\phi_1(\boldsymbol{y})$ and $\phi_2(\boldsymbol{y})$ are the zeroth-order disturbance fields, $\phi_{21}(\boldsymbol{y})$ and $\phi_{12}(\boldsymbol{y})$ are the first reflection fields and $\phi_{121}(\boldsymbol{y})$ and $\phi_{212}(\boldsymbol{y})$ are the second reflection fields produced by S_1 and S_2, respectively.

The zeroth-order solution to the problem is

$$V_1^{(0)} = Q_1 \frac{\operatorname{arctanh} e_1}{4\pi a_1 \varepsilon_0 e_1}, \quad V_2^{(0)} = Q_2 \frac{\operatorname{arctanh} e_2}{4\pi a_2 \varepsilon_0 e_2}. \tag{2.100}$$

Since ϕ_1 and ϕ_2 are the potentials due to isolated spheroids S_1 and S_2, they are given by equations (2.56) and (2.57) as

$$\phi_1(\boldsymbol{y}) = \frac{Q_1}{8\pi \varepsilon_0 a_1 e_1} \int_{-a_1 e_1}^{a_1 e_1} \mathcal{G}(\boldsymbol{y}, \boldsymbol{x}_1 + \xi_1 \boldsymbol{p}_1)\, d\xi_1, \tag{2.101a}$$

$$\phi_2(\boldsymbol{y}) = \frac{Q_2}{8\pi \varepsilon_0 a_2 e_2} \int_{-a_2 e_2}^{a_2 e_2} \mathcal{G}(\boldsymbol{y}, \boldsymbol{x}_2 + \xi_1 \boldsymbol{p}_2)\, d\xi_1. \tag{2.101b}$$

The first-order correction comes through the first reflection as

$$V_1^{(1)} = \frac{1}{2a_1 e_1} \int_{-a_1 e_1}^{a_1 e_1} \phi_2(\boldsymbol{x}_1 + \xi_1 \boldsymbol{p}_1)\, d\xi_1, \tag{2.102a}$$

$$V_2^{(1)} = \frac{1}{2a_2 e_2} \int_{-a_2 e_2}^{a_2 e_2} \phi_1(\boldsymbol{x}_2 + \xi_1 \boldsymbol{p}_2)\, d\xi_1, \tag{2.102b}$$

with the first reflection fields ϕ_{21} and ϕ_{12} represented to the leading order in a/R by the dipole moments $\boldsymbol{d}_1^{(1)}$ and $\boldsymbol{d}_2^{(1)}$. The explicit expression for the first reflection field ϕ_{12} by spheroid S_2 is (see equation (2.68))

$$\begin{aligned} \phi_{12}(\boldsymbol{y}) = \frac{3}{8\pi a_2^3 e_2^3 \varepsilon_0} \Bigg[& \boldsymbol{d}_2^{(1)} \cdot \boldsymbol{p}_2 \int_{-a_2 e_2}^{a_2 e_2} \xi_2 \mathcal{G}(\boldsymbol{y}, \boldsymbol{x}_2 + \xi_2 \boldsymbol{p}_2)\, d\xi_2 \\ & - \frac{\boldsymbol{d}_2^{(1)}}{2} \cdot (\boldsymbol{\delta} - \boldsymbol{p}_2 \boldsymbol{p}_2) \cdot \boldsymbol{\nabla}_y \int_{-a_2 e_2}^{a_2 e_2} (a_2^2 e_2^2 - \xi_2^2) \mathcal{G}(\boldsymbol{y}, \boldsymbol{x}_2 + \xi_2 \boldsymbol{p}_2)\, d\xi_2 \Bigg]. \end{aligned} \tag{2.103}$$

The dipole moment $\boldsymbol{d}_2^{(1)}$ is given by the Faxén's laws as (see equation (2.83))

$$\begin{aligned} \boldsymbol{d}_2^{(1)} = -4\pi a_2^3 \frac{3}{8\pi a_2^3 e_2^3} \Bigg[& X_{p2}^C \boldsymbol{p}_2 \int_{-a_2 e_2}^{a_2 e_2} \xi_2\, d\xi_2 \int_{-a_1 e_1}^{a_1 e_1} \frac{Q_1}{2a_1 e_1} \mathcal{G}(\boldsymbol{x}_2 + \xi_2 \boldsymbol{p}_2, \boldsymbol{x}_1 + \xi_1 \boldsymbol{p}_1)\, d\xi_1 \\ & + \frac{Y_{p2}^C}{2} (\boldsymbol{\delta} - \boldsymbol{p}_2 \boldsymbol{p}_2) \cdot \boldsymbol{\nabla}_{x_2} \\ & \int_{-a_2 e_2}^{a_2 e_2} d\xi_2\, (a_2^2 e_2^2 - \xi_2^2) \int_{a_1 e_1}^{a_1 e_1} \frac{Q_1}{2a_1 e_1} \mathcal{G}(\boldsymbol{x}_2 + \xi_2 \boldsymbol{p}_2, \boldsymbol{x}_1 + \xi_1 \boldsymbol{p}_1)\, d\xi_1 \Bigg], \end{aligned} \tag{2.104}$$

where we have used equation (2.101) for $\phi_1(\boldsymbol{y})$ in place of ϕ^∞ in equation (2.83). Here $X_{p2}^C = X_p^C(e_2)$ and $Y_{p2}^C = Y_p^C(e_2)$ are given by equation (2.64). The corresponding first reflection field $\phi_{21}(\boldsymbol{y})$ and the dipole moment $\boldsymbol{d}_1^{(1)}$ is obtained by simply switching the labels 1 and 2.

The next order correction comes through the second reflection as

$$V_1^{(2)} = \frac{1}{2a_1e_1}\int_{-a_1e_1}^{a_1e_1} \phi_{12}(\boldsymbol{x}_1 + \xi_1\boldsymbol{p}_1)\,d\xi_1, \tag{2.105a}$$

$$V_2^{(2)} = \frac{1}{2a_2e_2}\int_{-a_2e_2}^{a_2e_2} \phi_{21}(\boldsymbol{x}_2 + \xi_1\boldsymbol{p}_2)\,d\xi_1, \tag{2.105b}$$

with the second reflection fields ϕ_{121} and ϕ_{212} represented to the leading order in a/R by the dipole moments $\boldsymbol{d}_1^{(2)}$ and $\boldsymbol{d}_2^{(2)}$. These dipole moments can again be obtained using Faxén's laws (equation (2.83)) with first reflection fields in place on ϕ^∞.

Therefore, up to second reflections, the potentials on the surface of the spheroids are related to their respective total charges as $V_\alpha = V_\alpha^{(0)} + V_\alpha^{(1)} + V_\alpha^{(2)}$, $\alpha \in \{1,2\}$. These interaction potentials are accurate up to $O(a^4/R^4)$.

2.8 Boundary Integral Formulation

We came across the integral representation of both the velocity field in Stokes flow (equation (2.27)) and the electrostatic potential (equation (2.47)). These convey an important idea that the velocity field and the electrostatic potential at any point in the domain can be obtained by evaluating integrals over the boundaries of the domain. This is the essential idea behind boundary integral methods. The mathematical beauty of the formulation, which involves linear functional theory, and the computational advantage of reduction in dimensions of the problem by having to discretize only the boundaries rather than the whole domain, make the boundary integral methods attractive. We shall discuss the boundary integral formulation for the easier case of electrostatics, and briefly outline it for microhydrodynamics. A detailed account of boundary integral methods in microhydrodynamics can be found in the work of Pozrikidis [16].

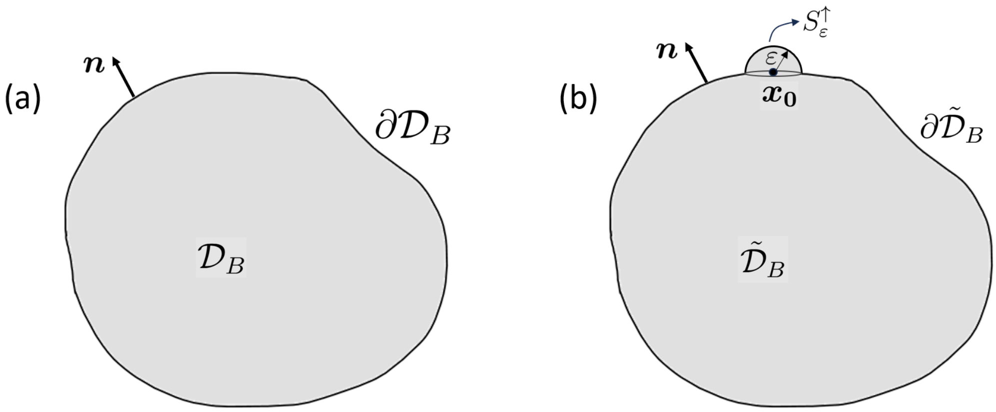

Figure 2.5: (a) The compact domain $\mathcal{D}_B \subset \mathbb{R}^3$ with the normal vector to the boundary $\partial\mathcal{D}_B$ indicated by $\boldsymbol{n}$. (b) The modified domain $\tilde{\mathcal{D}}_B$ which is union of $\mathcal{D}_B$ and the region inside the hemisphere $S_\varepsilon^{\uparrow}$ of radius ε centered at $\boldsymbol{x_0}$.

2.9 Boundary Integral Method for Arbitrary-Shaped Conductors in Electrostatics

Recall the integral representation of the electrostatic potential given by equation (2.47) as

$$\frac{1}{4\pi}\oint_{\partial\mathcal{D}} \phi(\boldsymbol{x})\hat{\boldsymbol{n}}(\boldsymbol{x})\cdot\nabla\mathcal{G}(\boldsymbol{x},\boldsymbol{x}_0)\,dS(\boldsymbol{x}) \\ -\frac{1}{4\pi}\oint_{\partial\mathcal{D}} \mathcal{G}(\boldsymbol{x},\boldsymbol{x_0})\hat{\boldsymbol{n}}(\boldsymbol{x})\cdot\nabla\phi(\boldsymbol{x})\,dS(\boldsymbol{x}) = \begin{cases}\phi(\boldsymbol{x_0}), & \boldsymbol{x_0}\in\mathcal{D},\\ 0, & \boldsymbol{x_0}\notin\overline{\mathcal{D}}.\end{cases}$$

Recall that $\hat{\boldsymbol{n}}$ points towards the domain of interest $\mathcal{D}$. The integral representation shows that there is a jump discontinuity across the boundaries $\partial\mathcal{D}$. This jump discontinuity comes from the double-layer potential, which represents the distribution of dipoles over the boundaries. Let's inspect the integral properties of the double-layer potential in more detail.

Claim:

$$\frac{1}{4\pi}\oint_{\partial\mathcal{D}_B} \boldsymbol{n}\cdot\nabla\mathcal{G}(\boldsymbol{x},\boldsymbol{x_0})dS(\boldsymbol{x}) = \begin{cases}-1, & \boldsymbol{x_0}\in\mathcal{D}_B,\\ 0, & \boldsymbol{x_0}\in\mathbb{R}^3\backslash\overline{\mathcal{D}}_B,\\ -1/2, & \boldsymbol{x_0}\in\partial\mathcal{D}_B,\end{cases} \tag{2.106}$$

where $\mathcal{D}_B$ represents a compact volume in $\mathbb{R}^3$ and $\boldsymbol{n}$ is the normal to the boundary $\partial\mathcal{D}_B$, *pointing out* of the bounded region of interest, as shown in Figure 2.5. **Proof:**

For $\boldsymbol{x_0} \in \mathcal{D}_B$ or $\boldsymbol{x_0} \in \mathbb{R}^3 \backslash \overline{\mathcal{D}}_B$, we use the divergence theorem to get

$$\oint_{\partial \mathcal{D}_B} \boldsymbol{n} \cdot \boldsymbol{\nabla} \mathcal{G}(\boldsymbol{x}, \boldsymbol{x_0}) dS(\boldsymbol{x}) = \int_{\mathcal{D}_B} \nabla^2 \mathcal{G}(\boldsymbol{x}, \boldsymbol{x_0})\, dV = -4\pi \int_{\mathcal{D}_B} \delta(\boldsymbol{x} - \boldsymbol{x_0})\, dV.$$

This proves the first two cases of equation (2.106). Now consider the case $\boldsymbol{x_0} \in \partial \mathcal{D}_B$. Consider a hemisphere $S_\varepsilon^\uparrow$ of radius ε, centered at $\boldsymbol{x_0} \in \partial \mathcal{D}_B$ as shown in Figure 2.5. We now have a modified domain $\tilde{\mathcal{D}}_B$ which is identical to $\mathcal{D}_B$ in all the regions except near $\boldsymbol{x_0}$ where it contains the region inside $S_\varepsilon^\uparrow$ as shown in the Figure 2.5. Since $\boldsymbol{x_0} \in \tilde{\mathcal{D}}_B$, we have

$$\frac{1}{4\pi} \oint_{\partial \tilde{\mathcal{D}}_B(\varepsilon)} \boldsymbol{n} \cdot \boldsymbol{\nabla} \mathcal{G}(\boldsymbol{x}, \boldsymbol{x_0}) dS(\boldsymbol{x}) = -1, \quad \boldsymbol{x_0} \in \tilde{\mathcal{D}}_B(\varepsilon).$$

But

$$\lim_{\varepsilon \to 0} \oint_{\partial \tilde{\mathcal{D}}_B(\varepsilon)} \boldsymbol{n} \cdot \boldsymbol{\nabla} \mathcal{G}(\boldsymbol{x}, \boldsymbol{x_0}) dS(\boldsymbol{x}) = \oint_{\partial \mathcal{D}_B}^{PV} \boldsymbol{n} \cdot \boldsymbol{\nabla} \mathcal{G}(\boldsymbol{x}, \boldsymbol{x_0}) dS(\boldsymbol{x}) + \lim_{\varepsilon \to 0} \int_{S_\varepsilon^\uparrow} \boldsymbol{n} \cdot \boldsymbol{\nabla} \mathcal{G}(\boldsymbol{x}, \boldsymbol{x_0}) dS(\boldsymbol{x})$$

where PV over the integral denotes *principal value* of the integral, which involves integrating over the boundary $\partial \mathcal{D}_B$ except over a small disc of radius ε centered at $\boldsymbol{x_0}$ and taking the limit $\varepsilon \to 0$. Therefore, we have

$$-1 = \frac{1}{4\pi} \oint_{\partial \mathcal{D}_B}^{PV} \boldsymbol{n} \cdot \boldsymbol{\nabla} \mathcal{G}(\boldsymbol{x}, \boldsymbol{x_0}) dS(\boldsymbol{x}) - \int_0^{\pi/2} \frac{1}{4\pi \varepsilon^2} \varepsilon^2 2\pi \sin(\theta) d\theta.$$

This finally gives

$$\frac{1}{4\pi} \oint_{\partial \mathcal{D}_B}^{PV} \boldsymbol{n} \cdot \boldsymbol{\nabla} \mathcal{G}(\boldsymbol{x}, \boldsymbol{x_0}) dS(\boldsymbol{x}) = -1/2,$$

which completes the proof.

2.9.1 Boundary Integral Equation for Laplace Equation

We have an integral representation of the potential field in the domain $\mathcal{D}$ given by equation (2.47). To obtain an integral equation over the boundary, consider taking the target point $\boldsymbol{x_0}$ to the boundary enclosing a compact region in $\mathbb{R}^3$. Let $\tilde{x}_0 \in \partial \mathcal{D}_B$, as shown in the Figure 2.6. Note that when $\mathcal{D}$ is multiply connected, $\partial \mathcal{D}_B$ forms one part of the boundary, with another part being 'surface at infinity'. The compact region in $\mathbb{R}^3$ enclosed by $\partial \mathcal{D}_B$ is denoted by $\mathcal{D}_B$. We take $\boldsymbol{x_0} \to \partial \mathcal{D}_B$ such that $\boldsymbol{x_0} = \tilde{x}_0 \pm \varepsilon \hat{\boldsymbol{n}}(\tilde{x}_0)$, where $\varepsilon > 0$ and the plus and minus signs correspond to approaching the boundary $\partial \mathcal{D}_B$ from outside and inside the enclosed region

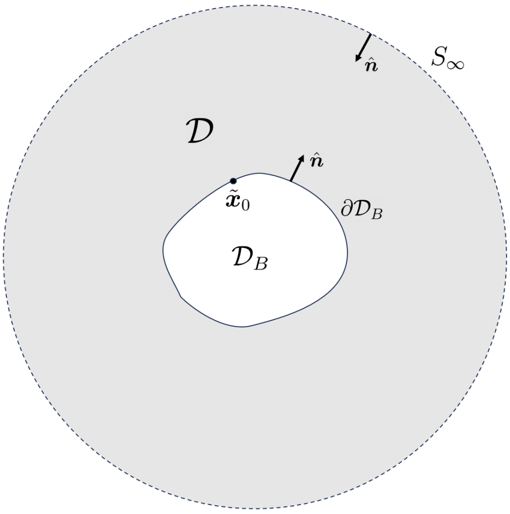

Figure 2.6: The multiply connected domain of interest, $\mathcal{D}$, with normal vectors $\hat{\boldsymbol{n}}$ pointing towards $\mathcal{D}$. The boundary of the domain, $\partial\mathcal{D}$, is formed by the boundary of the compact region $\mathcal{D}_B \subset \mathbb{R}^3$ and the 'surface at infinity' S_∞.

$\mathcal{D}_B$, respectively. Now, consider the integral

$$\begin{aligned}\lim_{\varepsilon\to 0^+} \oint_{\partial\mathcal{D}_B} & \hat{\boldsymbol{n}} \cdot \nabla \mathcal{G}(\boldsymbol{x}, \tilde{\boldsymbol{x}}_0 \pm \varepsilon \hat{\boldsymbol{n}}(\tilde{\boldsymbol{x}}_0)) \phi(\boldsymbol{x})\, dS(\boldsymbol{x}) \\ &= \underbrace{\lim_{\varepsilon\to 0^+} \oint_{\partial\mathcal{D}_B} [\phi(\boldsymbol{x}) - \phi(\tilde{\boldsymbol{x}}_0)] \hat{\boldsymbol{n}} \cdot \nabla \mathcal{G}(\boldsymbol{x}, \tilde{\boldsymbol{x}}_0 \pm \varepsilon \hat{\boldsymbol{n}}(\tilde{\boldsymbol{x}}_0))\, dS(\boldsymbol{x})}_{I_1} \\ &\qquad + \phi(\tilde{\boldsymbol{x}}_0) \lim_{\varepsilon\to 0^+} \oint_{\partial\mathcal{D}_B} \hat{\boldsymbol{n}} \cdot \nabla \mathcal{G}(\boldsymbol{x}, \tilde{\boldsymbol{x}}_0 \pm \varepsilon \hat{\boldsymbol{n}}(\tilde{\boldsymbol{x}}_0))\, dS(\boldsymbol{x}). \qquad (2.107)\end{aligned}$$

The second integral I_2 on the right-hand side of equation (2.107) can be written using equation (2.106) as

$$\lim_{\varepsilon\to 0^+} \frac{1}{4\pi} \oint_{\partial\mathcal{D}_B} \hat{\boldsymbol{n}} \cdot \nabla \mathcal{G}(\boldsymbol{x}, \tilde{\boldsymbol{x}}_0 \pm \varepsilon \hat{\boldsymbol{n}}(\tilde{\boldsymbol{x}}_0))\, dS(\boldsymbol{x}) = \pm\frac{1}{2} + \frac{1}{4\pi} \oint_{\partial\mathcal{D}_B}^{PV} \hat{\boldsymbol{n}} \cdot \nabla \mathcal{G}(\boldsymbol{x}, \tilde{\boldsymbol{x}}_0)\, dS(\boldsymbol{x}). \qquad (2.108)$$

The limit in the first integral I_1 on the right-hand side of equation (2.107) can be taken inside the integral since the integrand is regular at $\tilde{\boldsymbol{x}}_0$, provided $\phi(\boldsymbol{x})$ has a Taylor expansion at $\tilde{\boldsymbol{x}}_0$. This can be seen as follows. With $r \equiv |\boldsymbol{x} - \tilde{\boldsymbol{x}}_0|$, the integral I_1 over a small patch of radius R centred at $\tilde{\boldsymbol{x}}_0$ has the form

$$\sim \pm \int_0^R r \frac{\varepsilon}{(r^2+\varepsilon^2)^{3/2}} r \underbrace{=}_{r=\varepsilon tan\theta} \pm \int \varepsilon^4 \frac{(\sec\theta)^2}{\varepsilon^3 |\sec\theta|^3} (\tan\theta)^2$$

which goes to zero as $\varepsilon \to 0^+$. Therefore, the integral I_1 is regular near $\tilde{x}_0$. Using $\lim_{\varepsilon \to 0} I_1 = I_1(\varepsilon = 0)$ and equation (2.108) in equation (2.107) we have

$$\lim_{\varepsilon \to 0^+} \frac{1}{4\pi} \oint_{\partial \mathcal{D}_B} \hat{\boldsymbol{n}} \cdot \boldsymbol{\nabla} \mathcal{G}(\boldsymbol{x}, \tilde{\boldsymbol{x}}_0 \pm \varepsilon \hat{\boldsymbol{n}}(\tilde{\boldsymbol{x}}_0)) \phi(\boldsymbol{x})\, dS(\boldsymbol{x}) = \pm \frac{1}{2} \phi(\tilde{\boldsymbol{x}}_0) + \frac{1}{4\pi} \oint_{\partial \mathcal{D}_B}^{PV} \phi(\boldsymbol{x})\, \hat{\boldsymbol{n}} \cdot \boldsymbol{\nabla} \mathcal{G}(\boldsymbol{x}, \tilde{\boldsymbol{x}}_0)\, dS(\boldsymbol{x}).$$

Using this result in the integral representation (equation (2.47)), we have the boundary integral equation

$$\frac{1}{4\pi} \oint_{\partial \mathcal{D}}^{PV} \phi(\boldsymbol{x}) \hat{\boldsymbol{n}}(\boldsymbol{x}) \cdot \boldsymbol{\nabla} \mathcal{G}(\boldsymbol{x}, \boldsymbol{x}_0)\, dS(\boldsymbol{x}) - \frac{1}{4\pi} \oint_{\partial \mathcal{D}} \mathcal{G}(\boldsymbol{x}, \boldsymbol{x}_0) \hat{\boldsymbol{n}}(\boldsymbol{x}) \cdot \boldsymbol{\nabla} \phi(\boldsymbol{x})\, dS(\boldsymbol{x}) = \frac{1}{2} \phi(\boldsymbol{x}_0), \quad \boldsymbol{x}_0 \in \partial \mathcal{D}. \tag{2.109}$$

The boundary integral equation (2.109) relates quantities at the boundaries to their surface integrals. Given a boundary condition, we have two types of integral equations

1. Dirichlet condition: where $\phi(\boldsymbol{x})$ is given on $\partial \mathcal{D}$. This leads to a first-kind integral equation, which is numerically ill-conditioned [16, 102].

2. Neumann condition: where $\hat{\boldsymbol{n}} \cdot \boldsymbol{\nabla} \phi(\boldsymbol{x})$ is given on $\partial \mathcal{D}$. This leads to the second-kind integral equation, which is desirable.

Unfortunately, in the case of conductors, the Dirichlet condition is more suitable, where $\phi(\boldsymbol{x})$ is constant on the boundary $\partial \mathcal{D}$. Thus, the boundary integral equation in its current form is not suitable for numerical implementation. In the following sections, we shall see that an integral representation based on the double-layer potential leads to a second-kind integral equation with the Dirichlet boundary conditions.

2.9.2 The Double-Layer Operator

From now on, we will denote the boundary of a compact region $\mathcal{D}_B$ using S_p. The domain of interest $\mathcal{D}$ is still exterior to this boundary S_p. Let us define the double-layer operator on a surface S_p as

$$\mathcal{L}^d[q](\boldsymbol{x}_0) \equiv \frac{1}{2\pi} \oint_{S_p}^{PV} q(\boldsymbol{x}) \hat{\boldsymbol{n}}(\boldsymbol{x}) \cdot \boldsymbol{\nabla} \mathcal{G}(\boldsymbol{x}, \boldsymbol{x}_0)\, dS(\boldsymbol{x}), \quad \boldsymbol{x}_0 \in S_p. \tag{2.110}$$

Here $q(\boldsymbol{x}) \in \mathcal{V}$ and $\mathcal{V}$ is Hilbert space of square-integrable functions defined on S_p with the inner product given by

$$\langle q_1, q_2 \rangle \equiv \oint_{S_p} q_1(\boldsymbol{x}) q_2(\boldsymbol{x})\, dS(\boldsymbol{x}),$$

Thus, $\mathcal{L}^d : \mathcal{H} \to \mathcal{H}$ is an operator on this Hilbert space $\mathcal{H}$. It can be shown that this double-layer operator is weakly singular for Lyapunov surfaces and hence is a compact operator [10, 16, 102].

Using equation (2.108), we have the jump discontinuity result as

$$\lim_{\varepsilon \to 0^+} \frac{1}{2\pi} \oint_{S_p} q(\boldsymbol{x}) \hat{\boldsymbol{n}}(\boldsymbol{x}) \cdot \nabla \mathcal{G}(\boldsymbol{x}, \boldsymbol{x_0} \pm \varepsilon \hat{\boldsymbol{n}})\, dS(\boldsymbol{x}) = (\mathcal{L}^d \pm \mathbb{1})[q](\boldsymbol{x_0}), \quad \boldsymbol{x_0} \in S_p, \tag{2.111}$$

where $\mathbb{1}$ is the identity operator over S_p. Let us look at the adjoint of $\mathcal{L}^d$, denoted as $\mathcal{L}^{d\dagger}$. For $q_1, q_2 \in \mathcal{H}$, we have

$$\langle q_1, \mathcal{L}^d q_2 \rangle = \frac{1}{2\pi} \oint_{S_p}^{PV} q_1(\boldsymbol{x}_0) \left(\oint_{S_p}^{PV} q_2(\boldsymbol{x}) \hat{\boldsymbol{n}}(\boldsymbol{x}) \cdot \nabla \mathcal{G}(\boldsymbol{x}, \boldsymbol{x_0})\, dS(\boldsymbol{x}) \right) dS(\boldsymbol{x_0})$$

$$= -\frac{1}{2\pi} \oint_{S_p}^{PV} q_2(\boldsymbol{x}) \hat{\boldsymbol{n}}(\boldsymbol{x}) \cdot \left(\oint_{S_p}^{PV} q_1(\boldsymbol{x_0}) \cdot \nabla_{\boldsymbol{x_0}} \mathcal{G}(\boldsymbol{x_0}, \boldsymbol{x})\, dS(\boldsymbol{x_0}) \right) dS(\boldsymbol{x}) = \langle \mathcal{L}^{d\dagger} q_1, q_2 \rangle$$

Therefore,

$$\mathcal{L}^{d\dagger}[q](\boldsymbol{x_0}) = -\frac{1}{2\pi} \hat{\boldsymbol{n}}(\boldsymbol{x_0}) \cdot \oint_{S_p}^{PV} q(\boldsymbol{x}) \nabla \mathcal{G}(\boldsymbol{x}, \boldsymbol{x_0})\, dS(\boldsymbol{x}), \quad \boldsymbol{x} \in S_p. \tag{2.112}$$

A jump discontinuity result similar to equation (2.111) follows for the adjoint operator, given by

$$\lim_{\varepsilon \to 0^+} \frac{-1}{2\pi} \hat{\boldsymbol{n}}(\boldsymbol{x_0}) \cdot \oint_{S_p} q(\boldsymbol{x}) \nabla \mathcal{G}(\boldsymbol{x}, \boldsymbol{x_0} \pm \varepsilon \hat{\boldsymbol{n}})\, dS(\boldsymbol{x}) = (\mathcal{L}^{d\dagger} \mp \mathbb{1})[q](\boldsymbol{x_0}), \quad \boldsymbol{x_0} \in S_p. \tag{2.113}$$

2.9.3 Spectrum of the Double-Layer Operator

Note that a constant function c_0 over S_p when acted on by the double-layer operator, gives

$$\mathcal{L}^d[c_0] = \frac{c_0}{2\pi} \oint_{S_p}^{PV} \hat{\boldsymbol{n}}(\boldsymbol{x}) \cdot \nabla \mathcal{G}(\boldsymbol{x}, \boldsymbol{x_0})\, dS(\boldsymbol{x}) = -c_0. \tag{2.114}$$

Therefore, a constant function over S_p is an eigenfunction of $\mathcal{L}^d$ with eigenvalue -1.

Claim: The spectrum of $\mathcal{L}^d$, lies in the real interval $[-1, 1)$.

Proof: Consider a function $w(\boldsymbol{x_0})$ defined in $\mathbb{R}^3$, given by a single-layer potential as

$$w(\boldsymbol{x_0}) = -\frac{1}{2\pi} \oint_{S_p} q'(\boldsymbol{x}) \mathcal{G}(\boldsymbol{x}, \boldsymbol{x_0})\, dS(\boldsymbol{x}), \tag{2.115}$$

where $\mathcal{L}^{d\dagger}[q'] = \lambda q'$, i.e., q' is an eigenfunction of $\mathcal{L}^{d\dagger}$ with eigenvalue λ. Take $\boldsymbol{x_0} \in S_p$ and define

$$\begin{aligned} &E_n^{\pm}(\boldsymbol{x_0}) \equiv -\lim_{\varepsilon\to 0^+} \hat{\boldsymbol{n}}(\boldsymbol{x_0}) \cdot \nabla_{\boldsymbol{x_0}} w(\boldsymbol{x_0} \pm \varepsilon\hat{\boldsymbol{n}}) \\ &= -\lim_{\varepsilon\to 0^+} \frac{1}{2\pi}\hat{\boldsymbol{n}}(\boldsymbol{x_0}) \cdot \oint_{S_p} q'(\boldsymbol{x})\nabla\mathcal{G}(\boldsymbol{x}, \boldsymbol{x_0} \pm \varepsilon\hat{\boldsymbol{n}})\, dS(\boldsymbol{x}) = (\mathcal{L}^{d\dagger} \mp \mathbb{1})[q'](\boldsymbol{x_0}), \quad \boldsymbol{x_0} \in S_p. \end{aligned}$$

This implies

$$E_n^{\pm}(\boldsymbol{x_0}) = (\lambda \mp 1)q'(\boldsymbol{x_0}). \tag{2.116}$$

Note that $E_n^{\pm}$ denotes normal components of the electric field associated with the potential w, just outside and inside the surface S_p. Now, for external flow in domain $\mathcal{D}$, we define $\boldsymbol{E}^+(\boldsymbol{x}) \equiv -\nabla w(\boldsymbol{x})$ in the domain $\mathcal{D}$, and

$$\mathcal{E}^+ \equiv -\oint_{S_p} w(\boldsymbol{x})\boldsymbol{E}^+(\boldsymbol{x})\cdot(-\hat{\boldsymbol{n}})\, dS(\boldsymbol{x}) = -\int_{\mathcal{D}} \nabla\cdot(w\boldsymbol{E}^+)dV = \int_{\mathcal{D}} |\nabla w|^2\, dV \geq 0, \tag{2.117}$$

where we have used the divergence theorem, $\nabla^2 w = 0$, and the fact that there is no contribution from 'surface at infinity'. Similarly, we define $\boldsymbol{E}^-$ in the domain $\mathcal{D}_B$, and

$$\mathcal{E}^- \equiv -\oint_{S_p} w(\boldsymbol{x})\boldsymbol{E}^-(\boldsymbol{x})\cdot\hat{\boldsymbol{n}}\, dS(\boldsymbol{x}) = -\int_{\mathcal{D}_B} \nabla\cdot(w\boldsymbol{E}^-)dV = \int_{\mathcal{D}_B} |\nabla w|^2\, dV \geq 0. \tag{2.118}$$

Using equation (2.116) we have

$$\mathcal{E}^{\pm} = \pm\oint_{S_p} w(\boldsymbol{x})E_n^{\pm}\, dS(\boldsymbol{x}) = \pm(\lambda \mp 1)\oint_{S_p} w(\boldsymbol{x})q'(\boldsymbol{x})\, dS(\boldsymbol{x}). \tag{2.119}$$

Therefore, we have

$$\frac{\mathcal{E}^+}{\mathcal{E}^-} = -\frac{(\lambda - 1)}{(\lambda + 1)} \equiv \delta \geq 0.$$

The last inequality follows from equations (2.117) and (2.118). For $\mathcal{E}^{\pm} \neq 0$, $\delta \in (0, \infty)$, which in turn gives

$$\lambda = \frac{1-\delta}{1+\delta} \in (-1, 1), \quad \text{for} \quad \mathcal{E}^{\pm} \neq 0. \tag{2.120}$$

1. Consider the case $\mathcal{E}^- = 0$. We have $|\nabla w(\boldsymbol{x_0})| = 0$ for $\boldsymbol{x_0} \in \mathcal{D}_B$. This implies that w is constant in $\mathcal{D}_B$. From equation (2.119) we have

   $$-(\lambda + 1)\oint_{S_p} w(\boldsymbol{x})q'(\boldsymbol{x})\, dS(\boldsymbol{x}) = 0.$$

   It follows that if $w \neq 0$ in $\mathcal{D}_B$, then $\lambda = -1$. From equation (2.116), we have $q' = -E_n^+/2$. Therefore, $\lambda = -1$ is an eigenvalue of $\mathcal{L}^{d\dagger}$ with eigenfunction

$q' = -E_n^+/2$. Since w is continuous across S_p, and w is constant over S_p, w represents the potential due to a perfect conductor with surface denoted by S_p. We noted previously that $\mathcal{L}^d[c_0] = -c_0$ for a constant function c_0 over S_p. Therefore, the eigenfunction of $\mathcal{L}^d$ with eigenvalue -1 is just a constant function.

2. Next, consider the case $\mathcal{E}^+ = 0$, which implies w is constant in $\mathcal{D}$. But $w \rightarrow 0$ at infinity. Therefore, $w = 0$ throughout $\mathcal{D}$, which in turn implies $q' = 0$ and hence $\lambda = 1$ is not an eigenvalue of $\mathcal{L}^{d\dagger}$.

Therefore, we conclude that the eigenvalues of $\mathcal{L}^d$ which are complex conjugate of the eigenvalues of $\mathcal{L}^{d\dagger}$ lies in the range $[-1, 1)$ with $\mathcal{L}^d[c_0] = -c_0$ and $\mathcal{L}^{d\dagger}[E_n^+] = -E_n^+$. This completes the proof.
Claim: The eigenvalue $\lambda = -1$ of $\mathcal{L}^d$ is non-degenerate.
Proof: Let ψ be a generalised eigenfunction of $\mathcal{L}^d$ such that

$$(\mathcal{L}^d + \mathbb{1})[\psi] = c_0, \quad \mathcal{L}^d[c_0] = -c_0. \tag{2.121}$$

Snice $\mathcal{L}^d$ is a compact operator, $\mathcal{L}^d + \mathbb{1}$, is a Fredholm operator [10, 16, 102]. Therefore, existence of solution to equation (2.121) requires that $\langle c_0, \chi \rangle = 0$, for all χ such that $(\mathcal{L}^{d\dagger} + \mathbb{1})[\chi] = 0$. Recall that $\chi = E_n^+$ is the normal component of the electric field just outside a perfect conductor with surface denoted by S_p. Therefore, existence of ψ requires $\langle c_0, E_n^+ \rangle = 0$. Let w be the associated potential outside this conductor such that $w(\boldsymbol{x}) = c_0$ for $x \in S_p$. Then we have

$$\int_{\mathcal{D}} |\nabla w|^2 \, dV = \oint_{S_p} w E_n^+ \, dS(\boldsymbol{x}) = \langle c_0, E_n^+ \rangle.$$

If $\langle c_0, E_n^+ \rangle = 0$, then w is constant in $\mathcal{D}$ which along with the decay condition of w at infinity requires $c_0 = 0$. Therefore, for $c_0 \neq 0$, no ψ exists for which $(\mathcal{L}^d + \mathbb{1})[\psi] = c_0$.

To summarize, we have the following two important results for the spectrum of the double-layer operator

1. For the spectrum of double-layer operator $\sigma[\mathcal{L}^d]$, we have $\sigma[\mathcal{L}^d] \in [-1, 1)$. Moreover, $\mathcal{L}^d[c_0] = -c_0$, where c_0 is a constant function.

2. The eigenvalue -1 is non-degenerate; therefore, any accumulation point of the spectrum must lie within the open interval $(-1, 1)$. This point is useful in projecting out the only eigenfunction with eigenvalue -1, as we shall see shortly.

2.9.4 The Range of the Double-Layer Operator

Consider

$$(\mathcal{L}^d + \mathbb{1})[q] = \chi \tag{2.122}$$

We ask, what is the condition on χ for the solution q to exist? From our previous discussion, we saw that χ cannot be a constant function. Since $\mathcal{L}^d + \mathbb{1}$ is a Fredholm operator, the existence of a solution requires $\langle \chi, E_n^+ \rangle = 0$, where $\mathcal{L}^{d\dagger}[E_n^+] = -E_n^+$, and E_n^+ represents the normal component of the electric field outside a perfect conductor with surface denoted by S_p. We apply the reciprocal theorem (equation (2.46)) on two potentials $\phi^{(1)} = \chi$ and $\phi^{(2)} = c_0$ (constant), both satisfying homogeneous Laplace equation in $\mathcal{D}$. The corresponding normal components of the electric field are denoted by E_n^χ and E_n^+, respectively. Using the reciprocal theorem, we have,

$$\langle \chi, E_n^+ \rangle = \langle c_0, E_n^\chi \rangle,$$

Therefore, the existence of a solution to equation (2.122), requires $\langle c_0, E_n^\chi \rangle = 0$, where $E_n^\chi = -\hat{\boldsymbol{n}} \cdot \nabla \chi \Big|_{S_p^+}$ and S_p^+ denotes the outer limit of the normal derivative to the surface. This is equivalent to the requirement that

$$\oint_{S_p} E_n^\chi \, dS = 0,$$

which says that the net charge enclosed inside the surface must be zero. Therefore, the double-layer operator can only represent potentials due to charge-free conductors.

2.9.5 Representation of Solution by Double-Layer Potential

Consider the Dirichlet problem of a perfect conductor carrying total charge Q, placed in an unbounded domain $\mathcal{D}$ in the presence of a background potential field $\phi^\infty(\boldsymbol{x})$, as given by:

$$\nabla^2 \phi(\boldsymbol{x}) = 0, \quad \boldsymbol{x} \in \mathcal{D}; \quad \phi(\boldsymbol{x}_s) = V, \quad \boldsymbol{x}_s \in S_p; \quad \phi(\boldsymbol{x}) \to \phi^\infty(\boldsymbol{x}) \text{ as } |\boldsymbol{x}| \to \infty, \tag{2.123}$$

where we have constant potential V on the surface of the conductor S_p. Representing the solution in terms of double-layer potential in the domain $\mathcal{D}$, we have

$$\epsilon_0 \phi(\boldsymbol{x_0}) = -\frac{1}{2\pi} \oint_{S_p} q(\boldsymbol{x}) \hat{\boldsymbol{n}}(\boldsymbol{x}) \cdot \nabla \mathcal{G}(\boldsymbol{x}, \boldsymbol{x_0}) \, dS(\boldsymbol{x}) + \underbrace{\frac{Q}{4\pi} \mathcal{G}(\boldsymbol{x}, \boldsymbol{x}_c)}_{\text{supplementary part}} + \epsilon_0 \phi^\infty(\boldsymbol{x_0}), \quad \boldsymbol{x_0} \in \mathcal{D}, \tag{2.124}$$

where ϵ_0 is the permittivity of free space and $\boldsymbol{x}_c$ is a point that lies inside the conductor. Here, the supplementary part is needed because the double-layer potential cannot represent the potential outside a charged body. Taking the target point $\boldsymbol{x_0}$ to the surface S_p from within the domain $\mathcal{D}$, using the constant potential boundary condition and equation (2.111), we have

$$(\mathcal{L}^d + \mathbb{1})[q](\boldsymbol{x_0}) = -\epsilon_0 V + \frac{Q}{4\pi}\mathcal{G}(\boldsymbol{x}, \boldsymbol{x}_c) + \epsilon_0 \phi^\infty(\boldsymbol{x_0}), \quad \boldsymbol{x_0} \in S_p \tag{2.125}$$

Now, the existence of a solution q requires the right-hand side of equation (2.125) to represent a charge-free potential field. Note that Q is a free parameter up to now, and hence we can choose Q so that a solution exists. However, we do not have a unique solution because if q is a solution to equation (2.125), so is $q + c_0$ for any constant $c_0 \in \mathbb{R}$. This non-uniqueness comes from the fact that $\mathcal{L}^d$ has an eigenvalue equal to -1. We can project out this eigenvalue from the left-hand side of the equation (2.125) using the projection operator $\mathcal{P}^c$, defined as

$$\mathcal{P}^c[q] \equiv \frac{1}{|S_p|}\oint_{S_p} q\, dS = \frac{1}{|S_p|}\langle 1, q\rangle. \tag{2.126}$$

Here $|S_p|$ is the surface area of the conductor. Note that the projection operator maps functions to constants over S_p. Using this projection operator, we have

$$(\mathcal{L}^d + \mathcal{P}^c + \mathbb{1})[q](\boldsymbol{x_0}) = -\epsilon_0 V + \frac{Q}{4\pi}\mathcal{G}(\boldsymbol{x}, \boldsymbol{x}_c) + \epsilon_0 \phi^\infty(\boldsymbol{x_0}) + \mathcal{P}^c[q], \quad \boldsymbol{x_0} \in S_p$$

Since the constant eigenfunction with eigenvalue -1 has been projected out, the spectrum of the operator $\mathcal{L}^d + \mathcal{P}^c + \mathbb{1}$ lies in $(-1, 1)$, and hence the operator can be inverted using the Neumann series. We choose the unique solution which corresponds to $\mathcal{P}^c[q] = -\epsilon_0 V$. This additional constraint requires us to solve the equation

$$(\mathcal{L}^d + \mathcal{P}^c + \mathbb{1})[q](\boldsymbol{x_0}) = \frac{Q}{4\pi}\mathcal{G}(\boldsymbol{x}, \boldsymbol{x}_c) + \epsilon_0 \phi^\infty(\boldsymbol{x_0}), \quad \boldsymbol{x_0} \in S_p, \tag{2.127}$$

which has a unique solution that can be obtained by inverting the operator on the left-hand side using the Neumann series. Therefore, for problems where the total charge on the conductor is given to be Q, one can solve equation (2.127), which gives the unique solution q. This solution can then be used to obtain the constant potential on the surface of the conductor using $\mathcal{P}^c[q] = \epsilon_0 V$.

2.9.6 Electrostatic Potential in the Presence of Multiple Conductors

The previous formulation generalizes easily in the presence of multiple conductors. The external Dirichlet problem of N charged conductors in the presence of a background potential field $\phi^\infty(\boldsymbol{x})$ in an unbounded domain $\mathcal{D}$ in electrostatics is

$$\nabla^2\phi(\boldsymbol{x}) = 0, \quad \boldsymbol{x} \in \mathcal{D}; \tag{2.128a}$$

$$\phi(\boldsymbol{x}_s) = V_\alpha, \ \text{ for } \ \boldsymbol{x}_s \in S_\alpha; \tag{2.128b}$$

$$\phi(\boldsymbol{x}) \to \phi^\infty(\boldsymbol{x}) \ \text{ as } \ |\boldsymbol{x}| \to \infty, \tag{2.128c}$$

where S_α denotes surface of conductor α and $\alpha \in \{1, 2, ...N\}$. In our cases of interest, the constant potentials V_α are to be determined in terms of the known total charges Q_α on each conductor. The potential field $\phi(\boldsymbol{x}_0)$ can be represented in terms of a double layer potential as

$$\varepsilon_0\phi(\boldsymbol{x}_0) = -\frac{1}{2\pi}\sum_{\alpha=1}^{N}\oint_{S_\alpha} q_\alpha(\boldsymbol{x})\hat{\boldsymbol{n}}_\alpha(\boldsymbol{x}) \cdot \nabla_{\boldsymbol{x}}\mathcal{G}(\boldsymbol{x}, \boldsymbol{x}_0)\, dS_\alpha(\boldsymbol{x}) \\ + \sum_{\alpha=1}^{N}\frac{Q_\alpha}{4\pi}\mathcal{G}(\boldsymbol{x}_0, \boldsymbol{x}_\alpha) + \epsilon_0\phi^\infty(\boldsymbol{x}_0), \quad \boldsymbol{x_0} \in \mathcal{D}. \tag{2.129}$$

Recall that $\mathcal{G}(\boldsymbol{x}, \boldsymbol{x_0})$ is the Green's function of the Laplace equation, given by

$$\mathcal{G}(\boldsymbol{x}, \boldsymbol{x_0}) = \frac{1}{|\boldsymbol{x} - \boldsymbol{x_0}|}.$$

In the equation (2.129), the first term denotes the double layer potential, q_α is an unknown double layer density, $\hat{\boldsymbol{n}}_\alpha$ is outward normal to the surface S_α, Q_α is the total charge on S_α and $\boldsymbol{x}_\alpha$ is a point lying inside the conductor S_α. The unknown double-layer densities q_α are determined using the boundary conditions

$$\lim_{\boldsymbol{x}_0 \to S_\alpha^+} \phi(\boldsymbol{x}_0) = V_\alpha, \quad \alpha \in \{1, 2, ...N\}, \tag{2.130}$$

where $\boldsymbol{x}_0 \to S_\alpha^+$ denotes the approach to the surface S_α is from the outside of the surface, i.e., along $\hat{\boldsymbol{n}}_\alpha$. Applying the boundary condition in equation (2.129), we obtain a second-kind integral equation given by

$$\sum_{\beta=1}^{N}(\mathcal{L}^d_{\alpha\beta} + \delta_{\alpha\beta})\,[q_\beta](\boldsymbol{x}_s) = \sum_{\beta=1}^{N}\frac{Q_\beta}{4\pi}\mathcal{G}(\boldsymbol{x}_s, \boldsymbol{x}_\alpha) - \varepsilon_0 V_\alpha + \epsilon_0\phi^\infty(\boldsymbol{x}_s), \quad \boldsymbol{x}_s \in S_\alpha, \tag{2.131}$$

where $\alpha \in \{1, 2, ...N\}$ and $\mathcal{L}^d_{\alpha\beta}$ is the double layer operator given by

$$\mathcal{L}^d_{\alpha\beta}[q_\beta](\boldsymbol{x}_s) \equiv \frac{1}{2\pi}\oint_{S_\beta} q_\beta(\boldsymbol{x})\,\hat{\boldsymbol{n}}_\beta \cdot \nabla_{\boldsymbol{x}}\mathcal{G}(\boldsymbol{x}, \boldsymbol{x}_s)\, dS_\beta(\boldsymbol{x}), \quad \boldsymbol{x}_s \in S_\alpha. \tag{2.132}$$

Given total charges Q_α's on each conductor, we are required to obtain the potentials V_α's on the surface of each conductor. Using $\mathcal{L}^d_{\alpha\beta}[c] = -c\,\delta_{\alpha\beta}$ where c is a constant function defined on the surface of S_β, we see that (2.131) has no unique solution. Since V_α's are unknown, one chooses the solutions q_α's such that the projection of q_α onto the subspace of constant functions (which are eigenfunctions of $\mathcal{L}^d_{\alpha\beta}$) is exactly V_α. The corresponding projection operator is given by

$$\mathcal{P}^c_{\alpha\beta}[q_\beta] \equiv \frac{1}{|S_\alpha|}\delta_{\alpha\beta}\oint_{S_\beta} q_\beta(\boldsymbol{x})\,dS_\beta(\boldsymbol{x}), \tag{2.133}$$

where $|S_\alpha|$ is the surface area of conductor S_α. Therefore, choosing $\sum_{\beta=1}^{N}\mathcal{P}^c_{\alpha\beta}[q_\beta] = V_\alpha$ not only fixes the non-uniqueness problem but also determines V_α's once the solutions q_α's are known. This leads to a well-defined second-kind integral equation given by

$$\sum_{\beta=1}^{N}(\mathcal{L}^d_{\alpha\beta} + \mathcal{P}^c_{\alpha\beta} + \delta_{\alpha\beta})\,[q_\beta](\boldsymbol{x}_s) = \sum_{\beta=1}^{N}\frac{Q_\beta}{4\pi}\mathcal{G}(\boldsymbol{x}_s,\boldsymbol{x}_\alpha) + \epsilon_0\phi^\infty(\boldsymbol{x_0}), \tag{2.134}$$

$\alpha \in \{1,2,...N\}$, with the potential fields given by

$$\varepsilon_0 V_\alpha = \frac{1}{|S_\alpha|}\oint_{S_\alpha} q_\alpha(\boldsymbol{x})\,dS_\alpha(\boldsymbol{x}), \quad \alpha \in \{1,2,...N\}. \tag{2.135}$$

Using the same arguments as discussed for a single conductor, it can be shown that the spectrum of the grand operator

$$\begin{bmatrix} \mathcal{L}^d_{11} + \mathcal{P}^c_{11} & \mathcal{L}^d_{12} & \cdots & \mathcal{L}^d_{1N} \\ \mathcal{L}^d_{21} & \mathcal{L}^d_{22} + \mathcal{P}^c_{22} & \cdots & \mathcal{L}^d_{2N} \\ \cdots & \cdots & \cdots & \cdots \\ \mathcal{L}^d_{N1} & \mathcal{L}^d_{N2} & \cdots & \mathcal{L}^d_{NN} + \mathcal{P}^c_{NN} \end{bmatrix}$$

lies in the interval $(-1,1)$ and hence the equation (2.134) admits a unique solution which can be obtained using the Neumann series [102]. To accurately evaluate the double-layer operator, which becomes singular when the evaluation point coincides with the quadrature point, we employ singularity subtraction as $\mathcal{L}^d[q](\boldsymbol{x_0}) = \mathcal{L}^d[q-q_0](\boldsymbol{x_0}) + \mathcal{L}^d[q_0](\boldsymbol{x_0}) = \mathcal{L}^d[q-q_0](\boldsymbol{x_0}) - q_0$, where $q_0 = q(\boldsymbol{x_0})$ and we have used the fact that $\mathcal{L}^d[q_0] = -q_0$.

2.10 Boundary Integral Formulation for Rigid Bodies in Stokes Flow

The boundary integral formulation presented in detail has been borrowed from its counterpart in microhydrodynamics, presented in detail in the works of Pozrikidis

[16] and Kim & Karilla [10]. Having understood the formulation for the electrostatic case, we shall briefly present the formalism for Stokes flow, and refer the reader to [10, 16] for a detailed in-depth discussion.

The external Dirichlet problem of N rigid bodies in an unbounded medium in Stokes flow is

$$-\nabla p(x) + \mu \nabla^2 \boldsymbol{u}(x) = 0; \quad \nabla \cdot \boldsymbol{u}(x) = 0; \tag{2.136a}$$

$$\boldsymbol{u}(\boldsymbol{x}_s) = \boldsymbol{V}_\alpha + \boldsymbol{\Omega}_\alpha \times (\boldsymbol{x}_s - \boldsymbol{x}_\alpha), \text{ for } \boldsymbol{x}_s \in S_\alpha; \quad \boldsymbol{u}(\boldsymbol{x}) \to \boldsymbol{u}^\infty(\boldsymbol{x}) \text{ as } |\boldsymbol{x}| \to \infty \tag{2.136b}$$

where S_α denotes surface of rigid body α, $\boldsymbol{x}_\alpha$ is location of the centre of mass of body S_α and $\alpha \in \{1, 2, ...N\}$. The velocity field at a point $\boldsymbol{x}_0$ in the exterior domain $\mathcal{D}$ can be represented in terms of a double layer potential as [10, 16]

$$\boldsymbol{u}(\boldsymbol{x}_0) = \boldsymbol{u}^\infty(\boldsymbol{x}_0) - \frac{1}{4\pi} \sum_{\alpha=1}^{N} \oint_{S_\alpha} \boldsymbol{q}_\alpha(\boldsymbol{x}) \cdot \boldsymbol{\mathcal{T}}(\boldsymbol{x}, \boldsymbol{x}_0) \cdot \hat{\boldsymbol{n}}_\alpha \, dS_\alpha(\boldsymbol{x}) + \boldsymbol{\mathcal{V}}^s(\boldsymbol{x}_0), \quad \boldsymbol{x_0} \in \mathcal{D}, \tag{2.137}$$

where

$$\boldsymbol{\mathcal{T}}(\boldsymbol{x}, \boldsymbol{x_0}) \equiv -\frac{6\boldsymbol{rrr}}{|\boldsymbol{r}|^5}, \quad \boldsymbol{r} \equiv (\boldsymbol{x} - \boldsymbol{x_0}), \tag{2.138}$$

$$\boldsymbol{\mathcal{G}}(\boldsymbol{x}, \boldsymbol{x_0}) \equiv \frac{\boldsymbol{\delta}}{|\boldsymbol{r}|} + \frac{\boldsymbol{rr}}{|\boldsymbol{r}|^3}, \quad \boldsymbol{\mathcal{R}}(\boldsymbol{x}, \boldsymbol{x_0}) \equiv \frac{1}{2} \nabla \times \boldsymbol{\mathcal{G}}(\boldsymbol{x}, \boldsymbol{x_0}), \tag{2.139}$$

$$\boldsymbol{\mathcal{V}}^s(\boldsymbol{x}_0) = \sum_{\alpha=1}^{N} [-\boldsymbol{F}^h_\alpha \cdot \boldsymbol{\mathcal{G}}(\boldsymbol{x}_0, \boldsymbol{x}^{in}_\alpha) + \boldsymbol{T}^h_\alpha \cdot \boldsymbol{\mathcal{R}}(\boldsymbol{x}_0, \boldsymbol{x}^{in}_\alpha)]. \tag{2.140}$$

The first term in equation (2.137) denotes the double-layer potential, $\boldsymbol{q}_\alpha$ is an unknown double-layer density, and $\hat{\boldsymbol{n}}_\alpha$ is an outward normal to the surface S_α. The second term $\boldsymbol{\mathcal{V}}^s(\boldsymbol{x}_0, \boldsymbol{x}_{in})$ is the sum of supplementary flows produced by a point force of magnitude $\boldsymbol{F}^h_\alpha$ and a point torque of magnitude $\boldsymbol{T}^h_\alpha$ located at a point $\boldsymbol{x}_\alpha$, inside the rigid body S_α. For a body S_α with its centre of mass located within it, $\boldsymbol{x}^{in}_\alpha$ is chosen to be the position of the centre of mass $\boldsymbol{x}_\alpha$. The unknown double layer densities $\boldsymbol{q}_\alpha$ are determined using the boundary conditions

$$\lim_{\boldsymbol{x}_0 \to S^+_\alpha} \boldsymbol{u}(\boldsymbol{x}_0) = \boldsymbol{V}_\alpha + \boldsymbol{\Omega}_\alpha \times (\boldsymbol{x_0} - \boldsymbol{x}_\alpha), \quad \alpha \in \{1, 2, ...N\}, \tag{2.141}$$

where $\boldsymbol{x}_0 \to S^+_\alpha$ denotes the approach to the surface S_α from outside of the surface, i.e., along $\hat{\boldsymbol{n}}_\alpha$[3].

In the mobility problem, the external forces and torques are known for each body, which for overdamped systems are negative of the hydrodynamic forces

---

[3] The direction of approach matters because the double layer potential has a jump discontinuity across the surface.

$\boldsymbol{F}^h_\alpha$ and hydrodynamic torques $\boldsymbol{T}^h_\alpha$. Thus, the supplementary flow $\boldsymbol{\mathcal{V}}^s$ is known and we are required to find velocities $\boldsymbol{V}_\alpha$ and $\boldsymbol{\Omega}_\alpha$. Using boundary conditions and projecting out the marginal eigenvalues ±1 [10, 16], we get a second kind integral equation for $\boldsymbol{q}_\alpha$ as

$$\sum_{\beta=1}^{N}\left(\boldsymbol{\mathcal{L}}^d_{\alpha\beta}+\boldsymbol{\mathcal{P}}^{rb}_{\alpha\beta}-\frac{\delta_{\alpha\beta}}{|S_\alpha|}\hat{\boldsymbol{n}}_\alpha\hat{\boldsymbol{n}}_\alpha+\boldsymbol{\delta}_{\alpha\beta}\right)[\boldsymbol{q}_\beta](\boldsymbol{x}_s)=\boldsymbol{u}^\infty(\boldsymbol{x}_s)+\boldsymbol{\mathcal{V}}^s(\boldsymbol{x}_s),\quad \boldsymbol{x}_s\in S_\alpha, \tag{2.142}$$

where $|S_\alpha|$ is the surface area of the body S_α, $\boldsymbol{\mathcal{L}}^d_{\alpha\beta}$ is the double layer operator given by

$$\boldsymbol{\mathcal{L}}^d_{\alpha\beta}[\boldsymbol{q}_\beta](\boldsymbol{x}_s)\equiv\frac{1}{4\pi}\oint_{S_\beta}\boldsymbol{q}_\beta(\boldsymbol{x})\cdot\boldsymbol{\mathcal{T}}(\boldsymbol{x},\boldsymbol{x}_s)\cdot\hat{\boldsymbol{n}}_\beta(\boldsymbol{x})\,dS_\beta(\boldsymbol{x}),\quad \boldsymbol{x}_s\in S_\alpha, \tag{2.143}$$

and $\boldsymbol{\mathcal{P}}^{rb}$ is a projection operator given by

$$\boldsymbol{\mathcal{P}}^{rb}_{\alpha\beta}[\boldsymbol{q}_\beta]\equiv\delta_{\alpha\beta}\left\{\frac{1}{|S_\alpha|}\oint_{S_\alpha}\boldsymbol{q}_\alpha(\boldsymbol{x})\,dS(\boldsymbol{x})+\left(\boldsymbol{I}^{-1}_\alpha\cdot\oint_{S_\alpha}(\boldsymbol{x}-\boldsymbol{x}_\alpha)\times\boldsymbol{q}_\alpha(\boldsymbol{x})\,dS(\boldsymbol{x})\right)\times(\boldsymbol{x}-\boldsymbol{x}_\alpha)\right\}, \tag{2.144}$$

and $\boldsymbol{I}_\alpha$ is the inertia tensor of S_α, given by [93]

$$\boldsymbol{I}_\alpha\equiv\oint_{S_\alpha}[\boldsymbol{\delta}(\boldsymbol{X}_\alpha\cdot\boldsymbol{X}_\alpha)-\boldsymbol{X}_\alpha\boldsymbol{X}_\alpha]\,dS(\boldsymbol{x}),\quad \boldsymbol{X}_\alpha\equiv\boldsymbol{x}-\boldsymbol{x}_\alpha. \tag{2.145}$$

Equation (2.142) has a unique solution $\boldsymbol{q}_\alpha$, $\alpha\in\{1,..N\}$. This solution is then used to determine the unknown velocities as

$$\boldsymbol{V}_\alpha=\frac{1}{|S_\alpha|}\oint_{S_\alpha}\boldsymbol{q}_\alpha(\boldsymbol{x})\,dS(\boldsymbol{x}),\quad \boldsymbol{\Omega}_\alpha=\boldsymbol{I}^{-1}_\alpha\cdot\oint_{S_\alpha}(\boldsymbol{x}-\boldsymbol{x}_\alpha)\times\boldsymbol{q}_\alpha(\boldsymbol{x})\,dS(\boldsymbol{x}). \tag{2.146}$$

It can be shown that the spectrum of the grand operator

$$\begin{bmatrix}
\boldsymbol{\mathcal{L}}^d_{11}+\boldsymbol{\mathcal{P}}^{rb}_{11}-|S_1|^{-1}\hat{\boldsymbol{n}}_1\hat{\boldsymbol{n}}_1 & \boldsymbol{\mathcal{L}}^d_{12} & \dots & \boldsymbol{\mathcal{L}}^d_{1N}\\
\boldsymbol{\mathcal{L}}^d_{21} & \boldsymbol{\mathcal{L}}^d_{22}+\boldsymbol{\mathcal{P}}^{rb}_{22}-|S_2|^{-1}\hat{\boldsymbol{n}}_2\hat{\boldsymbol{n}}_2 & \dots & \boldsymbol{\mathcal{L}}^d_{2N}\\
\dots & \dots & \dots & \dots\\
\boldsymbol{\mathcal{L}}^d_{N1} & \boldsymbol{\mathcal{L}}^d_{N2} & \dots & \boldsymbol{\mathcal{L}}^d_{NN}+\boldsymbol{\mathcal{P}}^{rb}_{NN}-|S_N|^{-1}\hat{\boldsymbol{n}}_N\hat{\boldsymbol{n}}_N
\end{bmatrix}$$

lies in the interval $(-1,1)$ and hence equation (2.142) admits a unique solution which can be obtained using the Neumann series [102]. To accurately evaluate the double-layer operator, which becomes singular when the evaluation point coincides with the quadrature point, we employ singularity subtraction, similar to the approach used in electrostatics, as $\boldsymbol{\mathcal{L}}^d_{\alpha\beta}[\boldsymbol{q}](\boldsymbol{x}_0)=\boldsymbol{\mathcal{L}}^d_{\alpha\beta}[\boldsymbol{q}-\boldsymbol{q}_0]-\boldsymbol{q}_0$, where $\boldsymbol{q}_0\equiv\boldsymbol{q}(\boldsymbol{x}_0)$ and we have used the fact that the $\boldsymbol{\mathcal{L}}^d_{\alpha\beta}[\boldsymbol{q}_0]=-\boldsymbol{q}_0$.

2.11 Numerical Solution of Boundary Integral Equations

For the surfaces with known parametric equations, the boundary integral equations (2.134) and (2.142) can be solved numerically with spectral accuracy. Let $\boldsymbol{x}(\theta, \phi)$ be a point lying on the surface S_p of a body, with (θ, ϕ) denoting polar and azimuthal angle, respectively. The surface S_p can be discretized using $N = n_\theta n_\phi$ grid points, with n_θ Gauss-Legendre nodes in the interval $[0, \pi]$ and n_ϕ uniformly spaced nodes in the periodic azimuthal direction $\phi \in [0, 2\pi)$. Integrating smooth periodic functions using the trapezoidal rule over a periodic grid provides spectral accuracy [103, 104]. Similarly, Gauss-Legendre points ensure spectral accuracy for smooth functions in the domain $[0, \pi]$ [104, 105]. Let (θ_i, ϕ_j) denote the grid points in the parametric space, with $i \in \{1, 2, .., n_\theta\}$ and $j \in \{1, 2, ..., n_\phi\}$. Then we have [104]

$$\theta_i = \frac{\pi}{2}(s_i + 1), \quad \phi_j = \frac{2\pi}{n_\phi}(j - 1); \quad i \in \{1, 2, .., n_\theta\}, \quad j \in \{1, 2, ..., n_\phi\}. \tag{2.147}$$

Here s_i are the roots n_θ roots of the Legendre polynomial $P_{n_\theta}(s)$ of degree n_θ. The surface integrals of the form

$$I \equiv \oint_{S_p} \boldsymbol{f}(\boldsymbol{x}) \cdot \hat{\boldsymbol{n}}(\boldsymbol{x})\, dS(\boldsymbol{x}) = \int_0^\pi d\theta \int_0^{2\pi} d\phi \boldsymbol{f}(\boldsymbol{x}(\theta, \phi)) \cdot \hat{\boldsymbol{n}}(\theta, \phi)\, J(\theta, \phi),$$

can be evaluated numerically as

$$I \approx \sum_{i=1}^{n_\theta} \sum_{j=1}^{n_\phi} \boldsymbol{f}(\boldsymbol{x}(\theta_i, \phi_j)) \cdot \hat{\boldsymbol{n}}(\theta_i, \phi_j) J(\theta_i, \phi_j) w_i^\theta w_j^\phi. \tag{2.148}$$

Here $J(\theta, \phi)$ is the Jacobian, w_i^θ and w_j^ϕ are the quadrature weights, given by:

$$\hat{\boldsymbol{n}}(\theta, \phi)\, W(\theta, \phi) = \left(\frac{\partial \boldsymbol{x}}{\partial \theta} \times \frac{\partial \boldsymbol{x}}{\partial \phi} \right), \quad w_i^\theta = \frac{\pi}{(1 - s_i^2)[P'_{n_\theta}(s_i)]^2}, \quad w_j^\phi = \frac{2\pi}{n_\phi}. \tag{2.149}$$

We use the Nyström method [106] in which the collocation points, where the boundary integral equations are imposed, are taken to be the same as the quadrature points. The generalised minimal residual method (GMRES) [104, 107] is used to converge on the solutions of equations (2.134) and (2.142).

To solve the integral equations for surfaces where parametric equations are not known, one can triangulate the surface and evaluate the integrals either over 3-node flat triangles or 6-node curved triangles, as described by Pozrikidis [98].

3

FLUTTERING WITHOUT WIND: STOKESIAN QUASI-PERIODIC SETTLING

"The junior Bat asked the senior Bat
A question most profound:
'How do the humans down below
Hang by their feet from the ground?'"
— Alphabet Zoop (1992), Dick Smithells and Ian Pillinger

This chapter is adapted from our article published in Physical Review Letters titled "Sedimentation Dynamics of Bodies with Two Planes of Symmetry" [108]. I gratefully acknowledge my advisor, Professor Rama Govindarajan, for her contributions to this work. I also acknowledge Saumav Kapoor for his help in designing the shape of flutterers.

3.1 Introduction

The complex and poetic dance of falling autumn leaves is a high Reynolds number phenomenon, which depends crucially on vortex shedding [109–111], a feature absent in Stokes flow. One would therefore expect settling at zero Reynolds number to be uneventful, especially for a body shape of high symmetry. In fact, in steady Stokes flow, the linear and angular motion of bodies with three planes of symmetry, like ellipsoids, are completely decoupled, and without external torque can only display linear motion [10, 12, 14, 38, 112]. But particles can have complex shapes with fewer symmetries, and understanding their sedimentation is crucial in diverse contexts, from marine snow sequestering atmospheric carbon to ice crystals in clouds and industrial powder production, like milk powder. Unlike ellipsoids, bodies with fewer symmetries can couple translation and rotation, opening up richer possibilities, e.g., chiral sedimenting trajectories of chiral objects like helices and Kelvin's isotropic helicoid [37, 40, 41]. The pioneering work of Brenner [44] examined the different possible terminal sedimentation behaviours allowed for various body symmetries. However, there are bodies that do not attain a steady terminal state. Recent work on sedimentation of a U-shaped disk [42] shows that achiral bodies can display quasi-periodic dynamics with chiral trajectories, and provides theory for the pitch and roll dynamics. This study also argues that the most complicated motion an arbitrary body can perform is quasi-periodic, and not chaotic. We present a general theory for the sedimentation of any body with two planes of symmetry, henceforth called *di-bilaterals*, and find three kinds of dynamics, the most interesting being quasi-periodic. The body shape allows for a priori classification in sedimentation behaviour. Our choice of dynamical variables brings out a new conserved quantity which restricts the dynamics of di-bilaterals. We explain the quasi-periodicity using Floquet theory.

Non-spherical particles are often modelled as ellipsoids to account for their orientation degrees of freedom. But ellipsoids sediment with persistent horizontal drift. We show that only a very narrow class of di-bilaterals, which includes ellipsoids, can show persistent drift. Moreover, we prove that generic bodies displaying quasi-periodic motion cannot show persistent drift. Our study is a strong indication that di-bilaterals, which can exhibit settling, drifting, helical, and quasi-periodic motion, are a far better model of achiral bodies than ellipsoids, capable of explaining a range of sedimentation behaviour. Elastic fibers provide a natural setting for observing di-bilateral sedimentation [113].

Our interest is in the sedimentation of a single *achiral* body in *zero background flow*. We opt for di-bilaterals, which support simple *translation-rotation coupling* (TRC), unlike ellipsoids. We show that all such bodies fall into one of three classes: settlers, drifters, and flutterers. Settlers asymptotically align one of their principal axes along gravity and fall vertically, while drifters fall obliquely at constant speed. Flutterers are the most interesting, showing quasi-periodic or periodic, but never chaotic, motion. We show that their motion is completely described by an overlaying of Floquet dynamics in the horizontal direction, onto periodic dynamics in the vertical direction. We design a set of di-bilaterals (see Figure 3.1) and obtain their resistance matrices, which relate the external forces to particle motion, numerically by the boundary integral method.

3.2 Reduction of mobility matrix through geometric symmetries

As we discussed in Chapter 1 and Chapter 2 of this thesis, the mobility matrix, $\boldsymbol{\mathcal{M}}$, of a body only depends on its size and geometry. For a generic-shaped body, the mobility matrix relates the linear velocity $\boldsymbol{V}$ and angular velocity $\boldsymbol{\Omega}$ of the body to the hydrodynamic force $\boldsymbol{F}^h$ and torque $\boldsymbol{T}^h$ acting on it. This relationship is expressed as

$$\begin{bmatrix} \boldsymbol{V} \\ \boldsymbol{\Omega} \end{bmatrix} = -\mu^{-1} \underbrace{\begin{bmatrix} \boldsymbol{a} & \boldsymbol{b}^T \\ \boldsymbol{b} & \boldsymbol{c} \end{bmatrix}}_{\boldsymbol{\mathcal{M}}} \begin{bmatrix} \boldsymbol{F}^h \\ \boldsymbol{T}^h \end{bmatrix}. \tag{3.1}$$

The symmetry property, $\boldsymbol{\mathcal{M}}^T = \boldsymbol{\mathcal{M}}$, is guaranteed by the Lorentz reciprocal theorem [10, 12, 14, 112]. Each sub-matrices $\boldsymbol{a}, \boldsymbol{b}, \boldsymbol{c}$ which compose $\boldsymbol{\mathcal{M}}$ are 3×3 matrices. Under a linear transformation, $\boldsymbol{U}$, the elements of the mobility matrix transforms as [14]

$$\boldsymbol{a} \to \boldsymbol{U}\boldsymbol{a}\boldsymbol{U}^T, \quad \boldsymbol{b} \to (\det \boldsymbol{U})\boldsymbol{U}\boldsymbol{b}\boldsymbol{U}^T, \quad \boldsymbol{c} \to \boldsymbol{U}\boldsymbol{c}\boldsymbol{U}^T.$$

Note that since $\boldsymbol{b}$ couples a vector and a pseudo-vector, one needs to take into account for transformations that map right-handed coordinates to left-handed coordinates via the determinant $\det \boldsymbol{U}$. For bodies with two planes of symmetry, as indicated by Figure 3.1, there are two reflection transformations $\boldsymbol{U}_1$ and $\boldsymbol{U}_2$, written in the body's coordinate axes ($\{\boldsymbol{p}_1, \boldsymbol{p}_2, \boldsymbol{p}_2\}$) as

$$\boldsymbol{U}_1 = \begin{bmatrix} -1 & 0 & 0 \\ 0 & 1 & 0 \\ 0 & 0 & 1 \end{bmatrix}, \quad \boldsymbol{U}_2 = \begin{bmatrix} 1 & 0 & 0 \\ 0 & 1 & 0 \\ 0 & 0 & -1 \end{bmatrix}. \tag{3.2}$$

Note that $\boldsymbol{p}_2 \to -\boldsymbol{p}_2$ is not a plane of symmetry. Since $\boldsymbol{U}_1$ and $\boldsymbol{U}_2$ are the symmetry transformations, they do not change the geometry of the body. Thus, the mobility matrix is identical after the transformation. This implies

$$\boldsymbol{a} = \boldsymbol{U}_1\boldsymbol{a}\boldsymbol{U}_1^T = \boldsymbol{U}_2\boldsymbol{a}\boldsymbol{U}_2^T, \tag{3.3a}$$

$$\boldsymbol{b} = -\boldsymbol{U}_1\boldsymbol{b}\boldsymbol{U}_1^T = -\boldsymbol{U}_2\boldsymbol{b}\boldsymbol{U}_2^T, \tag{3.3b}$$

$$\boldsymbol{c} = \boldsymbol{U}_1\boldsymbol{c}\boldsymbol{U}_1^T = \boldsymbol{U}_2\boldsymbol{c}\boldsymbol{U}_2^T. \tag{3.3c}$$

Using equation (3.3), each sub-matrix of the mobility matrix gets reduced to the following structure

$$\boldsymbol{a} = L^{-1} \begin{bmatrix} G_1 & 0 & 0 \\ 0 & G_2 & 0 \\ 0 & 0 & G_3 \end{bmatrix}, \quad \boldsymbol{b} = -L^{-2} \begin{bmatrix} 0 & 0 & \alpha_p \\ 0 & 0 & 0 \\ \alpha_r & 0 & 0 \end{bmatrix}, \quad \boldsymbol{c} = L^{-3} \begin{bmatrix} c_1 & 0 & 0 \\ 0 & c_2 & 0 \\ 0 & 0 & c_3 \end{bmatrix}. \tag{3.4}$$

Here L is the typical size of the body, which has been scaled out to make the rest of the parameters non-dimensional. The parameters of interest will be α_p and α_r, which couple the translation and rotation degrees of freedom.

3.3 Dynamics of vertical projections of the principal axes

In the overdamped limit where we work, gravity is balanced by viscous drag. The Stokesian dynamics is conveniently written in the body-fixed coordinate system of unit vectors $\{\boldsymbol{p}_1, \boldsymbol{p}_2, \boldsymbol{p}_3\}$ (see Figure 3.1), as [14, 15, 42]:

$$\begin{pmatrix} v_1 \\ v_2 \\ v_3 \\ \Omega_1 \\ \Omega_2 \\ \Omega_3 \end{pmatrix} = \underbrace{\begin{pmatrix} G_1 & 0 & 0 & 0 & 0 & -\alpha_r \\ 0 & G_2 & 0 & 0 & 0 & 0 \\ 0 & 0 & G_3 & -\alpha_p & 0 & 0 \\ 0 & 0 & -\alpha_p & c_1 & 0 & 0 \\ 0 & 0 & 0 & 0 & c_2 & 0 \\ -\alpha_r & 0 & 0 & 0 & 0 & c_3 \end{pmatrix}}_{\mathcal{M}} \begin{pmatrix} F_1 \\ F_2 \\ F_3 \\ 0 \\ 0 \\ 0 \end{pmatrix}, \tag{3.5}$$

where $\boldsymbol{F} = F_1\boldsymbol{p}_1 + F_2\boldsymbol{p}_2 + F_3\boldsymbol{p}_3$ is the external force due to gravity, and $\boldsymbol{V} = v_1\boldsymbol{p}_1 + v_2\boldsymbol{p}_2 + v_3\boldsymbol{p}_3$ and $\boldsymbol{\Omega} = \Omega_1\boldsymbol{p}_1 + \Omega_2\boldsymbol{p}_2 + \Omega_3\boldsymbol{p}_3$ the translational and angular velocities respectively. Equation 3.5 has been non-dimensionalized by characteristic length and time scales L and $\tau = \mu L^2/(mg_r)$, μ being the fluid's dynamic viscosity, and mg_r the body's buoyancy-corrected weight. Note that we have assumed that the body's geometric centre coincides with its center of mass, and hence no external torque acts on the body. The non-dimensional mobility matrix $\mathcal{M}$ depends only on the body shape. The geometry allows for TRC of a particularly simple form, with two independent entries α_p and α_r. The lab-fixed and body-fixed coordinate axes are related by $\boldsymbol{p}_i = \boldsymbol{R}_{ji}\boldsymbol{e}_j$, $i, j \in \{1, 2, 3\}$ with $\boldsymbol{e}_1 = \hat{\boldsymbol{x}}, \boldsymbol{e}_2 = \hat{\boldsymbol{y}}$ anti-parallel to gravity, and $\boldsymbol{e}_3 = \hat{\boldsymbol{z}}$. So, in the lab frame

$$\boldsymbol{R} = \begin{pmatrix} p_{1x} & p_{2x} & p_{3x} \\ p_{1y} & p_{2y} & p_{3y} \\ p_{1z} & p_{2z} & p_{3z} \end{pmatrix}, \quad \boldsymbol{R}^T\boldsymbol{R} = \boldsymbol{R}\boldsymbol{R}^T = \mathbb{I}. \tag{3.6}$$

Rotational invariance in the body frame about the gravity axis provides, for any arbitrary-shaped body, a decoupling of the dynamics of the vertical projections of the body's coordinate axes from that of their horizontal projections [38, 42, 45, 114].

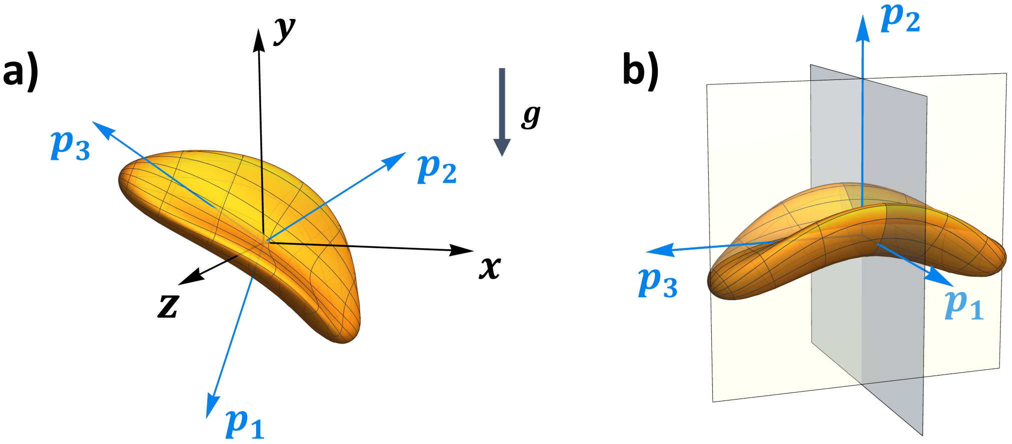

Figure 3.1: (a) A body with two mutually perpendicular planes of symmetry, and the coordinate systems. (b) Showing that $\boldsymbol{p}_1 - \boldsymbol{p}_3$ is not a plane of symmetry.

For the vertical projections, using equations (3.5), (3.6) and $\dot{\boldsymbol{p}}_i = \boldsymbol{\Omega} \times \boldsymbol{p}_i$, $i \in \{1, 2, 3\}$, we get

$$\dot{p}_{1y} = \alpha_r p_{1y} p_{2y}, \tag{3.7a}$$

$$\dot{p}_{2y} = \alpha_p p_{3y}^2 - \alpha_r p_{1y}^2, \tag{3.7b}$$

$$\dot{p}_{3y} = -\alpha_p p_{3y} p_{2y}, \tag{3.7c}$$

with the constraint $|\boldsymbol{p}_y|^2 = 1$, where $\boldsymbol{p}_y \equiv (p_{1y}, p_{2y}, p_{3y})$, as required by equation (3.6). Equation (3.7) admits a conserved quantity

$$H = |p_{1y}|^{\alpha_p} |p_{3y}|^{\alpha_r}. \tag{3.8}$$

The relationship between H and the continuous symmetries of (3.7) is discussed in Section 3.6. Since $p_{1y} = 0$ and $p_{3y} = 0$ are invariant solutions of (3.7), the signs of p_{1y} and p_{3y} are preserved. We have exploited this to define H to be a positive real number. The conserved quantities H and $|\boldsymbol{p}_y|^2 = 1$ render the system (3.7), integrable, and restrict the solutions to go towards a fixed point or be periodic. Solutions lie on the intersection of the unit sphere $\mathcal{S}^2$ with surfaces of constant H. H is a generalisation to arbitrary di-bilaterals, of a conserved quantity shown by [38, 45] for any body whose mobility centre coincides with the centre of mass, which for di-bilaterals is those with $\alpha_p = \alpha_r$.

Earlier studies [38, 45, 114] on the possible sedimentation dynamics of bodies of arbitrary shapes focused on the part of the dynamics described by the gravity vector viewed in the body frame. This dynamical quantity is equivalent to our $\boldsymbol{p}_y$.

They showed that the $\boldsymbol{p}_y$ dynamics of a generic body can have stable, unstable, saddle, and centre fixed points along with limit cycles. Our conserved quantity H removes the possibility of a limit cycle in the $\boldsymbol{p}_y$ dynamics of di-bilaterals, but retains all other possible fixed points, as shown in figure 3.2.

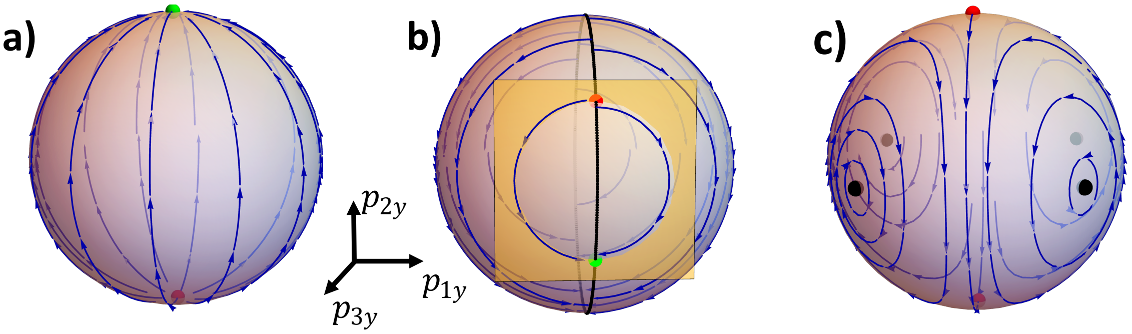

Figure 3.2: Phase portraits of the $\boldsymbol{p}_y$ dynamical system. Red, green, and black dots denote unstable, stable, and centre fixed points, respectively, and blue lines with arrows are sample trajectories. (a) Settlers and (b) drifters ultimately align their $\boldsymbol{p}_2$ axis along and obliquely to gravity, respectively. The beige plane in (b) represents a particular H. (c) Flutterers rotate forever.

3.4 Classification of di-bilaterals based on their rotational dynamics

Equation (3.7) supports the fixed points

$$\boldsymbol{p}_y^* = \{0, \pm 1, 0\} \cup \left\{ \pm\sqrt{\frac{\alpha_p}{\alpha_p + \alpha_r}}, 0, \pm\sqrt{\frac{\alpha_r}{\alpha_p + \alpha_r}} \right\}, \tag{3.9}$$

and presents three different dynamics for bodies whose $\alpha_p \alpha_r \lesseqgtr 0$, as seen in their phase portraits in figure 3.2. This provides a systematic classification of di-bilaterals based on their settling behaviours.

3.4.1 Settlers

Di-bilaterals with $\alpha_p\alpha_r < 0$ are termed 'settlers', whose phase-portrait has one globally attracting stable fixed point and an unstable fixed point. Asymptotically in time, settlers orient their $\boldsymbol{p}_2$ parallel/anti-parallel to gravity and thence fall vertically, without rotating. Similar behaviour occurs in bent achiral fibres [115] and non-deformable chains [116]. Incidentally, a body lying in this class shows settler-like dynamics at moderate Reynolds number [117]. One can show that one of the fixed points of settlers is globally attracting, while the other is globally repelling, as follows.

For settlers, which have $\alpha_r\alpha_p < 0$, a Lyapunov function exists that shows that the stable fixed point is globally stable. Consider first the case where $\alpha_p > 0$ and $\alpha_r < 0$: here $\boldsymbol{p}_y^{*1} = (0, 1, 0)$ is a non-hyperbolic fixed point corresponding to the eigenvalues $(0, -\alpha_p, -|\alpha_r|)$. The Lyapunov function is

$$f_1(\boldsymbol{p}_y) = p_{1y}^2 + p_{3y}^2 + (p_{2y} - 1)^2. \tag{3.10}$$

Clearly, $f_1(\boldsymbol{p}_y^{*1}) = 0$ and $f_1(\boldsymbol{p}_y) > 0$ for $\boldsymbol{p}_y \neq \boldsymbol{p}_y^{*1}$. Now, $\dot{f}_1 = -2(\alpha_p p_{3y}^2 + |\alpha_r| p_{1y}^2) < 0$ for all $\boldsymbol{p}_y \neq \boldsymbol{p}_y^{*1}$, showing $\boldsymbol{p}_y^{*1}$ to be a globally attracting fixed point.

Similar arguments may be made for the other case, where $\alpha_p < 0$ and $\alpha_r > 0$, using the Lyapunov function

$$f_2(\boldsymbol{p}_y) = p_{1y}^2 + p_{3y}^2 + (p_{2y} + 1)^2, \tag{3.11}$$

with $\boldsymbol{p}_y^{*1} = (0, -1, 0)$ being the stable fixed point.

3.4.2 Drifters

The class we term 'drifters' has $\alpha_p\alpha_r = 0$. Their dynamics supports infinitely many fixed points lying along the great circles $\mathcal{A}$, of $p_{1y} = 0$ if $\alpha_p = 0$ or $p_{3y} = 0$ if $\alpha_r = 0$ (figure 3.2(b)). The dynamics occur in the intersection of $\mathcal{S}^2$ with the plane of constant p_{3y} (p_{1y}), provided $\alpha_p = 0$ ($\alpha_r = 0$). This invariant manifold (a circle) intersects $\mathcal{A}$ at a stable and an unstable fixed point. Drifters eventually fall with their principal axes inclined at some constant angle to gravity and, like ellipsoids, display persistent horizontal drift and no rotation.

3.4.3 Flutterers

A range of behaviour, all involving perpetual rotation, is displayed by 'flutterers', whose $\alpha_p\alpha_r > 0$. Every fixed point here is either a centre or a saddle point, as for a U-shaped disk [43]. The maximum in H,

$$H_{\text{max}} = \frac{|\alpha_p|^{\alpha_p/2}|\alpha_r|^{\alpha_r/2}}{|\alpha_p + \alpha_r|^{\alpha_p/2+\alpha_r/2}}, \tag{3.12}$$

corresponds to centre fixed points, and the minimum, $H_{\text{min}} = 0$, corresponds to stable and unstable manifolds of the saddle points. The trajectory for a given initial condition lies on a closed curve representing a constant H surface (figure 3.3), indicating periodic behaviour of $\boldsymbol{p}_y$. A similar periodic behaviour in the inclination angles of a U-shaped disk relative to gravity has also been explained in the context of its sedimentation [42]. The time period T_y of orbits near the centre fixed points can be obtained upon linearizing equation (3.7) about them: $\lim_{H\to H_{\text{max}}} T_y \equiv T_{ym} = 2\pi/\sqrt{2\alpha_p\alpha_r}$. Also, T_y everywhere can be obtained numerically, and is shown in figure 3.4. Flutterers of different shapes show qualitatively similar trends in the time period. Generically, displacing the mobility centre from the centre of mass leads to bifurcation in $\boldsymbol{p}_y$ dynamics [38, 46, 114]. However, such displacement in our flutterers preserves the nature of fixed points. This can be understood as follows.

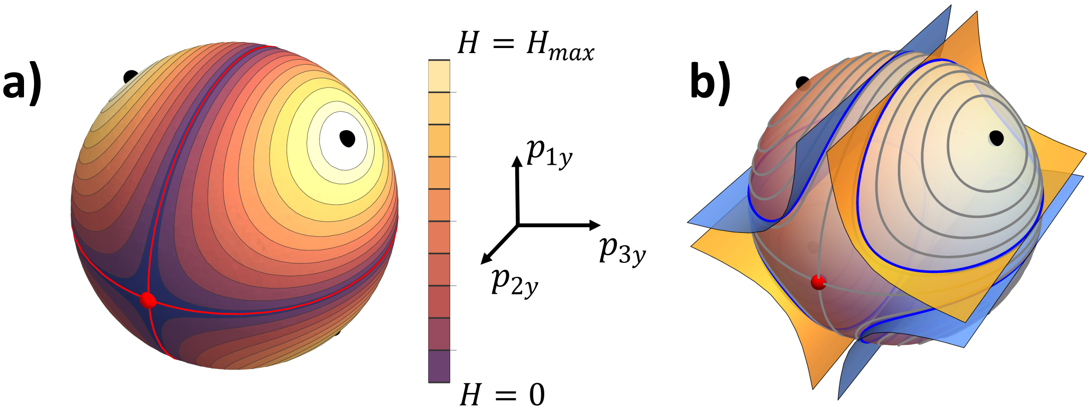

Figure 3.3: (a) Contour plot of the conserved quantity H for flutterers. Closed curves are of constant H, with H_{max} shown by the black dots, and $H = 0$ corresponding to the red heteroclinic orbits of the saddle points (red dots). (b) Trajectories on the yellow surfaces with $p_{1y}p_{3y} > 0$ have different translational chirality from those with $p_{1y}p_{3y} < 0$ on the blue surfaces, as shown in the section 3.8.2.

We refer to the submatrix $\boldsymbol{b}$ of the mobility matrix $\boldsymbol{\mathcal{M}}$ in equation (3.1) as the coupling tensor. The elements of the coupling tensor $\boldsymbol{b}$ depend on the origin of

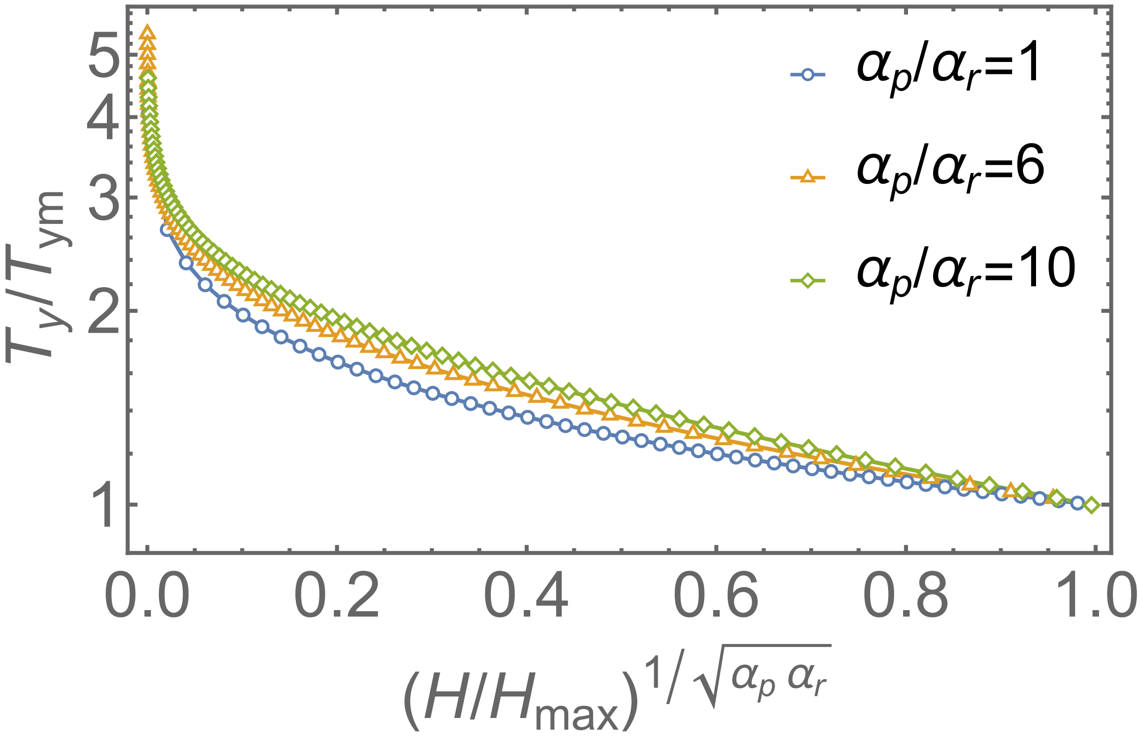

Figure 3.4: Time period of the $\boldsymbol{p}_y$ dynamics of flutterers for different H. As $H \to 0$, T_y can increase without bound. A given ratio α_p/α_r and its inverse yield the same curve.

the coordinate system in which it is written. The mobility centre of a generic body is that point about which the coupling tensor of the body is a symmetric matrix [10, 14]. It has been reported [38, 114] that any body sedimenting with the mobility centre coincident with its centre of mass (symmetric $\boldsymbol{b}$ tensor) has six fixed points in the $\boldsymbol{p}_y$ dynamics. Two of these are saddles, and four are centre fixed points. Typically, the centre fixed points undergo bifurcations and become stable or unstable points when the coupling tensor $\boldsymbol{b}$ departs from being symmetric, i.e., when the mobility centre of a body departs from its centre of mass. For flutterers, however, we show that the stability properties of the centre fixed points do not change even when the coupling tensor $\boldsymbol{b}$ is asymmetric. The reason for this is that the condition for the change in stability, as given in [46], is not met. This condition is stated as follows: The centre fixed points undergo bifurcations if $\boldsymbol{b}$ has three distinct real eigenvalues, and the corresponding normalized eigenvectors $\boldsymbol{\eta}_k$ satisfy

$$\boldsymbol{\eta}_i \cdot \boldsymbol{\eta}_j \neq (\boldsymbol{\eta}_i \cdot \boldsymbol{\eta}_k)(\boldsymbol{\eta}_j \cdot \boldsymbol{\eta}_k) \quad (i,\, j,\, k \quad \text{distinct}),$$

for values of the index k corresponding to the maximum and minimum eigenvalues.

For di-bilaterals, the eigen-system of

$$\boldsymbol{b} = \begin{bmatrix} 0 & 0 & -\alpha_p \\ 0 & 0 & 0 \\ -\alpha_r & 0 & 0 \end{bmatrix}$$

is given by $\boldsymbol{b} \cdot \boldsymbol{\eta}_i = \lambda_i \boldsymbol{\eta}_i$, $i \in \{1, 2, 3\}$, where:

$$\begin{aligned} \lambda_1 = 0, &\quad \boldsymbol{\eta}_1 = (0, 1, 0), \\ \lambda_2 = -\sqrt{\alpha_p \alpha_r}, &\quad \boldsymbol{\eta}_2 = \left(-\sqrt{\frac{\alpha_p}{\alpha_p + \alpha_r}}, 0, \sqrt{\frac{\alpha_r}{\alpha_p + \alpha_r}} \right), \\ \lambda_3 = \sqrt{\alpha_p \alpha_r}, &\quad \boldsymbol{\eta}_3 = \left(\sqrt{\frac{\alpha_p}{\alpha_p + \alpha_r}}, 0, \sqrt{\frac{\alpha_r}{\alpha_p + \alpha_r}} \right). \end{aligned}$$

Therefore,

$$\boldsymbol{\eta}_1 \cdot \boldsymbol{\eta}_2 = 0 = (\boldsymbol{\eta}_1 \cdot \boldsymbol{\eta}_3)(\boldsymbol{\eta}_2 \cdot \boldsymbol{\eta}_3), \tag{3.13}$$

where λ_3 is the maximum eigenvalue of $\boldsymbol{b}$. Thus, flutterers do not satisfy the condition in [46], and there is no bifurcation in their centre fixed points.

3.5 Dynamics of horizontal projections of the principal axes

For the remaining part of the dynamics, we write equations for the projection of $\boldsymbol{p}_i$'s along the x-axis:

$$\begin{pmatrix} \dot{p}_{1x} \\ \dot{p}_{2x} \\ \dot{p}_{3x} \end{pmatrix} = \boldsymbol{A}(t) \begin{pmatrix} p_{1x} \\ p_{2x} \\ p_{3x} \end{pmatrix}, \tag{3.14a}$$

$$\boldsymbol{A}(t) \equiv \begin{pmatrix} 0 & \alpha_r p_{1y}(t) & 0 \\ -\alpha_r p_{1y}(t) & 0 & \alpha_p p_{3y}(t) \\ 0 & -\alpha_p p_{3y}(t) & 0 \end{pmatrix}. \tag{3.14b}$$

Note that equation (3.6) provides three constraints:

$$|\boldsymbol{p}_y(t)|^2 = 1, \tag{3.15a}$$

$$|\boldsymbol{p}_x(t)|^2 = 1, \tag{3.15b}$$

$$\boldsymbol{p}_x(t) \cdot \boldsymbol{p}_y(t) = 0, \quad \forall \quad t. \tag{3.15c}$$

Equations (3.7), (3.14) and (3.15) fully describe the rotational dynamics of di-bilaterals. Equation (3.14) shows that $\boldsymbol{p}_x$ is driven by $\boldsymbol{p}_y$. Since the latter is time-periodic for flutterers, $\boldsymbol{p}_x(t)$ can be solved using Floquet theory [118]. We define a T_y period Poincare map of the $\boldsymbol{p}_x$ dynamical system as:

$$\mathcal{P}_{t_0}^{t_0+T_y} = \boldsymbol{\Phi}_{t_0}^{t_0+T_y}, \tag{3.16a}$$

$$\dot{\boldsymbol{\Phi}}_{t_0}^{t} = \boldsymbol{A}(t)\boldsymbol{\Phi}_{t_0}^{t}; \quad \boldsymbol{\Phi}_{t_0}^{t_0} = \mathbb{I}, \tag{3.16b}$$

where $\boldsymbol{\Phi}_{t_0}^{t}$ is the solution operator of equation (3.14), i.e., $\boldsymbol{p}_x(t) = \boldsymbol{\Phi}_{t_0}^{t}\boldsymbol{p}_x(t_0)$. Since $\boldsymbol{A}^T(t) = -\boldsymbol{A}(t)$, equation (3.16) ensures that $\boldsymbol{\Phi}_{t_0}^{t} \in SO(3)$. Therefore, both the solution operator and the Poincaré map correspond to some 3D rotations. Consequently, the eigenvalues of the Poincaré map are given by 1 and $e^{\pm i\gamma T_y}$, where $\gamma \in \mathbb{R}$ is the Floquet exponent. The constraints of (3.15) restrict $\boldsymbol{p}_x(t)$ to lie normal to $\boldsymbol{p}_y(t)$. Since $\boldsymbol{p}_y(t_0 + T_y) = \boldsymbol{p}_y(t_0)$, the image set of the Poincare map $\{\mathcal{P}_{t_0}^{t_0+nT_y}\boldsymbol{p}_x(t_0)\}_{n\in\mathbb{N}}$ is a subset of the great circle lying normal to $\boldsymbol{p}_y(t_0)$. Thus, the Poincare map $\mathcal{P}_{t_0}^{t_0+T_y}$ acting on $\boldsymbol{p}_x$ corresponds to the rotation of $\boldsymbol{p}_x$ by an angle $\theta \equiv \gamma T_y$ about the axis $\boldsymbol{p}_y(t_0)$. The appendix A shows that θ depends only on H and not on t_0. By Floquet theory, any solution of equation (3.14) can be decomposed as

$$\boldsymbol{p}_x(t) = e^{i\gamma t}\boldsymbol{b}(t), \tag{3.17}$$

where $\boldsymbol{b}(t) = \boldsymbol{b}(t + T_y)$ is some T_y-periodic function. Thus, if the driving frequency $\omega_y \equiv 2\pi/T_y$ is incommensurate with the response frequency γ, i.e., if $\theta/2\pi = \gamma/\omega_y$ is an irrational number, flutterers' motion is quasi-periodic, whereas if it is rational, we have periodic dynamics. In the quasi-periodic case, the image set of the Poincaré map fills up the entire great circle.

Figure 3.5 shows the dependence of the frequency ratio on H. There are differences in detail for different flutterer shapes, but in all cases, the frequency ratio varies continuously on $[1 - 1/\sqrt{2}, 0.5]$, showing dense existence of periodic and quasi-periodic orbits. Figure 3.6 shows phase trajectories and image sets of Poincaré maps for a periodic and quasi-periodic case.

Another class of periodic orbits is obtained on the centre fixed points of the $\boldsymbol{p}_y$ dynamics, characterized by $H = H_{\text{max}}$. In this case $\boldsymbol{A}(t) = \boldsymbol{A}^*$ is a constant matrix with the eigenvalues $0, \pm i\sqrt{\alpha_p\alpha_r}$. The eigenvector corresponding to the zero eigenvalue is not orthogonal to $\boldsymbol{p}_y$, and is dropped from the discussion since it violates the constraints. In this case, the body simply rotates about gravity and falls in a helical trajectory [38].

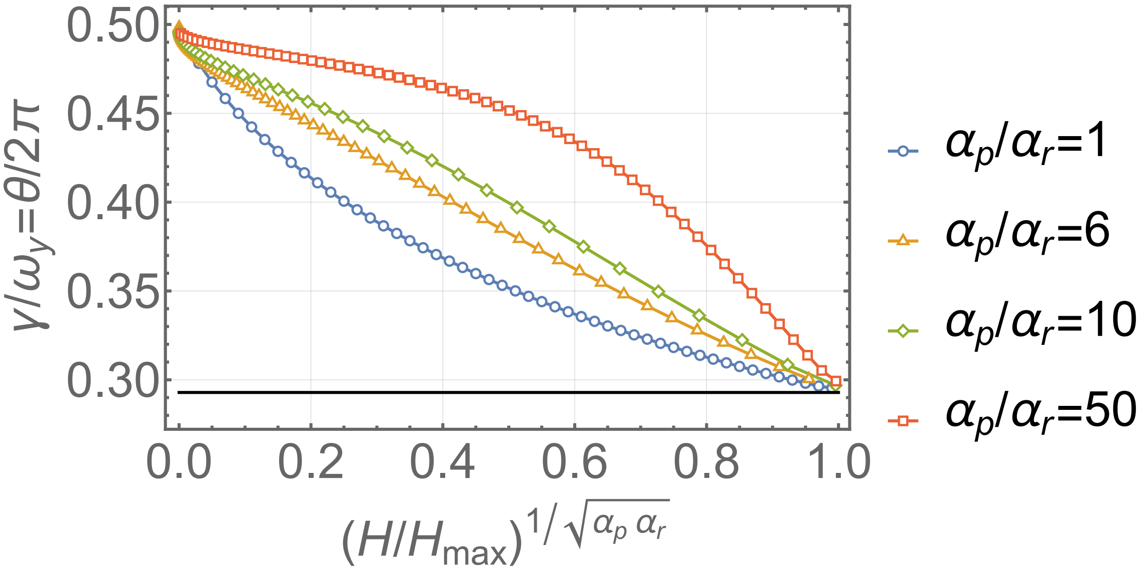

Figure 3.5: The $\boldsymbol{p}_x$ dynamics of flutterers involves two frequencies, γ and ω_y. Their ratio, shown here, is the rotation angle $\theta/2\pi$ of the Poincaré map. The black horizontal line is the lower limit $1 - 1/\sqrt{2}$ of the ratio.

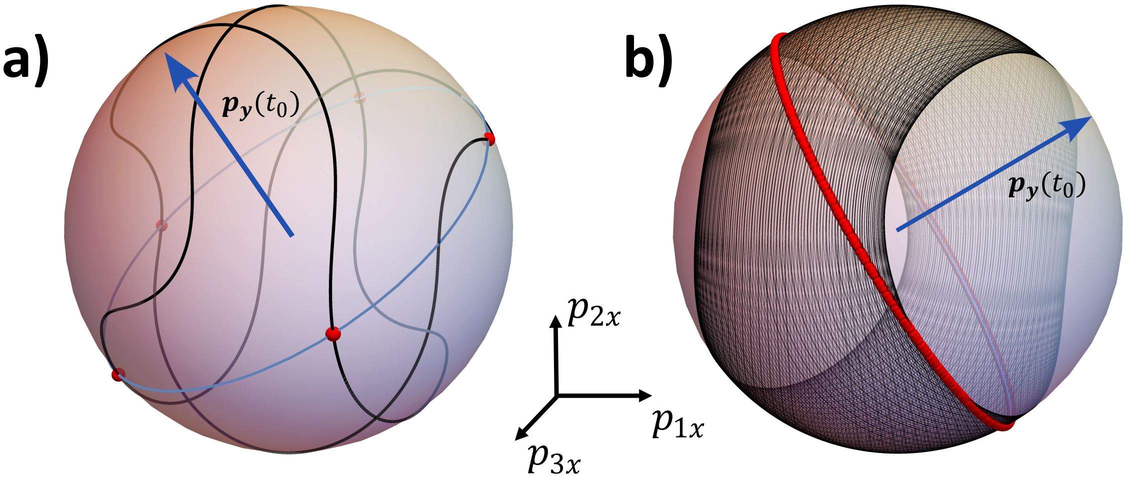

Figure 3.6: Sample $\boldsymbol{p}_x$ trajectories shown as black curves on $\mathcal{S}^2$. (a) Period-5 trajectory. The red dots show the Poincaré map $\mathcal{P}_{t_0}^{t_0+T_y}$ which lie on the great circle shown by the blue curve. This great circle lies normal to $\boldsymbol{p}_y(t_0)$. (b) Quasi-periodic trajectory. The Poincaré map covers the entire great circle lying normal to $\boldsymbol{p}_y(t_0)$. The filled black region has the inversion symmetry $\boldsymbol{p}_x \to -\boldsymbol{p}_x$.

3.6 Discrete and continuous symmetries of the rotational dynamics of di-bilaterals

Before we analyze some important aspects of the dynamics of flutterers in more detail in Section 3.8, it is useful to look at the discrete and continuous symmetries of the rotational dynamics. The discrete symmetry group of the rotational dynamical equations (3.7) and (3.14) is $\mathcal{G}_R = \mathbb{Z}_2 \times \mathbb{Z}_2 \times \mathbb{Z}_2$. The group $\mathcal{G}_R$ is an abelian group containing 8 elements, which corresponds to the following eight transformations of dynamical variables:

Element	Action on $(p_{1y}, p_{2y}, p_{3y}, p_{1x}, p_{2x}, p_{3x})$
e	$(p_{1y}, p_{2y}, p_{3y}, p_{1x}, p_{2x}, p_{3x})$
$a = g * h$	$(-p_{1y}, p_{2y}, -p_{3y}, p_{1x}, -p_{2x}, p_{3x})$
$b = a * c$	$(-p_{1y}, p_{2y}, p_{3y}, p_{1x}, -p_{2x}, -p_{3x})$
$c = a * b$	$(p_{1y}, p_{2y}, -p_{3y}, p_{1x}, p_{2x}, -p_{3x})$
$d = a * f$	$(p_{1y}, p_{2y}, -p_{3y}, p_{1x}, -p_{2x}, -p_{3x})$
$f = b * h$	$(-p_{1y}, p_{2y}, p_{3y}, -p_{1x}, p_{2x}, p_{3x})$
$g = a * h$	$(-p_{1y}, p_{2y}, -p_{3y}, -p_{1x}, p_{2x}, -p_{3x})$
$h = c * d$	$(p_{1y}, p_{2y}, p_{3y}, -p_{1x}, -p_{2x}, -p_{3x})$

Table 3.1: Discrete symmetries of rotational dynamics

The binary operations between the elements is shown in the first column of table 3.1. The corresponding multiplication table of this group is isomorphic to the group $\mathbb{Z}_2 \times \mathbb{Z}_2 \times \mathbb{Z}_2$. For the dynamics of flutterers, the group element h is used to establish that there is no persistent drift for quasi-periodic orbits, while the element g is used to show the dependence of the chirality on the sign of $p_{1y}p_{3y}$. Here we have restricted ourselves to transformations that only act on the dynamical variables and not on time t.

The continuous Lie symmetries of the rotational dynamics are simply scaling symmetries and time translational symmetries. The linearly independent generators of these continuous symmetries are given by

$$X_1 = \boldsymbol{p}_y \cdot \boldsymbol{\nabla}_{\boldsymbol{p}_y} - t\partial_t, \quad X_2 = \boldsymbol{p}_x \cdot \boldsymbol{\nabla}_{\boldsymbol{p}_x}, \tag{3.18a}$$

$$X_3 = \dot{\boldsymbol{p}}_y \cdot \boldsymbol{\nabla}_{\boldsymbol{p}_y} + \dot{\boldsymbol{p}}_x \cdot \boldsymbol{\nabla}_{\boldsymbol{p}_x}, \quad X_4 = \partial_t. \tag{3.18b}$$

The corresponding Lie algebra of these generators is:

$$[X_1, X_2] = 0, \tag{3.19a}$$

$$[X_1, X_3] = X_3, \quad [X_1, X_4] = X_4, \tag{3.19b}$$

$$[X_2, X_3] = [X_2, X_4] = [X_3, X_4] = 0. \tag{3.19c}$$

The generators X_1 and X_2 correspond to scaling symmetries:

$$e^{\lambda X_1}(\boldsymbol{p}_y, \boldsymbol{p}_x, t) = (e^{\lambda}\boldsymbol{p}_y, \boldsymbol{p}_x, e^{-\lambda}t), \quad e^{\lambda X_2}(\boldsymbol{p}_y, \boldsymbol{p}_x, t) = (\boldsymbol{p}_y, e^{\lambda}\boldsymbol{p}_x, t),$$

while the other two generators correspond to time translation. These Lie symmetries can be used to construct the conserved quantities or the first integrals of the rotational dynamics, as described in [119]. The four generators with three unique transformations give three unique characteristics as:

$$\boldsymbol{Q}_1 = (\boldsymbol{p}_y + t\dot{\boldsymbol{p}}_y,\, t\dot{\boldsymbol{p}}_x), \quad \boldsymbol{Q}_2 = (\boldsymbol{0},\, \boldsymbol{p}_x), \quad \boldsymbol{Q}_3 = (\dot{\boldsymbol{p}}_y,\, \boldsymbol{p}_x). \tag{3.20a}$$

The three co-characteristics are given by:

$$\boldsymbol{\Lambda}_1 = (\boldsymbol{p}_y,\, \boldsymbol{0}), \quad \boldsymbol{\Lambda}_2 = (\alpha_p/p_{1y},\, 0,\, \alpha_r/p_{3y},\, \boldsymbol{0}), \quad \boldsymbol{\Lambda}_3 = (\boldsymbol{0},\, \boldsymbol{p}_x). \tag{3.21a}$$

The conserved quantity H is obtained as a first integral using:

$$\boldsymbol{Q}_1 \cdot \boldsymbol{\Lambda}_2 = \alpha_p + \alpha_r + t\frac{d}{dt}\log(p_{1y}^{\alpha_p} p_{3y}^{\alpha_r}).$$

The other scalar products of $\boldsymbol{Q}$'s and $\boldsymbol{\Lambda}$'s yield the constraints (3.15) as the conserved quantities.

3.7 Dependence of settling velocities on the conserved quantity

The translational velocity of di-bilaterals can be obtained from equations (3.5) and (3.6). In the lab frame

$$v_x = -G_1 p_{1x} p_{1y} - G_2 p_{2x} p_{2y} - G_3 p_{3x} p_{3y}, \tag{3.22a}$$

$$v_y = -G_1 p_{1y}^2 - G_2 p_{2y}^2 - G_3 p_{3y}^2, \tag{3.22b}$$

$$v_z = -G_1 p_{1z} p_{1y} - G_2 p_{2z} p_{2y} - G_3 p_{3z} p_{3y}, \tag{3.22c}$$

where $(p_{1z}, p_{2z}, p_{3z}) \equiv \boldsymbol{p}_z \equiv \boldsymbol{p}_x \times \boldsymbol{p}_y$. Positive viscous dissipation rate requires $G_1, G_2, G_3 > 0$ [10, 12, 14, 112]. Equation (3.22) shows the direct dependence of the translational velocity on the orientation of the body. For $H = 0$, the settling velocity v_y reaches $v_{y0} = -G_2$ exponentially fast in time with the rate $|\alpha_p|$ or $|\alpha_r|$, depending on the initial condition, and for $H = H_{\max}$, $v_y = v_{ym} \equiv -(G_1\alpha_p + G_3\alpha_r)/(\alpha_p + \alpha_r)$. The shape of the body determines whether the mean vertical velocity $\langle v_y \rangle$ (averaged over time period of $\boldsymbol{p}_y$ dynamics) increases or decreases with H, and a sample of each is shown in figure 3.7.

3.8 Details of dynamics of flutterers

Given that flutterers exhibit the most complex dynamical features, the following sections are devoted to exploring two important aspects of their behaviour.

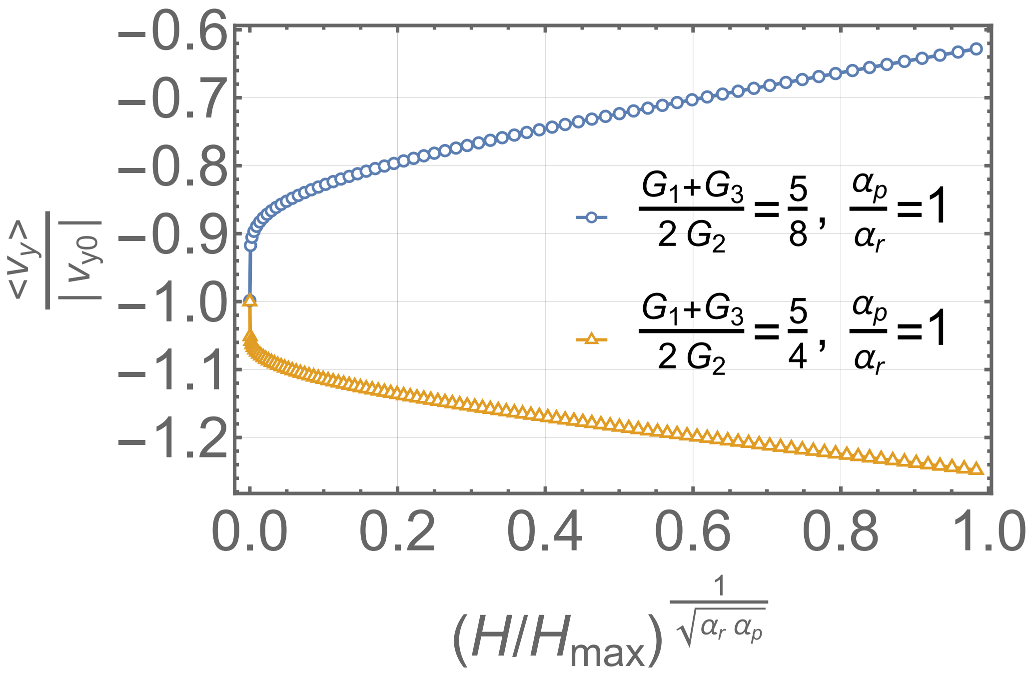

Figure 3.7: For a given body, the mean vertical velocity is a function only of H, and two samples are shown here.

3.8.1 Persistent horizontal drift

In this section, we ask if a di-bilateral, which is a flutterer, can ever show persistent drift in the horizontal plane and answer the question separately for the quasiperiodic and the periodic cases. For the former, following Thorp & Lister [15], we exploit the discrete symmetries of the rotational dynamical equations to rule out persistent drift.

Claim: Flutterers can have persistent drift in the plane perpendicular to gravity only if the driving frequency ω_y of the $\boldsymbol{p}_y$ dynamics is exactly equal to the response frequency γ of the $\boldsymbol{p}_x$ dynamics, i.e., $\gamma = \omega_y$. In this case, the Poincare map $\mathcal{P}_{t_0}^{t_0+T_y}$ is just the identity map.

Proof: The rotational dynamical equations (3.7) and (3.14) have a discrete symmetry group $\mathcal{G}_R = \mathbb{Z}_2 \times \mathbb{Z}_2 \times \mathbb{Z}_2$. If a given rotational trajectory is invariant under $g \in \mathcal{G}_R$ and $g(v_i) = -v_i$ then there can be no persistent drift along the x_i direction for that trajectory, for the drift at one point is exactly cancelled by the other mapped point. Note that $g : (p_{1y}, p_{2y}, p_{3y}, p_{1x}, p_{2x}, p_{3x}) \longrightarrow (p_{1y}, p_{2y}, p_{3y}, -p_{1x}, -p_{2x}, -p_{3x})$ is a symmetry of equations (3.7) and (3.14) with $g(v_x) = -v_x$ and $g(v_z) = -v_z$. Thus, the invariance of trajectories of the rotational dynamical system under g is sufficient to rule out any persistent horizontal drift.

For quasi-periodic cases, any point $\boldsymbol{p}_x(t)$ in a given trajectory will be mapped to the point $-\boldsymbol{p}_x$ at time $t + kT_y$, for some $k \in \mathbb{N}$. This is due to the fact that the Poincaré map $\mathcal{P}_t^{t+T_y}$ fills up the entire great circle with normal vector $\boldsymbol{p}_y(t)$. Since this great circle has an inversion symmetry, there exists a $k \in \mathbb{N}$ such that $\boldsymbol{p}_x(t + kT_y) = -\boldsymbol{p}_x$. Therefore, the region occupied by quasi-periodic orbits on S^2 has inversion symmetry $\boldsymbol{p}_x \to -\boldsymbol{p}_x$. This rules out any persistent drift in the horizontal plane owing to the discrete symmetry element $g \in \mathcal{G}_R$.

For the periodic case, we have closed trajectories subject to constraints (3.15) which may not have the inversion symmetry $\boldsymbol{p}_x \to -\boldsymbol{p}_x$ (see Figure 3.6). The discrete symmetry argument to rule out persistent drift is inconclusive in this case. A necessary condition for persistent drift can be obtained as follows: owing to equation (3.17), each term on the right hand side of v_x and v_z in equation (3.22) is of the form $e^{i\gamma t} f(t)$, where $f(t) = f(t + T_y)$ is some T_y periodic function. The contribution of such terms to the displacement over one time period T of a periodic trajectory is

$$\Delta(T) \equiv \frac{1}{T} \int_0^T e^{i\gamma t} f(t)\, dt = \frac{1}{T} \sum_{k\in\mathbb{Z}} \hat{f}_k \int_0^T e^{i(\gamma+\omega_y k)t}\, dt, \tag{3.23}$$

where we used the Fourier expansion: $f(t) = \sum_{k\in\mathbb{Z}} \hat{f}_k e^{i\omega_y t}$ with $\omega_y T_y = 2\pi$. Now, for the periodic case, $\gamma/\omega_y = n_1/n_2 \in \mathbb{Q}$, where $n_1, n_2 \in \mathbb{N}$ and $T = 2\pi n_2/\omega_y = 2\pi n_1/\gamma$. Using these in equation (3.23), we have

$$\Delta(T) = \sum_{k\in\mathbb{Z}} \hat{f}_k \int_0^1 e^{2\pi i(n_1+kn_2)q}\, dq = \sum_{k\in\mathbb{Z}} \hat{f}_k \delta_{n_1+kn_2,0}, \tag{3.24}$$

where $q = t/T$. Since $k \in \mathbb{Z}$, the contribution can be non-zero if $n_2 = 1$ which implies $\gamma/\omega_y \in \mathbb{N}$. Now, $\gamma = k\omega_y$ for $k \in \mathbb{N}$ implies $\boldsymbol{p}_x(t + T_x) = \boldsymbol{p}_x(t)$ with $T_x = T_y/k$. But $\dot{\boldsymbol{p}}_x(t + T_x) = \dot{\boldsymbol{p}}_x(\boldsymbol{p}_y(t + T_x), \boldsymbol{p}_x(t)) \neq \dot{\boldsymbol{p}}_x(\boldsymbol{p}_y(t), \boldsymbol{p}_x(t))$, unless $T_y = T_x$. Thus, the $\boldsymbol{p}_x$ trajectory cannot repeat itself after T_x since the tangent vector $\dot{\boldsymbol{p}}_x$ at time $t + T_x$ is different from what it was at time t, unless $k = 1$. Therefore, the only periodic trajectory for which $\Delta(T)$ can be non-zero is the case $\omega_y = \gamma$.

For flutterers, numerics suggests that the ratio γ/ω_y is bounded between the interval $[1 - 1/\sqrt{2}, 0.5]$ (see Figure 3.5) in which case there is no persistent drift. The lower limit of the ratio can be obtained by linearizing $\boldsymbol{p}_y$ dynamics near $H = H_{\text{max}}$, in which case the time period of $\boldsymbol{p}_y$ dynamics is periodic with time period $T_{ym} = 2\pi/\sqrt{2\alpha_p\alpha_r}$. The $\boldsymbol{p}_x$ dynamics up to the zeroth order in $H - H_{\text{max}}$ is given by $\dot{\boldsymbol{p}}_x = \boldsymbol{A}^* \boldsymbol{p}_x$, where $\boldsymbol{A}^*$ is the matrix in equation (3.14), evaluated at one of the centre fixed points of the $\boldsymbol{p}_y$ dynamics. Therefore, upto the zeroth order the $\boldsymbol{p}_x$ dynamics is also periodic with the time period $T_{xm} = 2\pi/\sqrt{\alpha_p\alpha_r}$. Now, using equation (3.17), $\boldsymbol{p}_x(t + T_{ym}) = \boldsymbol{p}_x(t) e^{i\gamma T_{ym}}$; and since $\boldsymbol{p}_x(t) \sim e^{\pm 2\pi i t/T_{xm}}$, we have $e^{\pm 2\pi i T_{ym}/T_{xm}} = e^{i\gamma T_{ym}}$, which gives $\gamma T_{ym}/2\pi = 1 - 1/\sqrt{2}$.

When $H = H_{\max}$, we still have no persistent drift, since the valid solutions of $\boldsymbol{p}_x : \boldsymbol{p}_x(t) = e^{\boldsymbol{A}^* t}\boldsymbol{p}_x(0)$ are periodic with zero mean. This is because the eigenvector of $\boldsymbol{A}^*$ with zero eigenvalue does not satisfy the constraint $\boldsymbol{p}_x \cdot \boldsymbol{p}_y = 0$ and thus cannot be part of the solution.

Finally, for $H = 0$, the body exponentially reaches one of the saddle points $\boldsymbol{p}_y^* = (0, \pm 1, 0)$ along its stable manifold as $t \to \infty$ and consequently the horizontal drift goes to zero exponentially.

3.8.2 Chirality of translational trajectories

We discuss the chirality of the translational trajectories of flutterers, as shown in Figure 3.8. As the body settles, its motion in the horizontal $x - z$ plane is either clockwise or anti-clockwise when viewed from below, corresponding to negative or positive chirality, respectively. In Figure 3.3, regions on $\mathcal{S}^2$ with $p_{1y}p_{3y} > 0$ correspond to different chirality in translation motion from regions with $p_{1y}p_{3y} < 0$. This can be seen as follows: for any given angular trajectory $(\boldsymbol{p}_y, \boldsymbol{p}_x)$ with $p_{1y}p_{3y} > 0$, the transformation $g : (p_{1y}, p_{1x}) \to (-p_{1y}, -p_{1x})$ maps the original trajectory to the trajectory in the region $p_{1y}p_{3y} < 0$ with the same H. Thus, the mapped trajectory has the same time period T_y in $\boldsymbol{p}_y$ dynamics and the same frequency ratio γ/ω_y in $\boldsymbol{p}_x$ dynamics. However, $g : v_z \to -v_z$, while the other velocity components remain invariant. So the trajectory of the translational dynamics $(x(t), y(t), z(t))$ is mapped to the trajectory $(x(t), y(t), -z(t))$, i.e., the original and mapped trajectories are of opposite chirality.

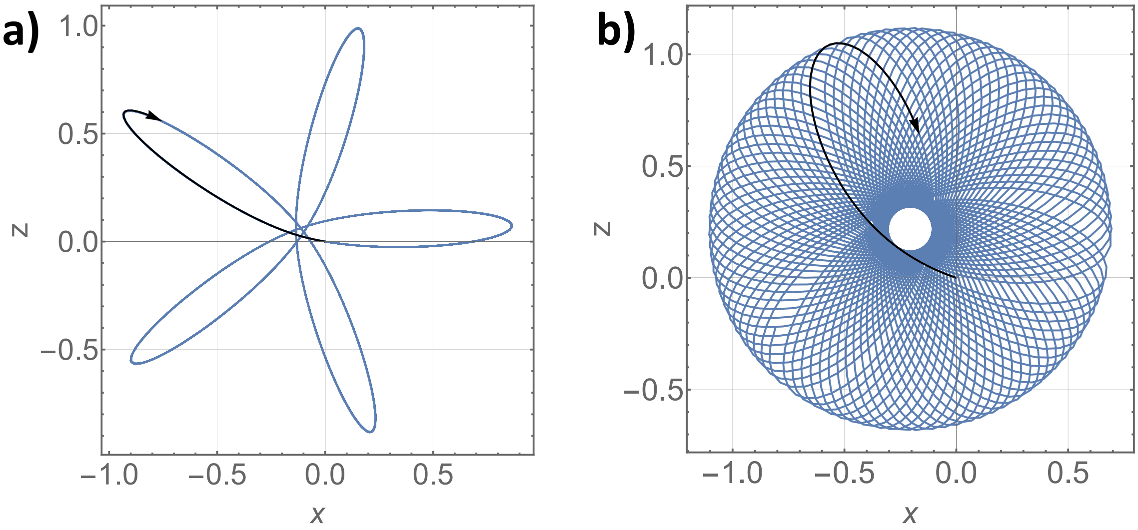

Figure 3.8: Sample trajectories in the horizontal plane for (a) quasi-periodic and (b) periodic orbits. The black arrows indicate the chirality of the settling trajectories.

3.9 Constructing a set of di-bilaterals

It remains to obtain the mobility matrix $\mathcal{M}$, and thence α_p and α_r, for a given di-bilateral. We design a set of bodies with two parameters: the bending parameter a, and the concavity parameter b, as shown in Figure 3.9. The parametric equation for a set of di-bilaterals is described in the following section.

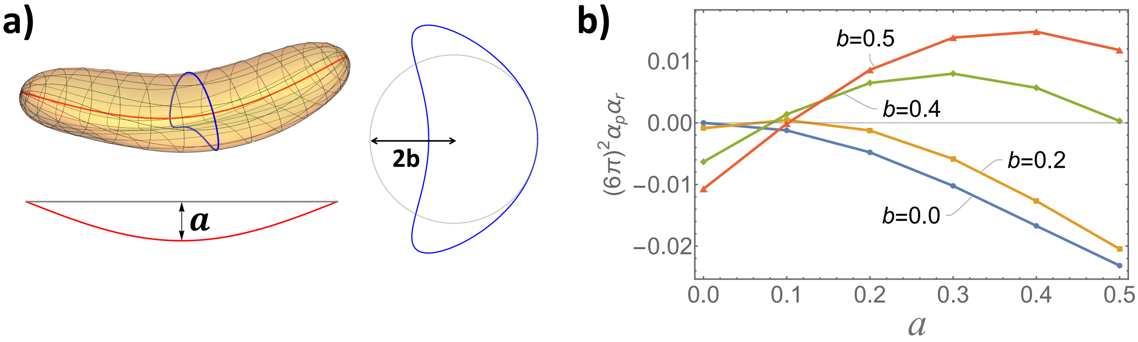

Figure 3.9: a) A set of bodies is defined by the parameters a and b. b) As a and b defined are varied, we obtain settlers ($\alpha_p\alpha_r < 0$), drifters ($\alpha_p\alpha_r = 0$), and flutterers ($\alpha_p\alpha_r > 0$). Increasing b turns settlers into flutterers, but increasing a at fixed b eventually turns flutterers back into settlers.

3.9.1 Parametric equation of a set of di-bilaterals

A class of bodies ranging from settlers through drifters to flutterers can be constructed using a parameterization as described here. The centerline of the bodies is a bent filament which is parameterized by a parameter s as:

$$\boldsymbol{r}_c(s) = a\cos(ks)\boldsymbol{p}_2 + s\boldsymbol{p}_3, \quad s \in [-1, 1], \tag{3.25}$$

where the parameterization is in non-dimensional form with half the size of the bent filament as the length scale, $k = \pi/2$, and a is the dimensionless bending parameter (see red filament in Figure 3.9). To construct a 2D surface, cross sections are drawn around this filament ranging from circular near the edges ($s = \pm 1$) to concavo-convex near the centre $s = 0$. The normal vector $\boldsymbol{n}_c$ and binormal vector $\boldsymbol{b}_c$ to the bent filament are given by

$$\boldsymbol{n}_c(s) = \frac{-\boldsymbol{p}_2 - ka\sin(ks)\boldsymbol{p}_3}{\sqrt{1 + k^2a^2\sin(ks)^2}} \tag{3.26a}$$

$$\boldsymbol{b}_c(s) = \boldsymbol{p}_1. \tag{3.26b}$$

The cross-section of the body uses another parameter ϕ and can be constructed in the plane spanned by $\boldsymbol{n}_c$ and $\boldsymbol{b}_c$. The parametric equation of the set of bodies is given by

$$\begin{aligned}\boldsymbol{r}(s,\phi) = \boldsymbol{r}_c(s) + R(s)\{&[(1-\hat{b}(s))\cos(\phi) + \hat{b}(s)\cos(2\phi)]\boldsymbol{n}_c(s)\\ &+[(1+\hat{b}(s))\sin(\phi) + \hat{b}(s)^3\sin(2\phi)]\boldsymbol{b}_c(s)\},\end{aligned} \tag{3.27}$$

where $R(s) = R_0\sqrt{1-s^4}$ describes the dimensionless size of the cross-section and $\hat{b}(s) \equiv b(1-s^2)$ describes the concavity of the cross-section (see Figure (3.9)). The value of $b = 0$ corresponds to a circular cross-section with the radius of the circle given by R_0 at the centre of the filament $s = 0$. This corresponds to a bent capsule, which is a settler. As b is varied, the cross-section becomes more and more concavo-convex. For a given $b > 0.2$, increasing the bending parameter a takes us from a settler to a flutterer, going through a drifter shape for a particular value of a. Further increase in a, however, results in the flutterer going back to a settler. The value of R_0 is kept fixed to be 0.3 for the numerical evaluation of the mobility matrix $\boldsymbol{\mathcal{M}}$.

We use the Boundary Integral Method [10, 16, 93, 98, 120], as outlined in the Chapter 2 of this thesis, to obtain $\boldsymbol{\mathcal{M}}$ numerically. The parameters α_p and α_r completely describe the rotational dynamics of di-bilaterals, with figure 3.9 showing their dependence on shape. For a given b, an optimal a maximizes $\alpha_p\alpha_r$, resulting in the highest fluttering frequency.

3.10 Summary and Conclusions

To summarize, we have shown that di-bilaterals show three kinds of Stokesian sedimentation, depending only on their shape, appearing through the parameter $\alpha_p\alpha_r$. Settlers and drifters asymptotically fall vertically and obliquely, respectively, without rotating. In flutterers, periodic dynamics in $\boldsymbol{p}_y$ drive a periodic or quasi-periodic response of $\boldsymbol{p}_x$, based on the ratio γ/ω_y. Both time-scales depend only on the conserved quantity H. All three classes of bodies can be obtained by bending a capsule about its central axis and making its cross-section concavo-convex. Previous studies on asymmetric bodies have well-understood $\boldsymbol{p}_y$ dynamics, predicting fixed points of differing character in [38, 45, 46, 114]. Among these, we rule out limit cycles for di-bilaterals due to the conserved quantity, H. Except for a qualitative argument which argues for non-chaotic dynamics [42], the $\boldsymbol{p}_x$ dynamics has not been studied before to our knowledge. The $\boldsymbol{p}_x$ dynamics enables an understanding and quantitative description of quasi-periodicity. In the appendix A, we also extend the proof of no persistent drift of torque-free skewed bodies [45] to any arbitrary body that performs periodic/quasi-periodic motion.

4

DYNAMICS AND CLUSTERING OF SEDIMENTING DISC LATTICES

"I wish I had acquired wisdom at less of a price."
— Hosea Matthews, Red Dead Redemption 2

This chapter is a verbatim reproduction of our published article in the Journal of Fluid Mechanics [121]. Minor formatting and notational changes have been made for consistency. I gratefully acknowledge all the co-authors in this work for their contributions. The experimental results are due to Rahul Chajwa, who conducted all the experiments. Figure 4.1, which explains the two instability mechanisms, and Figure 4.14, with the corresponding stability analysis, are also credited to Rahul Chajwa.

4.1 Introduction

Particle sedimentation through fluid is ubiquitous in natural and industrial processes, such as the settling of clay particles onto a riverbed, precipitates in a chemical reaction, diatoms in pelagic algal blooms, and ice crystals in cirrus clouds. Collections of sedimenting spherical particles have a tendency to clump [47], leading to the formation of large aggregates and thence to increased sedimentation rates. In an otherwise quiescent fluid, clumping is a consequence of hydrodynamic interactions between settling particles, which in turn depend on the shape and relative orientation of particles and inter-particle separations.

Most particles in nature are not perfect spheres, and shape anisotropies in sedimenting particles leads to qualitatively new dynamical features. Spheroids offer a simple model to describe departures in particle shape from sphericity, and exhibit much richer sedimentation dynamics than spheres, both because isolated spheroids can drift horizontally and pairs are coupled through their orientational and translational degrees of freedom [94, 122–124]. These new elements in the dynamics can affect particle collision rates and their tendency to form aggregates.

Spheroidal particles range from disc-like (oblate) to rod-like (prolate). The Stokesian sedimentation of a suspension of slender fibres has been studied experimentally [125] and numerically [126, 127] with a focus on the dependence of velocity fluctuations and structure factor on length scale and particle concentration. In very low volume fractions, these studies report large-scale inhomogeneities, with dense patches, termed streamers [128], in which the mean particle orientation aligns with gravity, harbouring fast-settling clusters of fibres [127] that spontaneously form and break [125]. The formation of clusters and streamers from an initially homogeneous suspension occurs in a highly nonlinear regime; how this nonlinear state is arrived at from a linear instability [95] and what sets the typical size of clusters, is unresolved [125]. Studies of sedimenting lattices of particles [47, 48, 129] shed light on how particle-level interactions yield long-wavelength collective modes, and offer a simple setting in which to study the clustering that results from perturbations about a well-defined reference configuration.

In this article, we investigate numerically and experimentally the sedimentation of one-dimensional arrays of oblate spheroids in the limit of negligibly small Reynolds number and Stokes number. Going beyond the linear stability analysis of Chajwa et al. [48], we elucidate the detailed dynamics at the level of individual particles, with emphasis on clustering due to hydrodynamic interactions. We show that, unlike spheres, discs display two qualitatively different behaviours of clustering depending on their initial spacing. At small initial spacing, clustering is dictated by the Crowley mechanism, where clumps typically form at valleys in the initial perturbation and consist of several particles. At larger spacing, the drift mechanism becomes dominant, and in the non-linear regime, instead of clumps, we obtain attracting pairs typically forming away from valleys in the initial perturbation pattern, which then fall together in a '$\perp$' configuration (see figure 4.6). The two competing mechanisms are illustrated in Figure 4.1. Two distinct forms of perturbation growth, arising from competing mechanisms, were analyzed earlier [48] in the linearized dynamics. Chajwa et al. [48] assumes a point particle approximation for hydrodynamic interactions and obtains a sharp boundary between unstable and neutrally stable configurations. Here, we improve the approximation by correcting the boundary conditions at each particle by the method of reflections, and find that incorporating corrections of sub-leading order in a/r (where a is a typical particle size and r the typical separation between particles), makes the system linearly unstable for all initial spacings and wavenumbers.

For larger initial inter-particle spacing, the exponential growth rates are extremely small, while transient algebraic growths of perturbations, driven by drift, are not, and dictate clustering into pairs at the antinodes, rather than clumps at the nodes.

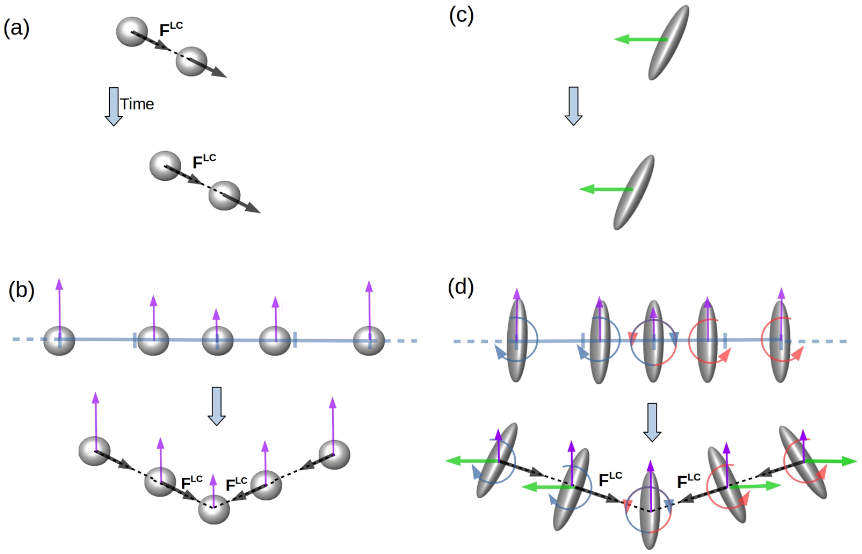

Figure 4.1: **Competition between orientation-dependent drift and the Crowley mechanism.** Schematic showing that the drift mechanism can potentially stabilize Crowley instability (adapted from Chajwa et al. [48]). (a) A pair of spheres starting at different vertical heights maintains a separation vector as it sediments. The pair falls downward faster than an isolated sphere. This reduction in drag increases if the spheres are started off closer. In addition to the velocity component in the gravity direction, the pair also drifts horizontally, due to the line-of-center forces F_{LC}. (b) F_{LC} along with reduced drag yield clumping instability [47]. The dense region falls faster, which leads to a drift towards the leading particle. (c) A settling spheroid with oblique orientation drifts laterally, as shown by the green arrows. (d) Orientations of the spheroids can rotate due to hydrodynamic interactions with the neighboring particles, and can lead to splay in the lattice. The Crowley mechanism, due to hydrodynamic interactions, is operative irrespective of the shape of the particles and tends to form clumps at valleys or at density nodes. However, as the spheroids sediment, they drift horizontally as a consequence of their orientation, as shown by the green arrows. This orientation-dependent drift mechanism, operating at the level of individual particles, can suppress the Crowley instability.

This chapter is organised as follows: the experimental setup and the theoretical approach we adopt are described in sections 2 and 3, respectively. We write down the evolution equations for the positions and orientations of the discs, emerging from the velocities and gradients of the Stokes flows generated by their gravitational force densities. The method of reflections is used to obtain the background disturbed flow produced by each spheroid. Near-contact dynamics without considering lubrication forces can lead to overlapping spheroids. We adopt a numerical procedure to avoid overlaps with a simple model for the lubrication regime. In section 4, we validate the governing equations by comparing them to our experimental results for the dynamics of a pair of discs. An interesting rocking motion was noticed during our validation exercises: two discs stacked in an '=' formation represent an equilibrium system that is neutrally stable to periodic perturbations. The stability analysis is conducted to understand the rocking dynamics. This exercise also brings out the limitations of a point-force approximation and justifies the use of the first-reflection approximation in our theory. Section 5 describes the clustering behaviour of perturbations of a one-dimensional array of sedimenting oblate spheroids. The clustering of spheroids is analyzed in two regimes dominated by two different mechanisms: the Crowley mechanism and a drift mechanism. The two regimes are explored numerically, and we construct statistical measures that allow us to distinguish the two regimes. Section 6 is devoted to the understanding of the long-lived inverted 'T' or '⊥' structures that form in the algebraic growth regime. We summarise our work and discuss the future avenues that emerge from it in Section 7.

4.2 Experiments

The sedimentation experiments were performed in a quasi-2D slab geometry (see Fig. 4.2) with height 45 cm, width 90 cm, and thickness 5 cm filled with silicone oil with density 0.98 g/cm^3 and kinematic viscosity 5000 cSt. Discs of diameter $2a = 8$ mm and thickness $2b = 1$ mm were 3D-printed with resin of density 1.164 g/cm^3. These discs are modelled in our theory as oblate spheroids of aspect ratio $b/a = 0.125$. The Reynolds number using the length scale set by the particle size was measured to be $\sim 10^{-4}$, ensuring that we are in a Stokesian regime. The quasi-2D geometry of the container has two effects: it leads to a modest reduction of the single-particle sedimentation speed, and it cuts off hydrodynamic interactions with neighbours beyond a length-scale set by the thickness.

Releasing multiple particles in a viscous fluid presents a challenge in synchronizing release times and controlling initial orientations, as pointed out by Jung et al. 2006, Chajwa 2020, and described in Chajwa [130]. Our release mechanism consists of an array of slots where discs can be selectively placed to define the initial (dimensional) lattice spacing d and dimensional perturbation wave-number $2\pi/\lambda$ [see figure 4.2]. The release mechanism is centered along the thickness of the slab and immersed in the fluid to remove bubbles attached to the discs. The

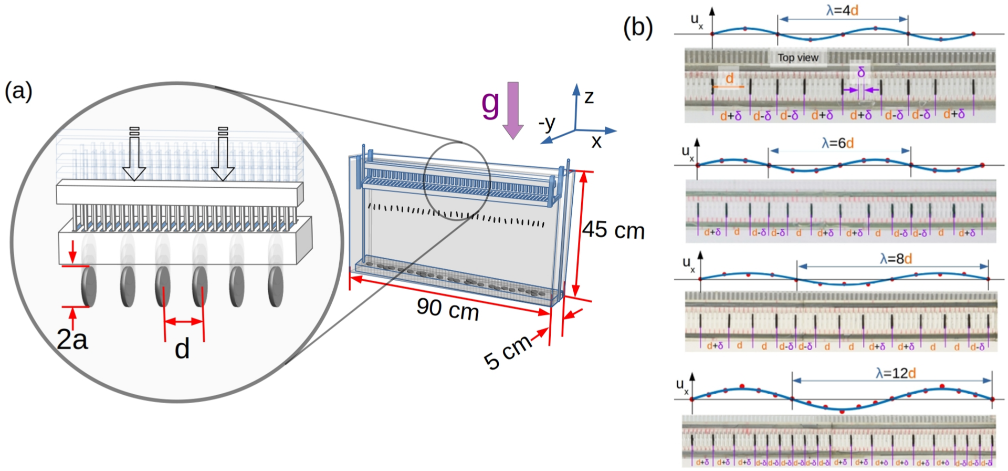

Figure 4.2: **Experimental setup:** (a) Shows the quasi-two-dimensional geometry of the container with gravity axis pointing along $-\hat{z}$. The mechanism simultaneously releases discs with controlled lattice spacing and perturbation wavenumber. (b) The bottom view of the release mechanism shows the array of discs moments before they were released into the fluid. The initial spacing is chosen to control the dimensional lattice spacing d and the dimensional perturbation wave-number $2\pi/\lambda$.

discs are ejected from the slots simultaneously using a 'comb' that inserts into the slots. This setup allows us to study the dependence of the particle dynamics on d and λ. A D-SLR camera is used to capture images of the discs every 3 seconds. The images are thresholded, and an ellipse is fit to each disc to determine its orientation and the location of its centroid. In the later stages, the thresholded images had to be manually segmented to separate closely-clustered discs.

4.3 Governing equations

Our system consists of hydrodynamically interacting oblate spheroids (discs) labeled by $\alpha \in \{1, \dots N_d\}$ sedimenting under gravity in an otherwise quiescent unbounded fluid. The αth disc is described by semi-major and semi-minor axes a and b, respectively, a centre position $\boldsymbol{x}_\alpha$, orientation unit vector $\boldsymbol{p}_\alpha$ which points along the symmetry axis of the disc, and instantaneous velocity $\boldsymbol{V}_\alpha$. For particle Reynolds number $Re_p \ll 1$, every disc generates a disturbance field that satisfies the Stokes equation [10, 124]. Moreover, when the particle relaxation time scale τ_p is much smaller than the time it takes to fall through its length, the Stokes number $St \equiv (\tau_p V_\alpha / a) \ll 1$ for each disc, so that its buoyancy corrected weight $\boldsymbol{F}^g$ is instantaneously balanced by hydrodynamic drag $\boldsymbol{F}^h_\alpha$ for each disc. The simplest approximation for the hydrodynamic interaction experienced by a given disc would be to sum the flows due to the other discs, treating each disc as a force monopole placed at its centroid. The resulting velocity, vorticity, and rate of strain at the location of the disc in question translate, rotate, and align it, leading to the equations of motion

$$\boldsymbol{V}_\alpha^{\mathrm{pt}} = \frac{\boldsymbol{F}^g}{6\pi\mu a}\cdot\left[\frac{\boldsymbol{p}_\alpha\boldsymbol{p}_\alpha}{X^A} + \frac{(\boldsymbol{\delta} - \boldsymbol{p}_\alpha\boldsymbol{p}_\alpha)}{Y^A}\right] + \sum_{\beta\neq\alpha}^{N_d}\frac{\boldsymbol{F}^g}{8\pi\mu}\cdot\boldsymbol{\mathcal{G}}(\boldsymbol{x}_{\alpha\beta}), \tag{4.1}$$

$$\frac{d}{dt}\boldsymbol{p}_\alpha = \sum_{\beta\neq\alpha}^{N_d}\left(\frac{\boldsymbol{F}^g\times\boldsymbol{x}_{\alpha\beta}}{8\pi\mu|\boldsymbol{x}_{\alpha\beta}|^3}\right)\times\boldsymbol{p}_\alpha + \frac{3e^2}{2-e^2}\sum_{\beta\neq\alpha}^{N_d}\left(\frac{\boldsymbol{F}^g\cdot\boldsymbol{x}_{\alpha\beta}}{8\pi\mu}\right)\left(\frac{\boldsymbol{p}_\alpha\cdot\boldsymbol{x}_{\alpha\beta}}{|\boldsymbol{x}_{\alpha\beta}|^5}\right)[\boldsymbol{x}_{\alpha\beta} - \boldsymbol{p}_\alpha(\boldsymbol{p}_\alpha\cdot\boldsymbol{x}_{\alpha\beta})], \tag{4.2}$$

where

$$\boldsymbol{\mathcal{G}}(\boldsymbol{x}) = \frac{\boldsymbol{\delta}}{|\boldsymbol{x}|} + \frac{\boldsymbol{x}\boldsymbol{x}}{|\boldsymbol{x}|^3} \tag{4.3}$$

is the Green's function of the steady Stokes equation. In (4.1) and (4.2), $\boldsymbol{x}_{\alpha\beta} \equiv \boldsymbol{x}_\alpha - \boldsymbol{x}_\beta$, μ is the dynamic viscosity of the fluid, $e = \sqrt{1 - b^2/a^2}$ is the eccentricity, and

$$X^A \equiv \frac{4}{3}e^3[(2e^2-1)K + e\sqrt{1-e^2}]^{-1}, \tag{4.4}$$

$$Y^A \equiv \frac{8}{3}e^3[(2e^2+1)K - e\sqrt{1-e^2}]^{-1}, \tag{4.5}$$

$$\text{with}\quad K \equiv \cot^{-1}\frac{\sqrt{1-e^2}}{e}, \tag{4.6}$$

are resistance functions for an oblate spheroid [10], which approximates the experimental discs with an aspect ratio of $b/a = 0.125$, corresponding to $e = 0.992$. The first term in (4.1) is the sedimentation velocity of an isolated disc falling under gravity, and the second is the sum of disturbance fields produced by other discs, in the point-force approximation. The two terms in equation (4.2) respectively are the contribution from the vorticity and the strain rate of the disturbance field on the orientational dynamics of the disc.

The point-force approximation captures the essential features of the periodic and unbounded dynamics of a pair of discs, and sharp transitions between these states, as the initial condition is varied [94]. It also provides a basic framework to understand the linear instability and wave-like modes observed in a one-dimensional array of sedimenting discs [48]. However, at late times, the initial lattice state is disrupted, giving rise to the formation of configurations with small inter-particle separations, for which the point-force description is expected to be inadequate, since this approximation is accurate only up to $O(a/r)$ where $r = |\boldsymbol{x}_{\alpha\beta}|$. Therefore, for nearly touching disc configurations observed during the late stages of instability in our experiments, we need to account for finite-size effects and to satisfy the no-slip boundary conditions on each particle. We use the method of reflections to study the close-range dynamics. This perturbative method is needed to iteratively satisfy the boundary conditions on the surface of each disc, with each iteration progressively correcting the errors from the previous one [10, 124]. At the n^{th} reflection, the velocity at the location of particle α satisfies the no-slip condition on it due to the velocities induced by all other particles calculated calculated at the $(n-1)^{th}$ reflection, and this corrected velocity of particle α will induce a small slip at the surfaces of all the other particles. As n increases, the error goes to higher and higher orders in the interparticle spacing. We find that the first reflection, combined with a simple lubrication correction and near-contact repulsion, is sufficient to predict the structural arrangement of discs observed in the experiments. The first reflection is accurate up to $O(a^3/r^3)$ in linear velocity and $O(a^4/r^4)$ in the angular velocity. The linear velocity $\boldsymbol{V}_\alpha$ and angular velocity $\boldsymbol{\Omega}_\alpha$ of a disc α can be expressed in terms of the hydrodynamic force $\boldsymbol{F}^h_\alpha$ and hydrodynamic torque $\boldsymbol{T}^h_\alpha$ acting on it, using the Faxén's laws as [10]:

$$\boldsymbol{V}_\alpha = \frac{-\boldsymbol{F}^h_\alpha}{6\pi\mu a}\cdot\left[\frac{\boldsymbol{p}_\alpha\boldsymbol{p}_\alpha}{X^A} + \frac{(\boldsymbol{\delta}-\boldsymbol{p}_\alpha\boldsymbol{p}_\alpha)}{Y^A}\right] + \frac{1}{2c}\int_{-c}^{c} d\xi\left\{1+\frac{(c^2-\xi^2)}{4e^2}\nabla^2\right\}\boldsymbol{u}^\infty_\alpha\bigg|_{\boldsymbol{x}_\alpha(\xi)}, \tag{4.7}$$

and

$$\begin{aligned}\boldsymbol{\Omega}_\alpha = {} & \frac{-\boldsymbol{T}^h_\alpha}{8\pi\mu a^3}\cdot\left[\frac{\boldsymbol{p}_\alpha\boldsymbol{p}_\alpha}{X^C} + \frac{(\boldsymbol{\delta}-\boldsymbol{p}_\alpha\boldsymbol{p}_\alpha)}{Y^C}\right] + \frac{3}{8c^3}\int_{-c}^{c} d\xi(c^2-\xi^2)\boldsymbol{\nabla}\times\boldsymbol{u}^\infty_\alpha\bigg|_{\boldsymbol{x}_\alpha(\xi)} \\ & - \frac{3}{4c^3}\frac{e^2}{2-e^2}\int_{-c}^{c} d\xi\left\{(c^2-\xi^2)\left[1+(c^2-\xi^2)\frac{1}{8e^2}\nabla^2\right]\right\}\boldsymbol{p}_\alpha\times[\boldsymbol{E}^\infty_\alpha\bigg|_{\boldsymbol{x}_\alpha(\xi)}\cdot\boldsymbol{p}_\alpha]. \end{aligned} \tag{4.8}$$

Here $c \equiv ae$, $\boldsymbol{E}^\infty_\alpha$ is the strain rate associated with u^∞_α and

$$X^C \equiv \frac{2}{3}e^3[K - e\sqrt{1-e^2}]^{-1}, \tag{4.9}$$

$$Y^C \equiv \frac{2}{3}e^3(2-e^2)[e\sqrt{1-e^2} - (1-2e^2)K]^{-1}. \tag{4.10}$$

In writing equations (4.7) and (4.8), we have used the fact that the singularity distribution of an oblate spheroid (disc) can be written in terms of a line distribution placed along an imaginary focal length [101]. This requires us to evaluate the background incidence field on disc α, $\boldsymbol{u}^\infty_\alpha$, at $\boldsymbol{x}_\alpha(\xi) \equiv \boldsymbol{x}_\alpha + i\xi\boldsymbol{p}_\alpha$. Up to the first reflection correction, the background incidence field on disc α, $\boldsymbol{u}^\infty_\alpha$, is given by the superposition of the disturbance fields generated by all the other discs, treating them as isolated and satisfying the no-slip boundary condition on their respective surfaces. Thus, we have

$$\begin{aligned}\boldsymbol{u}_{\alpha}^{\infty}(\boldsymbol{x}) \approx \sum_{\beta\neq\alpha}^{N_d}\Bigg[&\frac{-\boldsymbol{F}_{\beta}^{h}}{8\pi\mu}\cdot\frac{1}{2c}\int_{-c}^{c}\left\{1+\frac{(c^2-\xi^2)}{4e^2}\nabla^2\right\}\boldsymbol{\mathcal{G}}(\boldsymbol{x}-\boldsymbol{x}_{\beta}-i\xi\boldsymbol{p}_{\beta})\,d\xi\\ &+\frac{1}{2}\frac{\boldsymbol{T}_{\beta}^{h}\times\boldsymbol{\nabla}}{8\pi\mu}\cdot\frac{3}{4c^3}\int_{-c}^{c}(c^2-\xi^2)\boldsymbol{\mathcal{G}}(\boldsymbol{x}-\boldsymbol{x}_{\beta}-i\xi\boldsymbol{p}_{\beta})\,d\xi\\ &-\boldsymbol{\mathcal{S}}_{\beta}^{h}\cdot\boldsymbol{\nabla}\cdot\frac{3}{4c^3}\int_{-c}^{c}(c^2-\xi^2)\left\{1+\frac{c^2-\xi^2}{8e^2}\nabla^2\right\}\boldsymbol{\mathcal{G}}(\boldsymbol{x}-\boldsymbol{x}_{\beta}-i\xi\boldsymbol{p}_{\beta})\,d\xi\Bigg],\end{aligned}\tag{4.11}$$

where N_d is the total number of discs and

$$\boldsymbol{\mathcal{S}}_{\beta}^{h}\equiv\frac{1}{2}\left(\frac{e^2}{2-e^2}\right)[(\boldsymbol{T}_{\beta}^{h}\times\boldsymbol{p}_{\beta})\boldsymbol{p}_{\beta}+\boldsymbol{p}_{\beta}(\boldsymbol{T}_{\beta}^{h}\times\boldsymbol{p}_{\beta})].\tag{4.12}$$

Substituting equation (4.11) into the equations (4.7) and (4.8), we get the far field mobility matrix $\boldsymbol{\mathcal{M}}^{\infty}$ which relates the generalized velocities $\boldsymbol{\mathcal{V}}$ to generalized forces $\boldsymbol{\mathcal{F}}^{h}$ as:

$$\boldsymbol{\mathcal{V}}\approx-\boldsymbol{\mathcal{M}}^{\infty}\cdot\boldsymbol{\mathcal{F}}^{h};\ \boldsymbol{\mathcal{V}}\equiv[\boldsymbol{V}_1\ldots\boldsymbol{V}_{N_d}\,\boldsymbol{\Omega}_1\ldots\boldsymbol{\Omega}_{N_d}]^T,\quad\boldsymbol{\mathcal{F}}^{h}\equiv[\boldsymbol{F}_1^{h}\ldots\boldsymbol{F}_{N_d}^{h}\,\boldsymbol{T}_1^{h}\ldots\boldsymbol{T}_{N_d}^{h}]^T\tag{4.13}$$

As the discs approach each other, the far field mobility matrix has to be supplemented with lubrication effects, which are dominant in the near contact configurations of the discs. The lubrication effects are preserved in the resistance formulation, which can be incorporated by inverting $\boldsymbol{\mathcal{M}}^{\infty}$ and adding the near-contact resistance matrix $\boldsymbol{\mathcal{R}}^{L}$ [131, 132]. We use a simple model to compute the localized lubrication interaction between the nearly touching discs [133–135]. The hydrodynamic lubrication force on disc α, nearly touching another disc β, is given by

$$\boldsymbol{F}_{\alpha\beta}^{L}=-\frac{6\pi\mu a[(\boldsymbol{V}_{\alpha}-\boldsymbol{V}_{\beta})\cdot\hat{\boldsymbol{\epsilon}}_{\alpha\beta}]}{8\sqrt{1-(\Gamma\boldsymbol{p}_{\alpha}\cdot\boldsymbol{p}_{\beta})^2}}\left(\frac{a}{|\boldsymbol{\epsilon}_{\alpha\beta}|}-\frac{1}{\Delta_c}\right)\hat{\boldsymbol{\epsilon}}_{\alpha\beta},\quad\Gamma\equiv\frac{a^2-b^2}{a^2+b^2},\tag{4.14}$$

where $\Delta_c=2/3$ is the critical value below which the lubrication forces (4.14) are computed [134, 135]. Here $\hat{\boldsymbol{\epsilon}}_{\alpha\beta}=\boldsymbol{\epsilon}_{\alpha\beta}/|\boldsymbol{\epsilon}_{\alpha\beta}|$ and $\boldsymbol{\epsilon}_{\alpha\beta}$ is the minimum separation vector between disc α and β which can be computed by a simple extension of the method by [132], explained in the appendix C. The near-contact resistance matrix $\boldsymbol{\mathcal{R}}^{L}$ is computed by summing over the lubrication forces between the discs for which the minimum separation is less than Δ_c. Therefore, the mobility matrix $\boldsymbol{\mathcal{M}}$ constructed by taking into account the far field hydrodynamic interactions and near contact lubrication effects is given by

$$\boldsymbol{\mathcal{V}}\approx\boldsymbol{\mathcal{M}}\cdot\boldsymbol{\mathcal{F}},\quad\boldsymbol{\mathcal{M}}\equiv[(\boldsymbol{\mathcal{M}}^{\infty})^{-1}+\boldsymbol{\mathcal{R}}^{L}]^{-1}.\tag{4.15}$$

Here, $\mathcal{F} = -\mathcal{F}^h$ represents the generalized external force, which in our case consists solely of buoyancy-corrected weights, $\boldsymbol{F}^g$, for each disc, with zero torques. Although the lubrication force mitigates violent particle approaches, numerical time-stepping can still cause unphysical particle overlap, which is generally prevented by incorporating repulsive near-contact forces [134, 136–139]. We therefore use a generalized external force $\mathcal{F}$ obtained by supplementing the buoyancy-corrected weight $\boldsymbol{F}^g$ of each disc with a repulsive near-contact force [137, 139]

$$\boldsymbol{F}^r_{\alpha\beta} = f_* e^{-\tau|\epsilon_{\alpha\beta}|}\hat{\boldsymbol{\epsilon}}_{\alpha\beta}. \tag{4.16}$$

Based on test runs, we choose $\tau = 80/a$ and $f_* = 50$ in the simulations. The choice of a large coefficient in τ ensures that the repulsive force is only active when two particles get extremely close, and, together with the choice of a large f_*, is operational only to prevent overlap of particles.

4.4 Validation of the dynamics

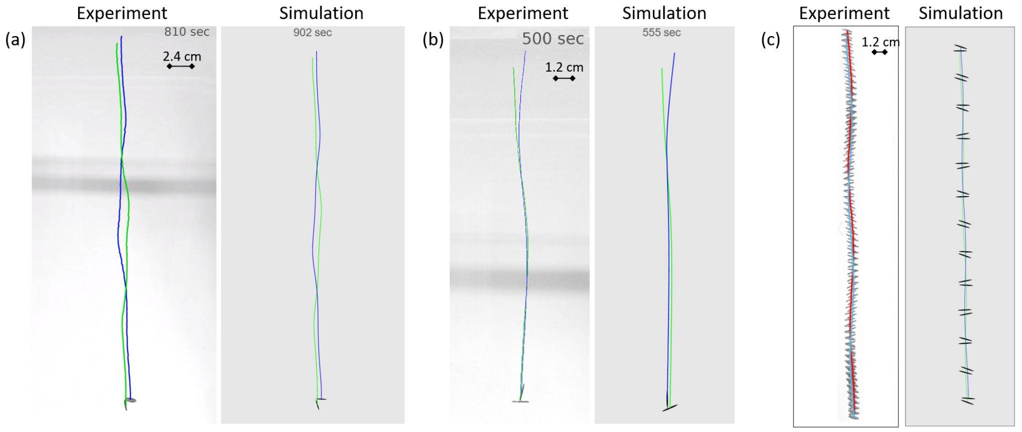

Figure 4.3: Comparison between experiments and simulations of pairs of discs sedimenting close to each other. (a) A bounded periodic oscillation of discs, categorized under 'rocking dynamics' in Chajwa, Menon, and Ramaswamy [94]. (b) 'Hydrodynamic screening' where one falling disc enters the 'hydrodynamic shadow' of the other, forming a '⊥' structure. This '⊥' configuration is often observed, both experimentally and through simulations, in a one-dimensional lattice of sedimenting discs. (c) Another case of 'rocking dynamics', arising from the linear instability of an equilibrium configuration forming an '=' shape.

The mobility matrix $\mathcal{M}$ accounts for both far-field hydrodynamic interactions and near-contact lubrication effects, but omits higher-order effects coming from the second reflection and logarithmic corrections in the lubrication forces, which may not always be negligible. We also emphasize that while we use the Greens function for an unbounded flow, we are comparing results from experiments performed in a container. As mentioned before, the presence of walls is modelled by cutting off the interaction range. The details of the cutoff are mentioned in the subsequent sections. The current approximation adequately captures the qualitative features of the cluster formation observed in our experiments. The rationale for approximating the wall effects in a minimal way but accounting for the method of reflections and lubrication comes from the fact that we are interested in the nature of cluster formations, which involves close-range dynamics of discs. One could account for wall effects by placing image singularities beneath the walls, but those effects would come in at $\sim O(a/D)$, where $D \approx 12.5a$ is the thickness of the container. Therefore, as long as a given disc has neighbours within a distance of D/a, the dominant contribution to the dynamics will be from the neighboring discs, rather than the wall effects. We therefore expect that higher-order corrections and wall effects would primarily improve quantitative aspects, such as sedimentation velocities, but approaching such a precision is beyond the scope of this work. Our simulation model does not completely capture all the late-time dynamics of cluster evolution seen in our experiments. Specifically, while pairs of discs that settle into a '⊥' structure largely maintain this configuration thereafter in simulations, experimental observations show that only a few discs retain the '⊥' arrangement for significantly longer after pairing. However, in experiments involving isolated disc pairs, the long-term stability of the '⊥' structure has been confirmed (see figure 4.3)(b). In any case, our analysis focuses on cluster formation, and we refrain from drawing conclusions about their late-time evolution based on our simulations.

Figure 4.3(a) demonstrates that our model successfully captures near-contact periodic oscillations, along with the phenomenon of 'hydrodynamic screening' shown in Figure 4.3(b), where one disc enters the 'hydrodynamic shadow' of another, forming a '⊥' structure. The initial configuration for figure 4.3(a) is: $\boldsymbol{x}_{21} = \{0.68, 0, 1.18\}$, $\boldsymbol{p}_1 = \{-0.04, 0, 0.99\}$ and $\boldsymbol{p}_2 = \{0.946, 0, 0.324\}$. Figure 4.3(b) has the initial configuration: $\boldsymbol{x}_{21} = \{1.5, 0, 1.813\}$, $\boldsymbol{p}_1 = \{0.879, 0, 0.476\}$ and $\boldsymbol{p}_2 = \{0.965, 0, -0.26\}$. It may be noticed from the figure that quantitative details, such as the time it takes for the discs to fall through the same distance in experiments and simulations, differ. An interesting case is that of the 'rocking dynamics' [94] shown in Figure 4.3(c). These dynamics can be viewed as the evolution of perturbations from a steady-state configuration in which the discs are vertically stacked, with their symmetry axes aligned along gravity, forming an '=' shape. This enables a linear stability analysis of such a structural arrangement, which we shall perform in the following subsection, revealing that at least the first reflection is essential to capture the periodic oscillations characteristic of the rocking dynamics, a phenomenon that the point-force approximation (equations (4.1) and (4.2)) fails to predict at small separations.

4.4.1 Stability analysis of the horizontal pair configuration

The configuration where both discs are horizontal, and one lies above the other at a vertical distance of z^* times the size of the disc a, is studied in this subsection in some detail, because it is a canonical example of pair interactions, and because it analytically demonstrates the inability of the point force approximation to accurately capture close-range dynamics. The rocking dynamics shown in figure 4.3(c) are periodic oscillations in the orientations and positions of the pair of discs about the '=' configuration represented by $(|\boldsymbol{p}_1 \cdot \boldsymbol{g}|, |\boldsymbol{p}_2 \cdot \boldsymbol{g}|) = (1, 1)$. Here $\boldsymbol{g}$ is a unit vector along gravity (along the $-z$ direction). The '=' configuration is a fixed point in the frame falling with the pair of discs. The system is non-dimensionalized using the semi-major axis a of the discs as the length scale and $\tau_p = 6\pi\mu a^2/F$ as the time scale, where F is the buoyancy-corrected weight of the spheroids. We shall henceforth work with dimensionless quantities, unless stated otherwise. Let the position of the disc 2 (upper disc) relative to disc 1 (lower disc) be given by $(\delta x, z^* + \delta z)$ and their corresponding orientation vectors be given by: $\boldsymbol{p}_1 = (\cos(\pi/2 + \delta\theta_1), \sin(\pi/2 + \delta\theta_1))$ and $\boldsymbol{p}_2 = (\cos(\pi/2 + \delta\theta_2), \sin(\pi/2 + \delta\theta_2))$; with their fixed point position and orientations being $(0, z^*)$ and $\boldsymbol{p}_1^* = \boldsymbol{p}_2^* = (0, 1)$, respectively. The dynamics of the pair, using the first reflection, leads to the following linear stability analysis:

$$\frac{d}{dt}\begin{pmatrix}\delta x\\ \delta\theta_1\\ \delta\theta_2\end{pmatrix} = \mathcal{B}_{R_1}\begin{pmatrix}\delta x\\ \delta\theta_1\\ \delta\theta_2\end{pmatrix}; \quad \mathcal{B}_{R_1} = \begin{pmatrix}0 & \kappa_0(e) & -\kappa_0(e)\\ J_1 & J_2 & J_3\\ -J_1 & -J_3 & -J_2\end{pmatrix}, \tag{4.17}$$

where

$$\kappa_0(e) \equiv \left(\frac{1}{Y^A} - \frac{1}{X^A}\right), \tag{4.18}$$

$$J_1 \equiv \frac{-3}{4}\int_{-1}^{1}\frac{3}{8}d\xi_1\int_{-1}^{1}d\xi_2\frac{1-\xi_1^2}{\xi_0^3}\left\{1 - \frac{e^2}{2-e^2}\left[-3 + \frac{24\kappa_1}{\xi_0^2}\right]\right\}, \tag{4.19}$$

$$J_2 \equiv \frac{-3}{4}\int_{-1}^{1}\frac{3}{8}d\xi_1\int_{-1}^{1}d\xi_2\frac{1-\xi_1^2}{\tilde{\xi}_0^3}\left\{ie\xi_1-\frac{e^2}{2-e^2}\left[(z^*+ie\xi_2)\left(-3+\frac{30\kappa_1}{\tilde{\xi}_0^2}\right)\right.\right.$$
$$\left.\left.-\frac{6\kappa_1(2z^*-ie\xi_1+2ie\xi_2)}{\tilde{\xi}_0^2}\right]\right\}, \quad (4.20)$$

and

$$J_3 \equiv \frac{-3}{4}\int_{-1}^{1}\frac{3}{8}d\xi_1\int_{-1}^{1}d\xi_2\frac{1-\xi_1^2}{\tilde{\xi}_0^3}\left\{-1+\frac{e^2}{2-e^2}\left[-3+\frac{24\kappa_1}{\tilde{\xi}_0^2}\right]\right\}ie\xi_2. \quad (4.21)$$

For shorthand notation, we define the following quantities appearing in integrands:

$$\tilde{\xi}_0 \equiv \sqrt{(z^*+ie(\xi_2-\xi_1))^2} \quad \text{and} \quad \kappa_1 \equiv \frac{3/2-\xi_1^2-\xi_2^2}{4}. \quad (4.22)$$

The vertical perturbation δz appears only at second order in the algebra, and therefore does not feature in the linear stability analysis. The corresponding Jacobian matrix of the perturbation evolution in the point force limit, obtained from equations (4.1) and (4.2), is given by

$$\mathcal{B}_{pt} = \begin{pmatrix} 0 & \kappa_0(e) & -\kappa_0(e) \\ \frac{-3}{4z^3}\left[1+\frac{3e^2}{2-e^2}\right] & \frac{-3}{4z^2}\left[\frac{3e^2}{2-e^2}\right] & 0 \\ \frac{3}{4z^3}\left[1+\frac{3e^2}{2-e^2}\right] & 0 & \frac{3}{4z^2}\left[\frac{3e^2}{2-e^2}\right]. \end{pmatrix} \quad (4.23)$$

Under the first reflection approximation, the eigenvalues of $\mathcal{B}_{R_1}$ are purely imaginary for any z^* and hence the linear dynamics is periodic about the '=' configuration. The oscillation frequency of this rocking dynamics is shown in Figure 4.4. The point force approximation, on the other hand, leads us to the incorrect conclusion that the fixed point '=' is a saddle below a certain value of $z = z_c$, given by

$$z_c \equiv \left[\frac{16}{27}\left(\frac{2+e^2}{e^4}-1\right)\kappa_0(e)\right]^{-1}. \quad (4.24)$$

A linear stability analysis using the point force approximation thus cannot predict the rocking dynamics seen in the experiment for small disc separations, which shows that the first reflection correction is crucial in this regime. Note that z^* is bounded below by $2b/a$, which corresponds to the case where the discs just touch.

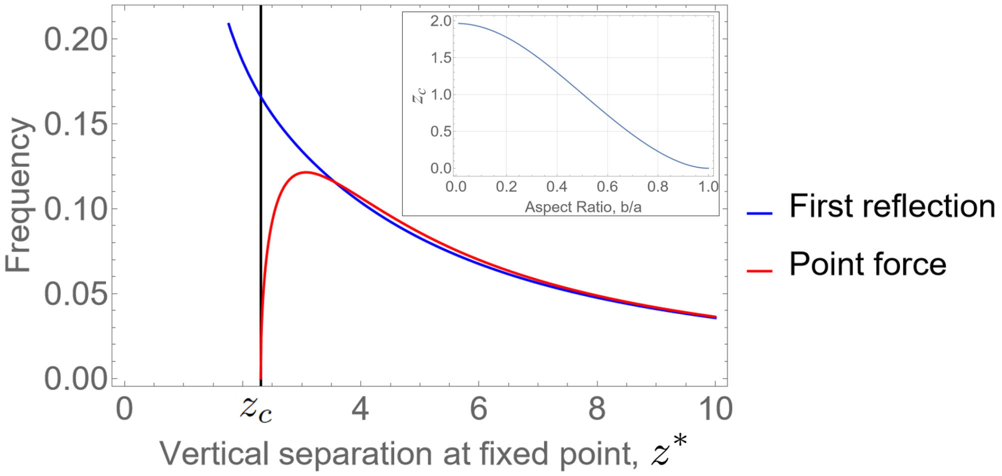

Figure 4.4: The frequency of oscillations in the rocking dynamics about the vertically stacked, or '=' configuration, as a function of vertical separation z^* at the fixed point. The aspect ratio here is $b/a = 0.125$, which is close to our experimental discs. The black vertical line denotes $z = z_c$ below which the point force approximation fails to predict the rocking dynamics. The inset shows the dependence of the z_c on the aspect ratio.

4.5 Planar dynamics of a one-dimensional lattice of sedimenting discs

In this section, we study the sedimentation dynamics of a regular one-dimensional lattice of identical spheroids, with their symmetry axes aligned with the horizontal. The corresponding problem for spheres was studied by Crowley [47], who established that any arbitrary perturbation in the initial positions of the spheres will always grow exponentially, i.e., the system is always unstable. Crowley also proposed a mechanism to explain the growth of perturbations, which leads to the formation of clumps of spheres. Chajwa et al. [48] investigated the planar sedimentation dynamics of a regular one-dimensional lattice of identical spheroids, both experimentally as well as theoretically, and showed, in contrast to spheres, that a system of spheroids is not always exponentially unstable: there is a regime where linear perturbations display algebraic rather than exponential growth. In the algebraically growing regime, Chajwa et al. [48] found that the modal perturbations are neutrally stable.

The analysis presented in Chajwa et al. [48] was based on the point force approximation (see equations (4.1) and (4.2)) with nearest-neighbour interactions. In this section, we show that this picture is crucially modified when we take into account more accurate hydrodynamic interactions through the first reflection. We find that the qualitative behaviour of modes changes from pure oscillations to weak exponential growth – the sharp boundary between these two regions is lifted, and the growth rate changes smoothly over the entire regime rather than becoming strictly zero.

For ease of distinguishing, we refer to clusters of three or more spheroids as clumps, and clusters of two spheroids as pairs. Visuals of disc clusters reveal that when clustering occurs, clumping takes place in the valleys when the Crowley mechanism dominates over the drift mechanism (figure 4.5). However, when the drift mechanism is stronger than the Crowley mechanism, there are no clumps, but pairing occurs away from the valley. Pairs typically take on a '⊥' shape, see figure 4.6.

To numerically investigate the distinction between clumps and pairs, as observed in the experiments, we use two different lattice spacings and wavenumbers, as indicated by the two coloured dots in the figure 4.7. The simulations are conducted by solving equation (4.15) as a system of ordinary differential equations using the Runge-Kutta-Fehlberg method for time integration [140]. Adaptive time stepping is employed with an error tolerance of 10^{-4} and a maximum step size of 0.1. In the Crowley-mechanism-dominated regime with lattice spacing $\tilde{d} = 1.875$ and dominant perturbation wavenumber $q = \pi/6$ (red dot in figure 4.7), the resulting clumps formed at the valleys are shown in figure 4.5. In the drift-mechanism-dominated regime with lattice spacing $\tilde{d} = 3.75$ and dominant perturbation wavenumber $q = \pi/2$ (green dot in figure 4.7), pairwise clumping is observed as shown in figure 4.6.

There are three degrees of freedom per disc: the horizontal position x_α of disc α, its vertical position z_α, and its orientation angle θ_α with respect to the horizontal (x) axis. About the fixed point $\tilde{d}(\mathbb{Z}, 0, 0)$[1], $\tilde{d}$ being the dimensionless lattice spacing, non-dimensionalized using the disc radius a, an infinitesimal perturbation of the disc $\alpha \in \mathbb{Z}$ is given by $(\hat{x}_q(t), \hat{z}_q(t), \hat{\theta}_q(t))e^{iq\alpha}$, where q is the dimensionless perturbation wavenumber. Under the first reflection and nearest-neighbour interactions, this perturbation evolves as

$$\frac{d}{dt}\begin{bmatrix}\hat{x}_q\\ \hat{z}_q\\ \hat{\theta}_q\end{bmatrix} = \mathcal{A}_{R_1}\begin{bmatrix}\hat{x}_q\\ \hat{z}_q\\ \hat{\theta}_q\end{bmatrix}; \quad \mathcal{A}_{R_1} \equiv \begin{bmatrix}0 & I_{12} & \kappa_0(e) + I_{13}\\ I_{21} & 0 & 0\\ I_{31} & 0 & 0\end{bmatrix}, \tag{4.25}$$

---

[1] This fixed point is in the frame of reference falling with the average terminal velocity of the undisturbed lattice.

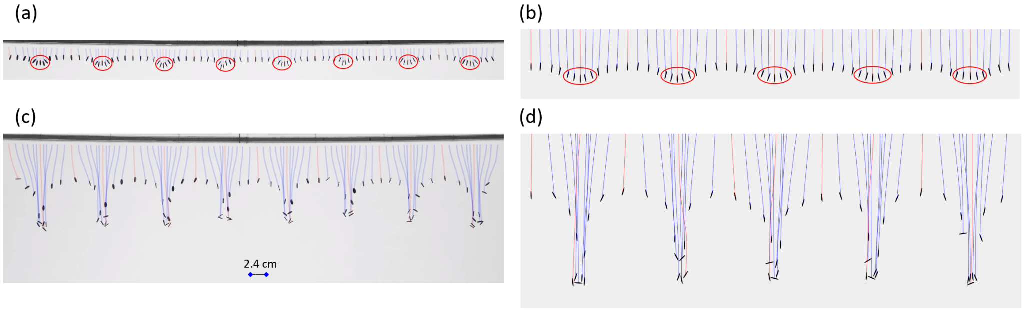

Figure 4.5: Experiments [(a) and (c)], and simulations [(b) and (d)] showing clumping due to the Crowley mechanism. [(a) and (c)] are aligned vertically, as are [(b) and (d)], to highlight that the locations where the clumps form correspond to the red ovals in (a) and (b). The lattice spacing and the dominant perturbation wavenumber are $\tilde{d} = 1.875$ and $q = \pi/6$, respectively. (a) and (b) show early evolution ($t \sim 5$). The valleys, marked by red ovals, represent regions where the discs begin to clump together. (c) and (d) show late time evolution ($t \sim 15$). Clumps, occurring at the valleys, consist of three or more discs.

where κ_0 is given by equation (4.18). The terms in the matrix $\mathcal{A}_{R_1}$ are given by

$$I_{12} \equiv \frac{3}{2}\int_{-1}^{1}\frac{1}{2}d\xi_1\int_{-1}^{1}\frac{1}{2}d\xi_2 i\sin q\frac{ie\xi_{12}-\tilde{d}}{\xi_0^3}\left[1-\frac{6\kappa_2}{\xi_0^2}\right], \tag{4.26}$$

$$I_{21} \equiv -\frac{3}{2}\int_{-1}^{1}\frac{1}{2}d\xi_1\int_{-1}^{1}\frac{1}{2}d\xi_2 i\sin q\frac{ie\xi_{12}-\tilde{d}}{\xi_0^3}\left[1+\frac{6\kappa_2}{\xi_0^2}\right], \tag{4.27}$$

$$I_{13} \equiv -\frac{3}{2}\int_{-1}^{1}\frac{1}{2}d\xi_1\int_{-1}^{1}\frac{1}{2}d\xi_2 ie[\xi_1-\xi_2\cos(q)]\frac{ie\xi_{12}-\tilde{d}}{\xi_0^3}\left[1-\frac{6\kappa_2}{\xi_0^2}\right], \tag{4.28}$$

$$I_{31} \equiv \frac{3}{2}\int_{-1}^{1}\frac{3}{8}d\xi_1\int_{-1}^{1}d\xi_2\frac{1-\xi_1^2}{\xi_0^3}\left\{[1-\cos(q)]\left(-2+\frac{6e^2\kappa_1}{(2-e^2)\xi_0^2}\right)+\frac{30e^2\kappa_1}{(2-e^2)\xi_0^2}\frac{i\sin q}{(ie\xi_{12}-\tilde{d})}\right\}, \tag{4.29}$$

where $\xi_{12} \equiv \xi_1-\xi_2$, $\xi_0 \equiv \sqrt{(ie\xi_{12}-\tilde{d})^2}$ and $\kappa_2 \equiv (2-\xi_1^2-\xi_2^2)/4$. The eigenvalues of $\mathcal{A}_{R_1}$ are $\{0, \sigma+i\omega, -\sigma-i\omega\}$ where σ represents the growth rate of perturbations, and ω denotes the oscillation frequency. The structure of the eigenvalues ensures that the system is always unstable provided $\sigma \neq 0$.

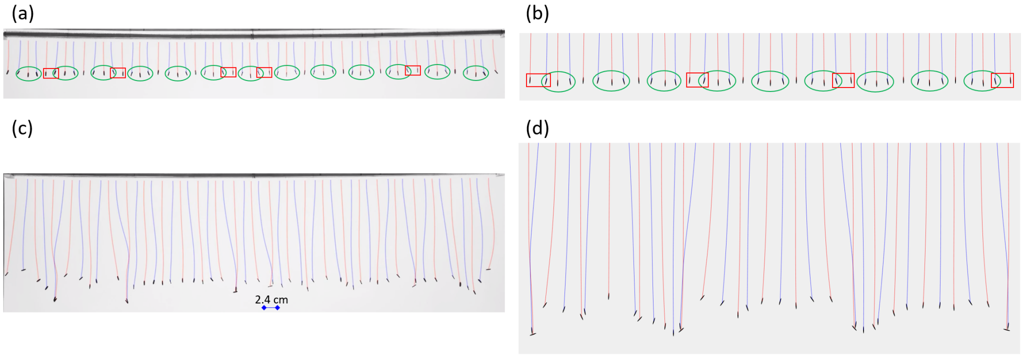

Figure 4.6: Experiments [(a) and (c)], and simulations [(b) and (d)] showing pairing due to the drift mechanism. [(a) and (c)] are aligned vertically, as are [(b) and (d)], to highlight that the locations where the pairs form correspond to the red boxes in (a) and (b). The lattice spacing and the perturbation wavenumber are $\tilde{d} = 3.75$ and $q = \pi/2$ respectively. (a) and (b) show initial evolution ($t \sim 20$). The valleys are highlighted with green ovals, while the discs that ultimately pair up are enclosed within red rectangular boxes and are seen to be located away from the valleys. (c) and (d) show late time evolution ($t \sim 45$). There is pairing but no clumping, and pairing dynamics is characterized by two discs coming together in the form of a '⊥', or inverted 'T'.

On the other hand, under the point-force approximation, the corresponding Jacobian matrix $\mathcal{A}_{pt}$ for the evolution of perturbations is given by [48]

$$\mathcal{A}_{pt} \equiv \begin{bmatrix} 0 & \frac{-3i \sin q}{2\tilde{d}^2} & \kappa_0(e) \\ \frac{3i \sin q}{2\tilde{d}^2} & 0 & 0 \\ \frac{-6 \sin^2 q/2}{\tilde{d}^3} & 0 & 0 \end{bmatrix}. \tag{4.30}$$

For a given wavelength, the point-force approximation predicts a neutrally stable regime characterized by a zero growth rate beyond a critical lattice spacing $\tilde{d}_c$, given by

$$\tilde{d}_c = \frac{3}{8\kappa_0(e)} \frac{\sin^2 q}{\sin^2 q/2}. \tag{4.31}$$

Figure 4.7 shows the logarithm of the growth rate of perturbations as a function of lattice spacing $\tilde{d}$ and perturbation wavenumber q. While the point-force approximation predicts zero growth rate above the red curve, the first reflection has a small but finite growth rate at high lattice spacings. The growth rate shows a power law behaviour $d^{-\gamma}$ for large lattice spacing with the dependence of the power on the wavenumber shown in figure 4.8. One must interpret this power law with caution, as wall effects may alter the exponent. This requires the lattice spacings in the power-law regime to be smaller than the container thickness. Numerical

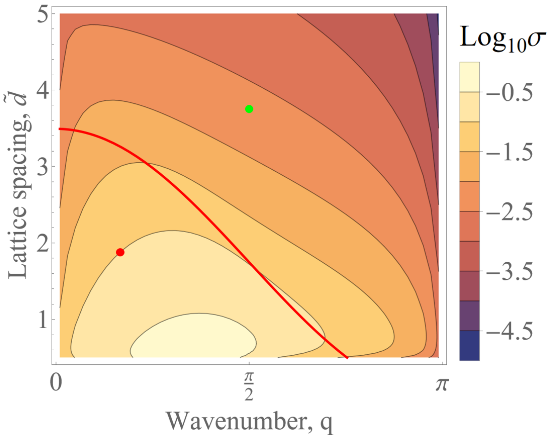

Figure 4.7: Contour plot of the log of the growth rate σ (the only positive real part among the eigenvalues of $\mathcal{A}_{R_1}$) for aspect ratio $b/a = 0.125$. The red curve denotes the critical lattice spacing $\tilde{d}_c$ above which the point force approximation [48] predicts neutral stability. The nonlinear evolution corresponding to the red dot, where $(q, \tilde{d}) = (\pi/6, 1.875)$ and the green dot, where $(q, \tilde{d}) = (\pi/2, 3.75)$, were shown to support clustering and pairing respectively (figures 4.5 and 4.6).

data show that the scaling exponent in the large-d limit is best fit by $\gamma \approx -4.5$ across perturbation wavenumbers, for a large range of spheroids with aspect ratios ranging from 0.19 to 0.8.

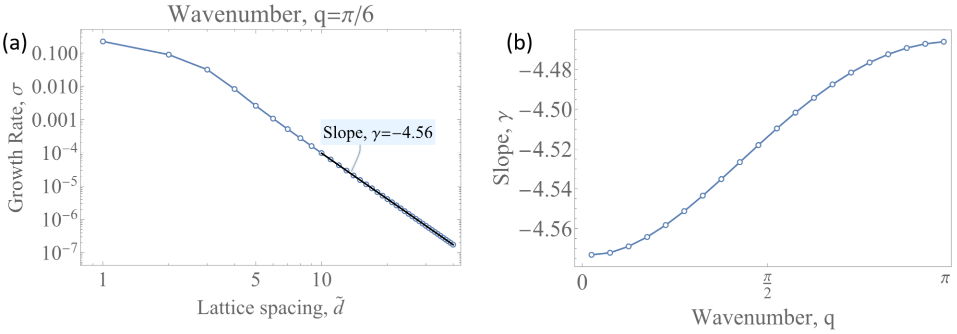

Figure 4.8: (a) Perturbation growth rate σ as a function of the lattice spacing for a wavenumber $q = \pi/6$ and aspect ratio $b/a = 0.125$. For large lattice spacing $\tilde{d}$, the growth rate shows a power law behaviour $\sigma \sim \tilde{d}^{\gamma}$ with $\gamma \approx -4.5$. (b) The variation of the exponent γ with wavenumber q. Note that for a lattice of spheres, the growth rate decays much more slowly, as $\sigma \sim \tilde{d}^{-2}$ for all wavenumbers.

The first reflection thus shows a qualitative change in the stability of the system as compared to the point-force approximation: the system is now linearly unstable at any lattice spacing, although with a growth rate that approaches zero with increasing spacing. An examination of the point-force approximation shows that this is to be expected. The non-normality of $\mathcal{A}_{pt}$ provides for a possible

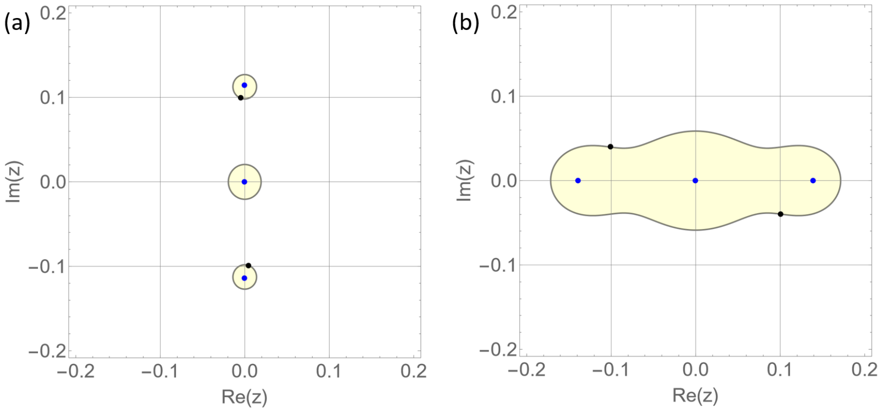

Figure 4.9: ε-pseudospectrum $\sigma_\varepsilon(\mathcal{A}_{pt})$ of $\mathcal{A}_{pt}$ for the aspect ratio $b/a = 0.125$. The blue dots denote the eigenvalues of $\mathcal{A}_{pt}$ and the black dots denote the eigenvalues of $\mathcal{A}_{R_1}$. The matrix perturbation size ε leads to the spreading of eigenvalues inside the yellow regions. The values of ε are chosen so that the black dots lie at the boundary of the yellow regions, indicating that the first reflection corrections to $\mathcal{A}_{pt}$ are of the order of ε. a) $\varepsilon = 4.8 \times 10^{-3}$ for the set of parameters $(q, \tilde{d}) = (\pi/2, 3.75)$ (green dot in figure 4.7) b) $\varepsilon = 1.2 \times 10^{-2}$ for the set of parameters $(q, \tilde{d}) = (\pi/6, 1.875)$ (red dot in figure 4.7). Note that the pseudospectra are much larger than ϵ.

large change in eigenvalues for a small perturbation in the stability operator ($\mathcal{A}_{pt}$ becoming $\mathcal{A}_{R_1}$). Since in the neutral regime the eigenvalues of $\mathcal{A}_{pt}$ lie on the imaginary axis, its pseudospectrum must protrude into the positive real axis, and $\mathcal{A}_{R_1}$ is a member of the pseudospectrum of $\mathcal{A}_{pt}$ which produces instability. The ε-pseudospectrum $\sigma_\varepsilon(\mathcal{A}_{pt})$ of $\mathcal{A}_{pt}$ is defined as [141]:

$$\sigma_\varepsilon(\mathcal{A}_{pt}) \equiv \{z \in \mathbb{C} : ||(z - \mathcal{A}_{pt})^{-1}|| > \varepsilon^{-1}\}. \tag{4.32}$$

Figure 4.9(a) and (b) show the pseudospectra of $\mathcal{A}_{pt}$ corresponding to the conditions of figures 4.5 and 4.6, respectively. In each case, ε is chosen such that the largest eigenvalue of $\mathcal{A}_{R_1}$ lies on the boundary of the pseudospectrum. While the oscillation frequency remains close to its original value, a non-zero growth rate appears, which changes the dynamics qualitatively. Therefore, in the drift regime (green dot in figure 4.7), the first reflection correction has a gentle destabilizing effect. In contrast to this, the first reflection has a significant stabilizing effect in the Crowley regime, and lies on a larger ε-pseudospectrum in figure 4.9(b). The net growth rate remains positive (red dot in figure 4.7).

With the first reflection bringing a qualitative change in the nature of stability, one may surmise that modeling wall effects beyond a simple nearest neighbor cutoff may lead to further qualitative change. This is not the case because the qualitative change occurred due to the structural instability of the system described by $\mathcal{A}_{pt}$: the eigenvalues lie exactly on the imaginary axis. With the first reflection, these eigenvalues are nudged off the imaginary axis, leading to a qualitative change. Inclusion of wall effects using image singularities might further nudge the eigenvalues, but they are not primarily responsible for the qualitative change already brought in by the more dominant first-reflection effects.

If only eigenvalue-based growth were in play, the extremely slow growth rate for large lattice spacing would contribute negligibly to perturbation growth during the time of our simulations. However, a large algebraic transient growth of the perturbations happens in this regime, due to the non-normal nature of $\mathcal{A}_{R_1}$. To highlight this, we look at the matrix norm of $e^{\mathcal{A}_{R_1} t}$ for time $t \in [0, 2\pi/\omega]$, where ω is the oscillation frequency given by the imaginary parts of non-zero eigenvalues of $\mathcal{A}_{R_1}$, see figure 4.10. The maximum non-modal growth can be quantified by the quantity G_r defined as:

$$G_r \equiv \frac{||e^{\mathcal{A}_{R_1} t^*}||^2}{e^{2\sigma t^*}}; \quad t^* \equiv \underset{t \in [0, 2\pi/\omega]}{\arg\max} ||e^{\mathcal{A}_{R_1} t}||, \tag{4.33}$$

where σ is the growth rate given by the real parts of eigenvalues of $\mathcal{A}_{R_1}$, and the matrix norm can be obtained using the singular value decomposition. Figure 4.10 shows the logarithm of G_r as a function of lattice spacing $\tilde{d}$ and perturbation wavenumber q. By definition $\log(G_r) \geq 0$. In the drift regime, the lattice is disrupted on the time scale t^*.

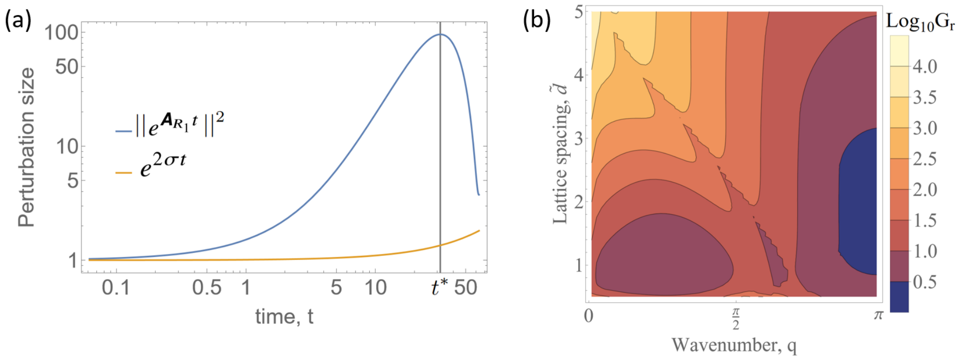

Figure 4.10: (a) Time evolution of the matrix norm of $e^{\mathcal{A}_{R_1} t}$ and the exponential growth $e^{2\sigma t}$ for the aspect ratio $b/a = 0.125$. The non-normal nature of $\mathcal{A}_{R_1}$ leads to transient growth of non-modal perturbations, which can be much larger than the exponential growth. The parameters $(q, \tilde{d})$ used to calculate $\mathcal{A}_{R_1}$ correspond to the green dot in figure 4.7. The non-modal growth reaches its maximum at time $t = t^*$. (b) Contour plot of the $\log_{10}$ of G_r defined in equation (4.33). In regimes of small $\log_{10}(G_r)$, the growth is exponential but very slow. Large values of $\log_{10}(G_r)$ indicate that transient algebraic growth will dominate.

4.5.1 Distinct clumping mechanisms in the exponential and algebraic growth regimes

As explained in Chajwa et al. [48], there are two mechanisms at play that decide the nature of clustering. The Crowley mechanism acts to form clumps at the valleys while the drift mechanism counteracts it (see figure 4.1). The fast decay of growth rate with increased lattice spacing (see figure 4.8) is because of the drift mechanism competing better against the Crowley mechanism. For a lattice of spheres, the drift mechanism is absent, and the growth rate follows $\sigma \sim \tilde{d}^{-2}$ for large lattice spacing $\tilde{d}$. In contrast, for increasingly flatter oblate ellipsoids, the growth rate is best fit by $\sigma \sim \tilde{d}^{-4.5}$, as shown in Figure 4.8.

Our objective is to develop a statistical measure that can differentiate between clustering in the Crowley regime and the drift regime. The drift mechanism leads to aggregation in pairs, whereas in the Crowley regime, a larger number of discs participate in forming an aggregate, thus suggesting $P_s(t)$, the fraction of particles participating in aggregates of size s, as a useful quantitative measure. Discs that are within a distance of $0.5a$ of each other are defined to be part of an aggregate. We conduct 500 simulations in both the Crowley and the drift regimes, each involving a lattice of 60 discs with periodic boundary conditions along the horizontal (x) direction. Each disc interacts with eight neighbors on either side. Changing the number of neighbors about this cutoff scale does not affect cluster sizes and types, provided there is a sufficient number of discs interacting with their neighboring ones upon spatial rearrangement as the system evolves. Although the effect of a distant disc [2] is weaker than that of the walls, the dynamics are primarily governed by the nearest neighbours. Thus, including the eighth disc while neglecting the wall effects has little impact, as both contribute marginally compared to the dominant influence of nearby discs. Each simulation is initialized with sinusoidal perturbations only in the x-direction, at a chosen dominant wavenumber, with amplitude $0.625a$, and additional random perturbations of amplitude $0.075a$, where a is the semi-major axis of the discs. The initial orientation angle is chosen from a uniform distribution of width 8 degrees. The amplitude of the perturbations and the noise in initial conditions emulate the perturbations in the experiments.

Figure 4.11 shows the time evolution in the Crowley regime of the fraction of discs participating in clusters of different sizes. The 500 samples are divided into 20 sub-samples, over which the mean and standard deviation are calculated. The most frequently occurring clump consists of four discs, while the largest clump contains five discs. Upon examination, we find no preferred relative orientations

---

[2] with the distance $r \gtrsim D/a$, $D \approx 12.5a$ being the thickness of the container

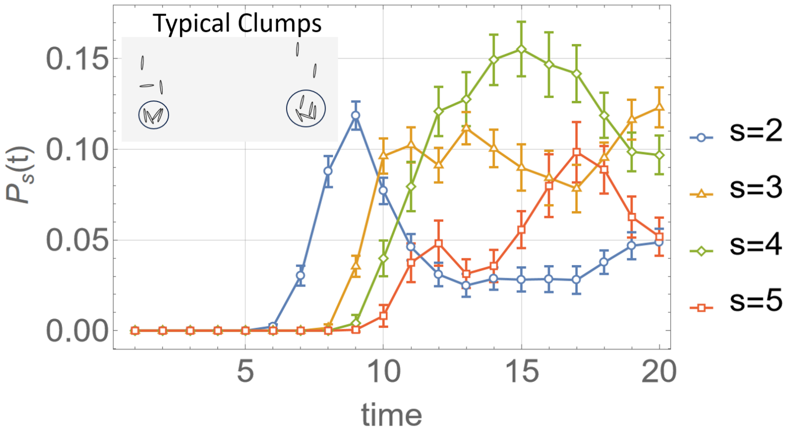

Figure 4.11: Probability distribution $P_s(t)$ as a function of non-dimensional time for different aggregate size s, in the Crowley regime $(q, \tilde{d}) = (\pi/6, 1.875)$. $P_s(t)$ is calculated as the ensemble average of the fraction of discs forming an aggregate of size s relative to the total number of discs in each ensemble. Discs that are within the distance of $0.5a$ are considered to be aggregated or clustered. The error bars represent the standard deviation.

among the discs within these clumps. A key characteristic of the drift regime is that pairing is by far the most frequent type of clustering observed. Each pair adopts a '⊥' shape (see figure 4.6). This is an instance of hydrodynamic screening, as discussed in section 4.4 and figure 4.3. With time, the paired discs separate out from the rest of the discs because they settle faster than isolated discs, usually without ever separating from each other. As a result, the fraction of pairs (or $s = 2$ aggregates) only increases with time, as shown in Figure 4.12. The relative orientation of a pair of discs is quantified by $\boldsymbol{p}_1 \cdot \boldsymbol{g}$ and $\boldsymbol{p}_2 \cdot \boldsymbol{g}$. Here, $\boldsymbol{g}$ is the gravity unit vector and $\boldsymbol{p}_1$ and $\boldsymbol{p}_2$ are respectively the orientations of the lower and upper disc of a pair. As previously mentioned, the discs come together in a '⊥' configuration, i.e. $(|\boldsymbol{p}_1 \cdot \boldsymbol{g}|, |\boldsymbol{p}_2 \cdot \boldsymbol{g}|) = (1, 0)$ as they begin to become a pair, as evident in figure 4.13. These '⊥' configurations, also observed in our experiments, are solely governed by two-body hydrodynamic interactions and are found to remain stable over time in numerical simulations. Although the experiments show the '⊥' signature at the time of pair formations, the pair orientations exhibit significant variability as the discs approach the base of the container. Given the uncertainty in the factors influencing the persistence of '⊥' structures in the experiments, we refrain from making conclusions about the late-time ($t \gtrsim 60$) dynamics and evolution of clustered pairs based on our simulations.

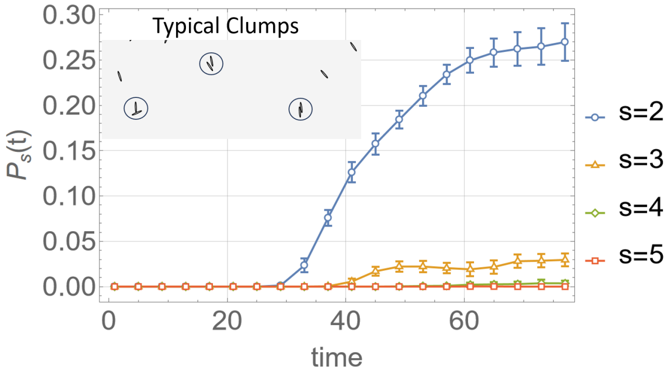

Figure 4.12: Probability distribution $P_s(t)$ as a function of non-dimensional time for different aggregate size s, in the drift regime $(q, \tilde{d}) = (\pi/2, 3.75)$. $P_s(t)$ is calculated as the ensemble average of the fraction of discs forming an aggregate of size s relative to the total number of discs in each ensemble. The pairs of discs separate out in a '$\perp$' configuration from the rest and keep on settling together, maintaining their orientations.

4.6 Formation of the $\perp$ shape

The phenomenon of pairing through drift merits attention as a distinctive property of the settling of non-spherical objects, ruled out for the Stokesian settling of two spheres. As two spheroids approach each other, they invariably rearrange themselves into a $\perp$ structure, both in our experiments and in our simulations. This process can be explained by a simple analysis similar to that of Koch and Shaqfeh [95] (see figure 1 in their paper). According to their description, the neighbors of a disc tend to align their 'thin' sides parallel to the direction of the extensional component of the flow generated by that disc. However, we point to a key difference coming from the vorticity disturbance due to the rotation of the spheroid. Consider a force monopole at the origin and a disc of radius a settling in its flow field at a radial distance r, with position $(x, 0, z)$. With contributions from both the vorticity and strain-rate of the flow produced by the monopole, it follows from equation (4.2) that the orientation of the disc $\boldsymbol{p} = (\cos\theta, 0, \sin\theta)$ evolves, to leading order in a/r as

$$\frac{d\theta}{dt} = \frac{3}{4r^2}\left[\cos\phi - \zeta \sin\phi \sin 2(\phi - \theta)\right]; \quad \zeta \equiv \frac{3e^2}{4 - 2e^2}. \tag{4.34}$$

Here $x = r\cos\phi$ and $z = r\sin\phi$. Equation (4.34) is non-dimensionalised using the same scales as described in section 4. Note that the first term on the right-hand side of equation (4.34) represents the vorticity contribution, and the second term represents the contribution of the strain-rate to the disc's rotation.

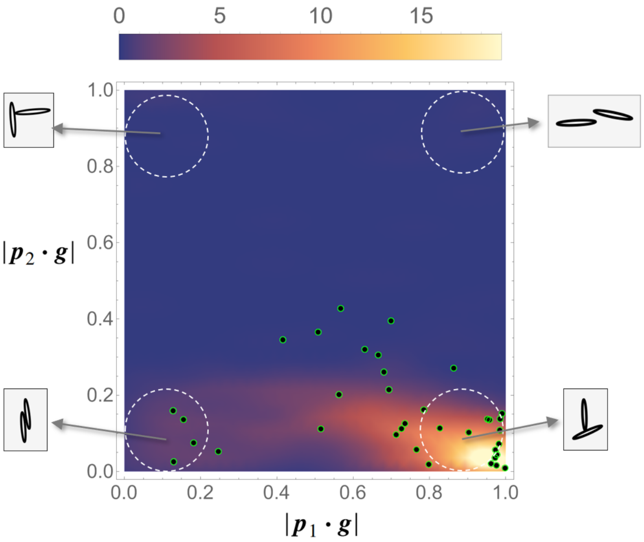

Figure 4.13: Probability density plot of orientations of pairs of discs in the drift regime $(q, \tilde{d}) = (\pi/2, 3.75)$. $\boldsymbol{p}_1$ refers to the orientation of disc 1, which is below disc 2, and $\boldsymbol{g}$ is the gravity unit vector. The black-green dots are experimentally observed orientations, and the background colour indicates the frequency of occurrence of a given pair of orientations in the simulations. A predominance of the '⊥' formation is seen in both experiments and simulations. The orientation statistics are acquired when the pairs start forming in the simulations, at a non-dimensional time of $t \sim 45$. This time is later than t^*, the time at which the non-normal growth reaches its maximum, as shown in Figure 4.10. The black-green dots, indicating experimental samples, are taken when pair formation is observed.

Now, without the vorticity contribution, one gets the stable orientations seen in the schematic figure 1 of Koch and Shaqfeh [95] and thereby an inward particle flux from all directions. In our study, both the vorticity and strain-rate contributions are crucial to the disc's rotation. To find the stable orientations while incorporating the vorticity contribution, we proceed by defining the angle

$$\beta \equiv \frac{1}{2} \arcsin \frac{\cot \phi}{\zeta}. \tag{4.35}$$

For any (r, ϕ), we set $d\theta/dt = 0$ in (4.34) to get the fixed point

$$\theta^* = \phi - \frac{n\pi}{2} - (-1)^n \beta, \quad n \in \mathbb{Z} \tag{4.36}$$

for the orientation angle θ. We can immediately see from (4.36) that solutions do not exist for all values of ϕ, which is a qualitatively distinct feature from the picture of Koch and Shaqfeh [95]. For $\Omega \equiv \arctan(1/\zeta)$, the solution for $d\theta/dt = 0$ is defined only for the values of ϕ in the intervals $(\Omega, \pi - \Omega)$ and $(\pi + \Omega, 2\pi - \Omega)$.

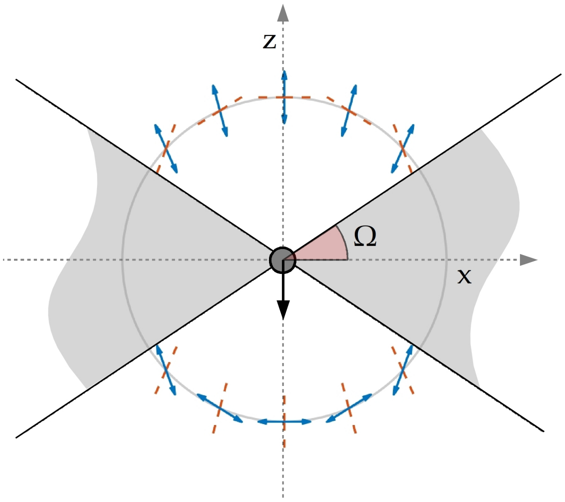

Figure 4.14: Stable orientations with both vorticity and strain-rate contributing to a disc's rotation: with a force monopole at the origin. Blue double-ended arrows and red-dashed lines are stable and unstable alignments of the thin side of the disc, respectively. The angle between stable and unstable orientations is $\pi/2 - 2\beta$. The shaded grey region represents the range of angles ϕ where there are no stable orientations, with $\Omega = \arctan(1/\zeta)$.

Even where the solution exists, we show below that the stable orientations are different from what one gets with just the strain-rate contribution.

We can study the stability by considering just the solutions $\theta_1^* = \phi - \beta$ and $\theta_2^* = \phi + \beta - \pi/2$, given the apolarity of discs. Perturbing the fixed points by small angles $\delta\theta_1$ and $\delta\theta_2$ respectively, substituting in (4.34) and Taylor expanding about the respective fixed points gives

$$\dot{\delta\theta}_k = (-1)^{k-1} \cos 2\beta \, \frac{3\zeta \sin\phi}{2\, r^2} \, \delta\theta_k, \quad k \in \{1, 2\}. \tag{4.37}$$

Since $\cos 2\beta > 0$, the fixed point θ_1^* is unstable in the upper half plane and stable in the lower half plane, and vice versa for the other fixed point θ_2^*.

To summarize, in the upper half-plane (when the disk is above the force monopole), the disc is stable with its orientation along the angle $\theta_2^* = \phi - \beta$. In the lower half-plane, the stable angle of the orientation is $\theta_1^* = \phi + \beta - \pi/2$. These stable orientations are shown in Figure 4.14 with blue arrows indicating the stable alignment of the thin side of the disc [3]. In both half-planes, solutions exist only with the azimuthal angle ϕ lying in the intervals $(\Omega, \pi - \Omega)$ and $(\pi + \Omega, 2\pi - \Omega)$, leaving out regimes shown as grey shaded region in figure 4.14, where there are no stable orientations.

---

[3] Note that the thin side of the disc is perpendicular to its orientation vector

With this picture in mind, we can explain the formation of '$\perp$' shapes as follows. For a pair of vertically separated settling discs, the force monopole flow created by the lower disc aligns the upper disc vertically, and that generated by the upper disc aligns the lower disc horizontally. Since a vertically aligned disc sediments more rapidly than a horizontal one, the upper disc catches up with the lower one, forming the '$\perp$' shape, frequently observed in disc pairs. In the drift regime, the lattice spacing is large enough, i.e., the system is dilute enough, for the above approximate analysis based on pair interactions and point-force flows to suffice. The absence of this '$\perp$' shape in the Crowley regime indicates that clusters in this regime are influenced by multi-particle interactions.

4.7 Conclusions

The slow collective sedimentation of discs is governed by two processes, the Crowley mechanism and orientation-dependent drift, whose competition was observed and the resulting stability problem studied in Chajwa et al. [48]. We have explored how these mechanisms lead to the disruption of a settling lattice of discs, creating two kinds of structures: clumps of several particles and pairs that remain together forever, respectively. We have shown that a satisfactory understanding of the near-contact dynamics of a pair of discs crucially requires the inclusion of the first-reflection contribution to their hydrodynamic interaction. We then analyzed the stability of a one-dimensional lattice of discs using the first reflection and contrasted it with the point force approximation used in the earlier work of Chajwa et al. [48]. Whereas the point force approximation predicts zero growth rate σ beyond a critical lattice spacing $\tilde{d}_c$, the first reflection shows that the configuration is unstable at all spacings, but is extremely weakly so at large lattice spacing $\tilde{d}$, with $\sigma \sim \tilde{d}^{-4.5}$, a much faster decay than in the case of spheres. Nevertheless, there are two regimes based on whether or not the Crowley mechanism overpowers the drift mechanism, which can be quantified by looking at the nature of clustering. In terms of perturbation growth, the Crowley regime leads to exponential growth while the drift regime shows transient algebraic growth, both of which eventually lead to the disruption of the lattice. The Crowley mechanism leads to clumping at the valleys of the disrupted lattice, while in the drift regime discs cluster in pairs, away from the valleys, forming '$\perp$' structures. These '$\perp$' configurations exemplify a type of hydrodynamic screening or shadowing, in which the upper disc descends vertically onto the lower disc, which has its flat side facing downward. These '$\perp$' structures are observed in both isolated disc pair experiments and one-dimensional disc lattices. In the isolated disc pair experiments, they demonstrate high stability and retain their configuration for an extended period. We have explained these structures through an analysis that builds on Koch and Shaqfeh [95]'s work by incorporating vorticity contributions to the rotation of the discs.

So far, we have seen how the clustering of a one-dimensional array of sedimenting spheroids is fundamentally different from spheres. Several directions for future investigation suggest themselves, and we mention a few. Studying the sedimentation of a specific arrangement provides a useful test bed for understanding how hydrodynamic effects operate at both single and multi-particle levels. But practical scenarios, like the settling of centric (*Coscinodiscus*) and pennate (*Pseudo-nitzschia*) diatoms in an algal bloom, often involve homogeneous suspensions of oriented particles, with clustering being crucial for 'marine snow' formation [142]. We may ask how clustering depends on the initial spatial distribution of non-spherical particles, especially in two and three dimensions. Secondly, our work has been restricted to the steady Stokes (zero Stokes number) limit. When the background fluid is turbulent, inertial particles, i.e., particles of non-zero Stokes number, are well known to form clusters even in the dilute limit where interparticle interactions are absent, see e.g. Bec [143], Monchaux, Bourgoin, and Cartellier [144], and Reade and Collins [145]. Our study indicates that a future theory that includes interparticle interactions in unsteady Stokes flow (finite Stokes number) is in order. During sedimentation, a single spheroid can only execute persistent drift at a constant speed. But this behaviour is seen only in a small fraction of anisotropic particles [146], which can exhibit settling, drifting, or quasiperiodic motion [38, 40, 42, 45, 46, 115]. Understanding how departures from spheroidal shape combine with hydrodynamic interactions among particles will yield interesting results relevant to ice formation in clouds and the clumping of marine snow.

5

Electrostatic Interactions Between Anisotropic Particles

> *"Fate only binds you if you let it.*
> *Do what is necessary, not because it is written."*
> *— Kratos, God of War Ragnarök*

This chapter is a verbatim reproduction of our article published in Physical Review E [147]. Minor formatting and notational changes have been made for consistency. I gratefully acknowledge my co-author, Professor Anubhab Roy, for his contributions to this work.

5.1 Introduction

Electrostatic interactions play a significant role in various natural and industrial processes, influencing behaviours across systems as diverse as atmospheric phenomena, biological assemblies, and colloidal suspensions [53, 148–151]. In atmospheric science, for example, electrostatic forces are integral to cloud formation, where charged particles, including ice crystals and droplets, cluster and interact in complex ways that impact precipitation and cloud evolution [53]. Even droplets bearing the same charge can coalesce due to electrostatic induction effects, enabling attraction through localized polarization despite net repulsion between like charges [74, 75]. This phenomenon, while extensively studied for simple geometries like spherical particles, is less understood in realistic cases involving anisotropic interactions and irregular shapes.

One of the simplest non-spherical shapes relevant in such studies is the spheroid, a shape commonly found in atmospheric ice crystals and approximations of biological and industrial particles. To better understand the interaction of such anisotropic objects, this study focuses on the electrostatic interaction between a conducting sphere and a spheroidal body. Specifically, this chapter presents the first known calculation of the electrostatic torque exerted on a spheroid by a nearby sphere, which represents a key contribution to modeling how such particles align and rotate under electrostatic forces. This torque, together with the corresponding interaction forces, could be incorporated into cloud microphysics models to complement hydrodynamic models that already consider droplet interactions driven by hydrodynamic forces [152]. In mixed-phase clouds, ice crystals collide with supercooled liquid droplets, becoming coated in a process called riming [153, 154]. Riming is a critical process in the formation of precipitation-sized hydrometeors within clouds. Precise calculation of the interaction forces between the anisotropic hydrometeor and the droplet is vital for accurately determining the collision efficiency during the riming process between ice particles and supercooled droplets.

Electrical charging mechanisms in clouds involve complex interactions between droplets, ice crystals, and graupel particles, driven by a combination of collisions and environmental factors [53, 75]. Field measurements in weakly electrified clouds show that ice crystal and droplet charges are proportional to their surface areas [55, 155, 156]. Mechanisms such as inductive charging, which arise from the polarization of particles in an existing electric field, and convective charging, where vertical air currents separate charged particles, also play a role in cloud electrification. However, the most significant mechanism is collisional charging, where charge transfer occurs during collisions between particles. For example, when supercooled water droplets freeze upon colliding with graupel particles, charge separation occurs due to differences in ion mobility and thermal properties. In this process, smaller ice crystals typically acquire a positive charge, while graupel or hailstones gain a negative charge, with the charge separated during each collision ranging from 1×10^{-14} to 5×10^{-14} coulombs. Since collisional charging is the dominant process driving charge separation in clouds, and ice crystals are inherently anisotropic, understanding the role of particle anisotropy and their electrostatic interactions is crucial for improving our understanding of cloud electrification.

Analytical methods for determining electrostatic forces and torques on multiple conductors are limited to simple geometries such as sphere-sphere [67] and spheroid-spheroid in specific configurations [61]. In this chapter, we extend this computation to two spheroidal conductors in a generic configuration in the far field regime. The far field calculations are carried out using the method of reflections, widely used in the problems of micro-hydrodynamics [10], and described in detail in Chapter 2. Having obtained the electrostatic interaction between two spheroids, we explore the role of anisotropy in the simpler, yet unexplored, electrostatic interaction between a spheroid and a sphere. This system is sufficient to capture the anisotropy in the problem and provides a manageable parameter space over which relevant quantities can be analyzed. We use the Boundary Integral Method (BIM) to uniformly capture the electrostatic interaction in both far and near field regimes. We compare BIM with the method of reflections to determine the proximity at which the method of reflections starts to lose accuracy for closely spaced conductors. We derive an analytical expression for the electrostatic force and torque in the far-field regime using the first reflection, applicable to both spheroid-sphere and spheroid-spheroid systems. It is speculated that incorporating electrostatic torque in a dilute suspension of charged spheroids may modify the previously observed instability in density fluctuations of uncharged spheroids.

5.2 Methods

5.2.1 Potential matrix formulation

The electrostatic interaction between multiple conductors involves determining the potential on the surface of each conductor, given the total charge on each conductor. This information is sufficient to determine the total electrostatic energy of the system and hence compute forces and torques on each conductor. The governing equation for the potential outside the conductors is simply the Laplace equation. The complexity of the problem comes from the boundary conditions that need to be satisfied at the surface of each conductor. The linearity of governing equations of electrostatics implies a linear relationship between the total charges on each conductor and the potential on their surfaces. The proportionality constant is called the potential matrix $\mathbf{\Phi}_M$ [58, 60, 64, 97, 100], which only depends on the permittivity of free space ε_0, size, and the geometry of the conductors [1]. Since we are interested in two-body electrostatic interaction, the connection between charges Q_1 and Q_2 and the potentials V_1 and V_2 on the surface of the conductors S_1 and S_2 is given by

$$\begin{pmatrix} V_1 \\ V_2 \end{pmatrix} = \frac{1}{4\pi\varepsilon_0 a} \begin{pmatrix} \Phi_{11} & \Phi_{12} \\ \Phi_{21} & \Phi_{22} \end{pmatrix} \begin{pmatrix} Q_1 \\ Q_2 \end{pmatrix}, \tag{5.1}$$

where a is the typical size of the conductors and Φ_{ij}, $i, j \in \{1, 2\}$, are the dimensionless elements of the potential matrix, $\mathbf{\Phi}_M$, which depends on the relative

---

[1] The more familiar capacitance matrix is simply the inverse of the potential matrix.

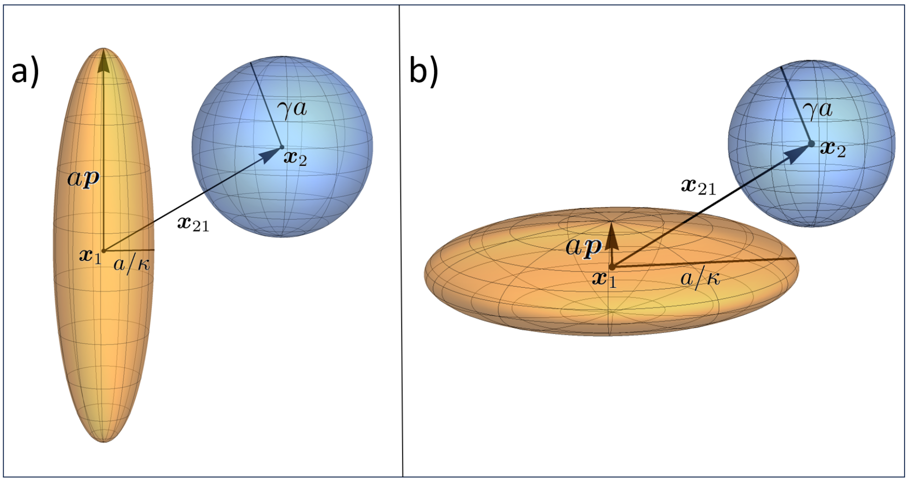

Figure 5.1: A schematic illustrating the geometric setup for electrostatic pair interactions between a spheroid and a sphere in a generic, non-axisymmetric configuration. The unit vector $\boldsymbol{p}$ represents the orientation of the spheroid, a denoting the size of the spheroid, κ denoting its aspect ratio, γ denoting the size ratio of sphere to spheroid. a) A prolate spheroid and a sphere. b) Oblate spheroid and a sphere.

position, orientations, and the geometry of the two conductors. Using the reciprocal theorem, one can show that the potential matrix is symmetric, i.e. $\boldsymbol{\Phi}_M^T = \boldsymbol{\Phi}_M$ [58, 60, 97].

The subsequent sections are concerned with the calculation of the potential matrix $\boldsymbol{\Phi}_M$ of a spheroid-sphere system in the far field, near field, and uniformly valid regimes. Before undertaking full numerical calculations, we will first examine two distinct asymptotic limits: when the particles are widely separated and when they are nearly touching.

5.2.2 Far field interactions: Method of reflections

The method of reflection is an iterative approach that progressively satisfies boundary conditions on surfaces by incorporating corrections from each preceding iteration [10]. The solution to each iteration is given by the multipole expansions, which yield a perturbation series in a/R, where a is the typical size of the conductors and R is their typical separation. A detailed description of this method in the context of electrostatics is given in Chapter 2 of this thesis. Here, we briefly mention the common terminologies of this method. Consider a *prolate* spheroid S_1, carrying a total charge Q_1, centered at $\boldsymbol{x}_1$ with a as the distance from its centre to the pole along the symmetry axis denoted by the unit vector $\boldsymbol{p}$ (see figure 5.1). The spheroid's aspect ratio $\kappa(> 1)$ is defined as the ratio of a to its equatorial radius lying perpendicular to $\boldsymbol{p}$, and its eccentricity is $e = \sqrt{1-\kappa^{-2}}$. The surface of this prolate spheroid is given by

$$(\boldsymbol{x}-\boldsymbol{x}_1)\cdot\left[\frac{\boldsymbol{pp}}{a^2}+\frac{(\boldsymbol{\delta}-\boldsymbol{pp})}{a^2\kappa^{-2}}\right]\cdot(\boldsymbol{x}-\boldsymbol{x}_1)=1,\ \ \boldsymbol{x}\in S_1. \tag{5.2}$$

The second conductor is a sphere S_2 centered at $\boldsymbol{x}_2$ with radius βa and total charge Q_2, the surface of which is given by

$$(\boldsymbol{x}-\boldsymbol{x}_2)\cdot(\boldsymbol{x}-\boldsymbol{x}_2)=(\beta a)^2,\quad \boldsymbol{x}\in S_2. \tag{5.3}$$

The relative separation vector between them is $\boldsymbol{x}_{21} \equiv \boldsymbol{x}_2-\boldsymbol{x}_1 \equiv -\boldsymbol{x}_{12}$. The *first reflection* approximation accounts for the correction of potential fields produced by the sphere and spheroids as if they were isolated. The corresponding potential matrix in this case is accurate only up to $O(a/R)$. The elements of the potential matrix for a *prolate spheroid* are given by (see appendix C):

$$\Phi_{11}^{(1)} = e^{-1}\operatorname{arctanh} e, \tag{5.4a}$$

$$\Phi_{12}^{(1)} = \Phi_{21}^{(1)}(\boldsymbol{x}_{12},\boldsymbol{p}) = \frac{1}{2e}\log\left(\frac{z_{12}-ae-R_-}{z_{12}+ae-R_+}\right), \tag{5.4b}$$

$$\Phi_{22}^{(1)} = \beta^{-1}, \tag{5.4c}$$

where

$$R_\pm \equiv \sqrt{\rho_{12}^2+(z_{12}\pm ae)^2}, \tag{5.5a}$$

$$\rho_{12}^2 \equiv \boldsymbol{x}_{12}\cdot(\boldsymbol{\delta}-\boldsymbol{pp})\cdot\boldsymbol{x}_{12}, \tag{5.5b}$$

$$z_{12} \equiv \boldsymbol{x}_{12}\cdot\boldsymbol{p}. \tag{5.5c}$$

Note that up to the first reflection correction, the effect of interaction is only captured by the off-diagonal terms. Now, the *second reflection* accounts for the correction in the potential fields produced in response to the first reflected fields. The corresponding potential matrix in this case is accurate upto $O(a^4/R^4)$, with the elements for a *prolate spheroid* given by:

$$\Phi_{11}^{(2)}(\boldsymbol{x}_{12},\boldsymbol{p}) = \Phi_{11}^{(1)} - \frac{a^2\beta^3}{4e^2}\left[\left(\frac{1}{R_-}-\frac{1}{R_+}\right)^2+\rho_{12}^2\left(\frac{1}{R_+(z_{12}+ae-R_+)} - \frac{1}{R_-(z_{12}-ae-R_-)}\right)^2\right], \tag{5.6a}$$

$$\Phi_{12}^{(2)}(\boldsymbol{x}_{12},\boldsymbol{p}) = \Phi_{21}^{(2)}(\boldsymbol{x}_{12},\boldsymbol{p}) = \Phi_{12}^{(1)}(\boldsymbol{x}_{12},\boldsymbol{p}) \tag{5.6b}$$

$$\Phi_{22}^{(2)}(\boldsymbol{x}_{12}, \boldsymbol{p}) = \Phi_{22}^{(1)} - \frac{9}{4a^2e^6}\left[X_p^C\left\{R_- - R_+ + z_{12}\log\left(\frac{z_{12} - ae - R_-}{z_{12} + ae - R_+}\right)\right\}^2 \right.$$
$$\left. + \frac{1}{4}Y_p^C\left\{\frac{z_{12}}{\rho_{12}}(R_- - R_+) + \frac{ae}{\rho_{12}}(R_- + R_+) - \rho_{12}\log\left(\frac{z_{12} - ae - R_-}{z_{12} + ae - R_+}\right)\right\}^2\right], \quad (5.6c)$$

where

$$X_p^C \equiv \frac{e^3}{3}(\operatorname{arctanh} e - e)^{-1}, \quad (5.7a)$$
$$Y_p^C \equiv \frac{2e^3}{3}\left(\frac{e}{1 - e^2} - \operatorname{arctanh} e\right)^{-1}. \quad (5.7b)$$

Now consider an *oblate* spheroid S_1 centered at $\boldsymbol{x}_1$ with a as the distance from its centre to the pole along the symmetry axis $\boldsymbol{p}$. Its aspect ratio is $\kappa(< 1)$, with an eccentricity of $e = \sqrt{1 - \kappa^2}$ and it carries a total charge Q_1. The surface of this oblate spheroid S_1 is again given by (5.2) with the only difference being $\kappa < 1$. The second conductor S_2 is again a sphere of radius βa, centered at $\boldsymbol{x}_2$, carrying a total charge Q_2. To obtain the corresponding potential matrix of the spheroid-sphere system, we use the eccentricity transformation $e \to \frac{ie}{\sqrt{1 - e^2}}$ on the corresponding expressions of the prolate spheroid [101]. Therefore, for an oblate spheroid and a sphere, we have

$$\Phi_{11}^{(1)} = \frac{\kappa \arcsin e}{e}, \quad (5.8a)$$
$$\Phi_{12}^{(1)} = \Phi_{21}^{(1)}(\boldsymbol{x}_{12}, \boldsymbol{p}) = \frac{\kappa}{e}\operatorname{arccot}\left(\frac{z_{12} - u}{v - ae/\kappa}\right), \quad (5.8b)$$
$$\Phi_{22}^{(1)} = \beta^{-1}, \quad (5.8c)$$

where z_{12} is given by equation (5.5) and u and v are given by

$$u \equiv \sqrt{\frac{\mu}{2} + \sqrt{\frac{\mu^2}{4} + \frac{a^2e^2}{\kappa^2}z_{12}^2}}; \quad \mu \equiv |\boldsymbol{x}_{12}|^2 - \frac{a^2e^2}{\kappa^2}, \quad (5.9a)$$
$$v \equiv \frac{aez_{12}}{\kappa u}. \quad (5.9b)$$

Similarly, the second reflection corrections are given by

$$\Phi_{11}^{(2)}(\boldsymbol{x}_{12}, \boldsymbol{p}) = \Phi_{11}^{(1)} - \frac{\kappa^2a^2\beta^3}{4e^2}\left[\left(\frac{2v}{u^2 + v^2}\right)^2 \right.$$
$$\left. + \rho_{12}^2\left\{\frac{4ae\kappa^{-1}z_{12} - 2(z_{12}v + ae\kappa^{-1}u)}{(u^2 + v^2)((z_{12} - u)^2 + (ae\kappa^{-1} - v)^2)}\right\}^2\right], \quad (5.10a)$$

$$\Phi_{12}^{(2)}(\boldsymbol{x}_{12},\boldsymbol{p}) = \Phi_{21}^{(2)}(\boldsymbol{x}_{12},\boldsymbol{p}) = \Phi_{12}^{(1)}(\boldsymbol{x}_{12},\boldsymbol{p}) \tag{5.10b}$$

$$\begin{aligned}\Phi_{22}^{(2)}(\boldsymbol{x}_{12},\boldsymbol{p}) = \Phi_{22}^{(1)} - \frac{9\kappa^6}{a^2e^6}\Bigg[& X_o^C \left\{ v - z_{12}\operatorname{arccot}\left(\frac{z_{12}-u}{v-ae\kappa^{-1}}\right)\right\}^2 \\ & + \frac{1}{4}Y_o^C\left\{\frac{ae\kappa^{-1}u - z_{12}v}{\rho_{12}} - \rho_{12}\operatorname{arccot}\left(\frac{z_{12}-u}{v-ae\kappa^{-1}}\right)\right\}^2\Bigg],\end{aligned} \tag{5.10c}$$

where

$$X_o^C \equiv \frac{e^3}{3}[e(1-e^2)-(1-e^2)^{3/2}\arcsin e]^{-1}, \tag{5.11a}$$

$$Y_o^C \equiv \frac{2e^3}{3}\left[e(1-e^2)^2-(1-e^2)^{3/2}\arcsin e\right]^{-1}. \tag{5.11b}$$

The potential matrix for two spherical conductors can be obtained by taking the limit $e \longrightarrow 0$ in the potential matrix expression for a prolate spheroid. Therefore, for a spherical conductor S_1 of radius a, centered at $\boldsymbol{x}_1$ and another spherical conductor S_2 of radius βa, centered at $\boldsymbol{x}_2$, the elements of the potential matrix up to the second reflection are given by:

$$\Phi_{11}^{(2)}(|\boldsymbol{x}_{21}|) = 1 - \frac{\beta^3 a^4}{|\boldsymbol{x}_{21}|^4}, \tag{5.12a}$$

$$\Phi_{12}^{(2)}(|\boldsymbol{x}_{21}|) = \Phi_{21}^{(2)}(|\boldsymbol{x}_{21}|) = \frac{1}{|\boldsymbol{x}_{21}|}, \tag{5.12b}$$

$$\Phi_{22}^{(1)}(|\boldsymbol{x}_{21}|) = \frac{1}{\beta} - \frac{a^4}{|\boldsymbol{x}_{21}|^4}. \tag{5.12c}$$

5.2.3 Near contact interaction: Lubrication approximation

Using the lubrication approximation for the spheroid-sphere system in the axisymmetric configuration involves solving the Laplace equation for the potential field $\phi(\boldsymbol{x})$ near the gap of thickness $a\epsilon$ between the conductors. Using polar coordinates with z coordinate along the symmetry axis $\boldsymbol{p}$ and r coordinate transverse to $\boldsymbol{p}$, the boundary value problem to be solved is

$$\nabla^2\phi = \frac{\partial^2\phi}{\partial z^2} + \frac{1}{r}\frac{\partial}{\partial r}\left(r\frac{\partial\phi}{\partial r}\right) = 0, \tag{5.13a}$$

$$\phi = \begin{cases} V_1 & z = h_1(r), \\ V_2 & z = h_2(r), \end{cases} \tag{5.13b}$$

The surface of the spheroid and the sphere can be expanded as

$$\frac{h_1(r)}{a\epsilon} = 1 + \frac{\kappa^2 r^2}{2\epsilon a^2} + \frac{1}{8}\frac{\kappa^4 r^4}{\epsilon a^4} + O\left(\frac{\kappa^6 r^6}{\epsilon a^6}\right), \tag{5.14a}$$

$$\frac{h_2(r)}{a\epsilon} = -\frac{1}{2}\frac{r^2}{\epsilon\beta a^2} - \frac{1}{8}\frac{r^4}{\epsilon\beta^3 a^4} + O\left(\frac{r^6}{\epsilon\beta^5 a^6}\right). \tag{5.14b}$$

Defining the stretched coordinates $R \equiv r/(a\sqrt{\epsilon})$ and $Z \equiv z/(a\epsilon)$, we have

$$H_1(R) = 1 + \frac{\kappa^2 R^2}{2} + \frac{\epsilon\kappa^4 R^4}{8} + O(\epsilon^2), \tag{5.15a}$$

$$H_2(R) = -\frac{R^2}{2\beta} - \frac{\epsilon R^4}{8\beta^3} + O(\epsilon^2). \tag{5.15b}$$

Rewriting the Laplace equation in terms of the stretched coordinates, we have

$$\frac{\partial^2\phi}{\partial Z^2} + \frac{\epsilon}{R}\frac{\partial}{\partial R}\left(R\frac{\partial\phi}{\partial R}\right) = 0, \tag{5.16a}$$

$$\phi = \begin{cases} V_1 & Z = H_1(R), \\ V_2 & Z = H_2(R), \end{cases} \tag{5.16b}$$

The solution can be expanded in the perturbation series as $\phi = \phi_0 + \epsilon\phi_1 + O(\epsilon^2)$. The total charge Q_1 and Q_2 on the spheroid S_1 and sphere S_2 are given by

$$Q_\alpha = -\epsilon_0 \oint_{S_\alpha} \nabla\phi \cdot \hat{\boldsymbol{n}}_\alpha \, dS_\alpha, \quad \alpha \in \{1, 2\}, \tag{5.17}$$

where $\hat{\boldsymbol{n}}_\alpha$ represents the unit normal pointing out of the surface S_α. The electrostatic force $\boldsymbol{F}_1$ on the spheroid is given by

$$\boldsymbol{F}_1 = \frac{\epsilon_0}{2}\oint_{S_1} \left|\nabla\phi \cdot \hat{\boldsymbol{n}}_1\right|^2 \hat{\boldsymbol{n}}_1 \, dS_1. \tag{5.18}$$

Using the zeroth order solution ϕ_0, the charge difference $\Delta Q_{12} = Q_1 - Q_2$ is given by (see Supplemental Material):

$$\Delta Q_{12} = \frac{4\pi a\epsilon_0\beta\Delta V_{12}}{1+\beta\kappa^2}\left[\log\left(\frac{1+\beta\kappa^2}{2\beta\kappa\epsilon}\right) + \delta\right] + O(\epsilon), \tag{5.19}$$

where $\Delta V_{12} \equiv V_1 - V_2$ and δ is an $O(1)$ constant which has to be determined using the outer solution. The weak logarithmic singularity is insufficient to overpower the δ correction, even at very small separations ϵ, and therefore δ cannot be neglected. The forces $\boldsymbol{F}_1$ and $\boldsymbol{F}_2$ are given by

$$\boldsymbol{F}_1 = \frac{-\hat{\boldsymbol{x}}_{12}(1+\beta\kappa^2)\Delta Q_{12}^2}{16\pi a^2\epsilon_0\beta\epsilon\left[\log\left(\frac{1+\beta\kappa^2}{2\beta\kappa\epsilon}\right) + \delta\right]^2} = -\boldsymbol{F}_2. \tag{5.20}$$

Note that for unequal total charges $\Delta Q_{12} \neq 0$, the electrostatic forces at close range are attractive, regardless of whether the conductors carry like or unlike charges. The force expression (5.20) reduces to the near contact force between two spheres for $\kappa = 1$ (**cite**).

We rewrite equation (5.19) in terms of δ as

$$\delta = \lim_{\epsilon \to 0} \left\{ \frac{(1+\beta\kappa^2)\Delta Q_{12}}{4\pi a \epsilon_0 \beta \Delta V_{12}} - \log\left(\frac{1+\beta\kappa^2}{2\beta\kappa\epsilon}\right) \right\}. \tag{5.21}$$

We shall use the Boundary Integral Method (BIM) to evaluate the right-hand side of the above equation for $\epsilon \ll 1$ and thus obtain δ. The numerical values of the RHS of equation (5.21) will have small variations with ϵ even when $\epsilon \ll 1$. This is due to the fact that the numerical errors in BIM increase as the surfaces approach each other [93, 104]. The error in the numerical measurement of δ, i.e. $\Delta\delta$, gives error on the forces $|\Delta F|$ (see equation (5.20)) as

$$|\Delta F| = |\boldsymbol{F}_1| \left| \frac{2\Delta\delta}{\left[\log\left(\frac{1+\beta\kappa^2}{2\beta\kappa\epsilon}\right) + \delta\right]} \right|. \tag{5.22}$$

Note that the relative error in the forces decreases with ϵ. Once the δ is obtained, the lubrication force (5.20) gives electrostatic forces in the configurations where the minimum separation between the conductors becomes vanishingly small.

5.2.4 Boundary Integral Method

The method of reflections is primarily effective for far-field interactions. Achieving higher accuracy requires additional reflections, but each successive reflection adds significant complexity to the analytical expressions. To compute the interactions in both far and near field regimes numerically, we use the Boundary Integral Method (BIM). The BIM formulation is well established for various linear partial differential equations, including the Laplace equation [98]. A detailed formulation of the BIM for the electrostatic problem with total charges specified on each conductor is given in Chapter 2 of this thesis. Here we outline the main integral equations to be solved numerically to compute the potential matrix for a spheroid S_1 (both prolate and oblate) and a sphere S_2. The potentials on the surface of the conductors are given by:

$$\epsilon_0 V_\alpha = \frac{1}{|S_\alpha|} \oint_{S_\alpha} q_\alpha(\boldsymbol{x})\, dS_\alpha(\boldsymbol{x}); \quad \alpha \in \{1, 2\}, \tag{5.23}$$

where $|S_\alpha|$ is the surface area of the conductor S_α. The fields q_α are obtained by solving the second kind integral equation on every point $\boldsymbol{x}_{s\alpha}$ on the surface of conductor S_α:

$$\begin{bmatrix} \mathcal{L}^d_{11} + \mathcal{P}^c_{11} + \mathbb{I} & \mathcal{L}^d_{12} \\ \mathcal{L}^d_{21} & \mathcal{L}^d_{22} + \mathcal{P}^c_{22} + \mathbb{I} \end{bmatrix} \begin{bmatrix} q_1 \\ q_2 \end{bmatrix} = \frac{1}{4\pi} \begin{bmatrix} Q_1 \mathcal{G}(\boldsymbol{x}_{s1}, \boldsymbol{x}_1) + Q_2 \mathcal{G}(\boldsymbol{x}_{s1}, \boldsymbol{x}_2) \\ Q_1 \mathcal{G}(\boldsymbol{x}_{s2}, \boldsymbol{x}_1) + Q_2 \mathcal{G}(\boldsymbol{x}_{s2}, \boldsymbol{x}_2) \end{bmatrix}, \tag{5.24}$$

where Q_1, Q_2 are the charges on the conductors S_1 and S_2, respectively, and $\mathcal{G}$ is the Greens function of the Laplacian, given by

$$\mathcal{G}(\boldsymbol{x}, \boldsymbol{x}_0) \equiv \frac{1}{|\boldsymbol{x} - \boldsymbol{x}_0|}. \tag{5.25}$$

The integral operators are defined as:

$$\mathcal{L}^d_{\alpha\beta} q_\beta(\boldsymbol{x}_s) \equiv \frac{1}{2\pi} \oint_{S_\beta} q_\beta(\boldsymbol{x})\, \hat{\boldsymbol{n}}_\beta \cdot \nabla_x \mathcal{G}(\boldsymbol{x}, \boldsymbol{x}_s)\, dS_\beta(\boldsymbol{x}), \tag{5.26a}$$

$$\mathcal{P}^c_{\alpha\beta} q_\beta \equiv \frac{1}{|S_\alpha|} \delta_{\alpha\beta} \oint_{S_\beta} q_\beta(\boldsymbol{x})\, dS_\beta(\boldsymbol{x}); \quad \boldsymbol{x}_s \in S_\alpha. \tag{5.26b}$$

The equations (5.23) and (5.24) are used to determine the potential matrix. The integral equation (5.24) is solved using GMRES iterations [107], and the integrals on the surfaces are evaluated using Gaussian quadrature [104].

5.2.5 Electrostatic force and Torque

The electrostatic force and torque on each conductor can be computed by taking derivatives of the electrostatic energy of the system. The electrostatic energy of the spheroid-sphere system is given by:

$$W(|\boldsymbol{x}_{21}|, \hat{\boldsymbol{x}}_{21} \cdot \boldsymbol{p}) = \frac{1}{2} \boldsymbol{Q}^T \cdot \boldsymbol{\Phi}_M(|\boldsymbol{x}_{21}|, \hat{\boldsymbol{x}}_{21} \cdot \boldsymbol{p}) \cdot \boldsymbol{Q}, \tag{5.27}$$

where $\boldsymbol{Q} \equiv [Q_1 \quad Q_2]^T$, where the spheroid centered at $\boldsymbol{x}_1$ carries a total charge Q_1 and the sphere centered at $\boldsymbol{x}_2$ carries a total charge Q_2. Here $\hat{\boldsymbol{x}}_{21}$ is a unit vector along the separation vector $\boldsymbol{x}_{21} = \boldsymbol{x}_2 - \boldsymbol{x}_1$. The differential change in the electrostatic energy upon differential change in the relative configuration is given by

$$dW = d\boldsymbol{x}_{21} \cdot \nabla_{21} W + d\boldsymbol{p} \cdot \nabla_p W. \tag{5.28}$$

The first term in equation (5.28) represents the negative of the work done by the electrostatic force on the sphere, $\boldsymbol{F}_2$, in moving the sphere by an amount $d\boldsymbol{x}_{21}$. Equivalently, it represents the negative of the work done by the electrostatic force on the spheroid, $\boldsymbol{F}_1$, in moving the spheroid by an amount $-d\boldsymbol{x}_{21}$. Therefore, the electrostatic forces on the conductors are given by:

$$\boldsymbol{F}_1 = -\boldsymbol{F}_2 = \nabla_{\boldsymbol{x}_{21}} W(|\boldsymbol{x}_{21}|, \hat{\boldsymbol{x}}_{21} \cdot \boldsymbol{p}). \tag{5.29}$$

The second term shows that there is an energy expense in changing the orientation of the spheroid. This shows that the electrostatic force on the spheroid does not act at its centre. Thus, an electrostatic torque $\boldsymbol{T}_1$ acts on the spheroid about its centre. The work done by the electrostatic force on the spheroid in changing its orientation can be written in terms of $\boldsymbol{T}_1$ as $\boldsymbol{T}_1 \cdot \hat{\boldsymbol{n}}\, d\theta$, where $\hat{\boldsymbol{n}}$ is the axis about which $\boldsymbol{p}$ is rotated by an angle $d\theta$, i.e. $d\boldsymbol{p} = d\theta\, \hat{\boldsymbol{n}} \times \boldsymbol{p}$. Equating this to the second term in equation (5.28) gives the torque on the spheroid about its centre as

$$\boldsymbol{T}_1 = -\boldsymbol{p} \times \nabla_{\boldsymbol{p}} W(|\boldsymbol{x}_{21}|, \hat{\boldsymbol{x}}_{21} \cdot \boldsymbol{p}). \tag{5.30}$$

The change in configuration due to the change in the orientation vector $\boldsymbol{p} = d\theta\, \hat{\boldsymbol{n}} \times \boldsymbol{p}$ is equivalent to keeping the spheroid's orientation fixed but rotating the separation vector $\boldsymbol{x}_{21}$ about the spheroid's centre, the opposite way, such that $d\boldsymbol{x}_{21} = -d\theta\, \hat{\boldsymbol{n}} \times \boldsymbol{x}_{21}$. The work done on the sphere by $\boldsymbol{F}_2$ in this case is simply, $\boldsymbol{F}_2 \cdot (-d\theta\, \hat{\boldsymbol{n}} \times \boldsymbol{x}_{21}) = -(\boldsymbol{x}_{21} \times \boldsymbol{F}_2) \cdot \hat{\boldsymbol{n}}\, d\theta \equiv \boldsymbol{T}_2 \cdot (-\hat{\boldsymbol{n}} d\theta)$. This shows the torque $\boldsymbol{T}_2$ on the sphere is simply

$$\boldsymbol{T}_2 = \boldsymbol{x}_{21} \times \boldsymbol{F}_2. \tag{5.31}$$

It is easy to see using equations (5.29), (5.30), and (5.31) that $\boldsymbol{T}_1 = -\boldsymbol{T}_2$, and hence the total angular momentum of the system is conserved.

5.3 Results

The parameter space to be explored contains the aspect ratio of spheroid κ and ratio of radius of sphere to the semi-major axis of the spheroid β, for various configurations given by $\boldsymbol{x}_{21}$ and $\boldsymbol{p}$. For a given κ, we fix the value of β such that the surface area of the spheroid is the same as that of the sphere. We look at three different aspect ratios $\kappa \in \{1, 4, 0.25\}$. The first case corresponds to the electrostatic interaction between two identical spheres, the results of which are well known [67]. This serves as a benchmark for our general results for spheroid-sphere interactions. The other two cases correspond to a prolate and an oblate spheroid, respectively.

5.3.1 Elements of the potential matrix

The elements of the potential matrix are defined in equation (5.1). For the case of two spheres ($\kappa = 1$), the exact expression is known from Lekner [67] and the

Run	κ	β
$R1$	1	1
$R2$	4	0.445
$R3$	0.25	3.01

Table 5.1: Values of κ and β used in the simulations.

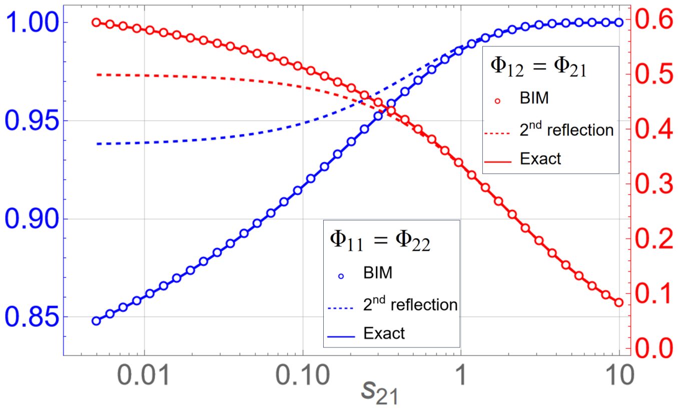

Figure 5.2: Elements of the potential matrix Φ_M (see (5.1)) as a function of dimensionless minimum separation between the two spheres, $s_{21} = |\boldsymbol{x}_{21}|/a - 2$. The second reflection is decent up to the separations of the order of the size of the spheres. The exact result in terms of an infinite series can be found in [67].

second reflection results are given by equation (5.12). The comparison between the second reflection, BIM, and exact expression shows that the second reflection performs well down to minimum separations between spheres comparable to their size, see figure 5.2. This also validates both the second reflection and the BIM.

For the case of electrostatic interactions between a spheroid and a sphere, the exact expressions of the potential matrix are not known to the best of our knowledge. The potential matrix depends on both the separation between the conductors $|\boldsymbol{x}_{21}|$ and the relative configuration of the conductors $\cos(\psi) \equiv \hat{\boldsymbol{x}}_{21} \cdot \boldsymbol{p}$. The minimum separation between the centres of the conductors when they are just touching depends on ψ and is denoted by $d_{\text{min}}(\psi)$. This minimum separation can be determined numerically by finding the roots $\boldsymbol{x}^*$ (point of contact) and d^* of

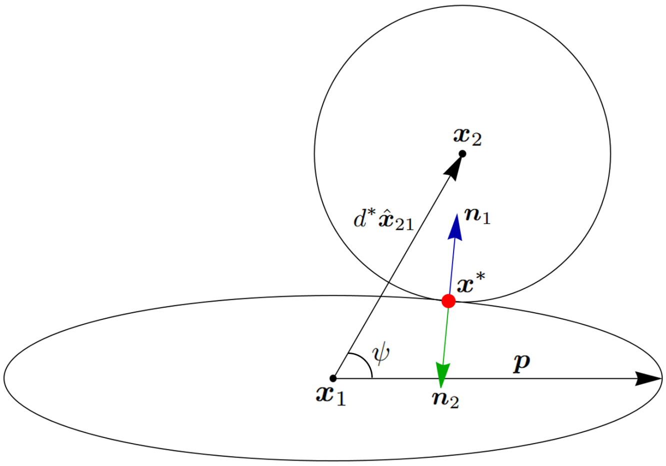

Figure 5.3: A schematic showing the point of contact x^*, the minimum distance $d^* = d_{\text{min}}(\psi)$, and other relevant quantities for the case of a prolate spheroid and a sphere. The relative sizes of the conductors are proportional to their respective scales.

the following equations

$$\left| \frac{\boldsymbol{n}_1}{|\boldsymbol{n}_1|} + \frac{\boldsymbol{n}_2}{|\boldsymbol{n}_2|} \right| = 0, \tag{5.32a}$$

$$\left| \boldsymbol{x}^* + \beta a \frac{\boldsymbol{n}_1}{|\boldsymbol{n}_1|} - d^* \hat{\boldsymbol{x}}_{21} \right| = 0, \tag{5.32b}$$

$$|\boldsymbol{n}_2|^2 = \beta^2 a^2 \tag{5.32c}$$

$$\boldsymbol{x}^* \cdot (\boldsymbol{p} \times \hat{\boldsymbol{x}}_{21}) = 0, \tag{5.32d}$$

where $\boldsymbol{n}_1$ and $\boldsymbol{n}_2$ are the (non-normalized) normal vectors to the spheroid and sphere at $\boldsymbol{x}^*$, given by:

$$\boldsymbol{n}_1 \equiv \left[\frac{\boldsymbol{pp}}{a^2} + \frac{(\boldsymbol{\delta} - \boldsymbol{pp})}{a^2 \kappa^{-2}} \right] \cdot (\boldsymbol{x}^* - \boldsymbol{x}_1), \tag{5.33a}$$

$$\boldsymbol{n}_2 \equiv \boldsymbol{x}^* - \boldsymbol{x}_1 - d^* \hat{\boldsymbol{x}}_{21}. \tag{5.33b}$$

The four equations (5.32) uniquely determines $\boldsymbol{x}^*$ and $d^* = d_{\text{min}}(\psi)$. Note that $\hat{\boldsymbol{x}}_{21}$ is given by a unit vector making an angle ψ with $\boldsymbol{p}$, which doesn't require specifying d^*.

A schematic representing $\boldsymbol{x}^*$, d^*, and other relevant quantities is shown in Figure 5.3.

The physical interpretation of equation (5.32) is as follows:

1. Equation (5.32a) enforces that the normals of the sphere and the spheroid are oriented anti-parallel to each other.

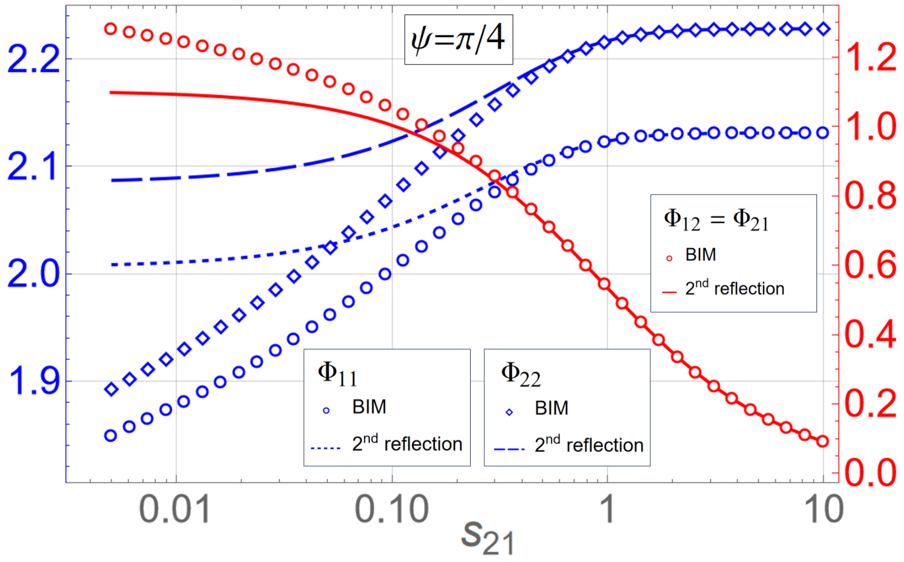

Figure 5.4: Elements of the potential matrix Φ_M (see (5.1)) as a function of dimensionless separation between the a prolate spheroid and a sphere, $s_{21} = (|\boldsymbol{x}_{21}| - d_{\min}(\psi))/a$. Here $\psi \equiv \arccos(\hat{\boldsymbol{x}}_{21} \cdot \boldsymbol{p})$ and $d_{\min}$ is the dimensionless center-to-center distance between the prolate spheroid and the sphere when they are just in contact.

2. Equation (5.32b) ensures that $\boldsymbol{x}^*$ is the point of contact.
3. Equation (5.32c) ensures that $\boldsymbol{x}^*$ lies at the surface of the sphere.
4. Equation (5.32d) ensures that $\boldsymbol{x}^*$ lies in the plane defined by $\boldsymbol{p}$ and $\hat{\boldsymbol{x}}_{21}$.

For the case of a prolate spheroid and a sphere ($\kappa = 4$), the exact expression of the potential matrix is not known to the best of our knowledge. The second reflection results are given in equation (5.6). Figure 5.4 shows the elements of the potential matrix for a fixed $\psi = \pi/4$ as a function of dimensionless separation $s_{21} = (|\boldsymbol{x}_{21}| - d_{\min}(\psi))/a$. The second reflection is reliable up to $s_{21} \sim 1$.

Similarly, for the case of an oblate spheroid and a sphere ($\kappa = 0.25$), the second reflection results (equation (5.10)) are reliable up to $s_{21} \sim 4$. This early deviation of the second reflection method from BIM arises because the length scale used for s_{21} does not correspond to the larger dimension of the oblate spheroid, specifically the equatorial radius of the oblate spheroid $a\kappa^{-1}$.

5.3.2 Electrostatic force

Equation (5.29) is used to obtain the electrostatic force between the pair of conductors. This relies on differentiating the electrostatic energy obtained using the potential matrix. The exact results are available for the sphere-sphere case by [67].

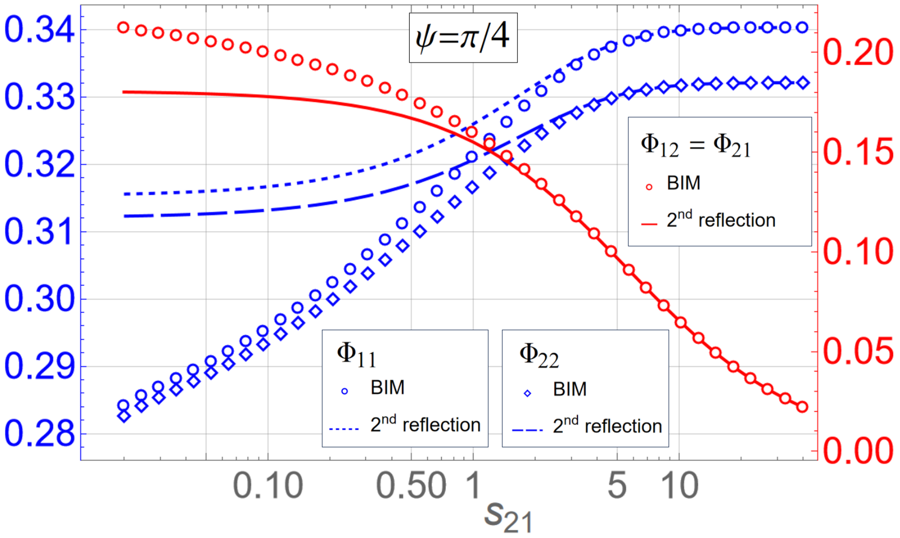

Figure 5.5: Elements of the potential matrix Φ_M (see (5.1)) as a function of dimensionless separation between the an oblate spheroid and a sphere, $s_{21} = (|\boldsymbol{x}_{21}| - d_{\min}(\psi))/a$. Here $\psi \equiv \arccos(\hat{\boldsymbol{x}}_{21} \cdot \boldsymbol{p})$ and $d_{\min}$ is the dimensionless center-to-center distance between the oblate spheroid and the sphere when they are just in contact.

The second reflection is again reliable up to $s_{21} \sim 1$. For very small separation $s_{21} \ll 1$, the BIM needs a large number of collocation points on the surfaces of the conductors to converge to the solution accurately. Lubrication approximation (equation (5.20)) has been used for $s_{21} \ll 1$, shown by the filled dots in figure 5.6, with the δ fitted using the BIM results.

The force acting on the sphere in the axisymmetric configuration $(\boldsymbol{p} \cdot \hat{\boldsymbol{x}}_{21})$ involving a prolate spheroid and a spherical conductor is shown in Figure 5.7. The lubrication force is given by equation (5.20) with the δ fitted using the BIM results. Figure 5.8 shows the corresponding force for the case of an oblate spheroid and a sphere. Note that the electrostatic forces are attractive in the near contact case for unequal charges and grow unboundedly.

Figure 5.9 shows the variation of electrostatic force as a function of dimensionless separation s_{21} and the relative configuration ψ. This captures the effect of anisotropy of the problem.

One is often interested in the dilute regime where particle separations are much larger than their size. In this regime, the first reflection is sufficient to capture the electrostatic force. Using equation (5.29) and (5.4), the electrostatic force for the

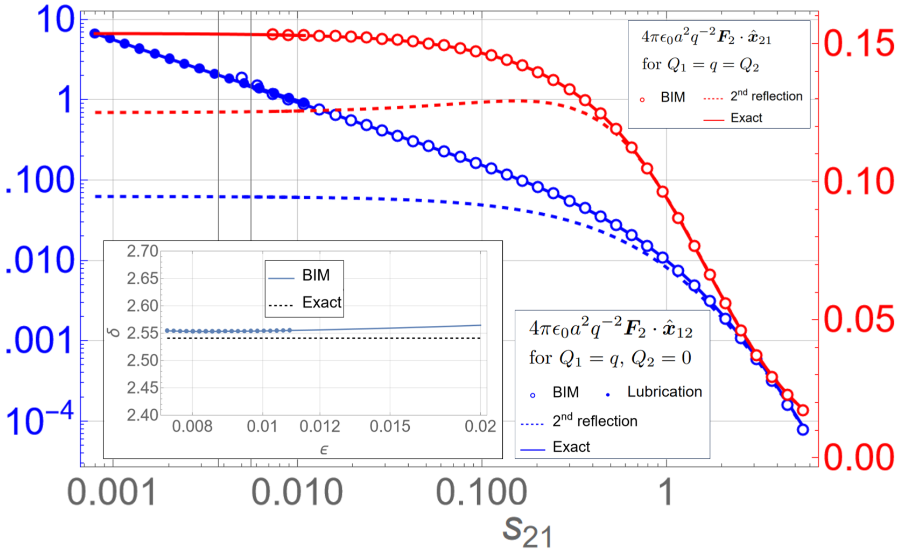

Figure 5.6: Dimensionless force on the second sphere as a function of dimensionless minimum separation between the two spheres, $s_{21} = |\boldsymbol{x}_{21}|/a - 2$. Note that the force is attractive in the case of unequal charges ($\boldsymbol{F}_2 \cdot \boldsymbol{x}_{12} > 0$). The filled dots are obtained using the lubrication approximation (see equation (5.20)) with δ obtained using BIM through equation (5.21). The inset shows δ as a function of ϵ, with the dots indicating the range of values over which δ is averaged to approximate it as a constant.

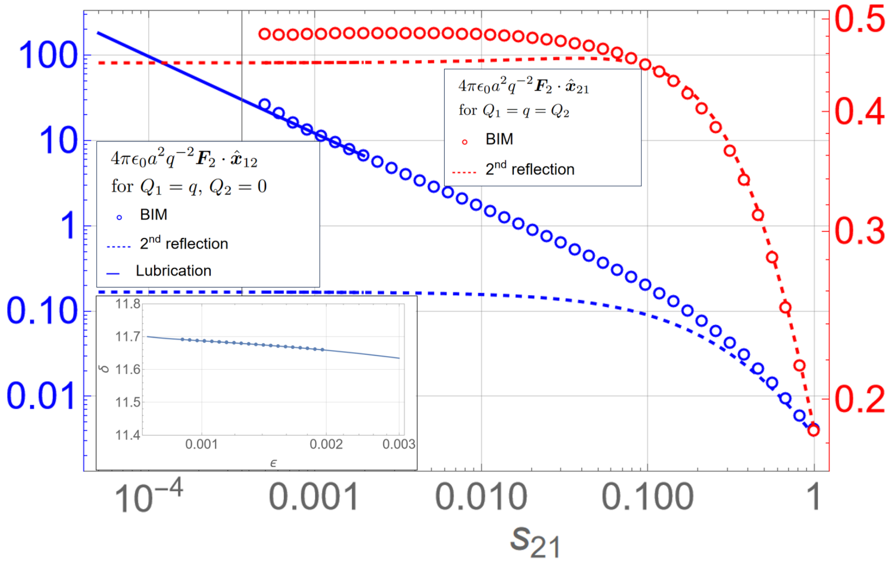

Figure 5.7: Dimensionless force on the second sphere as a function of dimensionless separation between the prolate spheroid and the sphere, $s_{21} = |\boldsymbol{x}_{21}|/a - (1 + \gamma)$, in the axisymmetric configuration ($\boldsymbol{p} = \hat{\boldsymbol{x}}_{21}$). Note that the force is attractive in the case of unequal charges ($\boldsymbol{F}_2 \cdot \boldsymbol{x}_{12} > 0$). The lubrication approximation is obtained using equation (5.20) with δ obtained using BIM through equation (5.21). The inset shows δ as a function of ϵ, with the dots indicating the range of values over which δ is averaged to approximate it as a constant.

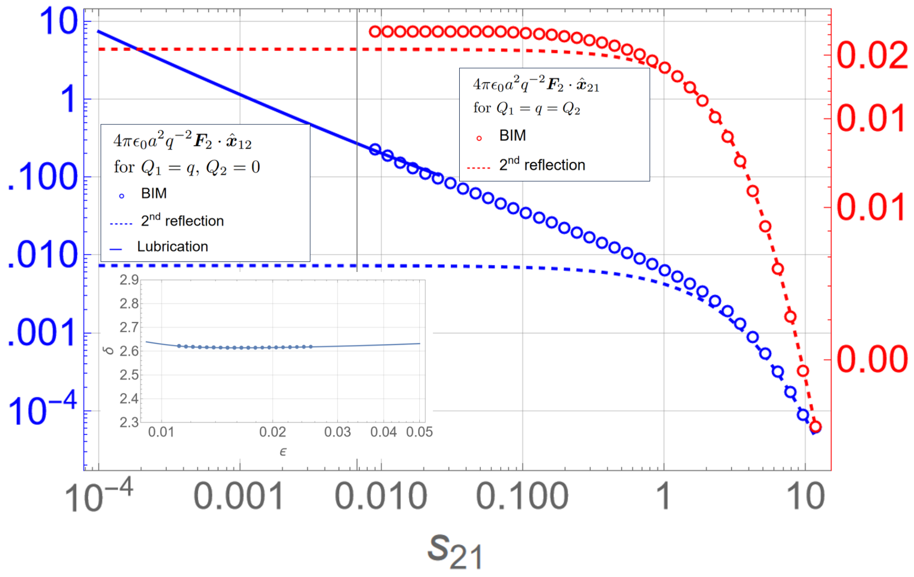

Figure 5.8: Dimensionless force on the second sphere as a function of dimensionless separation between the oblate spheroid and the sphere, $s_{21} = |\boldsymbol{x}_{21}|/a - (1+\gamma)$, in the axisymmetric configuration ($\boldsymbol{p} = \hat{\boldsymbol{x}}_{21}$). Note that the force is attractive in the case of unequal charges ($\boldsymbol{F}_2 \cdot \boldsymbol{x}_{12} > 0$). The lubrication approximation is obtained using equation (5.20) with δ obtained using BIM through equation (5.21). The inset shows δ as a function of ϵ, with the dots indicating the range of values over which δ is averaged to approximate it as a constant.

prolate spheroid and sphere system is given by

$$\boldsymbol{F}_2 \sim \frac{Q_1 Q_2}{8\pi\varepsilon_0 |\boldsymbol{x}_{21}|} \left\{ \left(\frac{1}{R_+} + \frac{1}{R_-} \right) \hat{\boldsymbol{x}}_{21} + \frac{|\boldsymbol{x}_{21}|}{ae} \right.$$

$$\left. \times \left(\frac{1 - ae/R_+}{R_+ - ae - z_{12}} - \frac{1 + ae/R_-}{R_- + ae - z_{12}} \right) (\boldsymbol{\delta} - \hat{\boldsymbol{x}}_{21}\hat{\boldsymbol{x}}_{21}) \cdot \boldsymbol{p} \right\} \quad (5.34)$$

where R_-, R_+ and z_{12} are given by equation (5.5). The corresponding electrostatic force due to the first reflection for the oblate spheroid and sphere system is given by

$$\boldsymbol{F}_2 \sim \frac{Q_1 Q_2}{4\pi\varepsilon_0 |\boldsymbol{x}_{12}|} \left\{ \frac{a^2 e^2 z_{12}^2 + \kappa^2 |\boldsymbol{x}_{12}|^2 u^2}{u(2u^2 - \mu)(a^2 e^2 + \kappa^2 u^2)} \hat{\boldsymbol{x}}_{12} \right.$$

$$\left. - \frac{a^2 e^2 |\boldsymbol{x}_{12}| z_{12}}{u(2u^2 - \mu)(a^2 e^2 + \kappa^2 u^2)} (\boldsymbol{\delta} - \hat{\boldsymbol{x}}_{21}\hat{\boldsymbol{x}}_{21}) \cdot \boldsymbol{p} \right\}, \quad (5.35)$$

where u and μ are given by equation (5.9). Note that the second term in the right-hand side of equations (5.34) and (5.35) are the non-central parts which arise due to the anisotropy of the systems and contribute to the electrostatic torques.

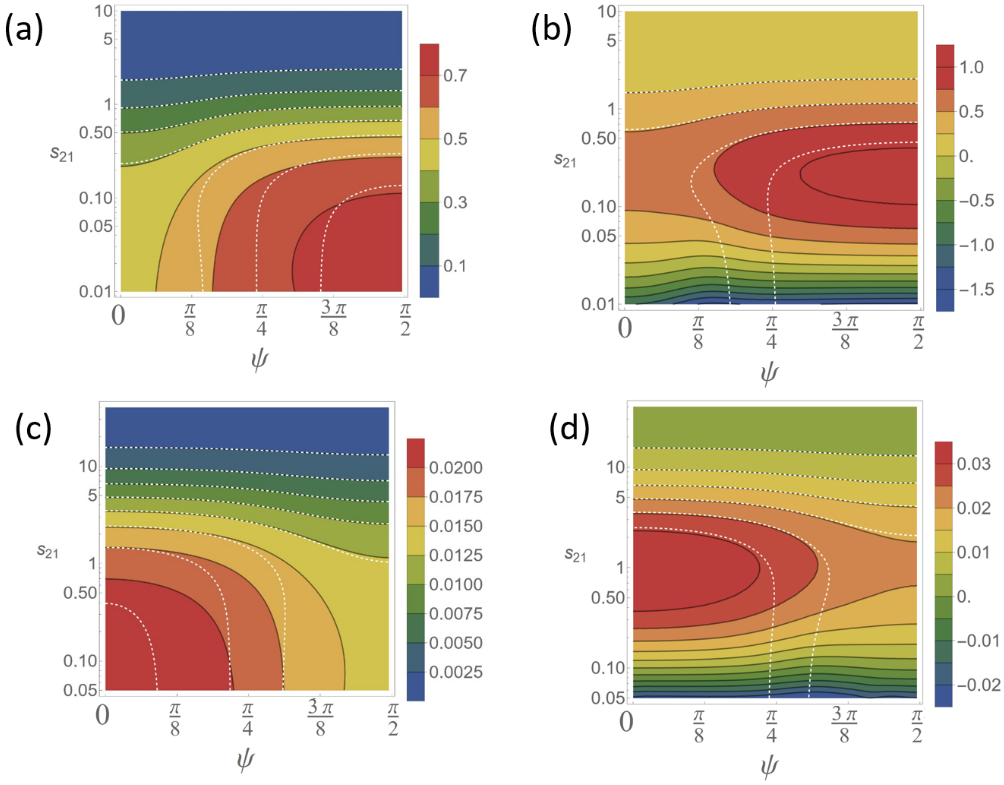

Figure 5.9: Contour plot of dimensionless force along the separation vector, $4\pi\varepsilon_0 a^2 q^{-2} \boldsymbol{F}_2 \cdot \hat{\boldsymbol{x}}_{21}$, as a function of $\psi \equiv \arccos(\hat{\boldsymbol{x}}_{21} \cdot \boldsymbol{p})$ and $s_{21} = (|\boldsymbol{x}_{21}| - d_{\min}(\psi))/a$. The white dotted lines are due to the second reflections. The spheroid has charge $Q_1 = q$ and the sphere has charge Q_2. (a) $Q_2 = q$, $\kappa = 4$. (b) $Q_2 = 2q$, $\kappa = 4$. (c) $Q_2 = q$, $\kappa = 0.25$. (d) $Q_2 = 2q$, $\kappa = 0.25$.

Because these force expressions are valid only for large separations, they fail to account for the attractive forces between like charges that arise at short distances due to electrostatic induction.

Similarly, one can obtain a closed form expression of force using equation (5.29) and the second reflection corrections to the potential matrix (equations (5.6) and (5.10)) which is reliable upto $s_{21} = (|\boldsymbol{x}_{21}| - d_{\min}(\psi))/a \sim 1$. The force from the second reflection can explain the attractive interaction between like charges; however, its accuracy diminishes at the separations where the attractive region begins.

5.3.3 Electrostatic Torque

The electrostatic torque is the result of electrostatic forces on the conductors not being central. In other words, there is an electrostatic energy cost in changing the orientation of the spheroid or changing the relative configuration ψ. Figure 5.10

shows the torque on the spheroid as a function of dimensionless separation s_{21} and ψ. As the separation decreases, the torque in the unequal charge case changes direction, indicating the onset of an attractive interaction between the conductors.

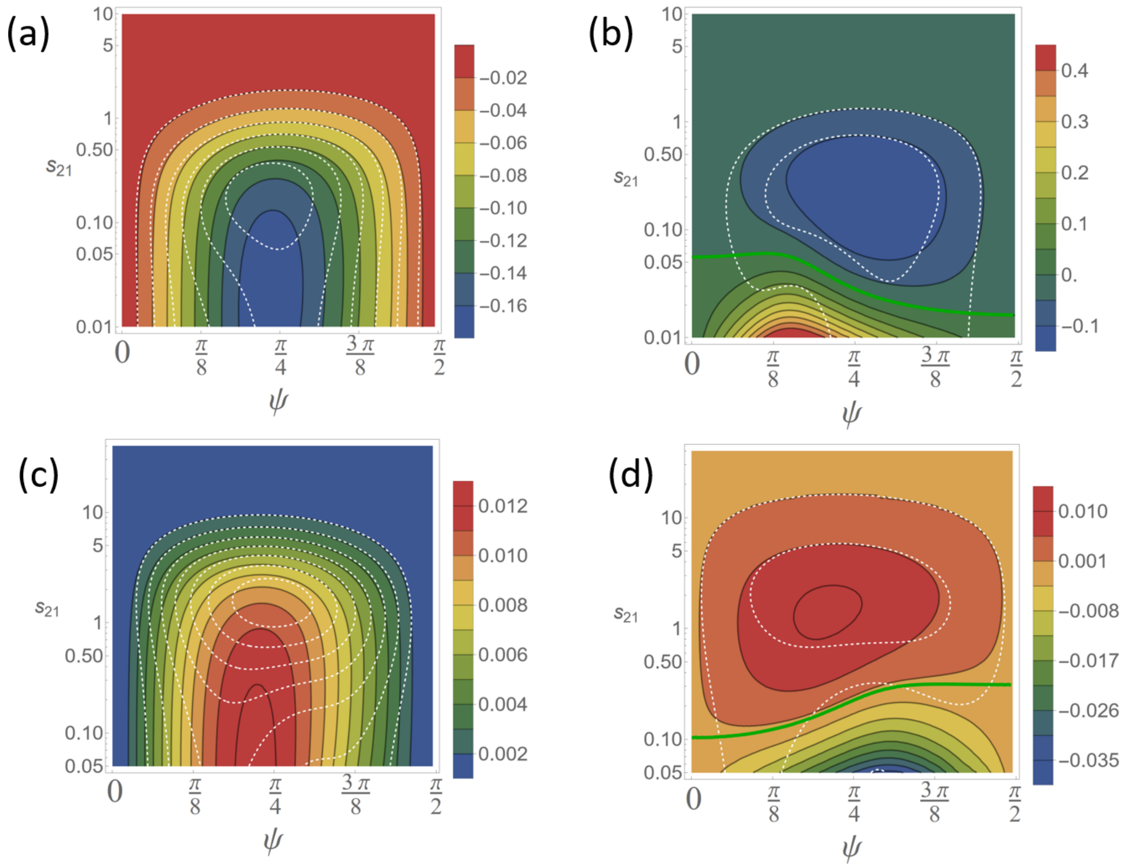

Figure 5.10: Contour plot of dimensionless torque on spheroids about their centre, $4\pi\varepsilon_0 a q^{-2}\boldsymbol{T}_1 \cdot \hat{\boldsymbol{k}}$, as a function of $\psi \equiv \arccos(\hat{\boldsymbol{x}}_{21} \cdot \boldsymbol{p})$ and $s_{21} = (|\boldsymbol{x}_{21}| - d_{\min}(\psi))/a$, where $\hat{\boldsymbol{k}}$ is a unit vector along $(\boldsymbol{p} \times \hat{\boldsymbol{x}}_{21})$. The white dotted lines are due to the second reflections. The green curves in (b) and (d) separate the repulsive and the attractive regions. The spheroid has charge $Q_1 = q$ and the sphere has charge Q_2. (a) $Q_2 = q$, $\kappa = 4$. (b) $Q_2 = 1.5q$, $\kappa = 4$. (c) $Q_2 = q$, $\kappa = 0.25$. (d) $Q_2 = 1.5q$, $\kappa = 0.25$.

A quantity of interest in the dilute regime is the electrostatic torque between a pair of particles. The torque computed using the first reflection is accurate enough to capture the anisotropic effects in the far field. Using equation (5.34), one can obtain the torque for the prolate spheroid and sphere system, given by

$$\boldsymbol{T}_1 \sim \frac{Q_1 Q_2}{8\pi\varepsilon_0 a e}\left(\frac{1 - ae/R_+}{R_+ - ae - z_{12}} - \frac{1 + ae/R_-}{R_- + ae - z_{12}}\right)\boldsymbol{p} \times \boldsymbol{x}_{21}. \tag{5.36}$$

Similarly, using equation (5.35), one can obtain the torque for the oblate spheroid and sphere system, given by

$$\boldsymbol{T}_1 \sim \frac{Q_1 Q_2}{4\pi\varepsilon_0 u(2u^2-\mu)}\left(\frac{-a^2e^2z_{12}}{(a^2e^2+\kappa^2u^2)}\right)\boldsymbol{p}\times\boldsymbol{x}_{21}. \tag{5.37}$$

Here R_-, R_+, z_{12}, u and μ are given by equations (5.5) and (5.9). Note that the electrostatic forces and torques up to the first reflection do not depend on the radius of the sphere[2]. This is because the electric field of a sphere, to a leading order in the far field regime, is identical to that of a point charge placed at the center of the sphere. Now, if one has a pair of spheroids in the far field regime, the electrostatic field of a spheroid can be approximated by the field due to a point charge located at its centre. Therefore, in the far field regime, the force and torque expressions (equations (5.34), (5.35), (5.36) and (5.37)) serve as good approximations even for a spheroid-spheroid system. The comparison between the torque due to the first and second reflections and BIM is shown in Figure 5.11

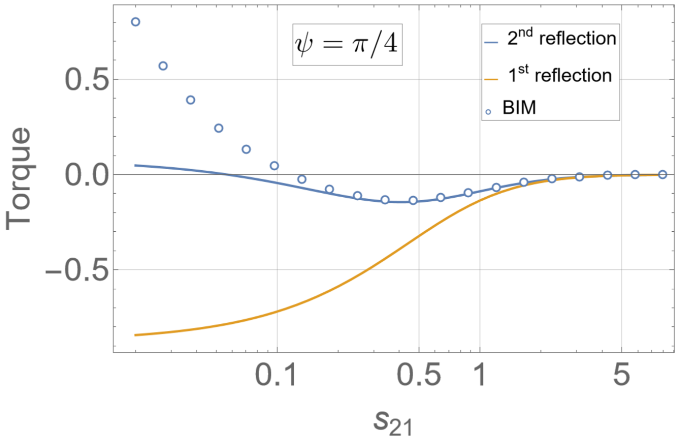

Figure 5.11: Dimensionless torque on the prolate spheroid $4\pi\varepsilon_0 a q^{-2}\boldsymbol{T}_1\cdot\hat{\boldsymbol{k}}$ for $Q_1 = q$, $Q_2 = 2q$, as a function of separation $s_{21} = (|\boldsymbol{x}_{21}| - d_{\min}(\psi))/a$ for a fixed $\psi \equiv \arccos(\hat{\boldsymbol{x}}_{21}\cdot\boldsymbol{p}) = \pi/4$, where $\hat{\boldsymbol{k}}$ is a unit vector along $(\boldsymbol{p}\times\hat{\boldsymbol{x}}_{21})$. The method of reflection aligns well with the BIM in the far field. The sign change in the torque at close range indicates an attractive electrostatic force due to induction. While the first reflection fails to predict this sign change, the second reflection captures it but loses accuracy in this close range.

Studies have shown that electrostatic interactions, when combined with hydrodynamic interactions, can result in stable configurations for a pair of spheres [157]. An array of spheres and spheroids, as well as a dilute suspension of hydrodynamically interacting spheroids, is unstable to density perturbations [47, 48, 95].

---

[2] Although the accuracy of the expression requires the radius of the sphere to be much less than the separation between the particles.

The potential role of electrostatics in altering the stability of such systems remains unexplored.

In the like-charged anisotropic system, the electrostatic torque tends to align the spheroid in a broadside orientation relative to the separation vector $\boldsymbol{x}_{21}$, as illustrated in Figure 5.12. In contrast, for oppositely charged particles, the stable orientation changes to the thin side, as evident from equations (5.36) and (5.37). These stable configurations contrast with the same system interacting hydrodynamically in a viscous flow [95], where a spheroid falling above another one tends to align its thin side along their separation vector, see figure 5.13. As a result, in a dilute suspension of sedimenting charged spheroids, the hydrodynamic torque on a spheroid counteracts the electrostatic torque in some regions while reinforcing it in others. Consequently, incorporating electrostatic effects in such systems could alter the instability typically observed in purely hydrodynamic interactions [95].

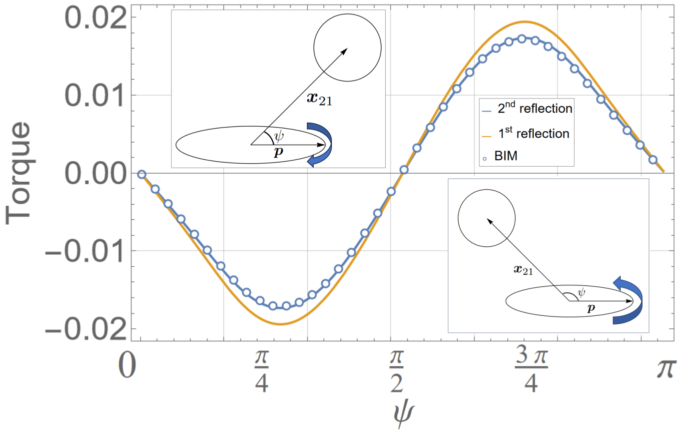

Figure 5.12: Dimensionless torque on the prolate spheroid $4\pi\varepsilon_0 a q^{-2}\boldsymbol{T}_1 \cdot \hat{\boldsymbol{k}}$ for $Q_1 = Q_2 = q$, as a function of $\psi \equiv \arccos(\hat{\boldsymbol{x}}_{21} \cdot \boldsymbol{p})$ for fixed $s_{21} = (|\boldsymbol{x}_{21}| - d_{\min}(\psi))/a = 2$, where $\hat{\boldsymbol{k}}$ is a unit vector along $(\boldsymbol{p} \times \hat{\boldsymbol{x}}_{21})$. The change in the sign of the torque shows a stable configuration of the prolate spheroid and sphere system about $\psi = \pi/2$, as indicated in the insets.

5.4 Conclusion

We have used the method of reflections to compute the potential matrix for sphere-sphere and spheroid-sphere conductors. This allows us to determine the electrostatic forces and torques acting on these conductors in the far field regime. The formulation is general enough to be applied to arbitrary shapes as long as their singularity solutions are known, as discussed in Chapter 2. We also compute the electrostatic force under the lubrication approximation for nearly touching

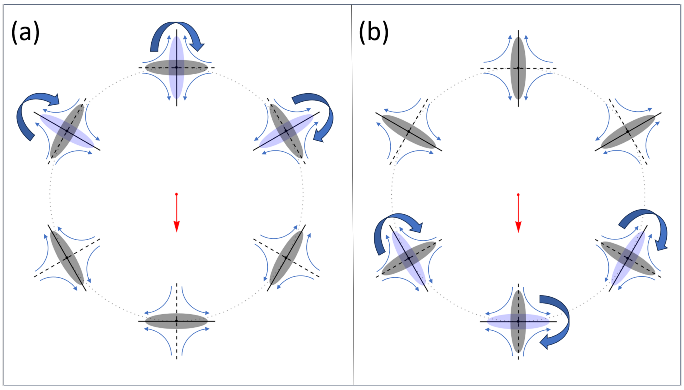

Figure 5.13: Schematic showing the favorable orientations of a sedimenting spheroid interacting with another sedimenting spheroid through electrostatic and hydrodynamic interactions in the far-field regime. In the case of purely hydrodynamic interactions, one spheroid disturbs the flow as a force monopole (indicated by the red arrow) and causes the other spheroid to align along the extensional axis of the locally disturbed strain field (indicated by blue arrows). When electrostatic interactions are included, the electrostatic torque can either compete with or reinforce the hydrodynamic alignment, depending on whether the spheroid is in a trailing or leading position. The black-shaded spheroids represent the favorable orientations due to electrostatic effects, while the light blue-shaded spheroids indicate those due to hydrodynamic effects. (a) For like-charged spheroids, the electrostatic torque competes with the hydrodynamic alignment for a trailing spheroid, as indicated by the arrows, while it reinforces the alignment for a leading spheroid. (b) For oppositely charged spheroids, the effects are reversed: the electrostatic torque competes with the hydrodynamic alignment for a leading spheroid and reinforces it for a trailing spheroid. This has implications for changing the stability of dilute suspensions of charged spheroids.

conductors in the axisymmetric configuration. To determine this close-range force accurately, an order one constant δ is needed, which has been determined using the Boundary Integral Method (BIM). We also test the validity of the method of reflections with the BIM when the conductors are closely separated. The results show that the second reflection works well until the separation is of the order of the size of the conductors.

The anisotropy of the problem of electrostatic interaction between a spheroid and a sphere results in the electrostatic torque. This torque tends to align the spheroid-sphere system in a manner different from the alignment due to pure hydrodynamic interactions [95], see figure 5.13. This naturally prompts the question: how does the instability in a dilute suspension of sedimenting spheroids change when electrostatic effects are taken into account? This chapter offers a foundational approach for computing electrostatic forces and torques on anisotropic particle pairs, demonstrated with example cases for a spheroid-sphere system, using the potential matrix. In the dilute regime, the simpler first-reflection expressions (equation (5.36) and (5.37)) can be used to account for electrostatic interactions between spheroids and study the evolution of density perturbations in a spheroid suspension.

This chapter draws extensively on concepts from micro-hydrodynamics but deliberately excludes its effects to avoid additional complexity. However, in natural settings, micro-hydrodynamics and electrostatic effects often act together. Understanding the role of electrostatic forces in clustering within clouds, for instance, sheds light on the formation and dynamics of ice crystals and droplets. While hydrodynamic-driven clustering through turbulence has been extensively explored [84, 158], the role of electrostatic interactions remains under-examined. Such insights can further our understanding of processes such as rain initiation, hail formation, and the structural evolution of clouds under varying atmospheric charge distributions. Beyond atmospheric science, applications extend to areas like the control of particulate matter in industrial filtration [149], the alignment of particles in electric fields in colloidal chemistry [151], and the behaviour of charged proteins in biophysics [150], where electrostatic torques influence assembly and organization.

6

Intermittency and Vorticity Fluctuations in Two-dimensional Dusty Turbulence

> *"The truth is, most of us discover where we are heading when we arrive."*
> *— Calvin, from Calvin and Hobbes by Bill Watterson*

This chapter is based on a work that is to be submitted for publication. I gratefully acknowledge Professor Samriddhi Sankar Ray and Professor Prasad Perlekar for their guidance and contributions.

6.1 Introduction

Turbulence is a ubiquitous phenomenon in nature, occurring in a wide range of systems from the chaotic flow of rivers and ocean currents [159–161] to the movement of gases in the atmosphere [162, 163] and the dynamics of astrophysical plasmas [164, 165]. In each of these settings, turbulence plays a critical role in determining the transfer and mixing of energy, momentum, and matter, shaping large-scale dynamics and structures. When particles such as droplets, dust, or biological entities are introduced into turbulent flows, their interactions with the turbulent environment add layers of complexity. Studying particles in turbulent flows is important across various fields: in atmospheric science, particle clustering may affect processes like cloud formation and rain initiation [87, 166]; in oceanography, particles impact nutrient transport and marine ecosystems [27, 167]; and in industrial contexts, they influence mixing and reaction rates in processes involving sprays or suspensions [168, 169].

Research has traditionally focused on the impact of turbulence on particles, often neglecting the influence of the particles on the turbulent flow itself [170]. These studies have shown that turbulent flows influence particle dynamics, often leading to particle clustering [143, 171]. This clustering effect has been implicated as a potential mechanism in phenomena like raindrop formation and sediment transport [87, 166, 172]. Even though a single particle may have a minimal effect on the flow field, dense clusters of particles formed due to turbulence can strongly influence the local flow dynamics. Therefore, understanding how particles influence the flow field is crucial.

Recent studies, however, have begun addressing this two-way interaction, often under the term "dusty flows" [91, 173, 174]. This two-way coupling is achieved by adding a feedback force in the Navier-Stokes equation, consistent with the momentum conservation of the complete fluid-particle system [93]. Previous research on the impact of particles in two-dimensional turbulence has shown reduced particle clustering and a flattening of the energy spectrum [91]. This work has motivated further studies into particle feedback in simpler background flows, such as a single vortex, the merging of co-rotating vortices, and simple shear flows. These investigations reveal the emergence of new instabilities arising from the two-way coupling between particles and flow [89, 90, 175, 176].

In this Chapter, we build on these considerations to systematically investigate the effects of particle feedback on the vorticity field of two-dimensional turbulence. After incorporating the dust feedback using point forces, as described in Section 6.2, we review the fundamental properties of energy and enstrophy cascades and spectral scaling in Section 6.3. In Section 6.4.1, we examine the effect of dust feedback on the Okubo–Weiss parameter, which characterizes the local topology of the fluid velocity field. This is followed by analyzing the one-point Eulerian vorticity statistics. To investigate the intermittency induced by dust, we study two-point Eulerian vorticity statistics and examine how the second-order vorticity structure function depends on the dust feedback. We then move on to the spectral-space analysis in Section 6.4.2. The observed dual scaling in the energy spectra motivates an analysis of the cumulative vorticity and velocity fluxes. We conclude the chapter with a summary of key findings in Section 6.5.

6.2 Model description

We implement the two-way coupling using the same model as described in [91]. The dust particles are assumed to be heavy inertial particles of size a, much smaller than the Kolmogorov length scale η. Under this assumption, the force exerted by the fluid on the i^{th} particle is best approximated by the linear Stokes drag. If the position of i^{th} particle is denoted by $\boldsymbol{X}$ and its velocity by $\boldsymbol{V}$, then its equation of motion is given by:

$$\frac{d\boldsymbol{X}_i}{dt} = \boldsymbol{V}_i(t), \quad \frac{d\boldsymbol{V}_i}{dt} = \frac{1}{\tau_p}[\boldsymbol{u}(\boldsymbol{X}_i, t) - \boldsymbol{V}_i], \tag{6.1}$$

where $\tau_p \sim a^2\rho_r/\nu$ is the relaxation time scale of a dust particle. Here $\rho_r = \rho_p/\rho_f$ denotes the density ratio between the particles and the fluid, and ν is the kinematic viscosity of the fluid. As discussed in **Chapter 2**, when the density ratio $\rho_r \gg 1$ such that the product $\rho_r Re_p \sim O(1)$, particle inertia becomes significant, and the system is no longer in the overdamped regime. In this Chapter, we will therefore drop the assumption of the overdamped limit. For the fluid-particle system to be momentum-conserving, an equal and opposite force must be included in the equation of motion for the fluid. This leads to the two-way coupling, which, in terms of the scalar vorticity field $\omega = \boldsymbol{\nabla} \times \boldsymbol{u}$ is given by

$$\partial_t \omega(\boldsymbol{x}, t) + \boldsymbol{u} \cdot \boldsymbol{\nabla}\omega(\boldsymbol{x}, t) = \nu\nabla^2\omega(\boldsymbol{x}, t) - \alpha\,\omega(\boldsymbol{x}) + f(\boldsymbol{x}) + \boldsymbol{\nabla} \times \boldsymbol{F}^d(\boldsymbol{x}, t). \tag{6.2}$$

Here α is the Ekman drag coefficient and $f(\boldsymbol{x}) = -f_0 k_f \cos(k_f y)$ is the vorticity contribution of the external forcing with amplitude f_0 at the forcing wavenumber k_f. The force per unit mass of the fluid, exerted by the particles on the fluid, is given by

$$\boldsymbol{F}^d(\boldsymbol{x}, t) = \sum_{i=1}^{N_p} \frac{m}{\tau_p \rho_f}[\boldsymbol{V}_i(t) - \boldsymbol{u}(\boldsymbol{X}_i, t)]\delta^2(\boldsymbol{x} - \boldsymbol{X}_i), \tag{6.3}$$

where m is the mass of a dust particle and N_p is the total number of particles. The relevant dimensionless numbers, apart from the Reynolds number Re, are the Stokes number St and the mass loading parameter ϕ_m. These are defined as

$$St \equiv \tau_p/\tau_\eta, \quad \phi_m \equiv mN_p/(\rho_f L^2), \tag{6.4}$$

where $\tau_\eta = \sqrt{\nu/\epsilon}$ is the Kolmogorov time scale, $L = 2\pi$ is the size of the periodic box and ϵ is the energy dissipation rate.

To implement the two-dimensional δ^2 function on the grids of linear dimension h, we use the following prescription for a 1D δ function [91, 92]:

$$\delta(x - X) = \begin{cases} \frac{1}{4h}\left\{1 + \cos\left[\frac{\pi(x-X)}{2h}\right]\right\}, & |x - X| \leq 2h, \\ 0, & \text{otherwise.} \end{cases} \tag{6.5}$$

With this prescription, the fluid velocity at the particle position $\boldsymbol{X}$ is interpolated as

$$\boldsymbol{u}(\boldsymbol{X}, t) = \sum_{\boldsymbol{x}} \boldsymbol{u}(\boldsymbol{x}, t)\delta^2(\boldsymbol{x} - \boldsymbol{X})h^2. \tag{6.6}$$

The localized cosine discrete δ-function defined in equation (6.5) is used both for spreading particle forces to the grid and for interpolating the fluid velocity to particle positions, as in equation (6.6), following the standard immersed boundary method formulation [92]. A uniform spatial discretization is done using N^2 collocation points inside the periodic domain of size $L \times L$, with $L = 2\pi$. The Fourier pseudo-spectral method is used with the maximum resolved wavenumber $k_{\max} = N/3$ after de-aliasing. We use a second-order Runge-Kutta scheme to evolve both fluid and particles in time. The vorticity initial condition is taken to be $\omega(\boldsymbol{x}, 0) = -f_0 k_f \nu[\cos(k_f x) + \cos(k_f y)]$. The particles are randomly distributed within the domain, following a uniform distribution, and their initial velocities are set to zero. Once the statistically steady state is reached, the simulations are continued for approximately $170\tau_\eta$. The corresponding kinetic energy as a function of time for various values of ϕ_m is shown in Figure 6.1. Since the particles require some time to evolve from their initial homogeneous distribution into clusters, we wait for about $35\tau_\eta$ before collecting the data for statistical analysis.

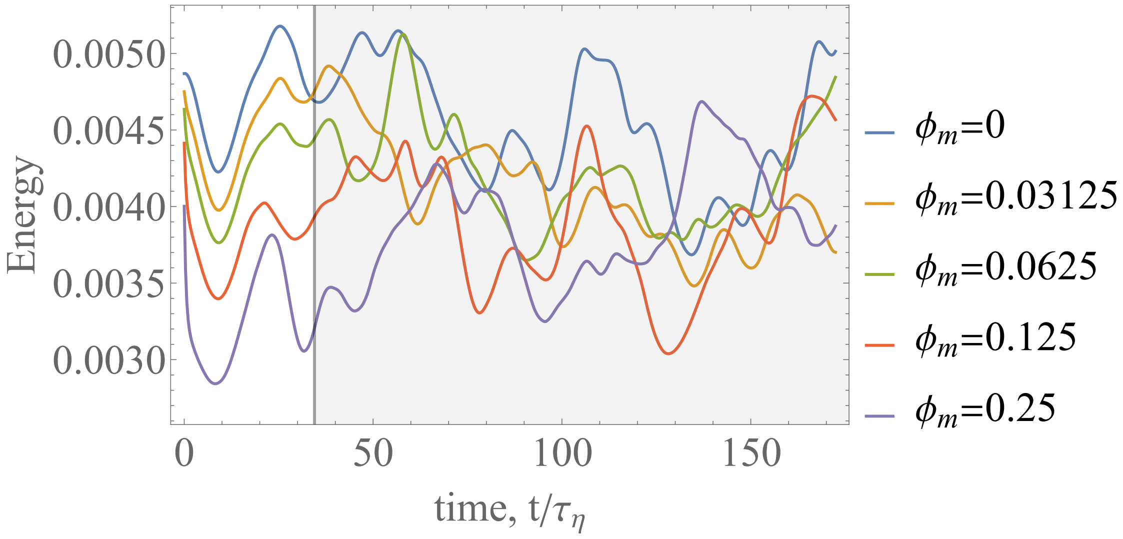

Figure 6.1: **Energy vs time.** Kinetic energy, $1/2 \sum_k |\hat{\boldsymbol{u}}_k|^2$, as a function of non-dimensional time for different values of mass loading ϕ_m, after the system has reached statistically steady state. The data gathered for statistical analysis is in the time range $t \in [34, 170]\tau_\eta$, as indicated by the shaded region.

The parameters used in the simulations are tabulated in Table 6.1. These parameters result in two-dimensional turbulence in the forward-cascade regime with the Taylor-microscale $\lambda = \sqrt{\nu E/\epsilon} \approx 0.2$, and the Taylor-based Reynolds number $Re = u_{rms}\lambda/\nu \approx 1866$, where $u_{rms} = \sqrt{2E} \approx 0.1$.

N	ν	α	f_0	k_f	ϵ	$\eta = (\nu^3/\epsilon)^{1/4}$	$\tau_\eta = \sqrt{\nu/\epsilon}$	β
1024	10^{-5}	0.01	5×10^{-3}	4	1.2×10^{-6}	5.4×10^{-3}	2.9	2.8×10^{-4}

Table 6.1: Table of Parameters used in the simulation.

We vary the number of particles N_p between $6.25 \times 10^4 - 5 \times 10^5$ to achieve the mass loading ϕ_m in the range $0.0325 - 0.25$. The numerical code is validated by successfully reproducing several results reported by Pandey et al. [91].

6.3 A brief review of 2D turbulence

Before moving on to the results, let us briefly review some relevant properties of *clean* 2D turbulence, where dust does not influence the fluid flow field. As discussed in [160–162, 177], two-dimensional turbulence exhibits markedly different behavior from its three-dimensional (3D) counterpart, owing primarily to the absence of vortex stretching. In 3D flows, vortex stretching acts as a key nonlinear mechanism that transfers energy to smaller scales, enabling the development of fine-scale structures and ultimately leading to the celebrated phenomenon of the energy cascade [160–162]. This lack of vortex stretching fundamentally alters the cascade dynamics [177–179].

Two-dimensional flows have two quadratic invariants in the inviscid limit, the kinetic energy $E = \langle|\boldsymbol{u}|^2\rangle/2$, and the enstrophy, $\Omega = \langle|\omega|^2\rangle/2$, where the angle brackets denote spatial averaging over a periodic domain [161, 177]. In the statistically stationary state of forced 2D turbulence, let $l_f \sim k_f^{-1}$ denote the characteristic forcing scale, $l_\alpha \sim k_\alpha^{-1}$ the large-scale friction (or drag) scale[1], and $l_\nu \sim k_\nu^{-1}$ the small-scale viscous dissipation scale. When these scales are well separated such that $l_\nu \ll l_f \ll l_\alpha$, the system exhibits a dual cascade behavior: enstrophy is transferred to smaller scales and dissipated near l_ν, while energy is transferred to larger scales and dissipated near l_α due to large-scale friction [177–179]. This behavior can be understood by considering the balance of energy and enstrophy fluxes in the statistically steady state [177]. Let ϵ_I and η_I denote the rates of energy and enstrophy injection at the forcing scale. These must balance the corresponding dissipation rates at the viscous and friction scales, denoted by

---

[1] Although friction removes energy from all modes equally, at a rate $-\alpha|\hat{\boldsymbol{u}}_k|^2$, it has significant effect only at small wavenumbers, where the modes contain most of the system's energy.

ϵ_ν, η_ν (viscous dissipation) and $\epsilon_\alpha, \eta_\alpha$ (frictional dissipation). The conservation laws then imply:

$$\epsilon_I = \epsilon_\nu + \epsilon_\alpha, \quad \eta_I = \eta_\nu + \eta_\alpha.$$

Since $l_\alpha^2 \sim \epsilon_\alpha/\eta_\alpha$, $l_f^2 \sim \epsilon_f/\eta_f$ and $l_\nu^2 \sim \epsilon_\nu/\eta_\nu$, we get

$$\frac{\epsilon_\nu}{\epsilon_\alpha} = \left(\frac{l_\nu}{l_\alpha}\right)^2 \frac{(l_\alpha/l_f)^2 - 1}{1 - (l_\nu/l_f)^2} \ll 1, \quad \frac{\eta_\nu}{\eta_\alpha} = \frac{(l_\alpha/l_f)^2 - 1}{1 - (l_\nu/l_f)^2} \gg 1. \tag{6.7}$$

This establishes the direction of the energy and enstrophy cascade. This separation of scales gives rise to two distinct inertial ranges [177]:

- An *inverse energy cascade* in the range $l_f \ll l \ll l_\alpha$, where the energy spectrum follows the scaling $E(k) \sim k^{-5/3}$.
- A *forward enstrophy cascade* in the range $l_\nu \ll l \ll l_f$, where the energy spectrum scales as $E(k) \sim k^{\xi(\alpha)}$,

with the exponent $\xi(\alpha)$ depending on the large-scale friction coefficient α, and hence non-universal. In the decaying two-dimensional turbulence without large-scale friction ($\alpha = 0$), the energy spectrum scaling of $\xi = -3$ follows in the forward enstrophy cascade regime [161, 177]. This work is concerned with the forward enstrophy cascade regime. A schematic illustration of this dual cascade picture is shown in Figure 6.2.

In the forward cascade regime, the parameters from Table 6.1 used in the simulation result in the energy scaling as $E(k) \sim k^\xi$, with $\xi \approx -3.9$ for the $\phi_m = 0$ case. It has been shown that as the mass loading increases, this scaling exponent decreases [91]. Interestingly, a dual scaling in the forward cascade regime has been observed across a critical wavenumber $k_c \approx 15$ [91]. For wavenumber $k < k_c$, the spectral exponent $\xi \approx -4$ with approximately no variation with the mass loading ϕ_m. For wavenumber $k > k_c$, the spectral exponent ξ decreases below -4 as the mass loading is increased. This dual scaling in the energy spectra prompts an important question: Can the effect of dust momentum feedback be modeled using a small-scale (large wavenumber) forcing? We address this by analyzing the cumulative energy and enstrophy flux in the subsequent section.

6.4 Results

6.4.1 Physical space analysis

We are interested in how dust particles modify the turbulence, focusing on Eulerian statistics of the vorticity field. Before examining the full Eulerian statistics, we first

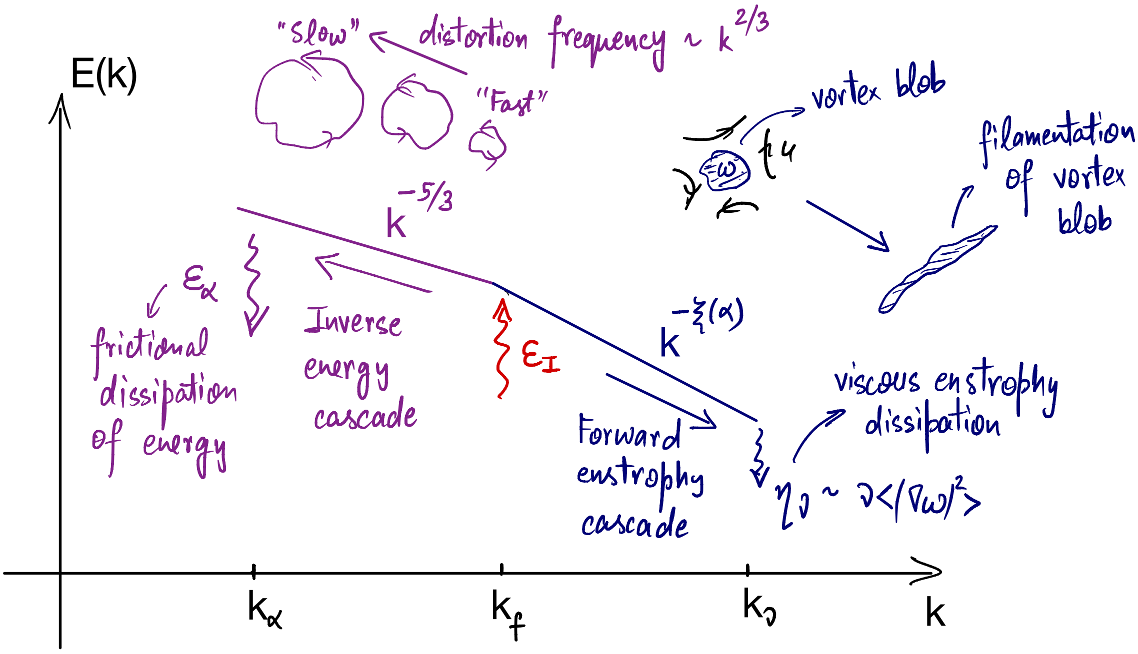

Figure 6.2: **Schematic of dual cascade in 2D turbulence.** Energy injected at an intermediate forcing scale k_f cascades inversely toward large scales ($k < k_f$), forming the inverse energy cascade with a $k^{-5/3}$ scaling and eventually dissipating via large-scale frictional drag ϵ_α. Simultaneously, enstrophy cascades forward to smaller scales ($k > k_f$), giving rise to a $k^{\xi(\alpha)}$ spectrum, where it is dissipated by viscosity at scale k_ν through the enstrophy dissipation rate $\eta_\nu \sim \nu\langle|\nabla\omega|^2\rangle$. Vortex blobs generated near k_f undergo filamentation due to shearing, contributing to the forward enstrophy cascade. The associated distortion frequency scales as $k^{2/3}$, with smaller blobs experiencing faster deformations [177]. The sketch also qualitatively illustrates the transformation of coherent structures during the cascade process.

analyze the local streamline topology at the particle positions. This is motivated by the fact that inertial particles tend to cluster in strain-dominated regions (open streamlines) and avoid vorticity-dominated regions (closed streamlines) [143]. Quantifying how often particles encounter each type of region can provide insight into their spatial distribution and interaction with the flow. A standard measure of local streamline topology is the Okubo–Weiss parameter, which we compute at the particle positions as described below.

To investigate whether momentum coupling alters the local topological features of the flow, we analyze the velocity gradient tensor $\partial_j u_i$ at a given point [180]. For incompressible flows, only one independent invariant remains, namely the determinant of the velocity gradient tensor, known as the Okubo–Weiss parameter [181]: $\Lambda = \det(\partial_j u_i)$. The sign of Λ distinguishes between vorticity-dominated (elliptic) regions with closed streamlines ($\Lambda > 0$) and strain-dominated (hyperbolic) regions with open streamlines ($\Lambda < 0$) [180, 182]. One can rewrite Λ as follows

$$\Lambda = \det(\partial_i u_j) = \frac{1}{2}(W_{ij}W_{ij} - S_{ij}S_{ij}), \quad W_{ij} \equiv \frac{1}{2}(\partial_j u_i - \partial_i u_j), \quad S_{ij} = \frac{1}{2}(\partial_j u_i + \partial_i u_j). \tag{6.8}$$

Therefore, the sign of Λ at a given point determines whether the flow is vortical

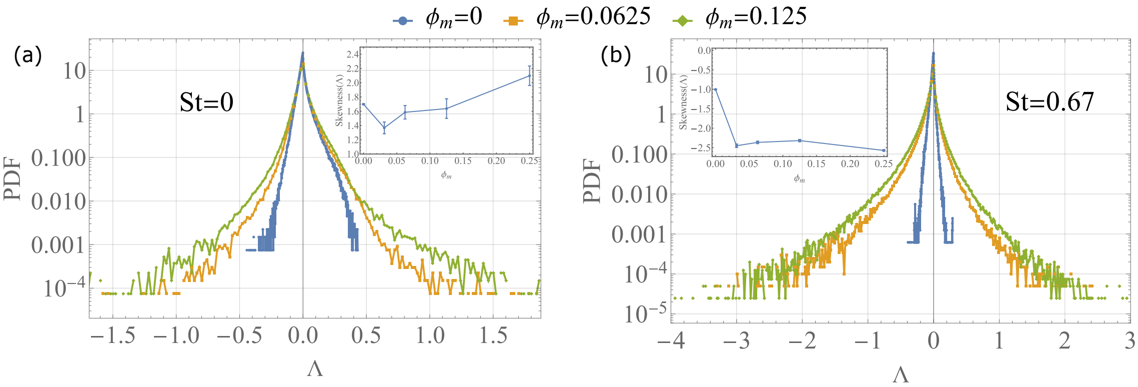

Figure 6.3: **Statistics of the Okubo-Weiss parameter**. (a) The probability distribution of the Okubo-Weiss parameter Λ computed at the location of the tracer particles. This is equivalent to the Eulerian computation of Λ. The positive skewness of the PDF shows that the fluid field is vorticity dominated. (b) The probability distribution of the Okubo-Weiss parameter Λ computed at the location of the inertial particles with Stokes number $St = 0.67$. Since inertial particles sample strain-dominated regions, the PDF shows negative skewness. The error bars for the kurtosis values in the insets of (a) and (b) are obtained via bootstrapping.

or strain-dominated in that region. The probability distribution function of Λ is plotted in Figure 6.3. For $St = 0$ case, we see that the increase in the mass loading ϕ_m increases the maximum and minimum values of Λ, indicating that the flow develops intense vortical and strain-dominated regions. The positive skewness of the PDF shows that vortical regions dominate the fluid flow field. The probability distribution function for non-zero Stokes number shows the nature of the flow field evaluated at the location of inertial particles. Since inertial particles leave the vortical regions and cluster in the strain-dominated regions, we see in Figure 6.3(b) that the PDF of Λ for non-zero Stokes number is negatively skewed.

We now focus on the Eulerian statistical properties of the dusty vorticity field over the entire domain, without conditioning on particle positions. We start by studying the one-point Eulerian vorticity statistics. Since there is a visible difference in the density plot of the vorticity field (see figure 6.4(a) and (b)), the probability distribution function (PDF) of normalized vorticity values provides a good quantitative measure of the effect of mass-loading ϕ_m. As shown in Figure 6.4(c), the PDF, which is Gaussian for zero mass-loading, becomes increasingly flat for higher mass-loading. Consequently, the kurtosis of the PDF increases monotonically with the mass-loading parameter ϕ_m. This shows that we are more likely to observe intense vortices as the momentum feedback of the dust becomes stronger.

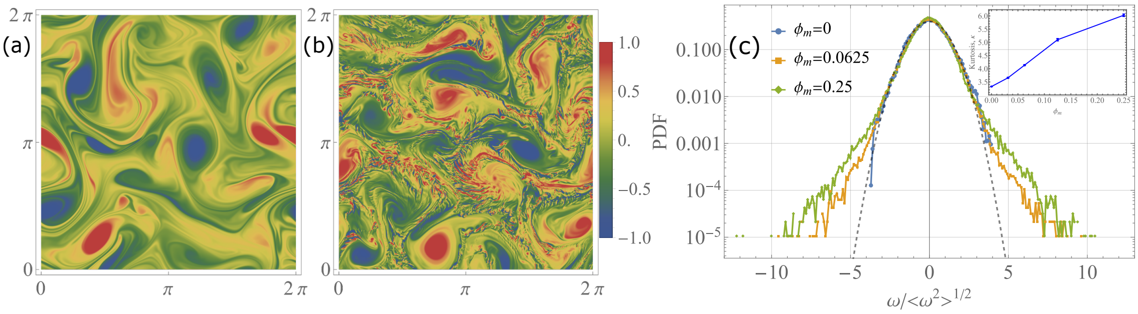

Figure 6.4: **One point Eulerian Vorticity Statistics.** Vorticity fields $\omega(\boldsymbol{x})$ for mass loading (a) $\phi_m = 0$ and (b) $\phi_m = 0.125$ with $N_p = 2.5 \times 10^5$ particles of Stokes numbers $St = 0.67$. (c) The probability distribution functions (PDF) of $\omega(\boldsymbol{x})$, normalized with its variance, for $\phi_m = 0$, $\phi_m = 0.0625$, and $\phi_m = 0.25$. The black dashed Gaussian curve is a guide to the eye. In the inset, we plot the kurtosis κ^{ω} as a function of ϕ_m. The error bars for the kurtosis values in the inset of (c) are obtained via bootstrapping.

To investigate the effect of dust momentum feedback on the intermittency, we examine the two-point Eulerian vorticity difference statistics. The p-th order vorticity structure function $S_p^{\omega}(r)$ is defined as

$$S_p^{\omega}(r) \equiv \langle|\delta_r \omega|^p\rangle = \langle|\omega(\boldsymbol{x}+\boldsymbol{r}) - \omega(\boldsymbol{x})|^p\rangle \sim r^{\zeta_p}, \tag{6.9}$$

where the average $\langle . \rangle$ is defined over the spatial positions $\boldsymbol{x}$ and all the directions $\boldsymbol{r}/|\boldsymbol{r}|$ for a given $r = |\boldsymbol{r}|$. The vorticity field is said to be intermittent if the structure function exponent ζ_p is a nonlinear function of p [183]. The intermittency is tied with the scale-invariance or self-similarity of this two-point correlation function. Following [183], let $X \equiv \delta_r \omega / \langle \delta_r \omega^2 \rangle^{1/2}$ have the probability distribution given by $P_r(X_r)$. If the vorticity statistics shows self-similarity in the forward cascade regime ($k_\nu^{-1} \ll r \ll k_f^{-1}$), we must have $P_{\lambda r}(X_{\lambda r}) = P_r(X_r)$, i.e. $P_r(X_r)$ is independent of r. Therefore, self-similarity in vorticity statistics implies

$$S_p^{\omega}(r) = \left\langle \left(\frac{\delta_r \omega}{\langle \delta_r \omega^2 \rangle^{1/2}} \right)^p \right\rangle \langle \delta_r \omega^2 \rangle^{p/2} = \langle \delta_r \omega^2 \rangle^{p/2} \int |X_r|^p P_r(X_r)\, dX_r \sim r^{p\,\zeta_2/2} = r^{\zeta_p} \tag{6.10}$$

This shows that the vorticity structure function exponent $\zeta_p = p(\zeta_2/2)$ is a linear function of p. Therefore, by looking at the PDF of the Eulerian vorticity difference at two different length scales, one can infer whether the vorticity field is intermittent.

This PDF is plotted in Figure 6.5(a). Regardless of the dust momentum feedback, the vorticity difference statistics are not scale invariant, indicating intermittency in the vorticity field. The presence of intermittency in the vorticity field, even in the absence of the dust feedback, is consistent with the results of [183]. The kurtosis of the PDF also depends sharply on the scale r/η. Note that for smaller values of r/η, we have a non-monotonic dependence of the kurtosis as a function of ϕ_m, as shown in the inset of Figure 6.5(b).

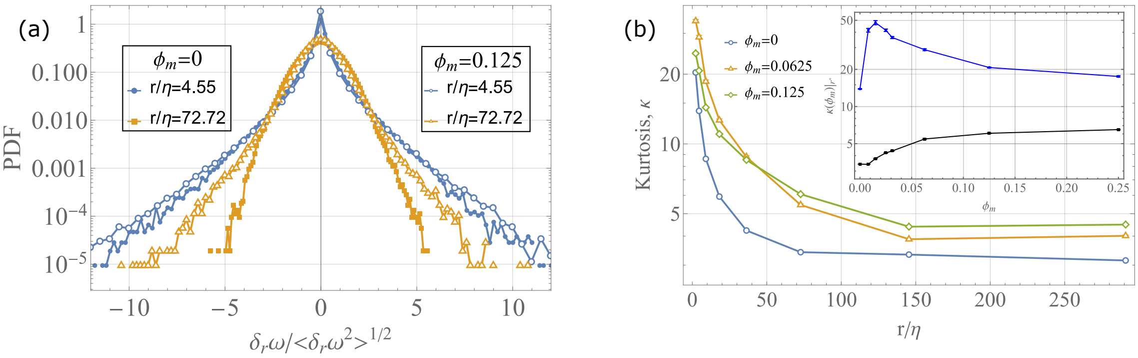

Figure 6.5: **Two-point Eulerian Vorticity Difference Statistics.** The probability distribution functions (PDF) of the normalized Eulerian vorticity differences $\delta_r \omega = \omega(\boldsymbol{x} + \boldsymbol{r}) - \omega(\boldsymbol{x})$, for two different values of the separation $r = |\boldsymbol{r}|$, and for $\phi_m = 0$ and $\phi_m = 0.125$. (b) We show plots of the kurtosis $\kappa(r)$ of such distributions, as a function of r, for different values of ϕ_m. In the inset, we show the values of the kurtosis $\kappa(\phi_m)|_{r_*}$ at a fixed r_* as a function of ϕ_m. The separations r are all chosen in the forward cascade inertial range. The error bars for the kurtosis values in the inset of (b) are obtained via bootstrapping.

We look at the scaling of second-order vorticity structure function $S_2^{\omega}(r) \sim r^{\zeta_2}$ as a function of the mass loading ϕ_m in Figure 6.6(a). As the mass loading parameter ϕ_m increases, the second-order structure function exponent ζ_2 tends toward zero (see Figure 6.6(b)). This behavior reflects a progressive loss of spatial correlations in the vorticity field, which becomes increasingly rough due to localized vorticity generation by the suspended particles. In this regime, particle-induced forcing at small scales disrupts coherent flow structures, leading to a breakdown of classical turbulent features. As a result, the utility of the vorticity structure function diminishes, signaling a transition to a highly disordered, particle-dominated flow.

6.4.2 Spectral-space analysis

As discussed in Section 6.3, the energy spectrum in dusty 2D turbulence exhibits a dual-scaling behavior across a critical wavenumber k_c (see Figure 6.7(a) and (b)). This observation motivates us to ask whether the momentum feedback from

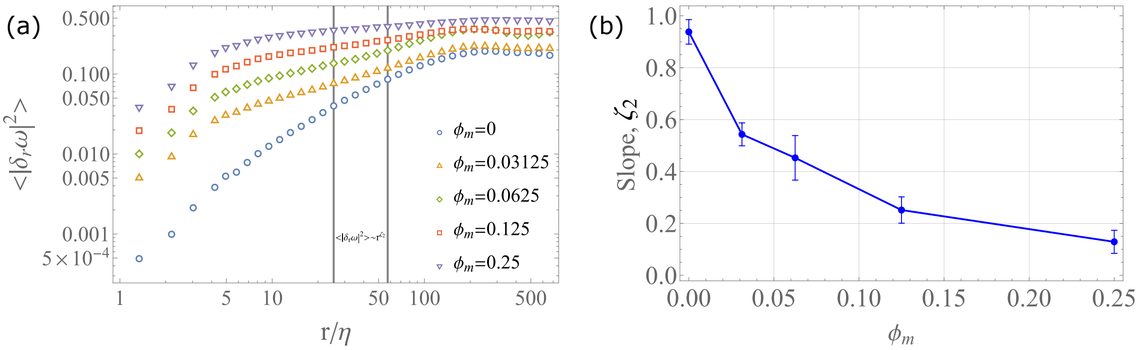

Figure 6.6: **Second-order vorticity structure function.** (a) Scaling of second-order vorticity structure function with r/η for various values of ϕ_m. The vertical lines indicate the inertial range over which structure function exponents are computed. (b) We show the scaling exponent ζ_2 as a function of ϕ_m, fitted using local slopes computed between the two vertical lines in the main plot. The error bars for the ζ_2 values are obtained via local slope analysis.

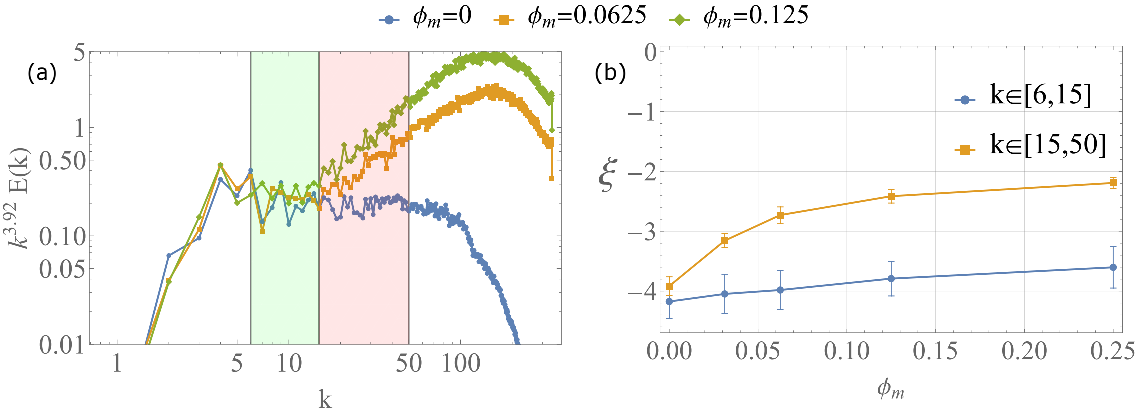

Figure 6.7: **Compensated energy spectra.** (a) Energy spectra compensated by $k^{3.92}$ for various values of ϕ_m, revealing two distinct scaling regimes. In the first regime (green shaded region), corresponding to wavenumbers $k \in [6, 15]$, the energy spectrum exhibits a scaling close to k^{-4} across all values of ϕ_m. In the second regime (red shaded region), for $k \in [15, 50]$, the spectral slope varies significantly with ϕ_m. (b) Scaling exponent ξ as a function of ϕ_m for the two regimes. In the range $k \in [6, 15]$, ξ shows minimal dependence on ϕ_m. In contrast, for $k \in [15, 50]$, the exponent decreases steadily from $\xi \approx -3.9$ at $\phi_m = 0$ to $\xi \approx -2.2$ at $\phi_m = 0.25$. The error bars for the ξ values are obtained via standard deviation across 400 samples.

dust can be effectively modeled as an additional small-scale forcing. From the phenomenology of two-dimensional turbulence, it is well known that forcing at a high wavenumber k_{f2} (i.e., small spatial scales) generates an inverse cascade of energy toward larger scales, for wavenumbers $k < k_{f2}$. In our system, where an existing large-scale forcing is already present at wavenumber k_f, the presence of a second forcing scale naturally leads to a dual-scaling regime in the energy spectrum, spanning the intermediate range between k_f and k_{f2}. Specifically, we observe a non-universal spectral scaling characterized by an exponent $\xi(\alpha)$ just above k_f, and a classical inverse cascade scaling of $-5/3$ just below k_{f2}. Given that the dust feedback acts as a distribution of point forces on the fluid, this dual-scaling suggests that a dual-forcing model may offer a reasonable approximation of the dust's momentum exchange. For such a model to be valid, however, it is essential that the dusty flow exhibits a cumulative negative energy flux at high wavenumbers, indicative of an inverse cascade driven by the small-scale (dust-induced) forcing. The cumulative energy and enstrophy flux are defined as

$$\Pi^u(k) \equiv \langle \sum_{m\leq k} \hat{\boldsymbol{u}}_m \cdot \widehat{(\boldsymbol{u}\cdot\nabla\boldsymbol{u})}_{-m} \rangle, \quad \Pi^\omega(k) \equiv \langle \sum_{m\leq k} \widehat{\omega}_m \widehat{(\boldsymbol{u}\cdot\nabla\omega)}_{-m} \rangle. \tag{6.11}$$

The classical picture of energy and enstrophy cascades requires that their respective fluxes remain scale independent in the inertial ranges. However, even in the absence of particles ($\phi_m = 0$), the presence of cumulative frictional drag leads to deviations from this ideal behavior, resulting in non-constant fluxes. As the mass loading ϕ_m is increased, the cumulative energy flux shows only a slight modification, with a weak signature of inverse energy transfer near the forcing scale k_f (see Figure 6.8(a)). Crucially, there is no evidence of negative cumulative energy flux at higher wavenumbers that would suggest an inverse cascade driven by dust feedback. This implies that the momentum exchange due to dust may not be adequately captured by modeling it as a simple small-scale forcing. In contrast,

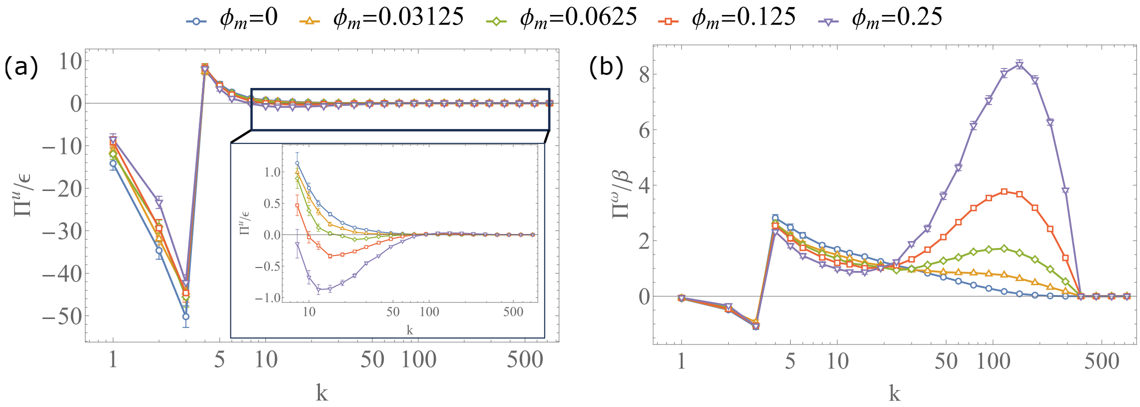

Figure 6.8: (a) Cumulative energy flux $\Pi^u(k) \equiv \langle \sum_{m\leq k} \widehat{\boldsymbol{u}}_m \cdot \widehat{(\boldsymbol{u}\cdot\nabla\boldsymbol{u})}_{-m} \rangle$ scaled by the energy dissipation rate ϵ, for various values of ϕ_m. The inset shows the cumulative energy flux for wavenumbers greater than the forcing wavenumber $k_f = 4$. (b) Cumulative enstrophy flux $\Pi^\omega(k) \equiv \langle \sum_{m\leq k} \widehat{\omega}_m \widehat{(\boldsymbol{u}\cdot\nabla\omega)}_{-m} \rangle$ scaled by the enstrophy dissipation rate β, for various values of ϕ_m. The error bars for the flux values in (a) and (b) are obtained via bootstrapping.

the influence of dust at small scales is reflected in the cumulative enstrophy flux, which increases with mass loading, especially at large wavenumber (see Figure 6.8(b)). These observations suggest that while dust particles enhance enstrophy transfer by injecting small-scale vortical structures, their contribution to energy transfer across small scales is absent.

6.5 Summary and conclusion

In this chapter, we investigated the collective influence of inertial particles on two-dimensional (2D) turbulence. We assumed that the dust particles are much smaller than any characteristic flow scale, which allowed us to neglect the particle Reynolds number and model the hydrodynamic force on the particles using linear Stokes drag. Given that the particles are significantly heavier than the fluid, dust inertia was included. To ensure momentum conservation in the fluid-dust system, we incorporated the feedback from particles onto the fluid using localized point forces modeled by Dirac delta functions. The strength of this momentum coupling is characterized by a dimensionless mass-loading parameter, ϕ_m.

After validating our model against the results of Pandey et al. [91], we examined the one-point Eulerian vorticity statistics. Since dust particles inject vorticity at small scales and roughen the vorticity field, the probability distribution function (PDF) of vorticity broadens with increasing ϕ_m, indicating a higher likelihood of extreme vorticity events. We also studied the local topology of the velocity field through the PDF of the Okubo–Weiss parameter, Λ. While the skewness of this PDF remains negative, implying a dominance of vortical regions, the increase in the extreme values of Λ with ϕ_m suggests that both vortical and strain-dominated regions intensify with stronger dust feedback.

To probe intermittency, we analyzed the PDF of two-point Eulerian vorticity differences. Although the vorticity field remains intermittent for all values of ϕ_m, the kurtosis of the normalized vorticity difference exhibits a non-monotonic dependence on ϕ_m. As mass loading increases, the vorticity field also loses spatial correlation, a trend further supported by the behavior of the second-order vorticity structure function.

Previous work has reported a dual-scaling regime in the energy spectra of dusty 2D turbulence [91]. Motivated by this, we examined the cumulative velocity and vorticity fluxes to assess whether the observed spectral features can be interpreted through a simple model of small-scale forcing. However, the absence of an inverse energy cascade in the cumulative energy flux at high wavenumbers suggests that the influence of dust feedback is more intricate than what a small-scale forcing analogy can capture.

In conclusion, the emergence of non-universal spectral and structure function scalings, along with the loss of spatial correlations in the vorticity field with increasing mass loading, highlights the nontrivial influence of dust feedback on two-dimensional turbulence. However, these results can be sensitive to modeling choices, such as the form of the drag law, and to numerical factors, including the accuracy of interpolation schemes [93]. As such, caution must be exercised when attempting to generalize these findings to the more commonly encountered three-dimensional dusty turbulence. The high computational cost of simulating 3D turbulence with fully resolved Lagrangian particle feedback [168], combined with the added complexity of incorporating finite-size effects and particle shape [184], makes it unlikely that a purely Lagrangian approach will be sufficient. A field-theoretic or coarse-grained modeling framework may offer a more practical and insightful alternative, although such approaches can introduce challenges of their own, for instance, the emergence of shock formations or caustics [180, 185, 186]. Nonetheless, Lagrangian studies like the present one remain essential, as they offer crucial benchmarks for validating and guiding such effective models.

7

FINAL THOUGHTS AND PERSPECTIVES

"Somewhere, something incredible is waiting to be known."
— Carl Sagan

This thesis began by examining how particle geometry gives rise to new dynamical behaviours in the overdamped regime of microhydrodynamics. These effects were explored at the single-particle level, through the sedimentation of asymmetric bodies, and at the multiparticle level, via the collective sedimentation of discs. Building on the structural analogy with electrostatics, the study extended to electrostatic interactions between anisotropic conductors. Recognizing particle inertia as another key driver of complex dynamics, the thesis then investigated the role of inertial effects in dusty two-dimensional turbulence using point-particle models. Across these varied settings, the work highlighted how geometry, inertia, and inter-particle interactions collectively shape the emergent dynamics of physical systems.

The sedimentation problems in the overdamped limit discussed in **Chapter 3** highlight the important role of symmetry methods and a dynamical systems approach. At the single-particle level, the geometric symmetries of a body determine the extent of coupling between its translational and rotational degrees of freedom. Such an analysis provides a robust and abstract framework, the predictions of which apply not only to a specific body but to a broader class of bodies that share the same symmetries.

Equally important is the choice of dynamical variables, which can significantly influence our understanding of the system's behaviour. For instance, in **Chapter 3**, the dynamics of di-bilaterals can be examined either using Euler angles or through vertical and horizontal projections of the principal axes. While the three Euler angles offer a seemingly simpler formulation, they obscure the mechanisms underlying the quasi-periodic motion of flutterers. In contrast, using the projections as the dynamical variables, though involving six variables and three constraints, offers deeper insights. The main advantage arises from the fact that these dynamical variables are bounded and constrained to lie on the surface of unit spheres. Moreover, the rotational symmetry about the gravity (vertical) axis leads to a decoupling of vertical and horizontal dynamics, which in turn enables a natural classification of di-bilaterals into settlers, drifters, and flutterers. The origin of quasi-periodicity in flutterers becomes clear when viewed as the ratio of the response frequency of horizontal projections to the periodic driving frequency of the vertical projections. This kind of understanding is difficult to extract using Euler angles alone. The use of continuous and discrete symmetries in the governing equations also allows us to make qualitative predictions, such as the absence of persistent drift or chirality in flutterers, without solving the full equations analytically. Such symmetry-based methods have been applied to more complex flows as well, such as asymmetric particles in shear flows [187]. A natural extension of **Chapter 3** would be to study di-bilaterals whose centres of buoyancy and mass do not coincide, an offset that introduces external torques and could give rise to entirely new dynamical behaviours. Another promising direction is to explore how effectively a flutterer can enhance mixing as it settles.

In **Chapter 4**, a dynamical systems framework is also crucial to understanding the collective sedimentation of discs. By using the method of reflections to improve upon a previously studied point-force model [48], we demonstrated how close-range hydrodynamic interactions change the nature of fixed points. The earlier model was structurally unstable, with eigenvalues lying on the imaginary axis, and non-normal, making it sensitive to perturbations. The improved model reveals that, despite small non-zero growth rates, the non-modal growth is responsible for lattice disruption. While a full understanding of the resulting clusters requires numerical simulations, the dynamical systems perspective offers powerful tools to understand the instability mechanisms. A natural next step would be to extend this study to the collective sedimentation of di-bilaterals. Given the richer dynamics of individual di-bilaterals compared to spheroids, one can expect that the drift mechanism may be replaced or significantly altered, leading to new clustering dynamics.

An important direction in theoretical physics lies in building analogies across domains. Such cross-pollination of ideas can reveal deep structural connections and inspire new methodologies. **Chapter 5** leverages an analogy between microhydrodynamics and electrostatics. The mathematical structure of Stokes flow is one tensorial order higher than that of electrostatics, a fact that has long guided the construction of singularity solutions in microhydrodynamics based on their electrostatic counterparts [188]. Classical electrostatic tools like the method of images have also been borrowed in microhydrodynamics. However, tools originally developed for microhydrodynamics, like Faxén's laws, have remained underexplored in electrostatics [58]. In **Chapter 2**, we extended Faxén's laws, originally formulated for Stokes flow, to electrostatics, enabling a new method of reflections to compute electrostatic interactions between anisotropic bodies. Much like in fluid mechanics, Faxén's laws offer an abstract and elegant framework for connecting the induced multipole moments on a body, due to an arbitrary external field, to the body's singularity solutions. As explored in **Chapter 5**, the electrostatic effects can either counteract or reinforce the hydrodynamic effects. Therefore, this study sets up the ground to investigate the instability of a dilute suspension of charged spheroids.

Chapter 6 marks a shift from the symmetry and geometry-focused earlier chapters to a study of how particle inertia and collective behaviour influence turbulence statistics. It highlights the richness of inertial systems and emphasises the importance of characterising their fundamental behaviours before adding complexity such as particle geometry. In that sense, this chapter stands as a conceptual 'edge' of the thesis, pointing toward a broader landscape of complex systems where geometry, inertia, and collectivity intersect to produce new emergent phenomena.

In summary, this thesis has explored how geometric asymmetries, collective dynamics, and cross-disciplinary analogies shape the behaviour of particles in fluid and electrostatic environments. From symmetry-driven classifications of sedimenting bodies to mathematical analogies that unify distinct physical theories, the work highlights the power of abstraction and structure in understanding complex systems. While many of the ideas presented here are grounded in idealised models, they open pathways for future investigations into more realistic and applied settings. These include sedimentation with buoyancy offsets, mixing due to quasi-periodic settling, collective sedimentation of asymmetric bodies, coupled electro-hydrodynamic systems, and turbulent suspensions of anisotropic particles. As we continue to uncover the rich dynamics of even the simplest objects in a fluid, the role of geometry, symmetry, and inertia will remain central to the ever-expanding landscape of soft matter physics and beyond.

BIBLIOGRAPHY

[1] J. M. Lourenço. *The NOVAthesis LaTeX Template User's Manual*. NOVA University Lisbon. 2021. URL: `https://github.com/joaomlourenco/novathesis/raw/main/template.pdf` (cit. on p. vi).

[2] B. Mandelbrot. *The Fractal Geometry of Nature*. Einaudi paperbacks. Henry Holt and Company, 1983. ISBN: 9780716711865. URL: `https://books.google.co.in/books?id=0R2LkE3N7-oC` (cit. on p. 1).

[3] A. R. Tao, S. Habas, and P. Yang. "Shape control of colloidal metal nanocrystals". In: *small* 4.3 (2008), pp. 310–325 (cit. on p. 1).

[4] J. G. Donaldson, E. S. Pyanzina, and S. S. Kantorovich. "Nanoparticle shape influences the magnetic response of ferro-colloids". In: *ACS nano* 11.8 (2017), pp. 8153–8166 (cit. on p. 1).

[5] A. Jákli, O. D. Lavrentovich, and J. V. Selinger. "Physics of liquid crystals of bent-shaped molecules". In: *Reviews of Modern Physics* 90.4 (2018), p. 045004 (cit. on p. 1).

[6] C. P. Lapointe, T. G. Mason, and I. I. Smalyukh. "Shape-controlled colloidal interactions in nematic liquid crystals". In: *Science* 326.5956 (2009), pp. 1083–1086 (cit. on p. 1).

[7] A. G. Athanassiadis et al. "Particle shape effects on the stress response of granular packings". In: *Soft Matter* 10.1 (2014), pp. 48–59 (cit. on p. 1).

[8] C. Alexandrou, C. N. Papanicolas, and M. Vanderhaeghen. "Colloquium: The Shape of Hadrons". In: *Rev. Mod. Phys.* 84 (3 2012-09), pp. 1231–1251. DOI: `10.1103/RevModPhys.84.1231`. URL: `https://link.aps.org/doi/10.1103/RevModPhys.84.1231` (cit. on p. 1).

[9] E. M. Purcell. “Life at low Reynolds number”. In: *Physics and our world: reissue of the proceedings of a symposium in honor of Victor F Weisskopf*. World Scientific. 2014, pp. 47–67 (cit. on pp. 3, 5, 6).

[10] S. Kim and S. J. Karrila. *Microhydrodynamics: principles and selected applications*. Butterworth-Heinemann, 2013 (cit. on pp. 4, 9–11, 15, 24–26, 30–32, 38, 40, 42, 45–51, 58, 60, 65, 66, 68, 70, 76, 81, 86, 91–93, 114, 116).

[11] M. D. Graham. *Microhydrodynamics, Brownian Motion, and Complex Fluids*. Cambridge Texts in Applied Mathematics. Cambridge University Press, 2018 (cit. on pp. 4, 5, 10, 11, 14, 15, 25, 26, 31, 34).

[12] E. Guazzelli and J. F. Morris. *A physical introduction to suspension dynamics*. Vol. 45. Cambridge University Press, 2011 (cit. on pp. 4, 5, 8, 10, 11, 15, 25, 68, 70, 81).

[13] E. Lauga. *The fluid dynamics of cell motility*. Vol. 62. Cambridge University Press, 2020 (cit. on pp. 4, 7, 9, 25, 34).

[14] J. Happel and H. Brenner. *Low Reynolds number hydrodynamics: with special applications to particulate media*. Vol. 1. Springer Science & Business Media, 2012 (cit. on pp. 4, 8–10, 68, 70, 71, 76, 81).

[15] I. R. Thorp and J. R. Lister. “Motion of a non-axisymmetric particle in viscous shear flow”. In: *Journal of Fluid Mechanics* 872 (2019), pp. 532–559 (cit. on pp. 4, 71, 82).

[16] C. Pozrikidis. *Boundary integral and singularity methods for linearized viscous flow*. Cambridge university press, 1992 (cit. on pp. 4, 22, 25, 53, 57, 58, 60, 65, 66, 86).

[17] M. Braza, R. Perrin, and Y. Hoarau. “Turbulence properties in the cylinder wake at high Reynolds numbers”. In: *Journal of fluids and Structures* 22.6-7 (2006), pp. 757–771 (cit. on p. 4).

[18] M. C. Thompson, T. Leweke, and K. Hourigan. “Bluff bodies and wake–wall interactions”. In: *Annual Review of Fluid Mechanics* 53.1 (2021), pp. 347–376 (cit. on p. 4).

[19] J. Dorrepaal, M. O’neill, and K. Ranger. “Axisymmetric Stokes flow past a spherical cap”. In: *Journal of Fluid Mechanics* 75.2 (1976), pp. 273–286 (cit. on p. 5).

[20] J. Dorrepaal. “Stokes flow past a smooth cylinder”. In: *Journal of Engineering Mathematics* 12.2 (1978), pp. 177–185 (cit. on p. 5).

[21] E. Lauga and T. R. Powers. “The hydrodynamics of swimming microorganisms”. In: *Reports on Progress in Physics* 72.9 (2009-08), p. 096601. DOI: `10.1088/0034-4885/72/9/096601`. URL: `https://dx.doi.org/10.1088/0034-4885/72/9/096601` (cit. on pp. 5–7).

[22] E. Lauga. “Life around the scallop theorem”. In: *Soft Matter* 7.7 (2011), pp. 3060–3065 (cit. on pp. 5, 6).

[23] S. Alben and M. Shelley. “Coherent locomotion as an attracting state for a free flapping body”. In: *Proceedings of the National Academy of Sciences* 102.32 (2005), pp. 11163–11166 (cit. on p. 6).

[24] M. J. Shelley and J. Zhang. “Flapping and bending bodies interacting with fluid flows”. In: *Annual Review of Fluid Mechanics* 43.1 (2011), pp. 449–465 (cit. on p. 6).

[25] S. M. Bollens et al. “Cascading migrations and implications for vertical fluxes in pelagic ecosystems”. In: *Journal of Plankton Research* 33.3 (2011), pp. 349–355 (cit. on p. 7).

[26] A. W. Visser and T. Kiorboe. “Going ballistic in the plankton: Anisotropic swimming behavior of marine protists”. In: *Limnology and Oceanography* 59.4 (2014), pp. 1167–1176 (cit. on p. 7).

[27] J. M. Sullivan et al. “Small-scale turbulence affects the division rate and morphology of two red-tide dinoflagellates”. In: *Harmful Algae* 2.3 (2003), pp. 183–199 (cit. on pp. 7, 136).

[28] E. Berdalet et al. “Species-specific physiological response of dinoflagellates to quantified small-scale turbulence 1”. In: *Journal of Phycology* 43.5 (2007), pp. 965–977 (cit. on p. 7).

[29] W. H. Thomas and C. H. Gibson. “Effects of small-scale turbulence on microalgae”. In: *Journal of Applied Phycology* 2 (1990), pp. 71–77 (cit. on p. 7).

[30] A. Sengupta, F. Carrara, and R. Stocker. “Phytoplankton can actively diversify their migration strategy in response to turbulent cues”. In: *Nature* 543.7646 (2017), pp. 555–558 (cit. on p. 7).

[31] B. Hannisdal, J. Henderiks, and L. H. Liow. “Long-term evolutionary and ecological responses of calcifying phytoplankton to changes in atmospheric CO 2”. In: *Global Change Biology* 18.12 (2012), pp. 3504–3516 (cit. on p. 8).

[32] D. A. Hutchins and F. Fu. “Microorganisms and ocean global change”. In: *Nature microbiology* 2.6 (2017), pp. 1–11 (cit. on p. 8).

[33] D. A. Siegel et al. “Quantifying the ocean’s biological pump and its carbon cycle impacts on global scales”. In: *Annual review of marine science* 15.1 (2023), pp. 329–356 (cit. on p. 8).

[34] M. R. Stukel et al. “Carbon sequestration by multiple biological pump pathways in a coastal upwelling biome”. In: *Nature Communications* 14.1 (2023), p. 2024 (cit. on p. 8).

[35] G. Batchelor. “Sedimentation in a dilute dispersion of spheres”. In: *Journal of fluid mechanics* 52.2 (1972), pp. 245–268 (cit. on p. 8).

[36] H. Lamb. *Hydrodynamics*. Dover Books on Physics. Dover publications, 1945. ISBN: 9780486602561. URL: `https://books.google.co.in/books?id=237xDg7T0RkC` (cit. on p. 8).

[37] D. Collins et al. “Lord Kelvin’s isotropic helicoid”. In: *Physical Review Fluids* 6.7 (2021), p. 074302 (cit. on pp. 9, 69).

[38] T. A. Witten and H. Diamant. “A review of shaped colloidal particles in fluids: anisotropy and chirality”. In: *Reports on progress in physics* 83.11 (2020), p. 116601 (cit. on pp. 9, 68, 71, 72, 75, 76, 78, 86, 112, 171–173).

[39] E. Huseby et al. “Helical ribbons: Simple chiral sedimentation”. In: *Physical Review Fluids* 10.2 (2025), p. 024101 (cit. on p. 9).

[40] N. W. Krapf, T. A. Witten, and N. C. Keim. “Chiral sedimentation of extended objects in viscous media”. In: *Physical Review E* 79.5 (2009), p. 056307 (cit. on pp. 9, 69, 112).

[41] M. Palusa et al. “Sedimentation of a rigid helix in viscous media”. In: *Phys. Rev. Fluids* 3 (12 2018-12), p. 124301. DOI: `10.1103/PhysRevFluids.3.124301`. URL: `https://link.aps.org/doi/10.1103/PhysRevFluids.3.124301` (cit. on pp. 9, 69).

[42] T. Miara et al. “Dynamics of inertialess sedimentation of a rigid U-shaped disk”. In: *Communications Physics* 7.1 (2024), p. 47 (cit. on pp. 9, 69, 71, 75, 86, 112).

[43] C. Vaquero-Stainer et al. “U-shaped disks in Stokes flow: chiral sedimentation of a non-chiral particle”. In: *Journal of Fluid Mechanics* 999 (2024), A71 (cit. on pp. 9, 75).

[44] H. Brenner. “The Stokes resistance of an arbitrary particle—II: An extension”. In: *Chemical Engineering Science* 19.9 (1964), pp. 599–629 (cit. on pp. 9, 69).

[45] M. Makino et al. “Sedimentation of particles of general shape”. In: *Physics of Fluids* 17.4 (2005) (cit. on pp. 9, 71, 72, 86, 112, 171, 173).

[46] O. GONZALEZ, A. B. A. GRAF, and J. H. MADDOCKS. “Dynamics of a rigid body in a Stokes fluid”. In: *Journal of Fluid Mechanics* 519 (2004), pp. 133–160. DOI: `10.1017/S0022112004001284` (cit. on pp. 9, 75–77, 86, 112, 171).

[47] J. M. Crowley. “Viscosity-induced instability of a one-dimensional lattice of falling spheres”. In: *Journal of Fluid Mechanics* 45.1 (1971), pp. 151–159 (cit. on pp. 11, 18, 87–89, 99, 132).

[48] R. Chajwa et al. “Waves, algebraic growth, and clumping in sedimenting disk arrays”. In: *Physical Review X* 10.4 (2020), p. 041016 (cit. on pp. 11, 12, 88, 89, 92, 99, 102, 103, 106, 111, 132, 151).

[49] L. N. Trefethen and M. Embree. “Spectra and pseudospectra: the behavior of nonnormal matrices and operators”. In: (2020) (cit. on p. 13).

[50] K. G. Libbrecht. *Ken Libbrecht’s field guide to snowflakes*. Voyageur Press, 2016 (cit. on p. 13).

[51] Z. Li, H. Xue, and F. Yang. “A modeling study of ice formation affected by aerosols”. In: *Journal of Geophysical Research: Atmospheres* 118.19 (2013), pp. 11–213 (cit. on p. 13).

[52] A. A. Jensen et al. “Predicting ice shape evolution in a bulk microphysics model”. In: *Journal of the Atmospheric Sciences* 74.6 (2017), pp. 2081–2104 (cit. on p. 13).

[53] H. R. Pruppacher and J. D. Klett. *Microphysics of clouds and precipitation*. Springer Science & Business Media, 2012 (cit. on pp. 13, 15, 113, 114).

[54] T. Takahashi. “Riming electrification as a charge generation mechanism in thunderstorms”. In: *Journal of Atmospheric Sciences* 35.8 (1978), pp. 1536–1548 (cit. on p. 13).

[55] S. Twomey. “The electrification of individual cloud droplets”. In: *Tellus* 8.4 (1956), pp. 445–452 (cit. on pp. 13, 114).

[56] C. Saunders and S. Peck. “Laboratory studies of the influence of the rime accretion rate on charge transfer during crystal/graupel collisions”. In: *Journal of Geophysical Research: Atmospheres* 103.D12 (1998), pp. 13949–13956 (cit. on p. 13).

[57] M. Y. Luque et al. “Charge separation in collisions between ice crystals and a spherical simulated graupel of centimeter size”. In: *Journal of Geophysical Research: Atmospheres* 125.3 (2020), e2019JD030941 (cit. on p. 13).

[58] R. Bonnecaze and J. Brady. “A method for determining the effective conductivity of dispersions of particles”. In: *Proceedings of the Royal Society of London. Series A: Mathematical and Physical Sciences* 430.1879 (1990), pp. 285–313 (cit. on pp. 14, 42, 115, 116, 152).

[59] J. D. Jackson. *Classical electrodynamics*. John Wiley & Sons, 2012 (cit. on pp. 14, 34, 35, 38).

[60] A. Zangwill. *Modern electrodynamics*. Cambridge University Press, 2013 (cit. on pp. 14, 34, 35, 38–40, 115, 116).

[61] I. N. Derbenev et al. “Electrostatic interactions between spheroidal dielectric particles”. In: *The Journal of Chemical Physics* 152.2 (2020) (cit. on pp. 14, 114).

[62] M. Gorman, X. Ruan, and R. Ni. “Electrostatic interactions between rough dielectric particles”. In: *Physical Review E* 109.3 (2024), p. 034902 (cit. on p. 14).

[63] A. S. Khair. “Electrostatic forces on two almost touching nonspherical charged conductors”. In: *Journal of Applied Physics* 114.13 (2013) (cit. on p. 14).

[64] J. Lekner. *Electrostatics of conducting cylinders and spheres*. AIP Publishing, 2021 (cit. on pp. 14, 39, 40, 115).

[65] J. Lekner. “Electrostatics of two charged cylinders”. In: *Journal of Electrostatics* 118 (2022), p. 103721 (cit. on p. 14).

[66] J. C. Maxwell. *A treatise on electricity and magnetism*. Vol. 1. Clarendon press, 1873 (cit. on p. 15).

[67] J. Lekner. “Electrostatics of two charged conducting spheres”. In: *Proceedings of the Royal Society A: Mathematical, Physical and Engineering Sciences* 468.2145 (2012), pp. 2829–2848 (cit. on pp. 15, 114, 123, 124, 126).

[68] M. H. Davis. “Two charged spherical conductors in a uniform electric field: Forces and field strength”. In: *The Quarterly Journal of Mechanics and Applied Mathematics* 17.4 (1964), pp. 499–511 (cit. on p. 15).

[69] S. Grashchenkov. “On the force of electrostatic interaction between two conducting spheres”. In: *Technical Physics* 56 (2011), pp. 914–918 (cit. on p. 15).

[70] K. Kolikov et al. “Electrostatic interaction between two conducting spheres”. In: *Journal of Electrostatics* 70.1 (2012), pp. 91–96 (cit. on p. 15).

[71] W. B. Smythe. “Static and dynamic electricity”. In: (1988) (cit. on p. 15).

[72] B. Budak et al. “A collection of problems on mathematical physics”. In: *American Journal of Physics* 33.10 (1965), pp. 862–862 (cit. on p. 15).

[73] J. Lekner. “Regions of attraction between like-charged conducting spheres”. In: *American Journal of Physics* 84.6 (2016), pp. 474–477 (cit. on p. 15).

[74] P. Patra and A. Roy. “Brownian coagulation of like-charged aerosol particles”. In: *Physical Review Fluids* 7.6 (2022), p. 064308 (cit. on pp. 15, 113).

[75] P. Patra, D. L. Koch, and A. Roy. “Collision efficiency of like-charged spheres settling in a quiescent environment”. In: *Journal of Fluid Mechanics* 968 (2023), A22 (cit. on pp. 15, 113, 114).

[76] N. Thiruvenkadam et al. “Pair trajectories of uncharged conducting spheres in an electric field”. In: *Physics of Fluids* 35.3 (2023) (cit. on p. 15).

[77] G. Batchelor. “The stress system in a suspension of force-free particles”. In: *Journal of fluid mechanics* 41.3 (1970), pp. 545–570 (cit. on p. 15).

[78] G. Batchelor and J. Green. “The determination of the bulk stress in a suspension of spherical particles to order c2”. In: *Journal of Fluid Mechanics* 56.3 (1972), pp. 401–427 (cit. on p. 15).

[79] E. Hinch. “The measurement of suspension rheology”. In: *Journal of fluid mechanics* 686 (2011), pp. 1–4 (cit. on p. 15).

[80] J. F. Morris. “A review of microstructure in concentrated suspensions and its implications for rheology and bulk flow”. In: *Rheologica acta* 48 (2009), pp. 909–923 (cit. on p. 15).

[81] W. Van Saarloos, V. Vitelli, and Z. Zeravcic. *Soft Matter: Concepts, Phenomena, and Applications*. Princeton University Press, 2024 (cit. on pp. 15, 22).

[82] P. J. Armitage. *Astrophysics of planet formation*. Cambridge University Press, 2020 (cit. on p. 15).

[83] J. F. Kok et al. “The physics of wind-blown sand and dust”. In: *Reports on progress in Physics* 75.10 (2012), p. 106901 (cit. on p. 15).

[84] J. Bec, H. Homann, and S. S. Ray. “Gravity-driven enhancement of heavy particle clustering in turbulent flow”. In: *Physical review letters* 112.18 (2014), p. 184501 (cit. on pp. 15, 135).

[85] M. Wilkinson and B. Mehlig. “Caustics in turbulent aerosols”. In: *Europhysics Letters* 71.2 (2005), p. 186 (cit. on p. 15).

[86] A. Bhatnagar et al. “Rate of formation of caustics in heavy particles advected by turbulence”. In: *Philosophical Transactions of the Royal Society A* 380.2219 (2022), p. 20210086 (cit. on p. 15).

[87] W. W. Grabowski and L.-P. Wang. “Growth of cloud droplets in a turbulent environment”. In: *Annual review of fluid mechanics* 45.1 (2013), pp. 293–324 (cit. on pp. 15, 136, 137).

[88] L. Brandt and F. Coletti. “Particle-laden turbulence: progress and perspectives”. In: *Annual Review of Fluid Mechanics* 54.1 (2022), pp. 159–189 (cit. on p. 15).

[89] A. Johansen and A. Youdin. “Protoplanetary disk turbulence driven by the streaming instability: nonlinear saturation and particle concentration”. In: *The Astrophysical Journal* 662.1 (2007), p. 627 (cit. on pp. 16, 137).

[90] A. N. Youdin and J. Goodman. “Streaming instabilities in protoplanetary disks”. In: *The Astrophysical Journal* 620.1 (2005), p. 459 (cit. on pp. 16, 137).

[91] V. Pandey, P. Perlekar, and D. Mitra. “Clustering and energy spectra in two-dimensional dusty gas turbulence”. In: *Physical Review E* 100.1 (2019), p. 013114 (cit. on pp. 16, 19, 137, 138, 140, 141, 148).

[92] C. S. Peskin. “The immersed boundary method”. In: *Acta numerica* 11 (2002), pp. 479–517 (cit. on pp. 16, 138, 139).

[93] A. Prosperetti and G. Tryggvason. *Computational methods for multiphase flow*. Cambridge university press, 2009 (cit. on pp. 16, 66, 86, 121, 137, 149).

[94] R. Chajwa, N. Menon, and S. Ramaswamy. “Kepler orbits in pairs of disks settling in a viscous fluid”. In: *Physical Review Letters* 122.22 (2019), p. 224501 (cit. on pp. 18, 88, 92, 95, 96).

[95] D. L. Koch and E. S. Shaqfeh. “The instability of a dispersion of sedimenting spheroids”. In: *Journal of Fluid Mechanics* 209 (1989), pp. 521–542 (cit. on pp. 18, 19, 88, 108, 109, 112, 132–134).

[96] G. K. Batchelor. *An introduction to fluid dynamics*. Cambridge university press, 2000 (cit. on p. 22).

[97] L. D. Landau et al. *Electrodynamics of continuous media*. Vol. 8. elsevier, 2013 (cit. on pp. 34, 35, 39, 40, 115, 116).

[98] C. Pozrikidis. *A practical guide to boundary element methods with the software library BEMLIB*. CRC Press, 2002 (cit. on pp. 35, 67, 86, 121).

[99] A. Alawneh and R. Kanwal. “Singularity methods in mathematical physics”. In: *SIAM Review* 19.3 (1977), pp. 437–471 (cit. on pp. 38–40, 177).

[100] J. A. Stratton. *Electromagnetic theory*. Vol. 33. John Wiley & Sons, 2007 (cit. on pp. 39, 40, 115).

[101] L. F. Shatz. “Singularity method for oblate and prolate spheroids in Stokes and linearized oscillatory flow”. In: *Physics of Fluids* 16.3 (2004), pp. 664–677 (cit. on pp. 39, 93, 118).

[102] B. Friedman. *Principles and techniques of applied mathematics*. Courier Dover Publications, 1990 (cit. on pp. 57, 58, 60, 64, 66).

[103] A. Kurganov and S. Tsynkov. “On spectral accuracy of quadrature formulae based on piecewise polynomial interpolations”. In: *Center for Research in Scientific Computation, North Carolina State University, Technical Report No. CRSC-TR07-11* (2007) (cit. on p. 67).

[104] J. Bagge. “Accurate quadrature and fast summation in boundary integral methods for Stokes flow”. PhD thesis. KTH Royal Institute of Technology, 2023 (cit. on pp. 67, 121, 122).

[105] M. Abramowitz and I. Stegun. *Handbook of Mathematical Functions with Formulas, Graphs, and Mathematical Tables*. Applied mathematics series. U.S. Government Printing Office, 1964. URL: `https://books.google.co.in/books?id=mlAs1jYzI_QC` (cit. on p. 67).

[106] K. Atkinson. *The Numerical Solution of Integral Equations of the Second Kind*. Cambridge Monographs on Applied and Computational Mathematics. Cambridge University Press, 1997. ISBN: 9780521583916. URL: `https://books.google.co.in/books?id=COI3n5sGpB8C` (cit. on p. 67).

[107] Y. Saad and M. H. Schultz. “GMRES: A generalized minimal residual algorithm for solving nonsymmetric linear systems”. In: *SIAM Journal on scientific and statistical computing* 7.3 (1986), pp. 856–869 (cit. on pp. 67, 122).

[108] H. Joshi and R. Govindarajan. “Sedimentation Dynamics of Bodies with Two Planes of Symmetry”. In: *Phys. Rev. Lett.* 134 (1 2025-01), p. 014002. DOI: `10.1103/PhysRevLett.134.014002`. URL: `https://link.aps.org/doi/10.1103/PhysRevLett.134.014002` (cit. on p. 68).

[109] S. B. Field et al. “Chaotic dynamics of falling disks”. In: *Nature* 388.6639 (1997), pp. 252–254 (cit. on p. 68).

[110] H. Zhong, S. Chen, and C. Lee. “Experimental study of freely falling thin disks: Transition from planar zigzag to spiral”. In: *Physics of Fluids* 23.1 (2011) (cit. on p. 68).

[111] F. Auguste, J. Magnaudet, and D. Fabre. “Falling styles of disks”. In: *Journal of Fluid Mechanics* 719 (2013), pp. 388–405 (cit. on p. 68).

[112] M. D. Graham. *Microhydrodynamics, Brownian motion, and complex fluids*. Vol. 58. Cambridge University Press, 2018 (cit. on pp. 68, 70, 81).

[113] M. Cosentino Lagomarsino, I. Pagonabarraga, and C. P. Lowe. “Hydrodynamic Induced Deformation and Orientation of a Microscopic Elastic Filament”. In: *Phys. Rev. Lett.* 94 (14 2005-04), p. 148104. DOI: `10.1103/PhysRevLett.94.148104`. URL: `https://link.aps.org/doi/10.1103/PhysRevLett.94.148104` (cit. on p. 69).

[114] B. Moths and T. Witten. “Orientational ordering of colloidal dispersions by application of time-dependent external forces”. In: *Physical Review E—Statistical, Nonlinear, and Soft Matter Physics* 88.2 (2013), p. 022307 (cit. on pp. 71, 72, 75, 76, 86, 171, 173).

[115] E. Tozzi et al. “Settling dynamics of asymmetric rigid fibers”. In: *Physics of Fluids* 23.3 (2011) (cit. on pp. 74, 112).

[116] M. L. Ekiel-Jeżewska and E. Wajnryb. “Hydrodynamic orienting of asymmetric microobjects under gravity”. In: *Journal of Physics: Condensed Matter* 21.20 (2009), p. 204102 (cit. on p. 74).

[117] S. Ravichandran and J. S. Wettlaufer. “Orientation dynamics of two-dimensional concavo-convex bodies”. In: *Phys. Rev. Fluids* 8 (6 2023-06), p. L062301. DOI: `10.1103/PhysRevFluids.8.L062301`. URL: `https://link.aps.org/doi/10.1103/PhysRevFluids.8.L062301` (cit. on p. 74).

[118] C. Chicone. *Ordinary differential equations with applications*. Springer, 2006 (cit. on p. 78).

[119] P. E. Hydon. *Symmetry methods for differential equations: a beginner's guide*. 22. Cambridge University Press, 2000 (cit. on p. 81).

[120] J. Bagge and A.-K. Tornberg. “Highly accurate special quadrature methods for Stokesian particle suspensions in confined geometries”. In: *International Journal for Numerical Methods in Fluids* 93.7 (2021), pp. 2175–2224 (cit. on p. 86).

[121] H. Joshi et al. “Dynamics and clustering of sedimenting disc lattices”. In: *Journal of Fluid Mechanics* 1017 (2025), A1. DOI: 10.1017/jfm.2025.10467 (cit. on p. 87).

[122] S. Jung et al. “Periodic sedimentation in a Stokesian fluid”. In: *Phys. Rev. E* 74 (3 2006-09), p. 035302. DOI: 10.1103/PhysRevE.74.035302. URL: https://link.aps.org/doi/10.1103/PhysRevE.74.035302 (cit. on p. 88).

[123] G. B. Jeffery. “The motion of ellipsoidal pArticles immersed in a viscous fluid”. In: *Proceedings of the Royal Society of London. Series A, Containing papers of a mathematical and physical character* 102.715 (1922), pp. 161–179 (cit. on p. 88).

[124] S. Kim. “Sedimentation of two arbitrarily oriented spheroids in a viscous fluid”. In: *International journal of multiphase flow* 11.5 (1985), pp. 699–712 (cit. on pp. 88, 91, 93).

[125] E. Guazzelli and J. Hinch. “Fluctuations and Instability in Sedimentation”. In: *Annual Review of Fluid Mechanics* 43.1 (2011-01), pp. 97–116. ISSN: 1545-4479. DOI: 10.1146/annurev-fluid-122109-160736. URL: http://dx.doi.org/10.1146/annurev-fluid-122109-160736 (cit. on p. 88).

[126] M. B. Mackaplow and E. S. G. Shaqfeh. “A numerical study of the sedimentation of fibre suspensions”. In: *Journal of Fluid Mechanics* 376 (1998-12), pp. 149–182. ISSN: 1469-7645. DOI: 10.1017/s0022112098002663. URL: http://dx.doi.org/10.1017/S0022112098002663 (cit. on p. 88).

[127] K. Gustavsson and A.-K. Tornberg. “Gravity induced sedimentation of slender fibers”. In: *Physics of Fluids* 21.12 (2009-12). ISSN: 1089-7666. DOI: 10.1063/1.3273091. URL: http://dx.doi.org/10.1063/1.3273091 (cit. on p. 88).

[128] B. Metzger, E. Guazzelli, and J. E. Butler. “Large-Scale Streamers in the Sedimentation of a Dilute Fiber Suspension”. In: *Physical Review Letters* 95.16 (2005-10). ISSN: 1079-7114. DOI: 10.1103/physrevlett.95.164506. URL: http://dx.doi.org/10.1103/PhysRevLett.95.164506 (cit. on p. 88).

[129] R. Lahiri and S. Ramaswamy. “Are Steadily Moving Crystals Unstable?” In: *Phys. Rev. Lett.* 79 (6 1997-08), pp. 1150–1153. DOI: 10.1103/PhysRevLett.79.1150. URL: https://link.aps.org/doi/10.1103/PhysRevLett.79.1150 (cit. on p. 88).

[130] R. Chajwa. “Driven Stokesian Suspensions: Particle Anisotropy, Effective Inertia and Transient Growth”. PhD thesis. 2021. URL: `https://thesis.icts.res.in/thesis/ICTS-1612347864` (cit. on p. 90).

[131] L. Durlofsky, J. F. Brady, and G. Bossis. “Dynamic simulation of hydrodynamically interacting particles”. In: *Journal of fluid mechanics* 180 (1987), pp. 21–49 (cit. on p. 94).

[132] I. L. Claeys and J. F. Brady. “Suspensions of prolate spheroids in Stokes flow. Part 1. Dynamics of a finite number of pArticles in an unbounded fluid”. In: *Journal of Fluid Mechanics* 251 (1993), pp. 411–442 (cit. on pp. 94, 174).

[133] B. J. Berne and P. Pechukas. “Gaussian model potentials for molecular interactions”. In: *The Journal of Chemical Physics* 56.8 (1972), pp. 4213–4216 (cit. on p. 94).

[134] F. Günther, S. Frijters, and J. Harting. “Timescales of emulsion formation caused by anisotropic particles”. In: *Soft Matter* 10.27 (2014), pp. 4977–4989 (cit. on pp. 94, 95).

[135] A. J. Ladd and R. Verberg. “Lattice-Boltzmann simulations of particle-fluid suspensions”. In: *Journal of statistical physics* 104 (2001), pp. 1191–1251 (cit. on p. 94).

[136] J. E. Butler and E. S. Shaqfeh. “Dynamic simulations of the inhomogeneous sedimentation of rigid fibres”. In: *Journal of Fluid Mechanics* 468 (2002), pp. 205–237 (cit. on p. 95).

[137] R. Mari et al. “Shear thickening, frictionless and frictional rheologies in non-Brownian suspensions”. In: *Journal of Rheology* 58.6 (2014), pp. 1693–1724 (cit. on p. 95).

[138] G. Drazer et al. “Deterministic and stochastic behaviour of non-Brownian spheres in sheared suspensions”. In: *Journal of Fluid Mechanics* 460 (2002), pp. 307–335 (cit. on p. 95).

[139] A. K. Townsend. “The mechanics of suspensions”. PhD thesis. UCL (University College London), 2017 (cit. on p. 95).

[140] E. Fehlberg. *Low-order classical Runge-Kutta formulas with stepsize control and their application to some heat transfer problems*. Vol. 315. National aeronautics and space administration, 1969 (cit. on p. 100).

[141] L. N. Trefethen. “Pseudospectra of linear operators”. In: *SIAM review* 39.3 (1997), pp. 383–406 (cit. on p. 104).

[142] A. B. Burd and G. A. Jackson. "Particle Aggregation". In: *Annual Review of Marine Science* 1.Volume 1, 2009 (2009), pp. 65–90. ISSN: 1941-0611. DOI: `https://doi.org/10.1146/annurev.marine.010908.163904`. URL: `https://www.annualreviews.org/content/journals/10.1146/annurev.marine.010908.163904` (cit. on p. 112).

[143] J. Bec. "Fractal clustering of inertial pArticles in random flows". In: *Physics of fluids* 15.11 (2003), pp. L81–L84 (cit. on pp. 112, 137, 142).

[144] R. Monchaux, M. Bourgoin, and A. Cartellier. "Preferential concentration of heavy particles: a Voronoi analysis". In: *Physics of Fluids* 22.10 (2010), p. 103304 (cit. on p. 112).

[145] W. C. Reade and L. R. Collins. "Effect of preferential concentration on turbulent collision rates". In: *Physics of Fluids* 12.10 (2000), pp. 2530–2540 (cit. on p. 112).

[146] H. Joshi and R. Govindarajan. "Sedimentation Dynamics of Bodies with Two Planes of Symmetry". In: *Phys. Rev. Lett.* 134 (1 2025-01), p. 014002. DOI: `10.1103/PhysRevLett.134.014002`. URL: `https://link.aps.org/doi/10.1103/PhysRevLett.134.014002` (cit. on p. 112).

[147] H. Joshi and A. Roy. "Electrostatic interactions between anisotropic particles". In: *Phys. Rev. E* 111 (3 2025-03), p. 035410. DOI: `10.1103/PhysRevE.111.035410`. URL: `https://link.aps.org/doi/10.1103/PhysRevE.111.035410` (cit. on p. 113).

[148] T. B. Jones. *Electromechanics of particles*. Cambridge university press, 1995 (cit. on p. 113).

[149] C.-S. Wang. "Electrostatic forces in fibrous filters—a review". In: *Powder Technology* 118.1-2 (2001), pp. 166–170 (cit. on pp. 113, 135).

[150] S. Sun et al. "Electrostatics in computational biophysics and its implications for disease effects". In: *International Journal of Molecular Sciences* 23.18 (2022), p. 10347 (cit. on pp. 113, 135).

[151] T. D. Edwards and M. A. Bevan. "Controlling colloidal particles with electric fields". In: *Langmuir* 30.36 (2014), pp. 10793–10803 (cit. on pp. 113, 135).

[152] J. Dhanasekaran, A. Roy, and D. L. Koch. "Collision rate of bidisperse, hydrodynamically interacting spheres settling in a turbulent flow". In: *Journal of Fluid Mechanics* 912 (2021), A5 (cit. on p. 114).

[153] P. K. Wang and W. Ji. “Collision efficiencies of ice crystals at low intermediate Reynolds numbers colliding with supercooled cloud droplets: A numerical study”. In: *Journal of the atmospheric sciences* 57.8 (2000), pp. 1001–1009 (cit. on p. 114).

[154] A. Naso et al. “Collision rate of ice crystals with water droplets in turbulent flows”. In: *Journal of Fluid Mechanics* 845 (2018), pp. 615–641 (cit. on p. 114).

[155] N. Krasnogorskaya. “Warm cloud electricity”. In: *Planetary Electrodynamics, Volume 1* 1 (1969), p. 427 (cit. on p. 114).

[156] S. A. Colgate and J. M. Romero. “Charge versus drop size in an electrified cloud”. In: *Journal of geophysical research* 75.30 (1970), pp. 5873–5881 (cit. on p. 114).

[157] C. Trombley and M. Ekiel-Jeżewska. “Stable configurations of charged sedimenting particles”. In: *Physical Review Letters* 121.25 (2018), p. 254502 (cit. on p. 132).

[158] J. Meibohm et al. “Paths to caustic formation in turbulent aerosols”. In: *Physical Review Fluids* 6.6 (2021), p. L062302 (cit. on p. 135).

[159] A. Tsinober. *An informal conceptual introduction to turbulence*. Springer, 2009 (cit. on p. 136).

[160] U. Frisch and A. Kolmogorov. *Turbulence: The Legacy of A. N. Kolmogorov*. Cambridge University Press, 1995. ISBN: 9780521457132. URL: `https://books.google.co.in/books?id=-JcjT4wYgfgC` (cit. on pp. 136, 140).

[161] P. Davidson. *Turbulence: an introduction for scientists and engineers*. Oxford university press, 2015 (cit. on pp. 136, 140, 141).

[162] S. B. Pope. *Turbulent Flows*. Cambridge University Press, 2000 (cit. on pp. 136, 140).

[163] G. K. Vallis. *Atmospheric and oceanic fluid dynamics*. Cambridge University Press, 2017 (cit. on p. 136).

[164] A. Brandenburg and A. Lazarian. “Astrophysical hydromagnetic turbulence”. In: *Space Science Reviews* 178.2 (2013), pp. 163–200 (cit. on p. 136).

[165] B. G. Elmegreen and J. Scalo. “Interstellar turbulence I: observations and processes”. In: *Annu. Rev. Astron. Astrophys.* 42.1 (2004), pp. 211–273 (cit. on p. 136).

[166] R. A. Shaw. “Particle-turbulence interactions in atmospheric clouds”. In: *Annual Review of Fluid Mechanics* 35.1 (2003), pp. 183–227 (cit. on pp. 136, 137).

[167] J. Ruiz, D. Macías, and F. Peters. “Turbulence increases the average settling velocity of phytoplankton cells”. In: *Proceedings of the National Academy of Sciences* 101.51 (2004), pp. 17720–17724 (cit. on p. 136).

[168] S. Balachandar and J. K. Eaton. “Turbulent dispersed multiphase flow”. In: *Annual review of fluid mechanics* 42.1 (2010), pp. 111–133 (cit. on pp. 137, 149).

[169] S. Elghobashi. “On predicting particle-laden turbulent flows”. In: *Applied scientific research* 52.4 (1994), pp. 309–329 (cit. on p. 137).

[170] F. Toschi and E. Bodenschatz. “Lagrangian properties of particles in turbulence”. In: *Annual review of fluid mechanics* 41.1 (2009), pp. 375–404 (cit. on p. 137).

[171] K. D. Squires and J. K. Eaton. “Preferential concentration of particles by turbulence”. In: *Physics of Fluids A: Fluid Dynamics* 3.5 (1991), pp. 1169–1178 (cit. on p. 137).

[172] M. R. Maxey. “The gravitational settling of aerosol particles in homogeneous turbulence and random flow fields”. In: *Journal of fluid mechanics* 174 (1987), pp. 441–465 (cit. on p. 137).

[173] A. Ferrante and S. Elghobashi. “On the physical mechanisms of two-way coupling in particle-laden isotropic turbulence”. In: *Physics of fluids* 15.2 (2003), pp. 315–329 (cit. on p. 137).

[174] J. K. Eaton. “Two-way coupled turbulence simulations of gas-particle flows using point-particle tracking”. In: *International Journal of Multiphase Flow* 35.9 (2009), pp. 792–800 (cit. on p. 137).

[175] A. V. Nath, A. Roy, and M. H. Kasbaoui. “Instability of a dusty shear flow”. In: *Journal of Fluid Mechanics* 1002 (2025), A17 (cit. on p. 137).

[176] S. Shuai et al. “Instability of a dusty vortex”. In: *Journal of Fluid Mechanics* 948 (2022), A56 (cit. on p. 137).

[177] G. Boffetta and R. E. Ecke. “Two-dimensional turbulence”. In: *Annual review of fluid mechanics* 44.1 (2012), pp. 427–451 (cit. on pp. 140–142).

[178] R. H. Kraichnan. *Inertial ranges in two-dimensional turbulence*. Tech. rep. 1967 (cit. on p. 140).

[179] G. K. Batchelor. “Computation of the energy spectrum in homogeneous two-dimensional turbulence”. In: *The Physics of Fluids* 12.12 (1969), pp. II–233 (cit. on p. 140).

[180] D. Mitra and P. Perlekar. "Topology of two-dimensional turbulent flows of dust and gas". In: *Physical Review Fluids* 3.4 (2018), p. 044303 (cit. on pp. 142, 143, 149).

[181] A. Okubo. "Horizontal dispersion of floatable particles in the vicinity of velocity singularities such as convergences". In: *Deep sea research and oceanographic abstracts*. Vol. 17. 3. Elsevier. 1970, pp. 445–454 (cit. on p. 142).

[182] G. Haller. *Transport Barriers and Coherent Structures in Flow Data*. Cambridge University Press, 2023 (cit. on p. 143).

[183] Y.-K. Tsang et al. "Intermittency in two-dimensional turbulence with drag". In: *Physical Review E—Statistical, Nonlinear, and Soft Matter Physics* 71.6 (2005), p. 066313 (cit. on pp. 144, 145).

[184] G. A. Voth and A. Soldati. "Anisotropic particles in turbulence". In: *Annual Review of Fluid Mechanics* 49.1 (2017), pp. 249–276 (cit. on p. 149).

[185] G. Falkovich, A. Fouxon, and M. Stepanov. "Acceleration of rain initiation by cloud turbulence". In: *Nature* 419.6903 (2002), pp. 151–154 (cit. on p. 149).

[186] M. Wilkinson, B. Mehlig, and V. Bezuglyy. "Caustic activation of rain showers". In: *Physical review letters* 97.4 (2006), p. 048501 (cit. on p. 149).

[187] I. R. Thorp and J. R. Lister. "Motion of a non-axisymmetric particle in viscous shear flow". In: *Journal of Fluid Mechanics* 872 (2019), pp. 532–559. DOI: `10.1017/jfm.2019.367` (cit. on p. 151).

[188] A. T. Chwang and T. Y.-T. Wu. "Hydromechanics of low-Reynolds-number flow. Part 2. Singularity method for Stokes flows". In: *Journal of Fluid mechanics* 67.4 (1975), pp. 787–815 (cit. on pp. 152, 177).

Publications based on this thesis

1. **Harshit Joshi** and Rama Govindarajan. *Sedimentation dynamics of bodies with two planes of symmetry.* *Physical Review Letters 134 (1), 014002*
2. **Harshit Joshi**, Rahul Chajwa, Sriram Ramaswamy, Narayanan Menon, and Rama Govindarajan. *Dynamics and clustering of sedimenting disc lattices.* *Journal of Fluid Mechanics , Volume 1017*
3. **Harshit Joshi** and Anubhab Roy. *Electrostatic interactions between anisotropic particles.* *Physical Review E 111 (3), 035410*

In-preparation

1. **Harshit Joshi**, Prasad Perleker and Samriddhi Sankar Ray. *Intermittency and vorticity fluctuations in two-dimensional dusty turbulence.*

Other Publications

1. **Harshit Joshi** and Rama Govindarajan. *Finding Optimal Solutions Using Direct-Adjoint-Looping.* *Resonance 30 (7), 925-941*

A

Appendix for Chapter 3

A.1 Similarity between Poincaré maps with different reference times

Consider two Poincare maps $\mathcal{P}_{t_1}^{t_1+T_y}$ and $\mathcal{P}_{t_2}^{t_2+T_y}$ with $t_2 > t_1$ and T_y the same in both the maps. This map satisfies the following equation:

$$\mathcal{P}_{t_1}^{t_1+T_y} = \boldsymbol{\Phi}_{t_1}^{t_1+T_y}; \quad \dot{\boldsymbol{\Phi}}_{t_1}^{t_1+t} = A(t)\boldsymbol{\Phi}_{t_1}^{t_1+t}, \quad \boldsymbol{\Phi}_{t_1}^{t_1} = \mathbb{I}, \tag{A.1a}$$

$$\mathcal{P}_{t_2}^{t_2+T_y} = \boldsymbol{\Phi}_{t_2}^{t_1+T_y}; \quad \dot{\boldsymbol{\Phi}}_{t_2}^{t_2+t} = A(t)\boldsymbol{\Phi}_{t_2}^{t_2+t}, \quad \boldsymbol{\Phi}_{t_2}^{t_2} = \mathbb{I}. \tag{A.1b}$$

Claim: The two Poincare maps $\mathcal{P}_{t_1}^{t_1+T_y}$ and $\mathcal{P}_{t_2}^{t_2+T_y}$ are related by a similarity transformation.
Proof: Since $\boldsymbol{\Phi}_{t_2}^{t_2+t}\boldsymbol{\Phi}_{t_1}^{t_2} = \boldsymbol{\Phi}_{t_1}^{t_2+t}$, we have,

$$\mathcal{P}_{t_2}^{t_2+T_y}\boldsymbol{\Phi}_{t_1}^{t_2} = \boldsymbol{\Phi}_{t_1}^{t_2+T_y}. \tag{A.2}$$

Now, $\boldsymbol{\Phi}_{t_1}^{t_2+T_y} = \boldsymbol{\Phi}_{t_1+T_y}^{t_2+T_y}\boldsymbol{\Phi}_{t_1}^{t_1+T_y}$. Since $A(t+T_y) = A(t)$, we have:

$$\boldsymbol{\Phi}_{t_1}^{t_2} = \boldsymbol{\Phi}_{t_1+T_y}^{t_2+T_y} \implies \boldsymbol{\Phi}_{t_1}^{t_2+T_y} = \boldsymbol{\Phi}_{t_1}^{t_2}\boldsymbol{\Phi}_{t_1}^{t_1+T_y}. \tag{A.3}$$

Using this in equation (A.2) we get,

$$\mathcal{P}_{t_2}^{t_2+T_y}\boldsymbol{\Phi}_{t_1}^{t_2} = \boldsymbol{\Phi}_{t_1}^{t_2}\mathcal{P}_{t_1}^{t_1+T_y}. \tag{A.4}$$

Thus, the two Poincaré maps are related by a similarity transformation. The eigenvalues of these maps are therefore the same, and given by 1, $e^{\pm i\theta}$, where θ is only a function of T_y and hence $\theta = \theta(H)$.

A.2 Comment on the sedimentation dynamics of generic shape

A.2.1 Angular dynamics

The rate of change of the body attached coordinate axes is given by:

$$\dot{\boldsymbol{p}}_i = \boldsymbol{\Omega} \times \boldsymbol{p}_i = (\boldsymbol{b} \cdot \boldsymbol{F}) \times \boldsymbol{p}_i, \quad i \in \{1, 2, 3\}, \tag{A.5}$$

where $\boldsymbol{b}$ is the coupling tensor of a generic body (see equation (3.1)) and $\boldsymbol{F}$ is the dimensionless buoyancy corrected weight of the body. For generic bodies, $\boldsymbol{b}$ has a fuller form than for the di-bilaterals. In the $\{\boldsymbol{p}_i\}_{i\in\{1,2,3\}}$ basis, $\boldsymbol{b}$ is a shape dependent constant matrix and the dimensionless force is $\boldsymbol{F} = -\hat{\boldsymbol{y}} = -(p_{1y}\boldsymbol{p}_1 + p_{2y}\boldsymbol{p}_2 + p_{3y}\boldsymbol{p}_3)$[1]. Therefore, from equation (A.5):

$$\dot{\boldsymbol{p}}_i \cdot \hat{\boldsymbol{y}} = \dot{p}_{iy} = \hat{\boldsymbol{y}} \cdot [(\boldsymbol{b} \cdot \boldsymbol{F}) \times \boldsymbol{p}_i] = \boldsymbol{p}_i \cdot [\hat{\boldsymbol{y}} \times (\boldsymbol{b} \cdot \boldsymbol{F})] \tag{A.6}$$

In the $\{\boldsymbol{p}_i\}_{i\in\{1,2,3\}}$ basis, $\hat{\boldsymbol{y}} = (p_{1y}, p_{2y}, p_{3y}) = -\boldsymbol{F}$. Using this in equation (A.6) we have:

$$\dot{p}_{iy} = [\hat{\boldsymbol{y}} \times (\boldsymbol{b} \cdot \boldsymbol{F})]_i = -[(p_{1y}, p_{2y}, p_{3y}) \times \boldsymbol{b} \cdot (p_{1y}, p_{2y}, p_{3y})]_i \tag{A.7}$$

Therefore, the dynamics of the vertical projections $\boldsymbol{p}_y$ can be written in a compact form as:

$$\dot{\boldsymbol{p}}_y = (\boldsymbol{b} \cdot \boldsymbol{p}_y) \times \boldsymbol{p}_y. \tag{A.8}$$

This shows explicitly that even for generic bodies the $\boldsymbol{p}_y$ dynamics is closed in itself, i.e., it doesn't depend on the $\boldsymbol{p}_x$. This can also be seen from the rotational invariance in the body frame about the gravity axis. This compact formulation can also be found in [38, 114].

The previous studies on sedimentation of a generic body [38, 45, 46, 114] have shown the existence of stable, unstable, as well as centre fixed points in the $\boldsymbol{p}_y$ dynamics. The most interesting $\boldsymbol{p}_y$ dynamics reported by [45] and [114] are the closed periodic orbits and limit cycles in $\boldsymbol{p}_y$ dynamics. Thus, asymptotically, $\boldsymbol{p}_y$ dynamics can be at most periodic, if not steady.

The remaining part of the angular dynamics involves analyzing the $\boldsymbol{p}_x$ dynamics, which, to the best of our knowledge, has not been done before. Similar to the $\boldsymbol{p}_y$ dynamical system the $\boldsymbol{p}_x$ dynamics can be written compactly as:

$$\dot{\boldsymbol{p}}_x = (\boldsymbol{b} \cdot \boldsymbol{p}_y) \times \boldsymbol{p}_x \equiv A[\boldsymbol{p}_y(t)]\boldsymbol{p}_x, \tag{A.9}$$

---

[1] Note that gravity is taken to be along $-\hat{\boldsymbol{y}}$

where $\boldsymbol{A}_{ik} = -\epsilon_{ijk}(\boldsymbol{b}\cdot\boldsymbol{p}_y)_j$ and $\boldsymbol{b}$ is the coupling matrix for a generic body written in the body frame (which will have a fuller form unlike the one for di-bilaterals). This shows that the $\boldsymbol{p}_x$ is still a linear non-autonomous dynamical system driven by $\boldsymbol{p}_y$ dynamics. If $\boldsymbol{p}_y$ settles into a stable fixed point, the $\boldsymbol{p}_x$ dynamics will be, in general, periodic, provided $\boldsymbol{b}\cdot\boldsymbol{p}_y \neq 0$. If $\boldsymbol{p}_y$ performs a periodic orbit asymptotically, the corresponding $\boldsymbol{p}_x$ dynamics can be either quasi-periodic or periodic, which can again be studied using Floquet theory.

A.2.2 Persistent drift in a generic body

The proof provided in section 3.8.1 for a di-bilateral flutterer is extended in this section to bodies of arbitrary shape that can flutter. The translational velocity of a generic body in the lab frame is given by:

$$v_x = \sum_{ij} c_{ij}^{(x)} p_{iy} p_{jx} \tag{A.10}$$

$$v_y = \sum_{ij} c_{ij}^{(y)} p_{iy} p_{jx} \tag{A.11}$$

$$v_z = \sum_{ij} c_{ij}^{(z)} p_{iy} p_{jx}, \tag{A.12}$$

where $c_{ij}^{(x/y/z)}$ are related to the mobility matrix of the generic body under consideration.

The case where $\boldsymbol{p}_y$ reaches a stable fixed point has been discussed in [38]. For completeness, we state their results below. As discussed in [38], there are the following two possibilities when $\boldsymbol{p}_y$ is at a fixed point:

1. $\boldsymbol{b}\cdot\boldsymbol{p}_y^* = \boldsymbol{0}$: In this case, the body ceases to rotate (just like settlers and drifters for di-bilaterals). The $\boldsymbol{p}_x$ becomes a constant, and v_x, v_z, or both can be non-zero, resulting in persistent drift.

2. $\boldsymbol{b}\cdot\boldsymbol{p}_y^* = \lambda\boldsymbol{p}_y^*$, $\lambda \neq 0$: In this case, the $\boldsymbol{p}_x$ performs a periodic orbit, resulting in no persistent drift in one time period. Note that $\dot{\boldsymbol{p}}_x = \lambda\boldsymbol{p}_y^* \times \boldsymbol{p}_x \neq 0$ and hence $\boldsymbol{p}_x$ cannot be static. In this case, the angular velocity of the body $\boldsymbol{\Omega}$ aligns with the gravity and the body falls in a helical trajectory.

Note that the $\boldsymbol{p}_y$ dynamical system for an arbitrary-shaped body is still quadratic in $\boldsymbol{p}_y$ and the $\boldsymbol{p}_x$ dynamical system has the same form as that for di-bilaterals. For the case where $\boldsymbol{p}_y$ remains in a closed periodic orbit, the proof given in section 3.8.1 works for an arbitrary body as well, and so there is a persistent drift only when the time period of $\boldsymbol{p}_y$ dynamics is exactly the same as the time period of the $\boldsymbol{p}_x$ dynamics. Since the limiting behaviours of the $\boldsymbol{p}_y$ dynamics are either fixed points or periodic orbits [38, 45, 114], the cases discussed are exhaustive. Therefore, we conclude that *any arbitrary body that performs periodic/quasi-periodic motion cannot drift persistently, except for the special case where its frequency of the* $\boldsymbol{p}_x$ *dynamics is exactly equal to the frequency of the* $\boldsymbol{p}_y$ *dynamics.*

B

APPENDIX FOR CHAPTER 4

B.1 Finding points of closest approach between two discs

This section describes the algorithm to find the minimum distance between two spheroids. We extend the algorithm of Claeys et al. [132] for prolate spheroids to the case of a pair of oblate spheroids (discs). The main idea is to exploit the fact that the outward normal vectors of two spheroids at their points of closest distance are antiparallel. Any point $\boldsymbol{x}$ on the surface of the disc α can be defined by

$$(\boldsymbol{x}-\boldsymbol{x}_\alpha)^T \cdot \boldsymbol{\Sigma}_\alpha \cdot (\boldsymbol{x}-\boldsymbol{x}_\alpha) = 1, \tag{B.1}$$

where $\boldsymbol{x}_\alpha$ is the centre of the disc α, and

$$\boldsymbol{\Sigma}_\alpha = \left[\frac{\boldsymbol{p}_\alpha \boldsymbol{p}_\alpha}{b^2} + \frac{(\boldsymbol{\delta} - \boldsymbol{p}_\alpha \boldsymbol{p}_\alpha)}{a^2}\right] \tag{B.2}$$

is known as the weight matrix with $b = a\sqrt{1-e^2}$. Taking the gradient of (B.1) gives us the normal vector to the disc at $\boldsymbol{x}$:

$$\boldsymbol{n}_\alpha(\boldsymbol{x}) = \frac{\boldsymbol{\Sigma}_\alpha \cdot (\boldsymbol{x}-\boldsymbol{x}_\alpha)}{|\boldsymbol{\Sigma}_\alpha \cdot (\boldsymbol{x}-\boldsymbol{x}_\alpha)|}. \tag{B.3}$$

We start with two points $\boldsymbol{y}_\alpha^{(0)}$ and $\boldsymbol{y}_\beta^{(0)}$ on discs α and β respectively, and construct a sequence of points $\boldsymbol{y}_\alpha^{(k)}$ and $\boldsymbol{y}_\beta^{(k)}$ following the iterative procedure outlined below to converge rapidly to the points of closest distance between discs α and β:

- Construct a normal vector $\boldsymbol{n}_\alpha$ at $\boldsymbol{y}_\alpha^{(k)}$. Find the point of intersection of the line along $\boldsymbol{n}_\alpha$ passing through $\boldsymbol{y}_\alpha^{(k)}$ and the mid-plane of the oblate spheroid α (see figure B.1). Call this point $\boldsymbol{\chi}_\alpha^{(k)}$. Repeat for the disc β.

- Construct a line joining $\chi_\alpha^{(k)}$ and $\chi_\beta^{(k)}$. The points of intersection of this line and the two discs give the next iterates $\boldsymbol{y}_\alpha^{(k+1)}$ and $\boldsymbol{y}_\beta^{(k+1)}$.

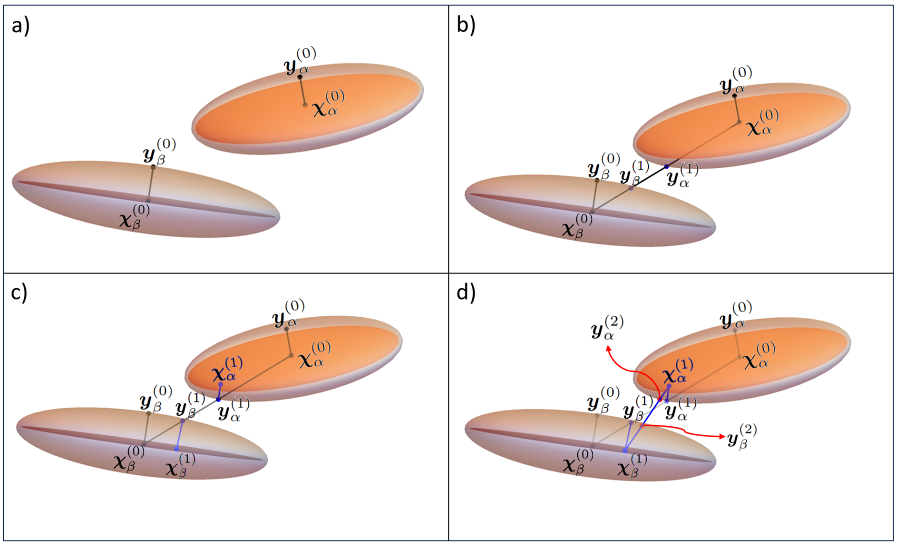

Figure B.1: Choosing any points $\boldsymbol{y}_\alpha^{(0)}$ and $\boldsymbol{y}_\beta^{(0)}$ on the discs, one can reach the closest points iteratively by following the algorithm described in the text. The panels a) to d) show the candidate points obtained for the closest points after two iterations. The dark plane in the figures defines the confocal disc at the midplane of the oblate spheroid.

Thus, one can find the minimum separation vector $\boldsymbol{\epsilon}_{\alpha\beta}$ as:

$$\boldsymbol{\epsilon}_{\alpha\beta} = \boldsymbol{y}_\alpha - \boldsymbol{y}_\beta, \quad \boldsymbol{y}_\alpha = \lim_{k\to\infty} \boldsymbol{y}_\alpha^{(k)}, \quad \boldsymbol{y}_\beta = \lim_{k\to\infty} \boldsymbol{y}_\beta^{(k)}. \tag{B.4}$$

The numerical value of the closest distance can be obtained by repeating the two steps described above until the current and the previous iterations differ by some small tolerance value. The algorithm described above converges to the points of closest distance when the discs are not overlapping, with a minimum separation vector $\boldsymbol{\epsilon}$.

C

Appendix for Chapter 5

C.1 Far field interaction of a prolate spheroid and a sphere

With the procedure for two spheroids explained in **Chapter 2** of this thesis, it is easy to look at a special case where the second spheroid is a sphere. This simplification is analytically tractable to obtain closed-form expressions without losing the flavor of anisotropy in the problem. Consider a spheroid S_1 centered at $\boldsymbol{x}_1$ with semi-major axis a, aspect ratio κ, eccentricity $e \equiv \sqrt{1-\kappa^{-2}}$ and orientation vector $\boldsymbol{p}$, carrying total charge Q_1. The second conductor is a sphere S_2 centered at $\boldsymbol{x}_2$ with radius γa and total charge Q_2. The relative separation vector between them is $\boldsymbol{x}_{21} \equiv \boldsymbol{x}_2 - \boldsymbol{x}_1 \equiv -\boldsymbol{x}_{12}$. The relation between the surface potentials of S_1 and S_2 can be found by either taking the limit $e_2 \longrightarrow 0$ in the analysis of **Chapter 2** or by applying the method of reflection to this system. The results up to the second reflection are stated as follows

$$V_1 = \frac{Q_1}{4\pi a \varepsilon_0}\left(\frac{\operatorname{arctanh} e}{e}\right) + V_1^{(1)} + V_1^{(2)}, \tag{C.1a}$$

$$V_2 = \frac{Q_2}{4\pi\varepsilon_0 \gamma a} + V_2^{(1)} + V_2^{(2)}, \tag{C.1b}$$

where

$$V_1^{(1)} = \frac{Q_2}{8\pi a e \varepsilon_0}\int_{-ae}^{ae} \mathcal{G}(\boldsymbol{x}_1 + \xi\boldsymbol{p}, \boldsymbol{x}_2)\, d\xi, \tag{C.2a}$$

$$V_2^{(1)} = \frac{Q_1}{8\pi a e \varepsilon_0}\int_{-ae}^{ae} \mathcal{G}(\boldsymbol{x}_2, \boldsymbol{x}_1 + \xi\boldsymbol{p})\, d\xi, \tag{C.2b}$$

and

$$V_1^{(2)} = -\frac{1}{8\pi a e \varepsilon_0}\int_{-ae}^{ae} \boldsymbol{d}_2^{(1)} \cdot \nabla_{x_1}\mathcal{G}(\boldsymbol{x}_1 + \xi\boldsymbol{p}, \boldsymbol{x}_2)\, d\xi, \tag{C.3a}$$

$$V_2^{(2)} = \frac{3}{8\pi a^3 e^3 \varepsilon_0} \int_{-ae}^{ae} \boldsymbol{d}_1^{(1)} \cdot \Big\{ \boldsymbol{p}\, \xi\, \mathcal{G}(\boldsymbol{x}_2, \boldsymbol{x}_1 + \xi \boldsymbol{p}) \\ - \frac{1}{2}(a^2 e^2 - \xi^2)(\boldsymbol{\delta} - \boldsymbol{pp}) \cdot \boldsymbol{\nabla}_{\boldsymbol{x}_2} \mathcal{G}(\boldsymbol{x}_2, \boldsymbol{x}_1 + \xi \boldsymbol{p}) \Big\}\, d\xi. \quad \text{(C.3b)}$$

Here, the dipole moments are given by

$$\boldsymbol{d}_1^{(1)} = -4\pi a^3 Q_2 \frac{3}{8\pi a^3 e^3} \int_{-ae}^{ae} \Big\{ X_p^C \boldsymbol{p}\, \xi\, \mathcal{G}(\boldsymbol{x}_1 + \xi \boldsymbol{p}, \boldsymbol{x}_2) \\ + \frac{1}{2} Y_p^C (a^2 e^2 - \xi^2)(\boldsymbol{\delta} - \boldsymbol{pp}) \cdot \boldsymbol{\nabla}_{\boldsymbol{x}_1} \mathcal{G}(\boldsymbol{x}_1 + \xi \boldsymbol{p}, \boldsymbol{x}_2) \Big\}\, d\xi, \quad \text{(C.4a)}$$

$$\boldsymbol{d}_2^{(1)} = -4\pi \gamma^3 a^3 Q_1 \frac{1}{2ae} \boldsymbol{\nabla}_{\boldsymbol{x}_2} \int_{-ae}^{ae} \mathcal{G}(\boldsymbol{x}_2, \boldsymbol{x}_1 + \xi \boldsymbol{p})\, d\xi. \quad \text{(C.4b)}$$

These line integrals over $\mathcal{G}$ can be computed analytically [99, 188]. After some algebra, we arrive at the closed-form expressions for the potentials given by

$$V_1^{(1)} = \frac{Q_2}{4\pi a \varepsilon_0} \frac{1}{2e} \ln \left(\frac{z_{12} - ae - R_-}{z_{12} + ae - R_+} \right), \quad V_2^{(1)} = \frac{Q_1}{Q_2} V_1^{(1)}, \quad \text{(C.5a)}$$

where

$$R_\pm \equiv \sqrt{\rho_{12}^2 + (z_{12} \pm ae)^2}, \\ \rho_{12}^2 \equiv \boldsymbol{x}_{12} \cdot (\boldsymbol{\delta} - \boldsymbol{pp}) \cdot \boldsymbol{x}_{12}, \quad z_{12} \equiv \boldsymbol{x}_{12} \cdot \boldsymbol{p}. \quad \text{(C.6)}$$

The second-order corrections are given by

$$V_1^{(2)} = -\frac{Q_1}{4\pi a \varepsilon_0} \frac{a^2 \gamma^3}{4e^2} \Bigg[\left(\frac{1}{R_-} - \frac{1}{R_+} \right)^2 \\ + \rho_{12}^2 \left(\frac{1}{R_+(z_{12} + ae - R_+)} - \frac{1}{R_-(z_{12} - ae - R_-)} \right)^2 \Bigg], \quad \text{(C.7)}$$

$$V_2^{(2)} = -\frac{Q_2}{4\pi a \varepsilon_0} \frac{9}{4a^2 e^6} \Bigg[X_p^C \left\{ R_- - R_+ + z_{12} \ln \left(\frac{z_{12} - ae - R_-}{z_{12} + ae - R_+} \right) \right\}^2 \\ + \frac{Y_p^C}{4} \left\{ \frac{z_{12}}{\rho_{12}} (R_- - R_+) + \frac{ae}{\rho_{12}} (R_- + R_+) - \rho_{12} \ln \left(\frac{z_{12} - ae - R_-}{z_{12} + ae - R_+} \right) \right\}^2 \Bigg]. \quad \text{(C.8)}$$

Recall that X_p^C and Y_p^C are given by equation (5.7).

C.2 Far field interaction of an oblate spheroid and a sphere

The eccentricity transformation $e \to \dfrac{ie}{\sqrt{1-e^2}}$ allows us to directly obtain the surface potential from the prolate spheroid and sphere case, given below.

$$V_1 = \frac{Q_1}{4\pi a \varepsilon_0}\left(\frac{\kappa \arcsin e}{e}\right) + V_1^{(1)} + V_1^{(2)}, \tag{C.9a}$$

$$V_2 = \frac{Q_2}{4\pi\varepsilon_0 \gamma a} + V_2^{(1)} + V_2^{(2)}, \tag{C.9b}$$

The first order corrections are:

$$V_1^{(1)} = \frac{Q_2}{4\pi a\varepsilon_0}\frac{\kappa}{e}\,\mathrm{arccot}\left(\frac{z_{12}-u}{v-ae/\kappa}\right), \quad V_2^{(1)} = \frac{Q_1}{Q_2}V_1^{(1)}, \tag{C.10a}$$

where

$$u \equiv \sqrt{\frac{\mu}{2}+\sqrt{\frac{\mu^2}{4}+\frac{a^2e^2}{\kappa^2}z_{12}^2}},$$
$$\mu \equiv |\boldsymbol{x}_{12}|^2 - \frac{a^2e^2}{\kappa^2}, \quad v \equiv \frac{aez_{12}}{\kappa u}. \tag{C.11}$$

The second-order corrections are given by:

$$V_1^{(2)} = -\frac{Q_1}{4\pi a\varepsilon_0}\frac{\kappa^2a^2\gamma^3}{4e^2}\left[\left(\frac{2v}{u^2+v^2}\right)^2 + \rho_{12}^2\left\{\frac{4ae\kappa^{-1}z_{12}-2(z_{12}v+ae\kappa^{-1}u)}{(u^2+v^2)((z_{12}-u)^2+(ae\kappa^{-1}-v)^2)}\right\}^2\right], \tag{C.12a}$$

$$V_2^{(2)} = -\frac{Q_2}{4\pi a\varepsilon_0}\frac{9\kappa^6}{a^2e^6}\left[X_o^C\left\{v - z_{12}\,\mathrm{arccot}\left(\frac{z_{12}-u}{v-ae\kappa^{-1}}\right)\right\}^2 + \frac{1}{4}Y_o^C\left\{\frac{ae\kappa^{-1}u-z_{12}v}{\rho_{12}} - \rho_{12}\,\mathrm{arccot}\left(\frac{z_{12}-u}{v-ae\kappa^{-1}}\right)\right\}^2\right]. \tag{C.12b}$$

Recall that X_o^C and Y_o^C are given by equation (5.11a).